ANISOTROPY STUDIES OF THE HIRES EHECR

By

Jose A. Bellido BSc, MSc.

Thesis

submitted for the degree of

DOCTOR OF PHILOSOPHY

at the

UNIVERSITY OF ADELAIDE

(Department of Physics and Mathematical Physics)

December 2002

Contents

Originality declaration ix

Abstract xi

Acknowledgments xiii

List of Figures xxxvi

List of Tables xxxviii

1 Introduction 1

1.1 Origin of EHECR 4

1.1.1 "Bottom-up" acceleration mechanisms 4

1.1.1.1 Fast rotating magnetic field scenarios: 5

1.1.1.2 Relativistic shock waves scenarios: 6

1.1.2 "Top-down" acceleration mechanisms 9

1.2 Propagation of the EHECR 10

1.3 Detection of the EHECR 14

1.3.1 The first generation of EHECR detectors 15

1.3.1.1 Volcano Ranch: 15

1.3.1.2 Haverah Park: 15

1.3.1.3 SUGAR: 15

1.3.1.4 Yakutsk: 16

1.3.1.5 Fly's Eye: 16

1.3.2 EHECR detectors currently in operation 17
1.3.2.1 The Akeno Giant Air Shower Array (AGASA) 17
1.3.2.2 The High Resolution Fly's Eye Cosmic Ray Detector (HiRes) 17
1.3.3 Future EHECR detectors 18
1.3.3.1 The Pierre Auger Detector 18
1.3.3.2 OWL and EUSA 19

2 Anisotropy studies of EHECRs (review) 21
2.1 Anisotropy of cosmic rays with energies around 10^{18} eV 24
2.1.1 Correlations with the Galactic Centre 24
2.1.2 Anisotropy from Cygnus X-3 28
2.2 Anisotropy of cosmic rays with energies above $10^{18.5}$ eV 30
2.2.1 Correlations with the Galactic and Supergalactic planes 30
2.2.2 Clustering of the EHECR 35
2.3 Correlation of the EHECR with galaxy directions 37

3 The SUGAR excess from the Galactic centre region 41
3.1 Analysis 41
3.2 Discussion 46
3.3 Conclusion 51

4 The HiRes Detector 53
4.1 Air fluorescence yield 56
4.2 HiRes-1 site 59
4.3 HiRes-2 site 61
4.4 Mirror-cluster calibration 62
4.5 Atmospheric calibration 64
4.5.1 Inter-Site flasher 64
4.5.2 Vertical flashers 65

4.5.3 Steerable YAG lasers 65
4.5.4 Cloud monitors 65
4.6 Energy reconstruction 66
4.7 Energy spectrum 69

5 Preparing for geometrical reconstruction **73**
5.1 Estimating the clock offset between HiRes1 and HiRes-2 74
5.1.1 Results of the time offset analysis 75
5.1.1.1 January 15, 2000 75
5.1.1.2 February 03, 2000 77
5.1.1.3 February 28, 2000 81
5.1.1.4 March 05, 2000 83
5.1.2 Time slewing and the intersite time offset 84
5.1.3 Conclusion 87
5.2 Algorithm to filter noise tubes at HiRes 88
5.2.1 Event trigger requirements 90
5.2.2 Description of the noise tubes filtering algorithm 92
5.2.3 Test of the algorithm 96
5.2.4 Interesting features 98

6 HiRes-1 monocular geometrical reconstruction **107**
6.1 Monocular data 108
6.2 Monocular results against stereo results 110
6.2.1 Interesting features 112
6.3 Monocular results against MC inputs 113
6.4 Quality cuts 121
6.5 Estimated uncertainty in psi 123
6.5.1 Quality code 125
6.6 Good quality events 129
6.7 Conclusions 135

7 HiRes stereo geometrical reconstruction **139**

7.1 Geometry reconstruction techniques 141

7.1.1 First Guess: 141

7.1.2 Stereo geometry reconstruction 142

7.1.3 Hybrid geometry reconstruction 145

7.1.3.1 Time slewing 145

7.1.3.2 Timing χ^2 function (χ^2_{time}) 149

7.2 Test of the reconstruction techniques 150

7.2.1 Uncertainty of the reconstructed orientation 153

8 HiRes anisotropy studies **167**

8.1 Shower density contour plots technique 168

8.1.1 Astrophysically smeared sources 171

8.1.2 Point Sources 172

8.1.3 Summary 173

8.1.4 Calculating the background density 175

8.2 HiRes-1 anisotropy results 179

8.2.1 Cosmic rays with energies above 10^{18} eV 179

8.2.1.1 Searching for point sources 179

8.2.1.2 Searching for astrophysically smeared sources 188

8.2.1.3 Cygnus X-3 195

8.2.2 Cosmic rays with energies above 10^{19} eV 195

8.2.2.1 Searching for point sources 195

8.2.2.2 Searching for astrophysical smeared sources 198

8.2.3 Cosmic rays with energies above 4×10^{19} eV 199

8.3 Preliminary HiRes stereo results 201

9 Summary and Conclusions **207**

A Fermi Acceleration **213**

B The Profile Constrained Geometry Fit (PCGF) **219**

References **223**

Originality declaration

This work contains no material which has been accepted for the award of any other degree or diploma in any university or other tertiary institution and, to the best of my knowledge and belief, contains no material previously published or written by another person, except where due reference has been made in the text.
I give consent to this copy of my thesis, when deposited in the University Library, being available for loan and photocopying.

Signed: . dated: 11/03/2003

Jose A. Bellido BSc, MSc.

Abstract

In this thesis I present studies of the EHECR ($E > 10^{18}$ eV) arrival directions using the data from the HiRes cosmic ray detector. The aims are to look for evidence of any cosmic ray anisotropy in any particular direction, especially in the directions of *a priori* selected source candidates (Cygnus X-3, Virgo A, the AGASA triplet and the supergalactic plane). To perform these anisotropy studies it was necessary to determine in advance the uncertainties of the reconstructed cosmic ray arrival directions.

The early chapters of my thesis give an introduction to cosmic ray physics and a review of anisotropy studies undertaken by several groups. In Chapter 4, I describe in some detail the High Resolution Fly's Eye (HiRes) detector. In Chapters 5, 6, and 7, I present details of the geometry reconstruction of the arrival directions of cosmic rays (monocular and stereo events) and estimations of the uncertainties in the reconstructed arrival directions. In Chapter 8, I present the results of the arrival direction anisotropy analysis. Finally in Chapter 9, I present a summary and conclusions.

Acknowledgments

In the past three months I was wishing for the moment of writing this last part of the thesis. It is not only because I wanted to say thanks to many people. But, it is also because it means that I finally finished writing my thesis.

Especial thanks go to my supervisors Roger Clay and Bruce Dawson. Thanks to their guidance and invaluable support it was possible to complete my PhD in the period of my scholarship. Another especial thanks to my lovely wife for her hard work in the last months caring of our little daughter, while I was writing my thesis. Thanks to my parents Wilbert and Vilma, "*Gracias papá y mamá*".

I also want to thanks to the present and former members of the astrophysics group at University of Adelaide for the discussions, suggestions and friendship, in particular to Greg Thornton, Ken Simpson, Hayley Bignal, Gail Higginbottom, Alina Donea and Martin Debes.

Thanks also to the people at the University of Utah for their hospitality while I was there. Thanks to Kevin Reil and Zhen Cao for their help in several processing and software issues.

I will not miss to thank my former supervisor Carlos Ourivio Escobar for introducing me to the fascinating world of energetic cosmic rays.

Finally I want to thanks the Australian Government and the University of Adelaide for granting my PhD scholarship.

List of Figures

1.1 Differential energy spectrum of cosmic ray flux as a function of energy [7]. On this figure, integrated fluxes above three energy values are also indicated. The data points are collected from the following experiments: LEAP, Proton, Akeno, AGASA, Fly's Eye, Haverah Park, Yakutsk. 3

1.2 Size and magnetic field strength of possible accelerations sites. Objects below the diagonal lines cannot accelerate the corresponding elements. This particular version of the Hillas diagram[13] was obtained from [7]. 8

1.3 Expected angular deflection (eq. 1.3) in the propagation of cosmic protons through the extragalactic magnetic field as a function of the proton energy. Assuming a largest turbulence scale of 1 Mpc, intergalactic magnetic field of 1 nG and $K = 4°$. The upper and lower lines correspond for 200 Mpc and 30 Mpc propagation distances respectively 12

1.4 Energy of a proton as a function of the propagation distance[32]. 14

1.5 Schematic representation of the EUSO field of view over the Earth's atmosphere. The EAS size through the atmosphere is also represented[12]. 20

2.1 Results of the first harmonic analysis in right ascension. The k value of the anisotropy in each energy bin is plotted as a function of the primary energy[47]. 25

2.2 Statistical significance of the observed AGASA excess and deficit [48]. The sky map is in equatorial coordinates. 26

2.3 Position of the Solar system in relation with the spiral arms of the galaxy [50]. The directions of the observed AGASA excesses are indicated by the hatched regions. 27

2.4 Cygnus X-3 is at the centre of this contour plot. The plot is 20° × 20°, with declination increasing vertically and right ascension increasing to left. (The horizontal dimension is 20° true, not 20° of right ascension.) The dots are points of the galactic plane separated by 1° longitude. The contour lines map represent the significance of the shower density excess observed by the **Fly's Eye experiment**. Their σ values are 1.0, 1.5, 2.0, 2.5, 3.0, 3.5, and 4.0. Only events with energies above 5×10^{17} were considered [51]. 29

2.5 The contour lines map represent the significance of the shower density excess observed by the **Akeno array**. Their σ values go in steps of 0.5 deg. The peak around the Cygnus region correspond to a 3.5σ excess. The dots represent the arrival direction of each event. Only events with energies above 5×10^{17} were considered [52]. 29

2.6 The Wdowczyk-Wolfendale parameter, f_E as a function of energy.The diagram includes data from: Akeno (solid circles), Haverah Park (diamonds), Yakutsk (crosses) and SUGAR (open circles)[56] 31

2.7 The Wdowczyk-Wolfendale parameter f_E as a function of energy estimated by AGASA[9]. The left plot is the f_E using galactic latitudes, and the right plot is using supergalactic latitudes. 32

2.8 The Wdowczyk-Wolfendale parameter f_E as a function of energy estimated by the Fly's Eye[8].The left plot is the f_E using galactic latitudes, and the right plot is using supergalactic latitudes. The open circles and open squares show the estimated f_E assuming an isotropic flux of cosmic rays. 32

2.9 Significance map of AGASA cosmic ray excess/deficit above 4×10^{19} eV. The dashed and dash-dotted curves indicate the Galactic and supergalactic planes respectively. This figure mainly reflects the arrival directions of individual events[9]. 36

2.10 Significance map of AGASA cosmic ray excess/deficit above 10^{19} eV. The dashed and dash-dotted curves indicate the Galactic and supergalactic planes respectively. The contour map has eight steps between [-3σ,+3σ]; two steps below -1.5σ are absent.[9] 36

2.11 Arriving direction probabilities assuming that the EHECRs are distributed according the galaxy distribution at 20 to 50 Mpc (top figure) and at 50 to 200 Mpc (bottom figure). The AGASA clustering regions are also indicated[62]. 39

3.1 Cosmic ray event density over the sky viewed by the SUGAR array for the 3732 events between $10^{17.9}$eV and $10^{18.5}$eV. The density scale represents the number of events viewed per true square degree of sky (see text for details). The galactic plane and Galactic Centre are indicated with the solid line and cross respectively. The 1950 epoch has been assumed for the equatorial coordinates displayed here and in other plots in this chapter. 43

3.2 The expected density of events for an isotropic flux of cosmic rays as viewed by SUGAR between $10^{17.9}$eV to $10^{18.5}$eV. Again, the density is given in units of events per true square degree (see text for details). . . 44

3.3 We compare Figures 3.1 and 3.2 and derive the fractional excess (or deficit) of the event density over the sky viewed by SUGAR. A value of 1 indicates that the measured density is in agreement with the expected density. 45

3.4 The significance sky map of the excess (or deficit) as calculated using synthetic data sets. The contours represent the chance probability of SUGAR detecting the observed density or greater. Thus, a contour level of 0.5 represents a measured density which is consistent with expectation. 46

3.5 Significance of the excess detected in the Galactic Centre region. The peak of the signal region has a chance probability of 0.005. The galactic plane and Galactic Centre are indicated by the solid line and cross respectively. The white circle of radius 5.5° represents the region over the S/N would be maximum according with the SUGAR angular resolution. The excess therefore appears to be consistent with that from a point source. 47

3.6 A comparison of the AGASA and SUGAR results. The SUGAR map from Figure 3.5 is overlaid with 2σ, 3σ and 4σ contours from reference [48] (fig. 2.2). Note that the limit of AGASA's view is close to $\delta = -24°$, indicated by the horizontal portion of the 2σ contour. The AGASA signal region size is significantly larger than seen by SUGAR. See the text for a discussion. 48

4.1 Schematic representation of a mirror-cluster module. 54

4.2 UV-pass filter process. The top plot shows the fluorescence spectrum as measured by Bunner[77] (the intensity scale is normalized to the peak at 337 nm), and the bottom plot shows the resultant fluorescence sensitivity taking into account the filter transmission curve and the PMT quantum efficiency. 55

4.3 Geometry of the shower detector plane (SDP). 56

4.4 Nitrogen fluorescence yield between 300 and 400 nm as a function of pressure. This function was obtained using 1000 MeV electrons in dry air at 15°C.[79]. 57

4.5 Fluorescence yield between 300 and 400 nm of an 80 MeV electron as a function of atmospheric altitude[79]. The slight temperature and density dependence of the fluorescence yield can be noticed when employing a typical mid-latitude summer atmospheric model with surface temperature 296 K (closed circles), and a similar winter model with a surface temperature of 273 K (open circles)[79]. 58

4.6 Energy dependence of nitrogen fluorescence between 300 and 400 nm in dry air at a pressure of 760 mm Hg. The dE/dx curve is shown as a solid line. The scale of the fluorescence yield is adjusted so that the 1.4 MeV point lies on the dE/dx curve[79]. 59

4.7 HiRes-1 site map. 60

4.8 HiRes-2 site map. 61

4.9 YAG mirror-cluster calibartion system[83]. 63

4.10 Transmission factor for Rayleigh scattering of 360 nm light by a molecular atmosphere. Curves shown are for tube elevation angles from 3 to 31 deg[91]. The assumed detector height above sea level is 1.5 km. . . . 67

4.11 Transmission factor for Mie scattering on aerosols in the atmosphere. The aerosols are described by a horizontal attenuation length $L^a(360nm) =$ 20 km, and a scale height $H_S = 1.2$ km. Curves shown are for tube elevation angles from 3 to 31 deg[91]. 68

4.12 Display of an event with reconstructed energy of 52 EeV. The top left hand side plot shows the four mirrors that triggered for this event. The top right hand side plot shows the elevation vs. azimuthal angles of the triggered tubes. The bottom left hand side plot shows the time of the tube hits vs. the tube emission angle (angle between the shower axis and the tube direction), with two fits superimposed: a straight line and the result of a time fit. The bottom right plot shows the reconstructed shower longitudinal profile[92]. 70

4.13 The functions for correcting the calorimetric energy to the primary energy, as a function of calorimetric energy. Shown are the corrections for proton showers (dotted line) and iron showers (short dashed line) and an average of the two (solid line). For comparison, Linsley's function[96] is also shown[93]. 71

4.14 Estimated HiRes-1 and HiRes-2 cosmic ray flux. This plot also shows the cosmic ray flux estimated by AGASA[92]. The solid line is a fit to the data assuming a model, described in [92], of galactic and extragalactic sources. 72

5.1 The histogram at the top is the nanosecond part of the time offset between sites. The middle plot shows the second part against the nanosecond part of the intersite offset. The bottom plot shows the data file part where the event was stored against the nanosecond part of the intersite offset. All time offsets are given in nanoseconds. January 15, 2000. . . . 76

5.2 time offset between fired mirrors within HiRes-2. Units are nanoseconds. January 15, 2000 77

5.3 Plot generated using the reprocessed fraw1 and fpho1 banks. The histogram shows the distribution of the time offset between sites. Units are nanoseconds. 77

5.4 The histogram at the top is the nanosecond part of the time offset between sites. The middle plot shows the seconds part against the nanosecond part of the intersite offset. The bottom plot shows the the part where the event was stored against the nanosecond part of the intersite offset. All time offsets are in nanoseconds. February 3, 2000. . 78

5.5 Zoom of the time offset between sites from fig. 5.4. time offset in nanoseconds. 79

5.6 time offset between fired mirrors within HiRes-2 during night of February 3, 2000 . time offset in nanoseconds units. 79

5.7 Plots generated using the reprocessed fraw1 and fpho1 banks. The histogram at the top is the nanoseconds part of the offset time between sites. The middle plot shows the seconds part of the time against the nanoseconds part of the intersite offset. The bottom plot shows the the part where the event was stored against the nanosecond part of the intersite offset. February 3, 2000. 80

5.8 Zoom of the time offset distribution between sites from fig. 5.7, ignoring the events at -0.45 and +0.55 sec. Units of the offset are nanoseconds. . 80

5.9 The histogram at the top is the nanosecond part of the time offset between sites. The middle plot shows the seconds part against the nanosecond part of the intersite offset. The bottom plot shows the the part where the event was stored against the nanosecond part of the intersite offset. All time offsets are given in nanoseconds. February 28, 2000 81

5.10 Zoom of time offset distribution between sites from fig. 5.9. 82

5.11 The histogram at the top is the distribution of mirror time offsets at HiRes-2. The bottom plot is the time sequence of the events against the mirror time offset . February 28, 2000. 82

5.12 The histogram at the top is the nanosecond part of the time offset between sites. The middle plot shows the seconds part against the nanosecond part of the intersite offset. The bottom plot shows the part where the event was stored against the nanosecond part of the intersite offset. All time offsets are given in nanoseconds. March 05, 2000. . . . 83

5.13 Zoom of time offset distribution between sites from fig. 5.12. Units are nanoseconds. March 05, 2000. 84

5.14 The histogram is the time offset distribution between mirrors within HiRes-2. Units are nanoseconds. March 05, 2000 84

5.15 The x (east - west) coordinate of the flasher positions against the time offset. March 05, 2000 86

5.16 The histograms are the time offset distribution between sites for different flashers. March 05, 2000 87
5.17 Estimated intersite time offset as a function of time using the 10 km North flasher. March 25, 2001. 89
5.18 Estimated intersite time offset as a function of time using the 4, 8 and 10 km North flashers (top plot). Distribution of the estimated intersite time offsets (bottom histogram). Because of the different effects of the time slewing for the 4 km N flasher compared with the 8 and 10 km N flashers, the intersite time offset estimated using the 4 km North flasher appears centred at -980 ns, while the the intersite time offset estimated using the 8 and 10 km North flashers appear centred at -700 ns. These data was taken on July 23, 2001 and for this period the HiRes-2 GPS clock location was correct. 90
5.19 Distribution of the percentage of signal tubes triggered in an event in relation to the total number of triggered tubes. Here we use the noise filtering algorithm described in this section. This set of events corresponds to cosmic ray events. HiRes-1 left plot and HiRes-2 right plot. 91
5.20 Distribution of the difference between the number of signal tubes triggered at HiRes-1 and HiRes-2 in an event. Figures 6.1 and 6.2 were generated using a set of 362 stereo cosmic ray events. 92
5.21 The normal to the SDP should have a zenith angle of 90o for these vertical flashers events. The plots show the deviation from this expectation versus event number (time ordered). The left plots are results from Fit_shower1 and right plots are for hpln1 and fpln1 results. The top plots correspond to HiRes-1 and the bottom plots correspond to HiRes-2. 97

5.22 Event display showing an event which does not have a defined track (this is a noise event). The left plot shows noise tubes identified using Fit_shower1 and the right plot shows the noise tube identification coming from the hpln1 analysis. The estimated HiRes-1 SDP (using Fit_shower1) for this event is 60 deg away from the expected SDP for a vertical flasher. The size of the boxes indicate the relative tube signals. 99

5.23 This event display shows a case where a noise tube far from the track was considered as good tube in the hpln1 analysis (right plot). This tube caused a deviation of 75 deg in the reconstructed SDP (see fig. 5.21). 100

5.24 Event display showing a case where a noise tube close to the track (within 3 deg) was considered as good tube (using the Fit_shower1 algorithm). This tube with a signal bigger than the rest of the tubes caused a deviation of around 5 deg in the reconstructed SDP. 101

5.25 Event display showing an event with intense noise tubes. Some tubes with intense signals close to or far from the track were considered as good tubes in fpln1 (right plot). These tubes caused a deviation of around 20 deg in the reconstructed SDP. 102

5.26 Locations of the radio controlled flashers. 103

5.27 These plots show the deviation of the reconstructed SDPs from a vertical SDP vs the estimated flasher core positions, corey is the 'y' coordinate (HiRes-1 top plots and HiRes-2 bottom plots). The left plots are results from Fit_shower1 and the right plots arefrom hpln1 and fpln1 results. These data correspond to vertical flashers from July 22, 2001. 104

5.28 Distribution of the deviation between the zenith angle of the reconstructed SDP normals and the SDP normals expected for a vertical event. Plots on the left correspond to HiRes-1 and plots on the right correspond to HiRes-2. The flasher identification is on each plot. Solid lines correspond to results from Fit_shower1 and dashed lines correspond to hpln1 (HiRes-1) and fpln1 (HiRes-2) results. 105
5.29 Same caption as figure 5.28. 106

6.1 Estimated energy, zenith, azimuth and psi distribution of the entire monocular data set ('y2001m05d13.a25sc10.ps4.dst'). Solid and dashed lines are distributions before and after applying pass4a cuts. 109
6.2 The top left plot shows the energy distribution of the stereo data set. Solid and dashed lines are before and after applying pass4a cuts. The dotted line represents the energy distribution of events where the monocular reconstructed psi angle deviates more than 20° from the stereo one. The top right plot shows the stereo reconstructed psi angle against the monocular reconstructed psi angle. The bottom plots show the longitudinal track length and the number of good tubes against the monocular-stereo psi deviation. The scatter plots are only considering events that passed pass4a cuts. 111
6.3 monocular - stereo psi deviation distributions for different longitudinal track length ranges (after pass4a cuts). 112
6.4 Psi angle (left plots) and longitudinal track length (right plots) distributions. Solid lines refer to stereo (top plots) and MC input values (middle and bottom plots) geometries and the dashed lines to the monocular reconstructed geometries. Middle plots are for reconstructed energies between 10^{18} and $10^{18.5}$ eV. Bottom plots are for reconstructed energies $> 10^{18.5}$eV (pass4a cuts have been applied to the monocular reconstructed distributions). 115

6.5 The top left plot shows the reconstructed energy distribution of the MC data set before (solid line) and after (dashed line) applying pass4a cuts. The dotted line represents the energy distribution of events where the monocular reconstructed psi angle deviates more than 20° from the MC psi angle. The top right plot shows the MC psi angle against the monocular estimated psi angle. The bottom plots show longitudinal track length and the number of good tubes against the PCGF-MC psi deviation. Scatter plots are after pass4a cuts. 116

6.6 Same as figure 6.5 but for events with reconstructed energies $> 10^{18.5}$ eV. 117

6.7 Angular track length against the monocular - MC psi deviation. Left hand plot is for reconstructed energies lower than $10^{18.5}$ eV and the right hand plot is for energies greater than $10^{18.5}$ eV. Only events that passed the pass4a cuts are shown. 118

6.8 monocular - MC psi deviation distributions for different longitudinal track length ranges (10^{18} eV $<$ reconstructed energies $< 10^{18.5}$eV) after applying pass4a cuts. 119

6.9 monocular - MC psi deviation distributions for different longitudinal track length ranges (reconstructed energies $> 10^{18.5}$eV) after applying pass4a cuts. 120

6.10 Estimated minimum χ^2 for time (top plots) and profile fitting (bottom plots) against the **monocular-stereo** psi angle deviation. The left plots only consider events with longitudinal track lengths shorter than 2.5 km and the right plots only longer than 2.5 km (after pass4a cuts). 121

6.11 Estimated minimum χ^2 for time (top plots) and profile fitting (bottom plots) against the **monocular-MC** psi angle deviation. The left plots only consider events with longitudinal track lengths shorter than 2.5 km and the right plots only longer than 2.5 km (10^{18} eV $<$ reconstructed energies $< 10^{18.5}$eV) (after pass4a cuts). 122

6.12 Estimated minimum χ^2 for time (top plots) and profile fitting (bottom plots) against the **monocular-MC** psi angle deviation (after pass4a cuts). The left plots only consider events with longitudinal track lengths shorter than 2.5 km and the right plots only longer than 2.5 km (reconstructed energies $> 10^{18.5}$eV). 122

6.13 The figure shows the estimated right (left plots) and left (right plots) psi angle uncertainty against the **monocular-stereo** psi angle deviation. The top plots only consider events with longitudinal track lengths shorter than 2.5 km and the bottom plots longer than 2.5 km (after pass4a cuts). 123

6.14 The figure shows the estimated right (left plots) and left (right plots) psi angle uncertainty against the **monocular-mc** psi angle deviation (after pass4a cuts). The top plots only consider events with longitudinal track lengths shorter than 2.5 km and the bottom plots longer than 2.5 km (10^{18} **eV** $<$ **reconstructed energies** $< 10^{18.5}$ **eV**). 124

6.15 The figure shows the estimated right (left plots) and left (right plots) psi angle uncertainty against the **monocular-mc** psi angle deviation (after pass4a cuts). The top plots only consider events with longitudinal track lengths shorter than 2.5 km and the bottom plots longer than 2.5 km (**reconstructed energies** $> 10^{18.5}$ **eV**). 124

6.16 Scatter plot of the quality code number against the (**monocular - stereo**) psi deviation (after pass4a cuts). In the left plot are quality code numbers ending in zero (20, 100,120, 200, 220, 1000, 1100 and 1120). In the right plot are quality code numbers not ending in zero (3, 5, 8, 23, 25, 103, 105, 123, 203, 1003 and 1103). 126

6.17 (**monocular - stereo**) psi distribution for events with quality code equal to 100 (left plot) and 200 (right plot). 126

6.18 Scatter plot of the quality code number against the (**monocular - MC**) psi deviation (after pass4a cuts). In the left plot are quality code numbers ending in zero (20, 100,120, 200, 220, 1000, 1100 and 1120). In the right plot are quality code numbers not ending in zero (3, 5, 8, 23, 25, 103, 105, 123, 203, 1003 and 1103). Reconstructed energies between 10^{18} and $10^{18.5}$ eV. 127

6.19 (**monocular - MC**) psi distribution for events with quality code equal to 100 and 200 (10^{18} eV < energies < $10^{18.5}$eV). 127

6.20 Scatter plot of the quality code number against the (**monocular - MC**) psi deviation (after pass4a cuts). In the left plot are quality code numbers ending in zero (20, 100,120, 200, 220, 1000, 1100 and 1120). In the right plot are quality code numbers not ending in zero (3, 5, 8, 23, 25, 103, 105, 123, 203, 1003 and 1103). Reconstructed energies greater than $10^{18.5}$ eV 128

6.21 (**monocular - MC**) psi distribution for events with quality code equal to 100 (left histogram) and 200 (right histogram) (energies> $10^{18.5}$eV). 128

6.22 **(monocular - stereo)** psi deviation distributions for different longitudinal track length ranges after applying pass4a and quality cuts 130

6.23 **(monocular - MC)** psi deviation distributions for different longitudinal track length ranges after applying pass4a and quality cuts (10^{18} eV < energies < $10^{18.5}$eV). 131

6.24 **(monocular - MC)** psi deviation distributions for different longitudinal track length ranges after applying pass4a and quality cuts (energies > $10^{18.5}$eV). 132

6.25 Scatter plot of the monocular reconstructed energy against the psi deviation from the true value. The top plots use real events and assume the stereo reconstructed geometry is the true value. The middle and bottom plots are using MC events with energies between 10^{18} - $10^{18.5}$ eV and energies above $10^{18.5}$ eV respectively. The left and right hand side plots are before and after applying all the quality cuts respectively. 133

6.26 Energy distribution of real monocular data set. The solid line is for events that passed pass4a cuts. The dashed line is for events that passed pass4a cuts and have quality codes equal to 0, 100 or 200. The dotted line distribution is considering only events passing pass4a cuts with quality codes equal to 0. 134

7.1 Estimated intersite time offset as a function of the flasher-HiRes-1 distance. Perfect vertical orientated flashers were assumed. 146

7.2 Firing laser position. The arrows show the azimuth direction of the fired lasers. The zenith angle of both laser shots is 21°. 148

7.3 The above distributions show the difference between the estimated laser firing time using *HiRes-1* and the programmed firing time at the GPSY clock. Two different laser orientations were analysed 148

7.4 Reconstructed zenith angle (mean value) and the RMS of the reconstructed zenith angle distribution as a function of the opening angle. A different mark is used for each reconstruction method. The circle 'o' is for hybrid aw, plus '+' is for hybrid af, asterisk '∗' is for stereo af and times '×' is for stereo aw. 151

7.5 Reconstruction efficiency. 151

7.6 Stereo and hybrid reconstructed zenith angle distribution for the 10 km N, and 2km S flashers. The 10 km N and the 2 km S flashers have opening angles 56° and 2.5° respectively 152

7.7 Error size as a function of the χ^2 variation ($\Delta\chi^2$). These values were calculated using MC data. The asterisks are for stereo af and the crosses are for stereo aw (see text for details). 154

7.8 Reconstructed orientation of the North vertical flashers. The upper and lower plots are for stereo-aw and stereo-af respectively. The radial distance represents the zenith and the polar angle represents the azimuth of the reconstructed axis. The lines represent the HiRes-1 and HiRes-2 SDP projections on the sky. 157

7.9 Reconstructed uncertainty region of the North vertical flashers (see caption in fig. 7.8). For stereo-aw the errors were estimated using $\Delta\chi^2 = 15$ (upper plots) and for stereo-af the errors were estimated using $\Delta\chi^2 = 90$ (lower plots). The values of $\Delta\chi^2$ are assigned **according to MC data**. 158

7.10 Error size as a function of the χ^2 variation ($\Delta\chi^2$). The error size is defined as $|(reconstructed\ parameter - expected\ value)|/(estimated\ error)$. These values were calculated using vertical flashers and laser shots. The circle 'o' is for hybrid aw, plus '+' is for hybrid af, asterisk '$*$' is for stereo-af and times '$\times$' is for stereo aw. 159

7.11 Reconstructed uncertainty region of the North vertical flashers (see caption in fig. 7.8). For stereo-aw the errors were estimated using $\Delta\chi^2 = 1$ (upper plots) and for stereo-af the errors were estimated using $\Delta\chi^2 = 3.5$ (lower plots). The values of $\Delta\chi^2$ are assigned **according to flasher and laser shot** events (see fig. 7.10). 160

7.12 Reconstructed orientation of the North and South vertical flasher, using the **hybrid-af** technique. The radial distance represents the zenith and the polar angle represents the azimuth of the reconstructed axis. 161

7.13 Reconstructed orientation of the North and South vertical flasher, using the **hybrid-aw** technique. The radial distance represents the zenith and theta represents the azimuth of the reconstructed axis. 162

7.14 Reconstructed uncertainty region of the North and South vertical flashers using the **hybrif-af** technique. The errors were estimated using a $\Delta\chi^2 = 4$. The value of $\Delta\chi^2$ is assigned **according to flasher and laser shot** events (see fig. 7.10). 163

7.15 Reconstructed orientation (upper plots) and uncertainty (lower plots) of the South vertical flashers using the **stereo-af** technique (upper plots). The errors were estimated using a $\Delta\chi^2 = 3.5$. The value of $\Delta\chi^2$ is assigned **according to flasher and laser shot** events (see fig. 7.10). 164

7.16 Reconstructed orientation (upper plots) and uncertainty (lower plots) of the South vertical flashers using the **stereo-aw** technique. The errors were estimated using a $\Delta\chi^2 = 1$. The value of $\Delta\chi^2$ is assigned **according to flasher and laser shot** events (see fig. 7.10). 165

8.1 Excess map calculated after having introduced 49 artificial events into the HiRes-1 mono data set. The artificial events are randomly distributed within a 5° radius circle centred at Cygnus X-3. The excess represents the ratio of the observed signal over the expected signal assuming an isotropic cosmic ray flux. The solid line represents the galactic plane. 169

8.2 Significance of the excess observed in figure 8.1. The significance represents the chance probability of having an excess similar to or greater than the observed excess at the particular bin. 169

8.3 Excess map after having introduced 49 artificial events into the HiRes-1 mono data within a circle centred at Cygnus X3 with approximately 5° radius. The number of events within a circle of 5° radius centred on each bin was counted. Then, this number of events was compare with the number expected from an isotropic arrival direction distribution. . 170

8.4 Statistical significance of the excess region in fig. 8.3. 170

8.5 Artificial events simulating a point source. The plot show the event density (events per square degree) of 49 artificial events distributed around Cygnus X-3 (see text for details). The elliptical error of each event is oriented toward Cygnus X-3. No background is included in this particular plot. 173

8.6 Excess map after having introduced 49 artificial events (simulating a point source) shown in figure 8.5 to the HiRes-1 mono data. 174

8.7 Statistical significance of the excess region in figure 8.6. 174

8.8 Estimated excess map using the traditional time shuffling technique. Three artificial sources were introduced at declinations of 0, 45 and 90 degrees. The number of artificial events at each source is 7 times the background at each declination level. The coordinates are projected over an Aitoff projection map. The celestial North pole is located at the centre of the map. 177

8.9 Chance probability of having in each bin an excess greater than or equal to that in figure 8.8 (Significance map). The 1000 isotropic background maps used in the analysis were estimated using the traditional time shuffling technique. 177

8.10 Estimated excess map using MC events (MC geometry) combined with real arrival times to produce the background maps used in the analysis (see text for details). 178

8.11 Chance probability of having in each bin an excess greater than or equal to that in figure 8.10 (Significance map). The 1000 isotropic background maps used in the analysis were estimated using MC events (MC geometry) associated with real event arrival times. Compare this map with figure 8.9. 178

8.12 Cosmic ray event density for the 3571 events above 10^{18} eV (HiRes-1 mono events). The density scale represents the number of events viewed per true square degree of sky. A three dimensional ellipsoid with total volume equal to one represents the angular uncertainty of each event. . 180

8.13 The expected density of events for an isotropic flux of cosmic rays above 10^{18} eV. The density is given in units of events per true square degree. The solid line indicates the galactic plane. 180

8.14 Fractional excess map. This map is obtained by comparing Figs. 8.12 and 8.13. A value of 1 indicates that the measured density is in agreement with the expected density. 181

8.15 The Significance of the excess regions (events above 10^{18} eV). The contours represent the chance probability of detecting the observed density or greater. This map is constructed using the 1000 background maps derived from MC data and real event arrival times. 181

8.16 This plot shows the bins that had a chance probabilty value lower than or equal to 0.005 in figure 8.15. 182

8.17 Cosmic ray event density for the 2309 events between $10^{18.0}$ and $10^{18.5}$ eV (HiRes-1 mono events). The density scale represents the number of events viewed per true square degree of sky. A three dimensional ellipsoid with total volume equal to one represents the angular uncertainty in each event. 183

8.18 The expected density of events for an isotropic flux of cosmic rays between $10^{18.0}$ and $10^{18.5}$ eV. The density is given in units of events per true square degree. 183

8.19 Fractional excess map. This map is obtained by comparing Figs. 8.17 and 8.18. A value of 1 indicates that the measure density is in agreement with the expected density. 184

8.20 The Significance of the excess regions (events between $10^{18.0}$ and $10^{18.5}$ eV). The contours represent the chance probability of detecting the observed density or greater. 184

8.21 Cosmic ray event density for the 920 events between $10^{18.5}$ and $10^{19.0}$ eV (HiRes-1 mono events). The density scale represents the number of events viewed per true square degree of sky. A three dimensional ellipsoid with total volume equal to one represents the angular uncertainty in each event. 185

8.22 The expected density of events for an isotropic flux of cosmic rays between $10^{18.5}$ and $10^{19.0}$ eV. The density is given in units of events per true square degree. 185

8.23 Fractional excess map. This map is obtained by comparing Figs. 8.21 and 8.22. A value of 1 indicates that the measure density is in agreement with the expected density. However, due to the small number of events (920 events), the magnitude of the excess becomes less meaningful. . . 186

8.24 The Significance of the excess regions (events between $10^{18.5}$ and $10^{19.0}$ eV). The contours represent the chance probability of detecting the observed density or greater. 186

8.25 Zoom of the significance map (fig.8.24) around the region RA=138°, DEC=47°. 187

8.26 Distribution of the number of sigmas of excess for different smearing sizes (see text for details). The smearing sizes are indicated in the plots. The upper plots correspond to the excess regions observed at energies between $10^{18.0}$ and $10^{18.5}$ eV. The upper left and right hand side plot are for the regions around RA=110°, DEC=39° and RA=242°, DEC=40° respectively. The bottom plot corresponds to the excess region observed at energies between $10^{18.5}$ and 10^{19} eV around RA=139°, DEC=47°. The bins inside the respective circle smearing size around each excess region were included in the histograms. 189

8.27 Probability of having by chance a greater or equal number of events (events between $10^{18.0}$ and $10^{18.5}$ eV) than that expected in the respective bin (Significance map). The computed signal in each bin corresponds to the number of events within 20° radius (20° maximizes the excess at this energy range, see fig. 8.26). 190

8.28 Probability of having by chance a greater or equal number of events (events between $10^{18.5}$ and $10^{19.0}$ eV) than that expected in the respective bin (Significance map). The computed signal in each bin corresponds to the number of equivalent events within 10° radius (10° maximizes the excess at this energy range, fig. 8.26). 190

8.29 Data derived from figure 8.27. The top left hand side plot shows the estimated significance against the observed excess/deficit (in terms of sigmas of excess). The top right hand side plot (solid line) shows the distribution of the observed sigmas of excess in all bins (2° bins in RA and in DEC). The peak present at -2.5 is because a deficit region is located at the pole region (see fig.8.27) and the true size of these bins (in terms of solid angle) are smaller. Thus, the deficit region involved more bins. The dashed lines shows the same distribution assigning to each bin a weight of $cos(DEC)$. The bottom left hand side plot is a zoom of the significance against the observed excess/deficit plot. The bottom right hand side plot shows the number of sigmas of excess distribution for bins with estimated significance 0.001 or lower. 193

8.30 Declination distribution of bins having at least 2.5σ of excess in 1000 synthetic data sets (top plot). The lower plot shows the weighted sum of bins having at least 2.5σ of excess in each of the synthetic data sets. The horizontal line indicates the weighted sum of bins having at least 2.5σ of excess in one of the excess regions in figure 8.27. 194

8.31 Cosmic ray event density for the 341 events above $10^{19.0}$ eV (HiRes-1 mono events). The density scale represents the number of events viewed per true square degree of sky. A three dimensional ellipsoid with total volume equal to one represents the angular uncertainty in each event. . 196

8.32 The expected density of events for an isotropic flux of cosmic rays above $10^{19.0}$ eV. The density is given in units of events per true square degree. 196

8.33 Fractional excess map. This map is obtained by comparing Figs. 8.31 and 8.32. A value of 1 indicates that the measure density is in agreement with the expected density. However, due to the small number of events (341 events), the magnitude of the excess becomes less meaningful. . . 197

8.34 The Significance of the excess regions (events above $10^{19.0}$). The contours represent the chance probability of detecting the observed density or greater. 197

8.35 Probability of having by chance a greater or equal number of events (events above 10^{19} eV) within each bin (Significance map). An smearing size of 5° was used. This smearing size maximizes the excess regions of interest (RA=170°, DEC=62° and RA=140°, DEC=36°). 198

8.36 Event density map for the highest energy ($> 4 \times 10^{19}$ eV) HiRes-1 monocular events (30 events). The map is in equatorial coordinates. The small circles show the '*a priori*' source candidates (the AGASA triplet and the galaxy M-87). The solid lines show the galactic (thicker line) and supergalactic (thinner line) planes. 199

8.37 Event density map (events per square degree) for the stereo events with energies above 10^{18} eV (998 events). The map is in equatorial coordinates. 202

8.38 Significance map for the HiRes stereo events above 10^{18} eV. The background was estimated using the traditional time shuffling technique. . . 203

8.39 Significance map for the HiRes stereo events above 10^{18} eV using a 15° radius smearing size. 204

8.40 Event density map for the mono events with energies above 4×10^{19} eV (30 events). Capital 'M' indicates the reconstructed arrival direction of the single mono event above 10^{20} eV. Also is shown in the map the arriving directions of the 7 stereo events above 4×10^{19} eV (small 's'). The bigger 'S' is for the highest energy stereo event. The arriving directions of the 11 AGASA events above 10^{20} eV are indicated with the letter 'A'. The locations of the AGASA triplet and Virgo/M87 are indicated with small circles. There is one mono event overlapping with the AGASA triplet. The estimated probability of having by chance an ellipse intercepting with the AGASA triplet within 2.5° is 0.04. The map is in equatorial coordinates. The solid lines indicate the galactic (thicker line) and supergalactic (thinner line) planes. 205

A.1 Accelaration by a moving magnetized cloud. θ_1 and θ_2 are the relative angles which the particles enter and leave the cloud. E_1 and E_2 are the particle energies before and after interacting with the magnetized cloud, and V is the cloud velocity 214

A.2 Acceleration at a shock wave. 217

List of Tables

2.1 Correlation of the arrival direction of UHECRs with the galactic and supergalactic plane[57]. Data (before 1991) from Haverah Park, AGASA, Volcano Ranch and Yakutsk. 34

2.2 Tests for SUGAR data clustering toward the galactic and supergalactic planes in four overlapping energy ranges for events with zenith angles less than 55° [58]. 34

2.3 Coordinates of the AGASA clustering regions. C1 is a doublet when considering only the AGASA data, but it became a triplet when considering other ground array data. The triplets and doublets are formed with $E > 4 \times 10^{19}$ eV events, and the broad scale cluster are formed with 10^{19} eV events 37

2.4 Astrophysical objects near the AGASA highest energy events. The redshift values for each object are given in parentheses[9] 39

4.1 Constants used in equation 4.2 [79] 58

6.1 Suggested psi angle corrections and uncertainties according to MC comparisons for events that successfully passed the suggested quality cuts. . 136

6.2 Special psi angle corrections and uncertainties suggested for events with quality codes 100 and 200. 137

8.1 Tests for HiRes-1 energetic events ($> 4 \times 10^{19}$ eV) clustering toward the galactic and supergalactic planes. The calculation of P is explained on page 33. 201

9.1 Estimated 95% upper limits of the source flux observed at around RA=130°, DEC=40°. 210

Chapter 1

Introduction

Since the discovery of cosmic rays (CR) by Victor Hess in 1912, investigations looking for a better understanding of the nature of these particles have led to unexpected important discoveries. In 1932 while watching the tracks of cosmic ray particles passing through his cloud chamber, Carl Anderson discovered antimatter in the form of the anti-electron, later called the positron. In 1937 Seth Neddermeyer and Carl Anderson discovered the elementary subatomic particle called the muon. The positron and the muon were the first of a series of subatomic particles discovered using cosmic rays. These discoveries gave birth to the science of elementary particle physics. Particle physicists used cosmic rays for their research until the advent of particle accelerators in the 1950s. Nowadays the study of the origin of the Extremely High Energy Cosmic Rays (EHECRs) may still introduce new topics of study, perhaps a new theory of high energy particle physics that could explain the origin and/or propagation of the detected EHECRs. Also EHECRs could give us valuable information about possible interesting new physics phenomena including topological defects in the cosmological context [1, 2], Lorentz invariant violations [3, 4] and atmospheric mini black holes [5]. For pleasant reading about the history of the discovery of cosmic rays and the evolution of the cosmic ray detectors in the previous century see [6].

Cosmic rays are particles that travel through space, these particles are mainly protons and other atomic nuclei (such as iron). The energy spectrum of cosmic rays

detected at the earth extends over many decades (fig 1.1). The energy of the most energetic cosmic rays detected on earth is around 10^{20}eV and it is approximately a hundred million times greater than the most energetic particle accelerated with the most powerful particle accelerator on earth. The observed cosmic ray flux decreases with the energy of the cosmic ray following a power-law function of energy ($flux \propto E^{-\gamma}dE$, where γ is called the spectral index). The differential spectral index is different for different energy ranges, $\sim$2.7 up to energies of 10^{15} eV (this region of the spectrum is often called the knee), and $\sim$3 from the knee region up to 10^{18} eV. The energy spectrum after 10^{18} eV becomes flatter and therefore this region is often called the ankle. The different spectral indices suggest different acceleration mechanisms for different energy ranges. The knee region may correspond to the maximum energy that particles can apparently be accelerated to in supernova remnants and the ankle region is thought to be the maximum energy that particles can be accelerated to inside our galaxy. Cosmic rays with energies above the ankle may come from outside our galaxy.

In recent times, using different kinds of cosmic ray detectors, many cosmic rays with very high energy (above 10^{19} eV) have been detected [8, 9] and the origin of these cosmic rays is still unknown. Lower energy evidence, from radio astronomy and gamma-ray astronomy in particular, indicates that known galactic objects can be associated with the origin of at least some of the energetic cosmic rays. These objects would include, for instance, supernova remnants and neutron star binary systems. At energies above 10^{19} eV, the situation is particularly unclear with these being some still controversial models of the origin of these extremely high energy cosmic rays [2, 10].

There are currently in operation two major experiments that focus on the study of EHECR: the Akeno Giant Air Shower Array (AGASA) and the High Resolution Fly's Eye Cosmic Ray Detector (HiRes). A third bigger experiment is now under construction, the Pierre Auger Experiment. Two other experiments that would observe extensive air showers (EAS) from space are being proposed, OWL (Orbiting Wide-angle Light collectors) [11] and EUSO (Extreme Universe Space Observatory) [12]. The low rate of EHECR arriving at the earth (one particle per square kilometre per year)

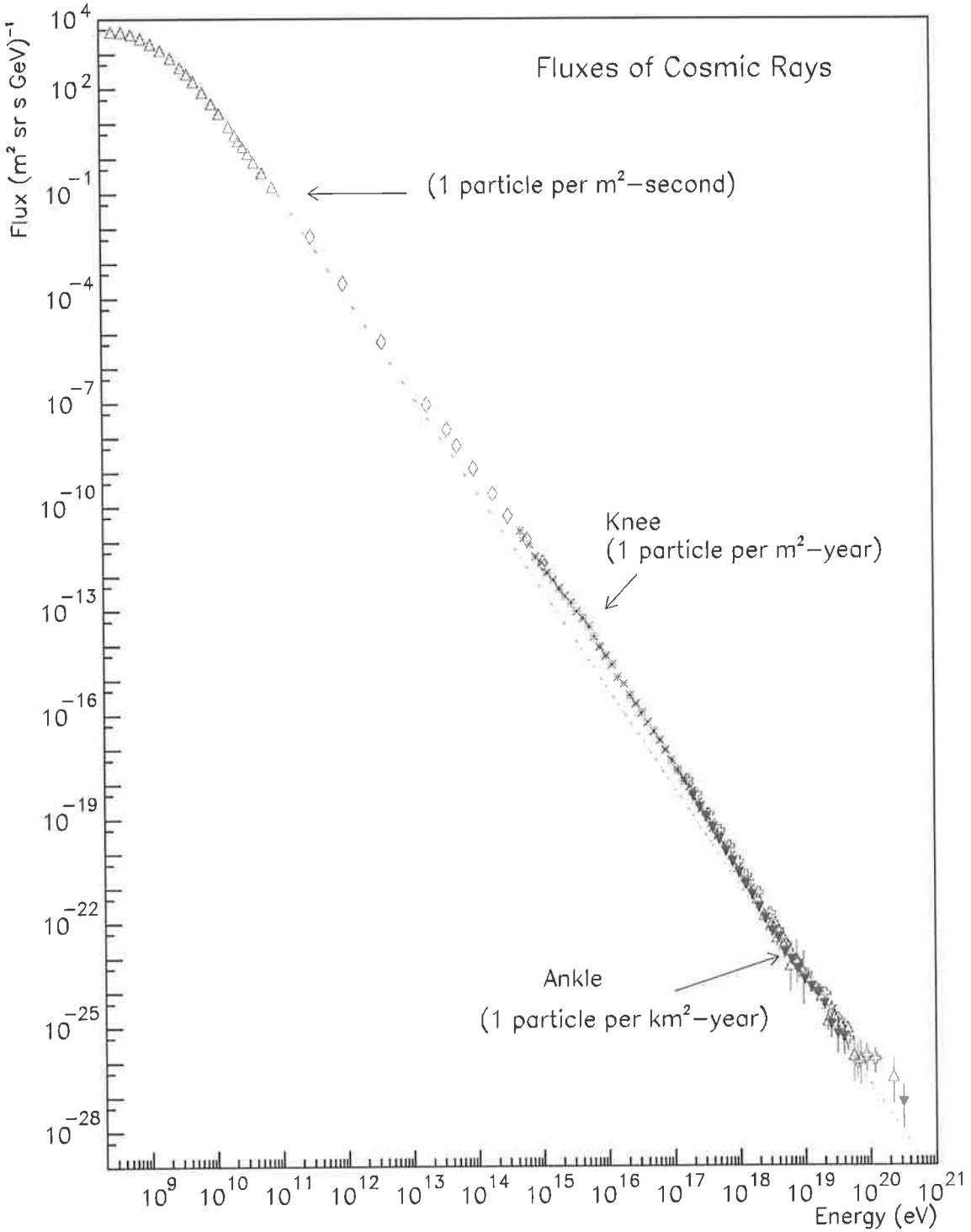

Figure 1.1: Differential energy spectrum of cosmic ray flux as a function of energy [7]. On this figure, integrated fluxes above three energy values are also indicated. The data points are collected from the following experiments: LEAP, Proton, Akeno, AGASA, Fly's Eye, Haverah Park, Yakutsk.

makes the study of their origin partucularly difficult. The goal of these experiments is to detect a high number of the EHECR in a reasonable period of time.

The author wishes to present a literature review briefly summarizing the current knowledge about the origin (mechanism of acceleration) and propagation of the highest energy cosmic rays. The literature review also describe the techniques used to detect energetic cosmic rays. Given that the scope of this thesis is to perform anisotropy studies with the HiRes detector, anisotropy studies of the arrival directions of cosmic rays performed by other groups will be presented in more detail in Chapter 2.

1.1 Origin of EHECR

The origins of the highest energy cosmic rays remains a great mystery in astrophysics. Several models attempt to explain their origins. These models can be classified into two groups: "bottom-up" acceleration mechanisms (also called astrophysical acceleration models) and "top-down" decay mechanisms (also called fundamental processes or exotic mechanisms).

1.1.1 "Bottom-up" acceleration mechanisms

For "bottom-up" acceleration mechanisms there are two popular scenarios, particles being accelerated in fast rotating magnetic fields, and by shock waves. In both scenarios, the size of the acceleration region (R) and the magnetic field strength (B), and consideration of Larmor containment of a particle of charge Ze within the acceleration region, implies that there is a maximum energy $E_{max} \propto ZeBR$ [13] up to which the particle can be accelerated before it escapes from the acceleration region, thus preventing further acceleration. The observed EHECR events above 10^{20} eV, therefore, pose a serious challenge for any acceleration mechanism because a value of $E_{max} \geq 10^{20}$ eV can barely be achieved in even the most powerful astrophysical objects for reasonable values of R and B associated with these objects [1, 14].

1.1.1.1 Fast rotating magnetic field scenarios:

a.- Neutron stars: Rotating neutron stars are associated with a rotating magnetosphere that generates an electric field of magnitude $\sim \frac{1}{c}|(\Omega \times R) \times B|$ (Ω is the angular velocity and B the magnetic field). This field multiplied by the stellar radius R translates into a voltage

$$\Delta\phi \sim \frac{B \times R^2}{T} \tag{1.1}$$

where T is the rotation period. For neutron stars, typical values of $B = 10^9$ T (10^{13} G), $R = 10^4$m (10^6 cm) and $T = 10^{-3}$ s lead to an electrical potential energy $e\Delta\phi = 100$ EeV, which could accelerate charged nuclei. However, due to some geometrical considerations and a possible short circuit due to (e^+, e^-) pairs created in the pulsar magnetosphere, the above electrical potential energy drops to a few orders of magnitude lower[7, 14].

b.- Ultra-relativistic winds: Rotating magnetized neutron stars can also be sources of ultra-relativistic winds. Therefore, if a nuclei can be injected from the star surface into the magnetosphere, they start to co-move with the forming wind, reaching its terminal velocity. Typical energies at young neutron star winds are $\approx 4 * 10^{20} Z_{26} B_{13} \Omega_3^2$ eV, where Z_{26} is the charge of the nuclei in multiples of the iron charge ($Z_{26} \equiv Z/26$), B_{13} is the magnetic field in units of 10^{13} G and Ω_3 is the angular velocity in radians per milli-second[15].

c.- 'Dead quasars': In the present epoch quasars do not populate our local universe, however remnants of 'dead quasars' are expected to populate our local universe in the present epoch. The name of 'dead quasars' is given because of the lack of luminosity of these objects. Dead quasars may be formed by a massive rotating black hole. Accreted magnetized plasma rotates with the black hole generating an electric force capable of accelerating EHECRs to energies of $\approx 4.4 \times 10^{20} B_4 M_9$ eV, where $B_4 \equiv B/(10^4 G)$ and $M_9 \equiv M/(10^9 M_\odot)$[16].

1.1.1.2 Relativistic shock waves scenarios:

Shock wave acceleration is also known as first order Fermi acceleration. The principle is that particles captured within the shock wave (downstream region) can suffer multiple scatterings due to irregularities in the magnetic field. Scatterings in the downstream region are elastic, so no energy is lost. After a few scatterings the accelerated particle can cross the boundary region toward the upstream region (outside the shock wave). The shock wave will eventually again reach the particle and capture it into the downstream region again. In each cycle of crossing the shock wave boundaries, the particle may gain or lose energy. However, on average particles gain energy. The accelerated particles may repeat a crossing cycle several times, until they reach an energy large enough to escape from the shock wave. First order Fermi acceleration is more efficient than the second order Fermi accelaration, since the average energy gained in each cycle is proportion to β with $\beta = V/c$ being the Lorentz factor, where V is the velocity of the shocked gas (downstream) relative to the unshocked gas (upstream). The Fermi acceleration predicts a power-law energy spectrum of cosmic rays [17]. For more details on Fermi acceleration see appendix A.

A recent review describing and discussing in some detail the most promising shock wave scenarios is in [14]. Below I will summarize the shock wave scenarios considered in [14].

a.- Particle acceleration in relativistic jets: Relativistic jets are a characteristic of Active Galactic Nuclei (AGN). Shock waves are believed to form in these jets accelerating EHECRs. However, considerations of energy losses due to interactions with the local gas and synchrotron radiation, limit considerably the maximum attainable energy. The FRII (Fanaroff-Riley class II) radio galaxies carry large quantities of energy up to the radio 'hot spots' situated far ($\sim$ 100 kpc) from the central energy source. These hot spots are believed to harbour strong, mildly relativistic shocks that may accelerate energetic particles. The energy lost due to interaction with the nearby material is lower for EHECRs

accelerated in these FRII 'hot spots' since they are already close to the extragalactic medium and propagate less distances thorough the galactic gas. For 'typical' hot-spot conditions $B \approx 0.5$ mG, $V = 0.3$ c (shock velocity), $R > H \approx 1$ kpc (R and H are the gyration radius of the EHECR particles and the 'hot spot' size respectively), protons can be accelerated up to energies of a few times 10^{20} eV[18].

b.- Shock waves formed in accretion flows: The universe is believed to be formed of cosmological structures of compressed matter. Diffuse plasma accreted with velocities $u \sim 10^3$ km/s at such extended (several Mpc) structures can form large scale shocks that may accelerate EHECRs[14]. A binary star can also accrete material from the companion star forming shock waves. A favorable scenario occurs particularly for neutron binary stars since the available magnetic field is higher[17]. When the available magnetic field is not big enough, Fermi diffusive acceleration meets serious obstacles in such shocks. The 10^{20} eV protons accelerated within a magnetic field of $B \sim 0.1\mu$G, posses a gyroradius $r_g \sim 1$ Mpc. Thus, the particle mean free path $\lambda > r_g$ leads to unreasonably large diffusive regions being required for acceleration. However, considering a regime in which the shock normal is perpendicular to the mean magnetic field ('Jokipii diffusion') the resulting particle mean free path λ_n may be $\lambda_n \ll r_g$ [19], allowing larger energies of accelerated particles.

c.- Ultra-relativistic shock waves in GRBs: Gamma ray bursts are believed to originate from ultra-relativistic shocks, with Lorentz factors Γ reaching values $\sim 10^3$. Vietri [20] and Waxman [21] suggested that such shocks could also provide EHECRs. These scenarios could be even more promising if the shock propagates in a region of strong magnetic field, such as in a pulsar wind zone.

Figure 1.2 (a diagram due to Hillas[13]) shows the combination of source size and magnetic field required to accelerate EHECRs by bottom-up acceleration mechanisms in most of the scenarios discussed in this section.

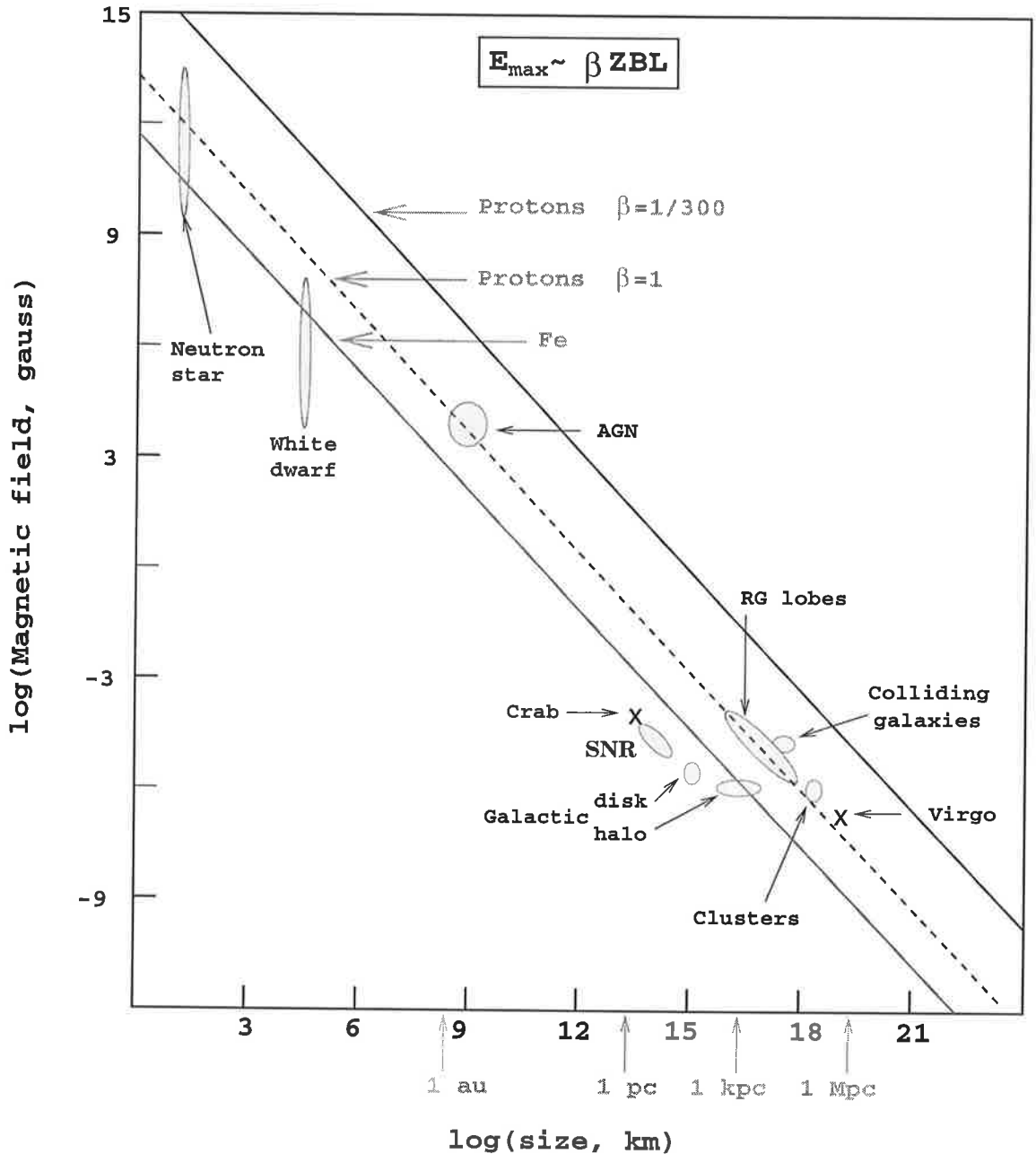

Figure 1.2: Size and magnetic field strength of possible accelerations sites. Objects below the diagonal lines cannot accelerate the corresponding elements. This particular version of the Hillas diagram[13] was obtained from [7].

1.1.2 "Top-down" acceleration mechanisms

The problem of finding the origin of EHECRs becomes more acute when one recognizes that the actual particle energy at the source has to be significantly larger than the observed energy of the particles because of energy loss during propagation, as well as in the immediate vicinity of the source. In addition, there is the problem of absence of any obviously identifiable sources for the observed EHECR events. Because of these difficulties, "top-down" decay mechanisms attempt to explain $> 10^{19}$eV cosmic rays as the result of decays of ultra heavy fundamental objects [10]. Because of the enormous kinetic energy liberated in these decays, no acceleration is needed. There are two scenarios to generate massive particles (X particles):

a.- **Supermassive relics:** X particles could be long-living metastable objects produced in the early evolution of the universe (supermassive relic particles) [22]. Their mass should be larger than 10^{12} GeV and their lifetime of the order of the age of the Universe since these relics must decay in the current epoch in order to explain the observed EHECRs . Unlike strings and monopoles , but like monopolonium (a metastable bound state of monopole-antimonopole), supermassive relics aggregate under the effect of gravity like ordinary matter and act as a cold dark matter component. Thus, the distribution of such relics should be enhanced towards galaxies and galaxy clusters. If galactic supermassive relic particles were the source of the EHECRs, then an anisotropy towards the galactic center region is expected [22, 23]. The predicted fluxes from decaying X particles from the halo are calculated in [24]

b.- **Topological Defects:** Cosmic Topological Defects (TDs) are predicted to form in the early Universe as a result of symmetry-breaking phase transitions envisaged in Grand Unified Theories (GUTs) [25, 10]. Topological defects associated with symmetry-breaking phase transitions are well-known in condensed matter systems.

TDs can be classified according to their dimensions: magnetic monopoles (0-dimensional, point-like); cosmic strings (1-dimensional); a sub-variety of the previous which carries current is the superconducting string; domain walls (2-dimensional); textures (3-dimensional). Also hybrid TDs formed by monopoles and cosmic strings are of interest as possible EHECR source. Topological defects may collapse, or annihilate, generating X particles. There is also a mechanism that allows strings to radiate X particles [10]. Predicted cosmic rays fluxes assuming different TDs characteristics are given in [22].

1.2 Propagation of the EHECR

Cosmic ray particles do not travel unhindered through space. They are subject to various interactions and their trajectories will be curved by magnetic fields. The result of these effects will characteristically alter the observed energy spectrum and arrival directions at earth.

The magnitudes of extragalactic magnetic fields are not precisely determined. Estimates using mainly Faraday rotation measurments (FRM) of linearly polarized radio sources show that B may reach $\sim 1\mu G$ in rich clusters and approximately $\sim 0.1\mu G$ in supergalactic accretion flows and in supergalactic structures [26]. However, little is known about the strength of the magnetic field outside the cluster boundaries (in the intergalactic medium). This is because the low density of the intergalactic medium makes it difficult to use indirect methods to measure the intergalactic magnetic field. Some upper limits for the intergalactic magnetic field suggest a magnitude of 1 nG[26, 27]. There is also evidence that the magnetic fields appear to be randomly oriented in space, suggesting that EHECR may not point back close to their sources [28]. However there are some observed directional pairs and triplets in the arrival distributions above 10^{19} eV[29] (these events will be discussed on section 2.2.2).

The deflection of the trajectory of EHECRs is proportional to the charge of the

particle (Ze). The Larmor radius R of a particle with charge Ze in kiloparsecs is

$$R_{kpc} \approx \frac{1}{Z}\left(\frac{E}{1EeV}\right)\left(\frac{B}{1\mu G}\right)^{-1}. \tag{1.2}$$

where E is the energy of the particle and B is the magnetic field of the propagating medium. Thus, the energy requiered by an iron nucleus in order to propagate inside the galaxy ($B \sim 2\mu$G) with a Larmor radius comparable to the size of the galaxy is $\approx 10^{21}$ eV. This means that if energetic iron nuclei are produced inside our galaxy, no anisotropry is expected toward the galactic plane, unless their energies were greater than $\approx 10^{21}$ eV.

Common intergalactic propagation models use a turbulent intergalactic magnetic field structure. It is assumed that the intergalactic medium is filled with many cells each having a different regular magnetic field structure. The size of the cells is often called the turbulence scale, scale length or coherence length, and depending on the propagation model the turbulence scale can be between 100 kpc to 1 Mpc. The associated field strengths depend on the turbulence spectrum. Thus, for smaller scale length cells the associated field strengths are lower, this is called Kolmogorov turbulence[30]. Using the propagation model described above and considerations of energy losses, Clay *et al.*[31] estimated the expected mean angular deviation for protons

$$\Delta\phi = K\left(\frac{2\times 10^{20}eV}{E}\right)\left(\frac{d}{10Mpc}\right)^{0.5}\left(\frac{L}{100kpc}\right)^{0.5}\left(\frac{B}{0.1\mu G}\right), \tag{1.3}$$

where E is the observational energy, d is the displacement, L is the largest turbulence scale and B is the magnetic field strength and K is a constant that depends on the details of the propagation model ($K = 4°$ in [31] and $K = 15°$ in [32]).

Figure 1.3 shows the effect of the intergalactic magnetic field over the trajectory of energetic cosmic protons as a function of the proton energy. Two different specific situations were assumed -protons propagating from our nearby extragalactic region (30 Mpc propagation distance) and protons propagating a distance of 200 Mpc. The assumed intergalactic magnetic field is 1 nG with a largest turbulence scale of 1 Mpc.

Since EHECR are less deflected by magnetic fields, they must exhibit a tendency to arrive from the galactic plane if their sources populate the galactic disk. However there

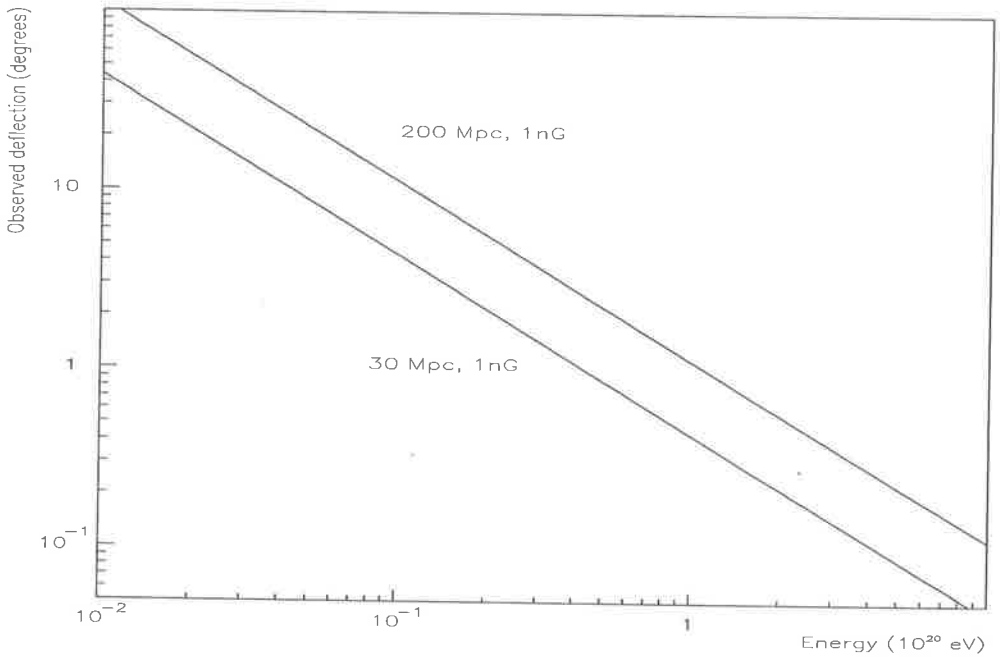

Figure 1.3: Expected angular deflection (eq. 1.3) in the propagation of cosmic protons through the extragalactic magnetic field as a function of the proton energy. Assuming a largest turbulence scale of 1 Mpc, intergalactic magnetic field of 1 nG and $K = 4°$. The upper and lower lines correspond for 200 Mpc and 30 Mpc propagation distances respectively

is no statistically significant evidence that EHECR arrival directions cluster along the galactic plane. So, it is reasonable to assume that particles with energies $E > 10^{19}$ eV are protons with extragalactic origin or are galactic heavy nuclei.

If EHECR seen at earth have extragalactic origins, then they have survived a very long time in travelling from their sources and there are several processes that can degrade the energy of particles as they propagate through the cosmos. These processes limit the maximum distances that EHECR sources can be from the earth:

- **Protons** may interact with the cosmic microwave background (CMB) radiation producing pions and nucleons. The nucleon (proton or neutron) threshold energy for a single pion production in the CMB is given by

$$E_{th} = \frac{m_\pi(m_N + m_\pi/2)}{\epsilon} \approx 6.8 \times 10^{16} \left(\frac{\epsilon}{eV}\right)^{-1} eV, \tag{1.4}$$

where ϵ is the typical CMB energy ($\epsilon \sim 10^{-3}$ eV). Therefore, protons with energies above $\approx 6.8 \times 10^{19}$ eV interact with the cosmic CMB. This is the Greisen Zatsepin - Kuzmin (GZK) effect [33, 34], and 6.8×10^{19} eV is the GZK cut off energy. This interaction produces pions and protons (or neutrons)

$$p + \gamma \rightarrow p + \pi^0 \quad , \quad p + \gamma \rightarrow n + \pi^+ \tag{1.5}$$

the resultant nucleon emerges with a reduced, but still very large, energy. Further interactions occur until its energy is below the GZK cut off energy. The interaction length of protons traveling through the CMB can be estimated from the photo-pion cross section and the CMB density[7],

$$L = (\sigma\rho)^{-1} \simeq 1.7 \times 10^{25} cm \simeq 6 Mpc \tag{1.6}$$

for $\rho = 410 cm^{-3}$ and $\sigma = 135 \mu$barns.

Figure 1.4 shows the energy of a proton as a function of the propagation distance. It shows that independently of the initial energy (10^{22}, 10^{21} and 10^{20}) after ~100 Mpc of propagation, the energy of the proton is reduced down to $\sim 10^{20}$ eV. This means that $> 10^{20}$ eV cosmic rays sources are unlikely to be farther than 100 Mpc.

- **Nuclei** also undergo photo-disintegration in the CMBR and infrared radiation, losing about 3-4 nucleons per Mpc traveled when their energy exceeds about 2×10^{19} eV[7]. Hence no nuclei can be observed at earth with such energy if the source is more distant than about 20 Mpc.

- **High energy photons** interact with the radio background radiation and produce electron-positron pairs. The attenuation length of photons with 10^{20} eV interacting with radio background radiation is just a few Mpc.

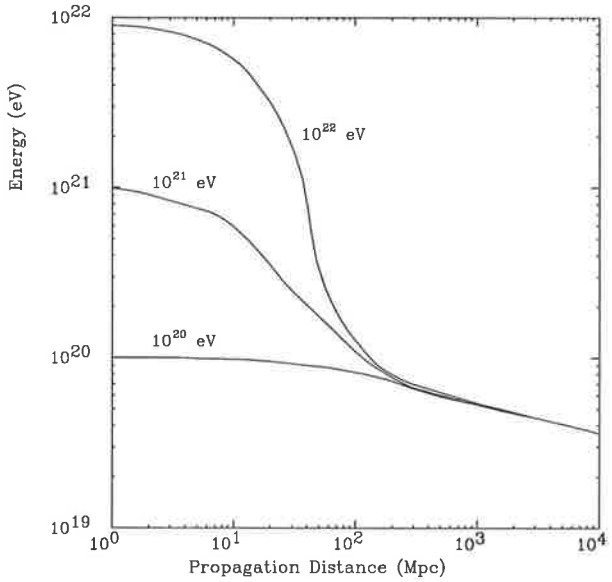

Figure 1.4: Energy of a proton as a function of the propagation distance[32].

1.3 Detection of the EHECR

The flux of arriving cosmic rays decreases very quickly with energy, e.g. particles with energies above 10^{20}eV occur at a rate of less than 1 per square kilometre per century. This makes it impossible to detect EHECR using direct methods, such as with balloons. Fortunately, when an EHECR hits the atmosphere it initiates a cascade of particles (EAS) [1] and loses energy through subsequent interactions (for simulation of EAS see [35], for studies on the EAS core structure see [36], and for studies on the EAS lateral distribution see [37]).

There are two indirect methods used to detect the EHECR. The first one consists of an array of particle detectors spread over a large area (ground array detector). Each particle detector will count the number of charged particles crossing through its surface. These particle detectors are used to measure the lateral distribution of the EAS at the ground and with this information we can determine the energy of the particle that hit the atmosphere. By looking at the firing times of the particle detectors we can determine the arrival direction of the EHECR.

[1] This cascade of particles is often referred in the literature as extensive air shower (EAS)

The second method relies on the fact that particles of the EAS cause the nitrogen present in the atmosphere to fluoresce, emitting light in the UV range (300-400 nm of wave length). The fluorescence rate is typically about 4 photons per metre per ionising particle. Even though the light per particle is so low, large air showers contain many billions of particles so that, overall, a measurable amount of light is produced. A wonderful method of determining the energy contained in the incident cosmic ray is provided by measuring the amount of light as the EAS develops through the atmosphere. This kind of detector is called "fluorescence detector".

1.3.1 The first generation of EHECR detectors

1.3.1.1 Volcano Ranch:

The Volcano Ranch ground array[38] was located in the state of New Mexico, USA. Initially, in 1959, it consisted of nineteen 3.3 m^2 scintillators. The detectors were distributed in a hexagonal grid covering 2 km^2. Later in 1960 the detector spacing was doubled to 864 m, to cover 8 km^2. This ground array operated until 1963 and it was the first experiment to register an EHECR above 10^{20} eV[39].

1.3.1.2 Haverah Park:

The Haverah Park ground array was located 17 miles from the University of Leeds (UK). This ground array consisted of 34 water Cerenkov detectors. The water Cerenkov detectors were 1.2 m deep, and had surface areas between 1 m^2 and 34 m^2. They were distributed inhomogeneously over an area of 12 km^2. The Haverah Park array operated for 20 years from 1968 to 1987[40].

1.3.1.3 SUGAR:

The Sydney University Giant Airshower Recorder (SUGAR) was located in the Pilliga State Forest in New South Wales, Australia (array latitude 30.53°S , longitude 149.60°E). The SUGAR ground array consisted of 47 independent stations distributed

over an area of 70 km^2. Each station contained two buried liquid scintillator counters separated by a distance of 50 m. The shielding over each detector was (1.5 ± 0.3)m of earth, and hence these detectors were sensitive to the penetrating muon component of extensive air showers. The SUGAR array operated between 1968 and 1979[41].

1.3.1.4 Yakutsk:

The Yakutsk ground array is located in the Lena river valley near the village of Oktyomtsy, 50 km south-west of Yakutsk (latitude 61.70 N, longitude 129.40 E). The Yakutsk ground array consists of 58 ground-based and 6 underground detectors of charged particles (electrons and muons), and 50 detectors of the atmospheric Cerenkov light. The total area covered by detectors is 12 km^2. In contrast to other ground arrays, atmospheric Cerenkov light is used to estimate the energy of primary particles. Yakutsky began operations in 1969 and it is the oldest EHECR detector still in operation[42].

1.3.1.5 Fly's Eye:

The Fly's Eye fluorescence detector was situated on the Dugway Proving Ground in the western Utah Desert. The Fly's Eye measured the fluorescence light emitted isotropically by the EAS charged particles. With this information, the air shower geometry and the energy of the primary particle was calculated. Initially in 1981, the Fly's Eye consisted of 67 spherical mirrors of 1.5 m diameter, with either 12 or 14 photomultiplier tubes (each tube with $5° \times 5°$ field of view) at the mirror focus. In 1986 a second site, 3.4 km distant was built (Fly's Eye II). The new site had 36 mirrors with similar characteristic to Fly's Eye I. Fly's Eye I and II operated in stereo mode until 1993[43].

1.3.2 EHECR detectors currently in operation

1.3.2.1 The Akeno Giant Air Shower Array (AGASA)

The AGASA observatory is situated at 138^o 30' E and 35^o 47' N(Tokyo, Japan). AGASA is a ground array detector and consists of 111 scintillation detectors. The detectors are distributed over an area of about 100 km^2 and have been in operation since 1990 [44, 45]. A20 (Akeno) was a prototype detector system of AGASA. The Akeno array covered an area of 20 km^2 and operated from 1984 to 1990. It is now a part of AGASA.

Each surface detector consists of a plastic scintillator of 2.2 m^2 area. The detectors are placed approximately 1 km apart. They are controlled and operated from a central computer through an optical fiber network. Relative times between the detectors are measured with 40 nsec accuracy; all clocks at detector sites are synchronized to the central clock and signal-propagation time in cables and electronic devices are regularly measured at the start of each run (twice a day). The details of the the AGASA instruments are described in [44, 45].

The AGASA experiment has an aperture of 125 km^2 sr for zenith angles less than 45^o for EAS with primary energy above 10^{18} eV. With this aperture the numbers of cosmic rays expected to be detected by AGASA per year are 9000, 90 and 1 $\sim$ 2 for energies above 10^{18} eV, 10^{19} and 10^{20} eV respectively. By August 1998 AGASA had observed 581 cosmic rays above 10^{19}eV, 47 above 4×10^{19}eV, and 7 above 10^{20}eV. The arrival direction distribution of these extremely high energy cosmic rays has been published by the AGASA collaboration. I will summarize the AGASA anisotropy results in Chapter 2.

1.3.2.2 The High Resolution Fly's Eye Cosmic Ray Detector (HiRes)

Given that the author's anisotropy studies (the focus of this thesis) are based on the HiRes data, the HiRes detector will be described in more detail in chapter 3.

1.3.3 Future EHECR detectors

1.3.3.1 The Pierre Auger Detector

The Pierre Auger project will consist of two similar sites, one located in the southern (Malargüe-Argentina) and one in the northern (Utah-USA) hemisphere. Both sites will have similar characteristics. The reason for having detectors with similar characteristics in each hemisphere, is because a uniform sky coverage is required for anisotropy studies. Also, there is no conclusive proof that the energy spectrum is the same in each hemisphere.

Each site will consist of a ground array detector covering approximately 3000 square kilometers and four fluorescence detectors. The number and location of the fluorescence detector is closely related to the shape of the ground array. The idea is that every shower detected by the ground array must be also detected by one of the fluorescence detectors (this is during night-time).

The Southern site is currently under construction. An engineering array and two prototype fluorescence detectors have already been built, and a few EAS have now been detected. The southern site is programmed to start operations on 2003.

- **The Auger Fluorescence Detector:** Each 3.8 m diameter mirror of the Auger Fluorescence Detector covers a field of view of 30° by 30° in the sky. The photomultiplier size is designed to cover a 1.5° field of view and the optical design will keep the spot diameter under 0.5°. The optics was designed to maximize the collecting area, to keep the uncertainty of the reconstructed arrival direction under 0.5° and the uncertainty in determining the depth of maximum size of the shower (X_{max}) under 20 g/cm^2. The hexagonal photomultipliers are placed across a spherical surface centered at the focal plane of the mirror. In addition, a 2.2 m diameter diaphragm is placed in front of the mirror to ensure an homogeneous spot size independently of the tube position (Schmidt optics). FADC electronics digitalize the PMT signal every 100 ns and the PMT pulse shape is well determined (HiRes-2 uses similar FADC electronics, see section 4.3).

- **The Auger Ground Array Detector:** The design of the ground array is driven by the goal to collect high statistics around and above the predicted GZK cut-off. This requires the instrumentation of an area of 3000 square kilometers per site. The spacing of 1.5 km between detection stations is defined by the requirement of full detection efficiency above 10^{19} eV and of a good sampling of the lateral density distributions. The low density of particles ($\approx 1/m^2$) to be measured with good statistical precision imposes an area of $\approx 10\ m^2$ for the water Cerenkov tanks.

  Thus, the surface array will comprise 1600 water Cerenkov detectors spaced by 1.5 km on a triangular matrix, covering an area of about 3000 square kilometers.

  Each detector consists of a cylindrical, opaque tank having a diameter of 3.6 m and a water height of 1.2 m. The water is contained in a sealed bag, or liner, that prevents contamination, provides a barrier against any remaining external light, and diffusely reflects the Cerenkov light emitted in the water. Three large diameter (≈20 cm) hemispherical photomultipliers are mounted facing down and looking at the water through sealed windows that are an integral part of the liner.

1.3.3.2 OWL and EUSA

- **Orbiting Wide-angle Light-collectors (OWL):** The OWL [11] is a NASA project and will measure the highest energy cosmic ray air showers by observing atmospheric scintillation light from orbit. By using the atmosphere as a target, OWL could get an effective detection aperture of 10^5 km^2 sr and could expect to see more than 10^2 events per year with energies above 2×10^{20} eV (assuming a flux of 1 particle per km^2 per millennium).

- **Extreme Universe Space Observatory (EUSO):** The EUSO [12] is a mission of the European Space Agency (ESA) now under study (Phase A). The EUSO will be accommodated on the International Space Station (ISS) with a goal of a three year flight starting in mid 2007. EUSO will investigate cosmic

rays and neutrinos of extreme energies ($E > 5 \times 10^{19}$ eV) by looking at fluorescence light produced when particles interact with the Earth's atmosphere. It is expected to detect of the order of 10^3 energetic ($E > 10^{20}$ eV) cosmic rays per year. Figure 1.5 shows a schematic representation of the EUSO field of view over the Earth's atmosphere.

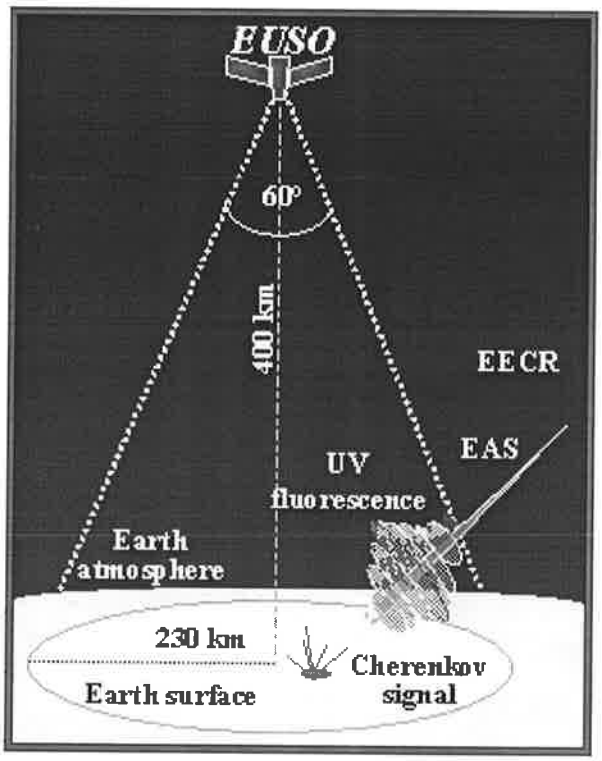

Figure 1.5: Schematic representation of the EUSO field of view over the Earth's atmosphere. The EAS size through the atmosphere is also represented[12].

Chapter 2

Anisotropy studies of EHECRs (review)

Studying the arrival directions of EHECRs is one of the most important methods for revealing the origin of these enigmatic particles, as well as studying the diffusion of EHECRs through the galactic magnetic field. However, this task is not simple. There are some considerations that cosmic ray researchers have learned to deal with in the past decades. There are also some technical limitations that upcoming cosmic ray detectors hopefully will overcome. Some of the considerations and limitations include:

- The non homogeneous exposure: This is especially the case for the fluorescence detectors which only operate at night-time. They have a very non-homogeneous exposure, even along the same declination level. More cosmic rays will be detected from the regions of the sky with greater exposure. Ground array detectors have homogeneous exposure along the same declination level. However, if the ground array stops working for some periods of time, or the detector efficiency varies, the exposure along the same declination level may also no longer be homogeneous. All these considerations of the exposure must be considered for the anisotropy analysis.

- Partial observation of the sky: Most of the cosmic ray detectors are located in

the northern hemisphere and they can only see a limited region of the southern declinations of the sky. For a reliable systematic broad-scale anisotropy study it is necessary to have good statistics of EHECRs in both hemispheres.

- The extremely low flux of EHECRs: Even though the AGASA array covers and extension of 100 km^2, currently only 10 events with energies above 10^{20} eV, and 64 above 4×10^{19} eV and 811 above 10^{19} eV have been detected in approximately 18 years of operation.

The cosmic ray anisotropy is conventionally defined as

$$\delta = \frac{I_{max} - I_{min}}{I_{max} + I_{min}} \tag{2.1}$$

where I_{max} and I_{min} are the maximum and minimum intensities of cosmic rays across the sky as a function of some coordinate. However, this definition is not often used to express the anisotropy. Instead, contour plots of the sky showing the magnitude of the excess (or deficit) rates [1] and the excess (or deficit) significance are used.

Anisotropy studies using harmonic analysis in the right ascension (RA) distribution of events is also possible for ground array detectors. The use of the standard technique is only possible when the expected right ascension distribution is flat as known. The method consists of fitting the RA distribution of events to a sine wave with period $2\pi/m$ (mth harmonic) to determine the amplitude and phase of the anisotropy. The mth harmonic amplitude, r, and phase of maximum, θ, are obtained for a sample of N measurements of phase (RA), $\phi_1, \phi_2, ...\phi_n (0 \leq \phi_i \leq 2\pi)$ from

$$r = (a^2 + b^2)^{1/2} \tag{2.2}$$

$$\theta = tan^{-1}(b/a) \tag{2.3}$$

where $a = (2/n) \sum_{i=1}^{n} cos(m\phi_i)$ and $b = (2/n) \sum_{i=1}^{n} sin(m\phi_i)$.

[1] The excess rate is obtained comparing the detected fluxes with the fluxes expected from an isotropic cosmic ray flux in each region of the sky

The statistical significance of any anisotropy is represented by k. If events with total number N are uniformly distributed in RA, the chance probability of observing the amplitude $\geq r$ is given by

$$P = exp(-k) \tag{2.4}$$

where,

$$k = Nr^2/4 \tag{2.5}$$

Most experiments so far, have shown that cosmic rays at lower energies ($< 10^{18}$ eV) arrive from all directions with almost equal probability. With limited statistics the Haverah Park[46] and Yakutsk[42] groups claimed small anisotropies in the energy region near 10^{17} eV. However the phases of the anisotropies were 90° apart (RA=212° and RA=124° respectively). The isotropy of lower energy cosmic rays is due to the scrambling effect of the diffusion of the particles in the chaotic and regular galactic magnetic field in the galaxy. The galactic magnetic field (in the μG scale) is strong enough to considerably deflect their trajectories. However, at higher energies, cosmic ray protons are expected to move in more rectilinear paths and have limited departure from isotropy (ie. anisotropy).

If our present understanding of the galactic field is correct, diffusive motion loses its importance as the energy of the particles increases much beyond 10^{18} eV. Instead, the motion is governed by the regular galactic magnetic field. One therefore expects, if galactic sources are distributed mainly in the galactic plane, that an anisotropy for the proton component of cosmic rays flux will develop toward the galactic disk (broad scale anisotropy). If sources are extra galactic and centred on the local supercluster of galaxies, we expect to see an anisotropy directed at higher galactic latitudes toward Virgo. If galactic sources produce a heavy, iron-rich composition, then galactic anisotropy may not be seen even beyond 10^{18} eV because of the smaller Larmor radius for such particles. Of particular interest are any correlations of anisotropy with changes in the spectral index and/or composition.

2.1 Anisotropy of cosmic rays with energies around 10^{18} eV

Around 10^{18} eV the actual statistics of cosmic rays are reasonable large, especially for the AGASA experiment. As a result, systematic anisotropy studies can lead us to high confidence level results. In this energy range there is a clear anisotropic feature observed by different experiments. This is an enhancement of cosmic rays arriving from the galactic plane regions. Recent studies indicate that the observed galactic plane enhancement is due to cosmic ray excesses from the Galactic centre and Cygnus regions.

2.1.1 Correlations with the Galactic Centre

In 1998 the AGASA group reported a study of data collected with their initial Akeno ($20\,\mathrm{km}^2$) and the final AGASA ($100\,\mathrm{km}^2$) extensive air shower arrays over the period from 1984 to mid-1995 [47]. In that report the AGASA collaboration performed a harmonic analysis of the RA distributions of the arriving cosmic ray directions. Some care was taken to ensure that the expected RA distribution was flat for an isotropic flux of cosmic rays. The RA distribution may change due to temporal efficiency changes [2] or due to days with partial operation. The first harmonic analysis was performed systematically using only events with energy greater than a certain energy. Then, the value of k was plotted as a function of energy (fig. 2.1).

Figure 2.1 shows a greater value of k ($k \sim 10$) for events with energies above 10^{18} eV. When considering only events within the $10^{17.9} - 10^{18.3}$ eV energy range, k reaches a maximum value of 11.1. The first harmonic analysis also indicated that the anisotropy was around 300° RA with an amplitude of 4%.

In order to identify the specific celestial coordinates (RA,dec) of the anisotropy, a two dimensional analysis using contour plots was performed. Only events in the region of $10^{17.9} - 10^{18.3}$ eV were considered. The expected back ground was calculated

[2] diurnal variations of temperature and barometric pressure affect the efficiency of the array

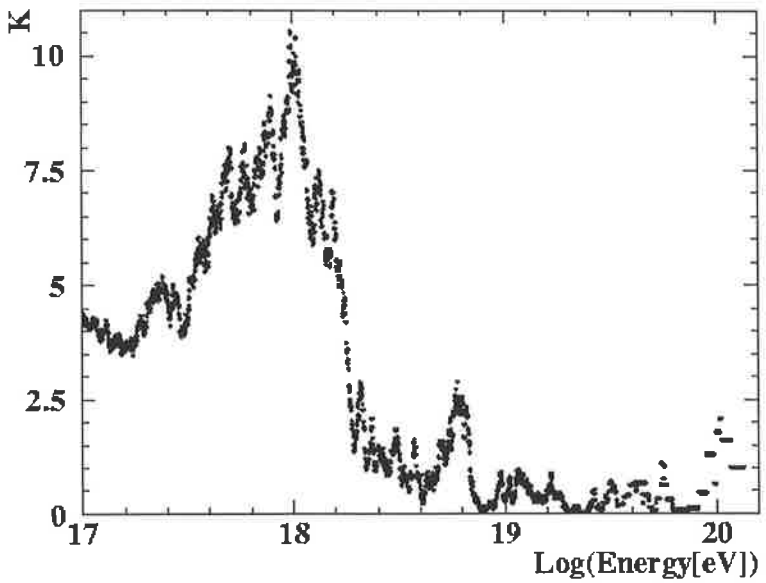

Figure 2.1: Results of the first harmonic analysis in right ascension. The k value of the anisotropy in each energy bin is plotted as a function of the primary energy[47].

assuming a homogeneous distribution of events in RA. Then, the sky was divided into declination bands of 1°. The event density (events per RA and dec bin) in each declination band was the total number of events divided by 360. The detected number of events within a circle of 20° centred near the Galactic Centre was compared with the expected number of events within this region, and a 4.1σ excess was obtained (308 events were observed and only 242.5 were expected). Three other different circle radii were tried, 10°, 15° and 30°. However their excesses (2.6σ, 2.7σ and 2.8σ respectively) were lower than when using a 20° radius.

A sky map of excess shower density, using a bin size of 20° showed that the observed excess in the harmonic analysis, was due to a 4.1σ excess in a region near the Galactic centre plus a 3σ excess from the region of Cygnus (both regions are around the same RA).

In 1999, the AGASA group presented a new analysis with better statistics. They incorporated new data (up to April 1999)[48]. The energy range used this time was slightly different ($10^{18.0}$ to $10^{18.4}$eV). The new results suported the previous results. They found a 4.5σ excess near the Galactic Centre (506 detected events where only 413.6 events were expected), with a smaller 3.9σ excess (3401 detected where only

3148 events were expected) seen in the Cygnus region (fig. 2.2). The excess from the Cygnus region will be discussed in the following sub-section.

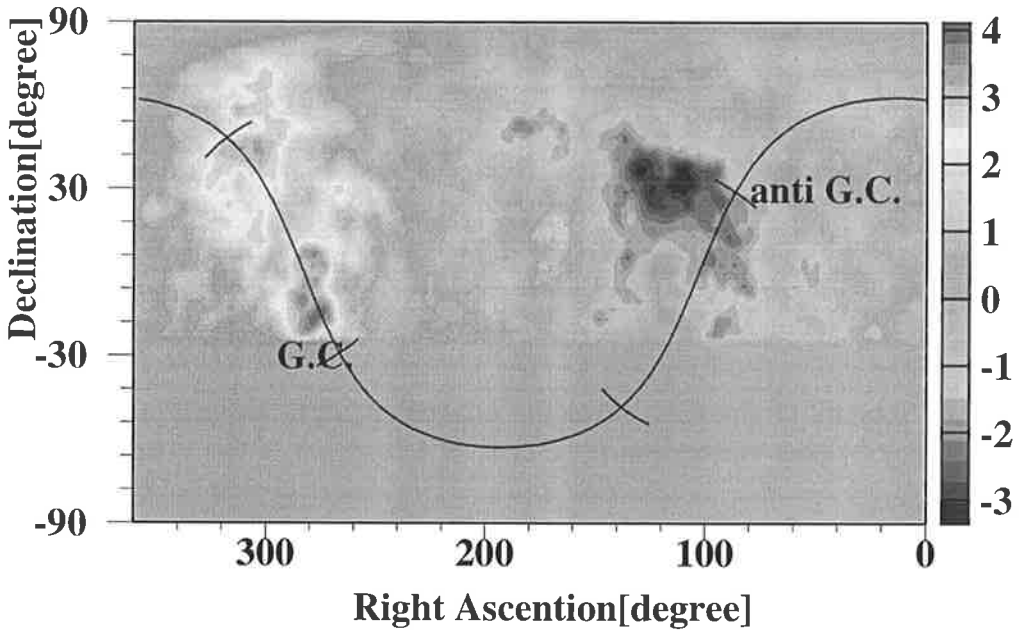

Figure 2.2: Statistical significance of the observed AGASA excess and deficit [48]. The sky map is in equatorial coordinates.

The Fly's Eye experiment also showed an excess of cosmic rays (with energies between $10^{17.6} - 10^{18}$ eV) from the Galactic plane[8]. In the Fly's Eye report, they do not attempt to identify any specific galactic longitudes of the excess. However, they mentioned that "*Detailed comparison between mono data and stereo data shows that there is in fact an excess of events near the galactic centre in the mono data*". Considering the possible energy scale difference between ground arrays and fluorescence detectors, the AGASA and Fly's Eye energy range of the excess may well overlap. As pointed out by the AGASA group, other experiments such as Haverah Park and Yakutsk are too northerly to see the excess region identified by AGASA near the Galactic Centre.

During the early stage of my PhD, I took part in a SUGAR Galactic centre anisotropy analysis. Chapter 3 will include a detailed description of that work. The results of the SUGAR analysis also confirmed an excess of cosmic rays from the Galactic centre region. The SUGAR energy range of the excess is consistent with the one

of AGASA.

A specific energy range of the anisotropy may offer a clue to the origin of the signal particles. The decay length of a 10^{18} eV neutron is approximately 10 kpc, roughly the distance to the Galactic Centre [49]. At energies lower than this, neutrons from the distance of the Galactic Centre would decay before reaching the Earth. This may be the reason of why we do not detect any excess from the Galactic centre region at lower energies ($< 10^{18}$ eV). The fact that the excess from the Galactic centre stops at $\sim 10^{18.4}$ eV, could identify the energy limit of this particular source. Other clues to the origin of the signal particles would include the scale of the anisotropy on the sky (point source-like or broad) and the response of different detector arrays to the signal events (a possible discriminant between hadronic and non-hadronic primary cosmic rays).

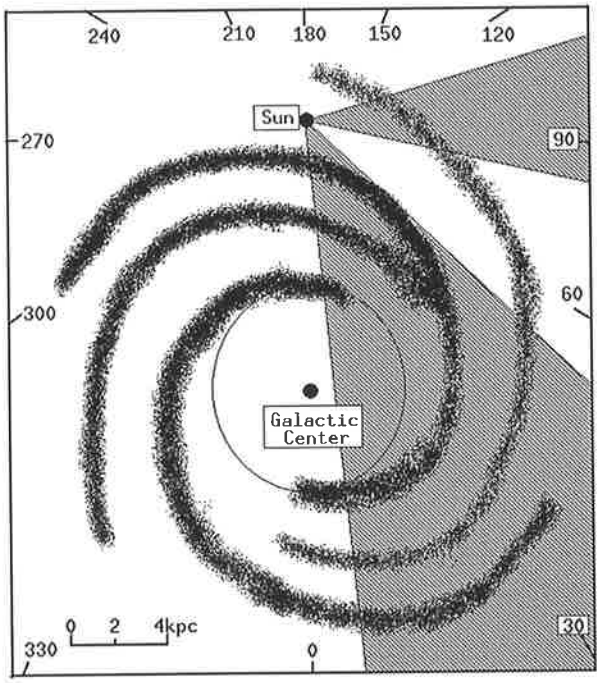

Figure 2.3: Position of the Solar system in relation with the spiral arms of the galaxy [50]. The directions of the observed AGASA excesses are indicated by the hatched regions.

Another possible explanation of the anisotropy involves protons coming from the nearby galactic arms. The excess is directed toward the galactic plane, pointing close

to the galactic centre, and this direction crosses a number of galactic spiral arms (fig 2.3). This hypothesis would naturally explain the deficit of events from the anti-galactic region observed in figure 2.2, since no galactic spiral arms are present in that direction.

2.1.2 Anisotropy from Cygnus X-3

In 1989 and 1990 the Fly's Eye[51] and the Akeno[52] groups respectively reported an excess of cosmic rays with energies above 5×10^{17} eV from the region of Cygnus X-3. However, contemporaneous data from Haverah Park experiment[53] did not observe any similar feature. The Akeno and the Fly's Eye estimated fluxes are fairly consistent at $(18 \pm 7$ and $20 \pm 6) \times 10^{-18}$ particles/cm^2 s respectively. However, the flux upper limit estimated by Haverah Park is, $< 4 \times 10^{-18}$ particles/cm^2 s for neutrons and $< 8 \times 10^{-18}$ particles/cm^2 s for gamma rays.

Figures 2.4 and 2.5 show the observed excess from the Cygnus region by the Fly's Eye and the Akeno experiments respectively. The excess is in terms of number of σ, which is given by $(\rho_{act} - \rho_{sim})/\delta$. Here ρ_{act} is the actual density, ρ_{sim} is the expected density, and the denominator δ is the rms deviation of the density values for that sky location. The 4σ peak in Fly's Eye and the 3.9σ peak in Akeno deviate from the direction of Cygnus X-3 ($\alpha = 307°$, $\delta = 40.8°$) by $2° - 3°$. The Fly's Eye group performed simulations in order to estimated the effect of the detector resolution in determining the centre of a source. They introduced artificial events in the Cygnus region. The artificial events were distributed according the geometry resolution of the detector. They found that the estimated centres of the excess were displaced from the true source location by an average 3.1°.

As mentioned in the previous section, the AGASA group with about 216,000 showers collected over 15 years (1984-1999)[48] also observed an excess (3.9σ) from the Cygnus region (fig.2.2). However, this excess was limited to events within a narrow energy range ($10^{18.0}$ to $10^{18.4}$eV).

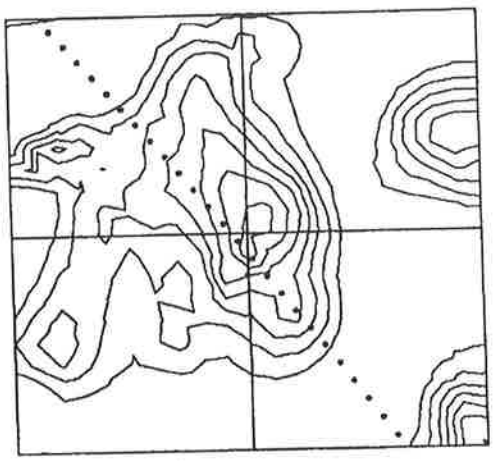

Figure 2.4: Cygnus X-3 is at the centre of this contour plot. The plot is $20° \times 20°$, with declination increasing vertically and right ascension increasing to left. (The horizontal dimension is 20° true, not 20° of right ascension.) The dots are points of the galactic plane separated by 1° longitude. The contour lines map represent the significance of the shower density excess observed by the **Fly's Eye experiment**. Their σ values are 1.0, 1.5, 2.0, 2.5, 3.0, 3.5, and 4.0. Only events with energies above 5×10^{17} were considered [51].

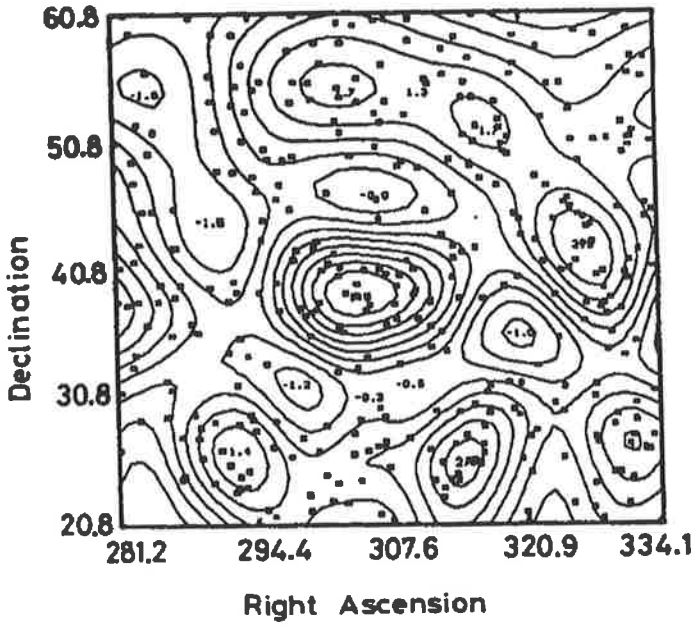

Figure 2.5: The contour lines map represent the significance of the shower density excess observed by the **Akeno array**. Their σ values go in steps of 0.5 deg. The peak around the Cygnus region correspond to a 3.5σ excess. The dots represent the arrival direction of each event. Only events with energies above 5×10^{17} were considered [52].

2.2 Anisotropy of cosmic rays with energies above $10^{18.5}$ eV

Above $10^{18.5}$ eV the statistics of cosmic rays are limited, and above 4×10^{19} eV they are even smaller. As mentioned above, the AGASA detector has so far detected (March-2002) 64 events above 4×10^{19} eV and only 10 events above 10^{20} eV with zenith angles smaller than 45°[54]. With these limited statistics at the highest energies, the confidence level of any anisotropy feature would not be high. Two anisotropy features were observed by different detectors within this energy range. These are a small correlation with the supergalactic plane and some clustering of events within a limited space angle.

2.2.1 Correlations with the Galactic and Supergalactic planes

In 1984 Wdowczyk and Wolfendale [55] using all the available data from ground arrays, found some evidence of a possible enhancement of cosmic rays above 10^{18} eV from the direction of the galactic plane. They showed that the galactic plane enhancement in arrival directions would have started by 10^{18} eV (at lower energies the galactic magnetic field would scramble the anisotropy) and be rather strong by 10^{19} eV (an absence of a galactic plane enhancement above 10^{19} eV would imply a non-galactic origin). As a result, they saw the necessity for a model for the galactic plane enhancement in which the angular width of the galactic plane as seen in cosmic rays shrinks slowly with increasing energy. As a first approach they presented a parameterization function for the galactic plane enhancement (eq.2.6),

$$I(b) = I(0)[(1 - f_E) + f_E * exp(-b^2)] \tag{2.6}$$

where b is the galactic latitude in radians (b can also be the super galactic latitude, in the case where we evaluate a possible super galactic plane enhancement), and f_E is an energy-dependent galactic latitude enhancement factor. A positive value of f_E means a galactic plane enhancement, a 0 value means that the arrival direction distribution

is isotropic, and negative values suggest an anisotropy not related with the galactic plane.

The Wdowczyk and Wolfendale parameterization is widely used by the cosmic ray community to express the anisotropy from the galactic plane. In 1991 Watson[56] summarized the cosmic ray status. In his report he presented the estimated f_E as a function of energy for the Akeno, Haverah Park, Yakutsk and SUGAR ground arrays (fig.2.6).

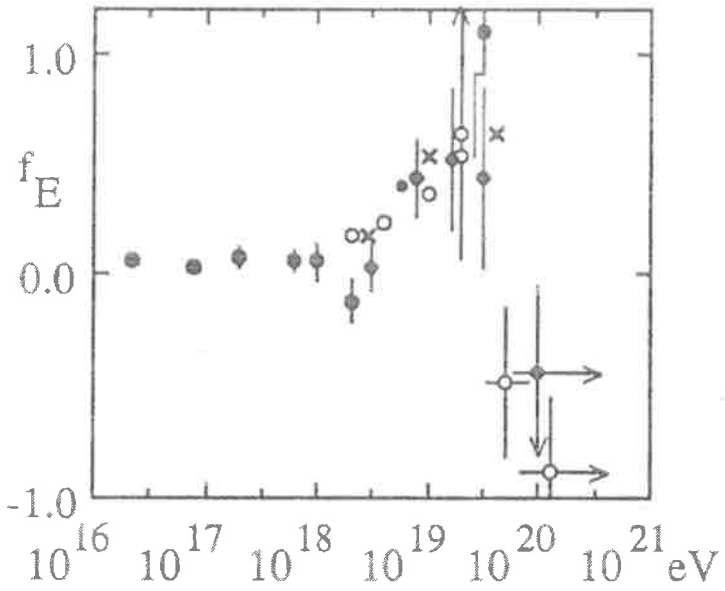

Figure 2.6: The Wdowczyk-Wolfendale parameter, f_E as a function of energy.The diagram includes data from: Akeno (solid circles), Haverah Park (diamonds), Yakutsk (crosses) and SUGAR (open circles)[56] .

Figure 2.6 shows a clear peak of f_E at energies around 2×10^{19} eV ($10^{19.3}$) eV, suggesting an anisotropy from the galactic plane in this energy range. Above this energy the f_E of SUGAR and Haverah Park become negative, implying that there is an anisotropy not associated with the galactic plane.

Recently, with better statistics, the AGASA[9] and the Fly's Eye[8] groups reported more anisotropy studies. Both reports estimated f_E as a function of the energy (fig.2.7 and fig.2.8). Both groups confirmed a negative value for f_E at energies above $10^{19.5}$. The peak around $10^{19.3}$ eV present in previous experiments, is not present in the

AGASA (fig.2.7 left hand side plot) or Fly's Eye (fig.2.8 left hand side plot) results. If we consider a possible energy scale difference between AGASA and Fly's Eye due to the difference between the techniques used to estimate the primary energy [3], the estimated shape of f_E in both detectors would be consistent.

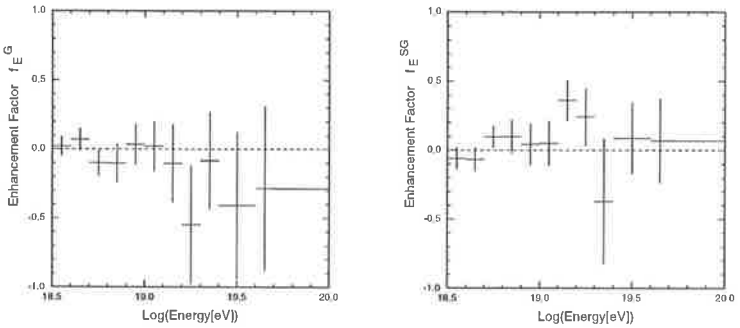

Figure 2.7: The Wdowczyk-Wolfendale parameter f_E as a function of energy estimated by AGASA[9]. The left plot is the f_E using galactic latitudes, and the right plot is using supergalactic latitudes.

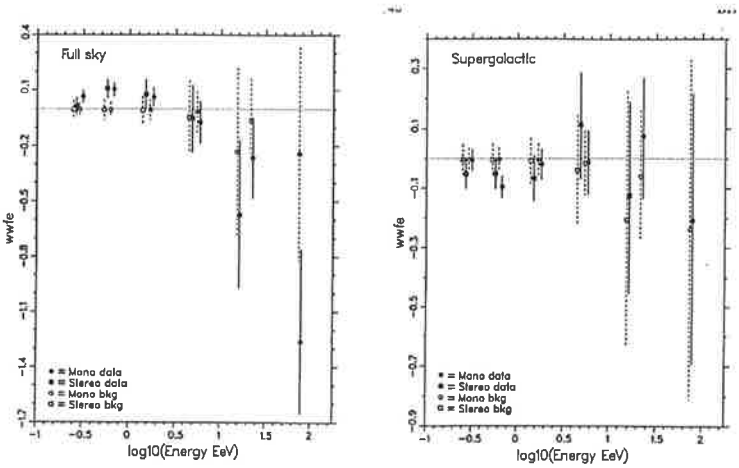

Figure 2.8: The Wdowczyk-Wolfendale parameter f_E as a function of energy estimated by the Fly's Eye[8].The left plot is the f_E using galactic latitudes, and the right plot is using supergalactic latitudes. The open circles and open squares show the estimated f_E assuming an isotropic flux of cosmic rays.

The chance probability that all first generation ground arrays had a peak of the galactic enhancement factor, f_E, around the same energy (2×10^{19} eV) as observed in figure 2.6 must be quite low. It is puzzling that this is not confirmed in Fly's Eye or AGASA.

[3] A possible energy scale difference, $10^{0.4}$, was pointed out in [8]

The Fly's Eye group showed that the low statistics at higher energies may bias the estimated value of f_E. In figure 2.8, the estimated f_E assuming an isotropic distribution is shown with open circles and open squares. The value of f_E is approximately 0 for energies below 10^{19} eV (as expected for an isotropic distribution), but above this energy f_E becomes negative. They suspect that the large negative f_E reported in some other studies could also be affected by the large bias inherent in low statistic data samples.

Using a different technique, in the higher energy range of $\geq 4 \times 10^{19}$ eV, Stanev et al. [57] have claimed that cosmic rays exhibit a correlation with the direction of the supergalactic plane. Their result was mainly based on the Haverah Park data set. They calculated the average (eq. 2.7) and rms (eq. 2.8) angular distance from the galactic and supergalactic planes:

$$< |b^{G(SG)}| >= \frac{\sum_i |b_i^{G(SG)}|}{N} \tag{2.7}$$

$$b_{RMS}^{G(SG)} = \sqrt{\frac{\sum_i (b_i^{G(SG)})^2}{N-1}} \tag{2.8}$$

where $b_i^{G(SG)}$ is the galactic (supergalactic) latitude of the ith event.

In order to understand the meaning of these quantities, they performed a Monte Carlo simulation of uniformly distributed arrival directions by using the declinations of the experimental showers and sampling a random right ascension value. This way, they took into account the exposure of each detector to generate the expected arrival directions assuming an isotropic cosmic ray flux. Ten thousand Monte Carlo sets were simulated for every sample and energy threshold. The probability that the correlation of the experimental data to one of the large scale structures due to chance coincidence is estimated by the fraction of Monte Carlo sets that have $< |b^{G(SG)}| >$ and b_{RMS} values smaller than the experimental one. Table 2.1 summarizes these results.

In the same energy range and using the same technique, a broad scale correlation with the supergalactic plane was not observed in the data set of SUGAR [58](see table 2.2). Neither AGASA [9], nor Fly's Eye [8] experiments (using the Wdowczyk and Wolfendale parameterization) found a supergalactic correlation in this energy

E > EeV	# evt	b^G_{RMS} °			b^{SG}_{RMS} °			$< \|b^G\| >$°			$< \|b^{SG}\| >$°		
		data	MC	P_μ	data	MC	P_μ	data	MC	P_μ	data	MC	P_μ
8 events above 100 EeV													
100	8	47.9	40.2	0.820	26.2	38.3	0.072	35.5	31.4	0.690	18.8	30.4	0.058
Haverah Park data													
20.	73	39.7	36.2	0.960	32.1	32.4	0.680	33.4	29.8	0.970	26.3	26.2	0.680
40.	27	46.5	36.7	0.996	23.3	33.5	0.006	39.5	30.2	0.995	18.6	26.9	0.013
60.	12	52.7	38.2	0.994	23.9	35.5	0.035	45.9	31.0	0.995	18.2	28.2	0.038
All available data													
20.	143	37.9	36.7	0.890	31.9	33.5	0.340	31.2	30.2	0.880	25.5	27.3	0.310
40.	42	45.6	36.8	0.998	26.2	33.8	0.012	38.3	30.0	0.998	20.3	27.4	0.012
60.	16	48.1	38.4	0.976	26.4	36.6	0.038	41.0	31.3	0.978	19.7	29.5	0.027

Table 2.1: Correlation of the arrival direction of UHECRs with the galactic and supergalactic plane[57]. Data (before 1991) from Haverah Park, AGASA, Volcano Ranch and Yakutsk.

min. E (EeV)	no. of events	b^G_{rms}			b^{SG}_{rms}			$<\| b^G \|>$			$<\| b^{SG} \|>$		
		data	MC	P	data	MC	P	data	MC	P	data	MC	P
10	252	38.4	39.5	0.20	40.9	40.1	0.72	32.1	33.0	0.25	34.4	33.5	0.72
20	130	37.9	39.7	0.19	40.9	39.8	0.76	31.4	32.9	0.21	34.3	33.2	0.76
40	49	37.3	40.0	0.20	42.3	39.9	0.80	31.3	33.0	0.29	35.4	33.2	0.80
60	24	33.1	39.8	0.08	44.0	39.0	0.89	27.5	32.4	0.13	37.2	32.0	0.89

Table 2.2: Tests for SUGAR data clustering toward the galactic and supergalactic planes in four overlapping energy ranges for events with zenith angles less than 55° [58].

range (right hand side plots in fig. 2.7 and 2.8). However, AGASA observed 3 pairs and 1 triplet of cosmic ray events above 4×10^{19} eV with angular separations of less than 2.5°. The triplet and one of the pairs are within 2° of the SG plane.

The Fly's Eye and the AGASA Supergalactic f_E data suggest a small correlation with the SG plane at energies around $10^{18.7}$ and $10^{19.1}$ eV respectively. This energy scale difference would again be consistent with a factor of $10^{0.4}$.

2.2.2 Clustering of the EHECR

The AGASA group did not find any statistically significance large-scale anisotropy for EHECRs. However, with a two dimensional analysis (see section 2.1.1 for a description of the analysis), they showed that there are a few regions in the sky with EHECRs clustered within 2.5°[9].

Figure 2.9 shows the significance contour map of cosmic ray excess/deficit above 4×10^{19} eV (47 events). In order to make the excess/deficit clearer, a bin size of 2.5° was used. This bin size was selected according to the resolution of the detector for this energy range ($\sqrt{2} \times \delta\theta$).The bright regions indicate an excess of events and darker regions a deficit of events. Three doublets and one triplet of events clustered within 2.5° were observed. The doublets are denoted in figure 2.9 by C1, C3 and C4. There is a fourth doublet, C5, that contains one event with energy 3.89×10^{19} eV. The triplet is denoted by C2. Including the data sets of Haverah Park, Yakutsk and Volcano Ranch another triplet is found at the C1 cluster position. It is remarkable that both triplets (C1 and C2) are close to the supergalactic plane.

Figure 2.10 shows the significance contour map of the AGASA cosmic ray excess/deficit above 10^{19} eV. The selected angular bin size for this energy range was 4°. The C2 excess region is also present in this energy range. Two different broader excess regions appear in this energy range, BC1 and BC2. Table 2.3 indicate the coordinates of the AGASA clustering regions.

In 1982, Lloyd-Evans performed a harmonic analysis using all the available data from Haverah Park, Yakutsk and Volcano Ranch[59]. He found an anisotropy of cosmic rays with energies $E > 4 \times 10^{19}$ eV with chance probability of 0.014%. The phase of the anisotropy was (12 ± 1.9)h. This anisotropy phase is consistent with the location of the triplet C2 (RA=169.65°).

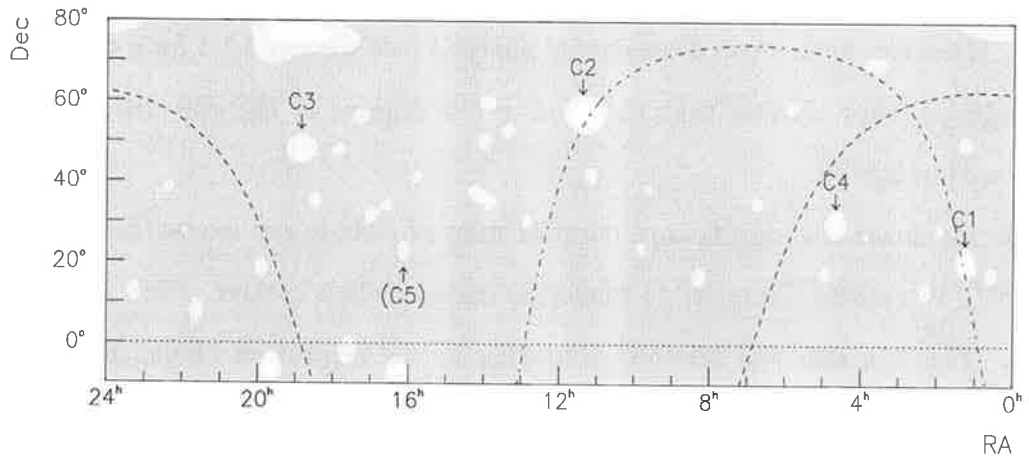

Figure 2.9: Significance map of AGASA cosmic ray excess/deficit above 4×10^{19} eV. The dashed and dash-dotted curves indicate the Galactic and supergalactic planes respectively. This figure mainly reflects the arrival directions of individual events[9].

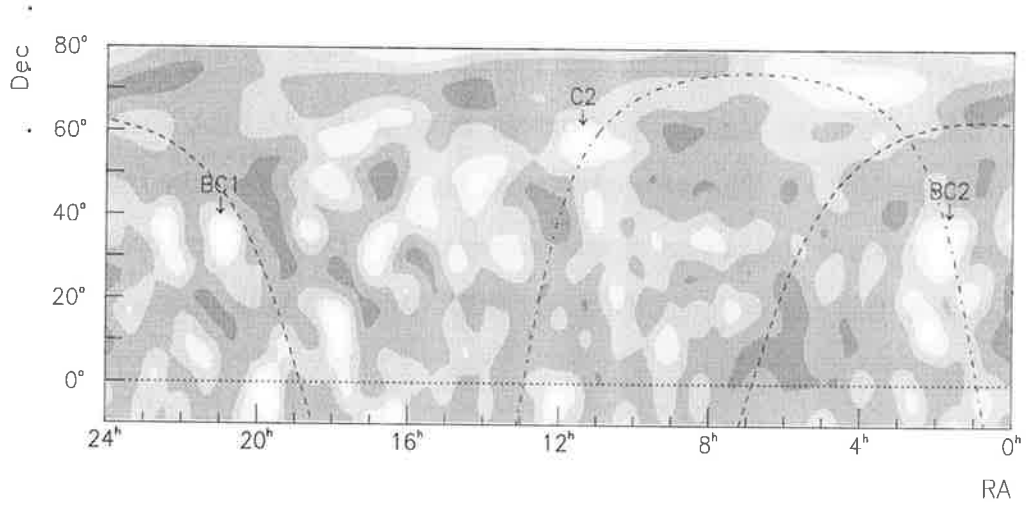

Figure 2.10: Significance map of AGASA cosmic ray excess/deficit above 10^{19} eV. The dashed and dash-dotted curves indicate the Galactic and supergalactic planes respectively. The contour map has eight steps between [-3σ,+3σ]; two steps below -1.5σ are absent.[9]

Region	characteristic	Coordinates			
		α (°)	δ (°)	l^G (°)	b^G (°)
C1	triplet	18.6	20.6	130.3	-41.8
C2	triplet	169.7	56.9	145.5	56.2
C3	doublet	283.0	48.1	77.8	20.1
C4	doublet	69.9	30.0	170.7	-11.0
C5	doublet	225.5	23.4	39.0	46.8
BC1	broad scale cluster	312.5	32.5	75	-6
BC2	broad scale cluster	25.1	35.0	134	-27

Table 2.3: Coordinates of the AGASA clustering regions. C1 is a doublet when considering only the AGASA data, but it became a triplet when considering other ground array data. The triplets and doublets are formed with $E > 4 \times 10^{19}$ eV events, and the broad scale cluster are formed with 10^{19} eV events

2.3 Correlation of the EHECR with galaxy directions

There are events detected by several experiments with energies above the GZK cut off. These particles cannot travel more than 50 Mpc without losing significant energy[60, 61]. Also such energetic particles are thought to be only slightly deflected by the intergalactic magnetic fields. This means that their arrival direction could be correlated with the luminous matter distribution if the cosmic rays originated in astrophysical sources such as hot spots of radio galaxies, active galactic nuclei, accretion flows around clusters of galaxies, or relativistic shocks in gamma ray bursts.

Assuming that the EHECR sources are distributed according to the actual distribution of extragalactic objects, Medina-Tanco simulated the propagation of individual particles from these sources through the intergalactic medium (IGM)[62]. He built an all-sky arrival probability distribution function of EHECRs. Figure 2.11 shows the arrival probability distribution considering only sources distributed between 20 - 50 Mpc (top plot), and between 50 -200 Mpc (bottom plot). In the plots, pair 1, pair

2 and pair 3 refer to C1, C2 and C3 (table 2.3). These were the only event clusters observed by AGASA in 1996 [63]. In a later report in 1999[9], AGASA reported that C2 had became a triplet and that two new doublets were observed (C4 and C5). They also identified two regions with a broader scale clustering of events with $E > 10^{19}$ eV (BC1 and BC2). I have included in figures 2.11 the locations of C4, C5, BC1 and BC2. The arrival direction of the triplet C2 coincides with a high probability arrival direction considering sources at 20 to 50 Mpc (fig.2.11, top plot). And the arrival direction of BC2 coincides with a high probability arrival direction considering sources at 50 to 200 Mpc (fig.2.11, bottom plot).

If some energetic cosmic ray directions are not correlated with any luminous matter, there is another possibility for their origin. As we saw above, they could be generated through the decay of supermassive "X" particles related to topological defects. If such particles are part of the dark matter and are concentrated in galactic halos, an anisotropy associated with our galactic halo and with others galaxy halos is expected.

The AGASA group performed a search for astrophysical objects capable of accelerating EHECRs. They attempted to correlate the directions of their cluster events with objects in three catalogs: The second EGRET catalog[64], the CFA redshift catalog [65], and the eighth extragalactic redshift catalog[66]. The selection criteria were:

- A separation angle within 4° for a member of each cluster and 2.5° for the 10^{20} eV cosmic ray.

- A redshift (z) below 0.002.

In the CFA catalog, only quasi-stellar objects and active galactic nuclei were selected. The candidate objects are listed in table 2.4. The AGASA group also noted that the BC1 cluster is in the direction of a famous supernova remnant, the Cygnus Loop ($20^h50^m, 30°34'$), but the Cygnus Loop is thought to be too small to accelerate cosmic rays up to 10^{19} eV.

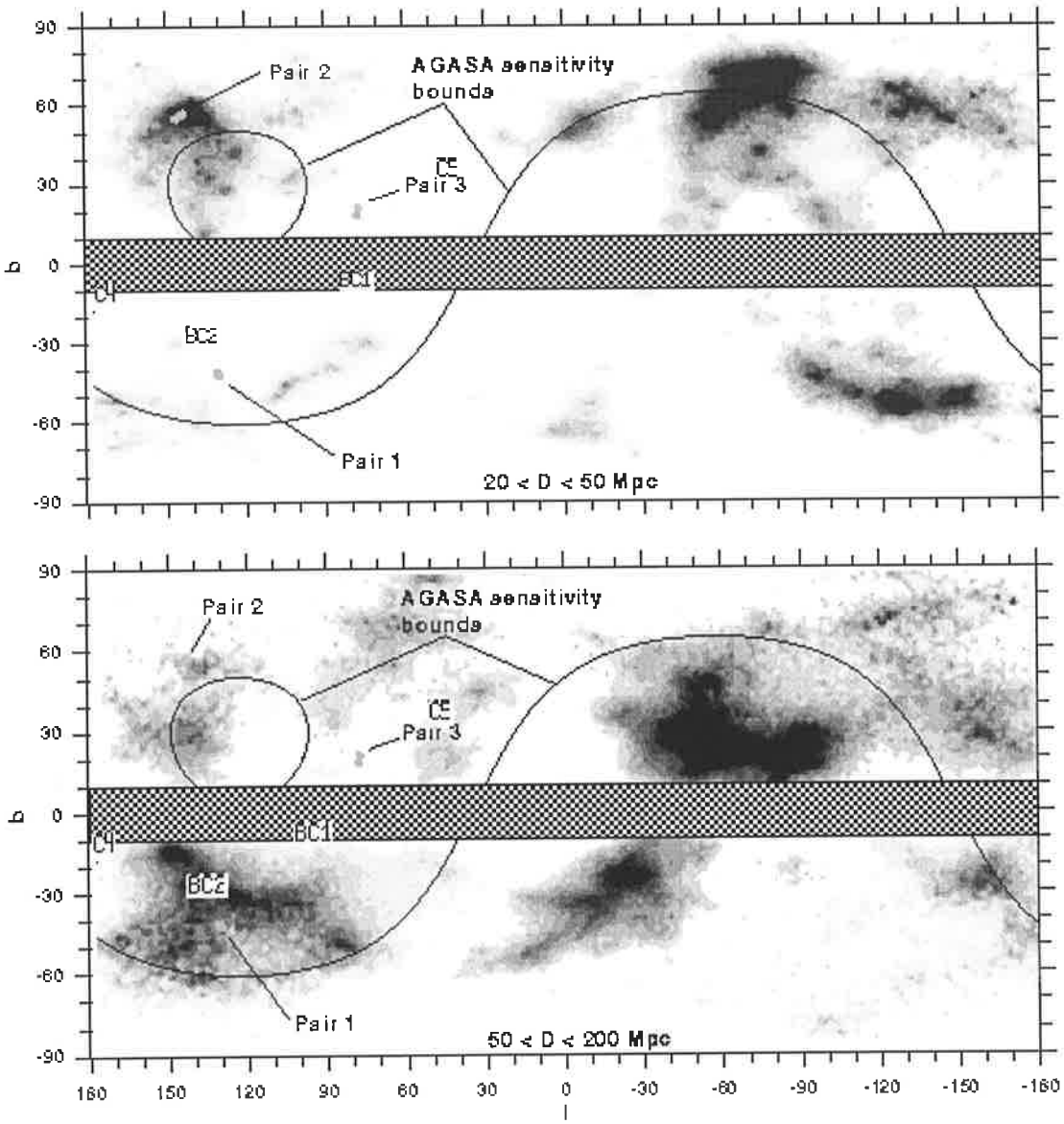

Figure 2.11: Arriving direction probabilities assuming that the EHECRs are distributed according the galaxy distribution at 20 to 50 Mpc (top figure) and at 50 to 200 Mpc (bottom figure). The AGASA clustering regions are also indicated[62].

Event ID	Astrophysical Object
C1	Mrk 359 (0.017)
C2	NGC 3642 (0.005), Mrk 40 (0.02), Mrk 171 (0.01)
970330(1.5×10^{20} eV)	H 1934-063 (0.011)

Table 2.4: Astrophysical objects near the AGASA highest energy events. The redshift values for each object are given in parentheses[9]

Chapter 3

The SUGAR excess from the Galactic centre region

At the time the AGASA collaboration pointed out the cosmic rays excess from the Galactic centre (GC) region, I was just starting my PhD studies. And as a matter of training and developing tools for the HiRes anisotropy studies, I was assigned to check whether any significant excess toward the GC was also observed in the SUGAR data. Then, I developed the software necessary to perform the anisotropy studies on the SUGAR data. In this chapter, I will describe the technique used for the SUGAR anisotropy analysis, and also I present a discussion of the results. The results of this work were published in [67].

3.1 Analysis

The statistics of the SUGAR experiment[1] are much lower than the AGASA experiment. So, any anisotropy feature observed by SUGAR could easily be an artefact of statistical fluctuations. These 'artificial' anisotropies could appear with the same probability anywhere in the observed sky, leading us to false anisotropy signals. One way to reduce this statistical problem and increase the confidence level in determining

[1] For a description of the SUGAR experiment see section 1.3.1.3

real anisotropy regions, is to define '*a priori*' the region of the sky that we want to study and in addition we can also define the energy range. We can base the *a priori* definition of these parameters on theoretical predictions, or on previous observations.

We based our SUGAR analysis on recent AGASA observations of an apparent excess of cosmic rays with energies between 10^{18} and $10^{18.4}$ eV from the Galactic Center region (see section 2.1.1 for details). We limited our anisotropy analysis to the Galactic Center region although we produced maps of the entire sky. In order to compare energy scales, we also checked that the SUGAR integral energy spectrum within this energy range was consistent with the AGASA spectrum[68]. As a result, we defined *a priori* the energy range between $10^{17.9}$ and $10^{18.5}$ eV. We choose a slightly wider energy range than that of AGASA, because the SUGAR events were reconstructed based on the information of only three detectors. Therefore we expected an energy resolution poorer than in AGASA.

The SUGAR data had 3732 events within this energy range over all right ascencions and declinations. We used these events to produce a shower density sky map. The technique consisted of generating a gaussian probability function around the reconstructed arrival direction of each event. The standard deviation of the gaussian function was determined by the directional uncertainty of each event. The directional uncertainty was defined as $3°sec(\theta)$, where θ is the zenith angle of the event[41]. The volume of the resulting function was normalized to one.

The sky map was divided into a 0.5° (RA) by 0.5° (DEC) grid. The gaussian probability functions of all events were added resulting in a shower density map. To estimate the shower density in proper units, the total density of events within each 0.5° (RA) by 0.5° (DEC) bin was counted. Then, this number is divided by $cos(\delta)$ and multiplied by 4 to give the number of showers per true square degree of the sky (fig. 3.1). The factor $1/cos(\delta)$ is introduced since a 0.5° (RA) bin at the pole ($\delta = \pm 90°$) represents a smaller angle in the sky than a 0.5° (RA) bin at the equator ($\delta = 0°$).

The next step of the analysis is to compare the estimated shower density map (fig. 3.1) with that expected assuming an isotropic flux of cosmic rays. To estimate

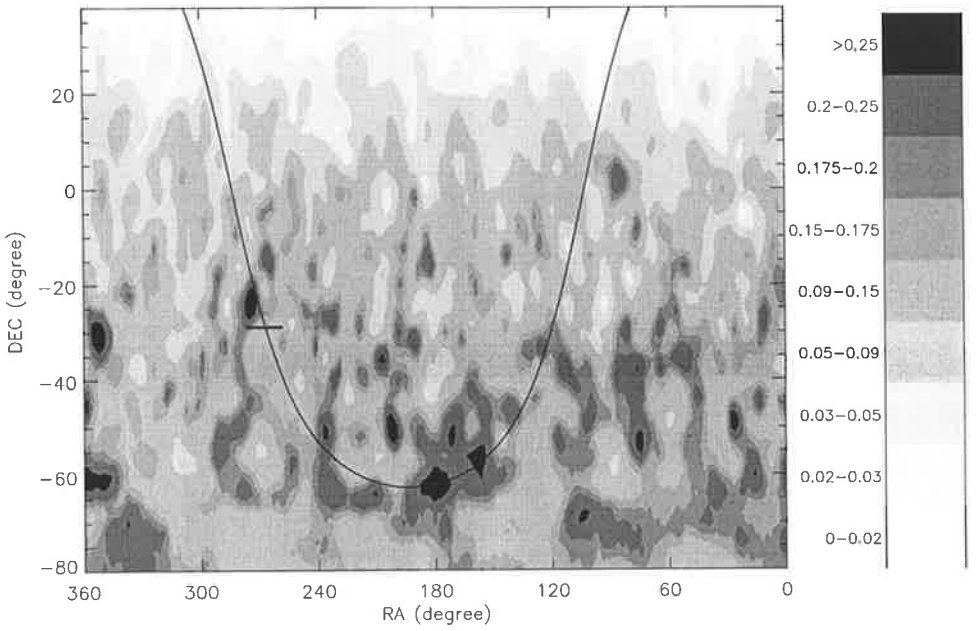

Figure 3.1: Cosmic ray event density over the sky viewed by the SUGAR array for the 3732 events between $10^{17.9}$eV and $10^{18.5}$eV. The density scale represents the number of events viewed per true square degree of sky (see text for details). The galactic plane and Galactic Centre are indicated with the solid line and cross respectively. The 1950 epoch has been assumed for the equatorial coordinates displayed here and in other plots in this chapter.

the expected shower density map, we should take into account the exposure of the detector (i.e. the zenith angle dependent efficiency and the times corresponding to the operation periods of the detector). A good technique that takes into account the exposure characteristics of the detector to generate an expected shower density map is the "shuffling" technique[51, 69]. The technique consists of randomly associating the arrival time (Julian Date) of each shower with the local arrival direction (zenith and azimuth) of another shower in the real data set. As a result, we obtain a synthetic data set with randomised celestial coordinates for each event (i.e. isotropic event flux). This technique washes out any possible anisotropy in the arrival directions and maintains the exposure characteristics of the detector (the same arrival time distribution and the same zenith and azimuth angle distributions as the real data set). Figure 3.2 shows the expected shower density map assuming an isotropic flux of cosmic rays. This map

was generated by taking an average of 1000 synthetic data sets.

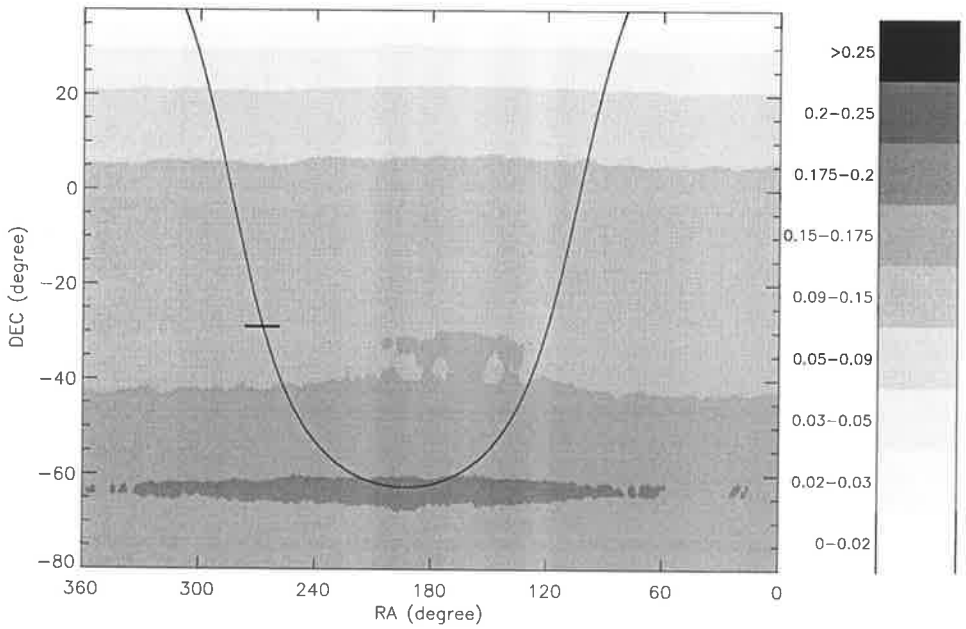

Figure 3.2: The expected density of events for an isotropic flux of cosmic rays as viewed by SUGAR between $10^{17.9}$eV to $10^{18.5}$eV. Again, the density is given in units of events per true square degree (see text for details).

Comparing bin by bin the real density map (fig. 3.1) with the isotropic expectation (fig. 3.2), we derive the fractional excess or deficit of event densities across the sky (fig. 3.3). Figure 3.3 shows that the excess regions (darker colors) are rare, only two significant excess regions are observed in the sky map, one of which is in our area of interest.

To calculate the statistical significance of the excess (or deficit) regions, we use again the 1000 synthetic data sets. Each synthetic density map is compared with the real density map. For each bin of the sky map (0.5° (RA) by 0.5° (DEC) bin), we compute how many synthetic maps had a shower density equal or larger than the real shower density in that bin. Given that each synthetic data set represents an isotropic cosmic ray flux, this gives us a bin-by-bin probability that the observed excess (or deficit) has occurred by chance. A probability close to zero will be obtained for excess regions and a probability close to one for deficit regions. Figure 3.4 shows

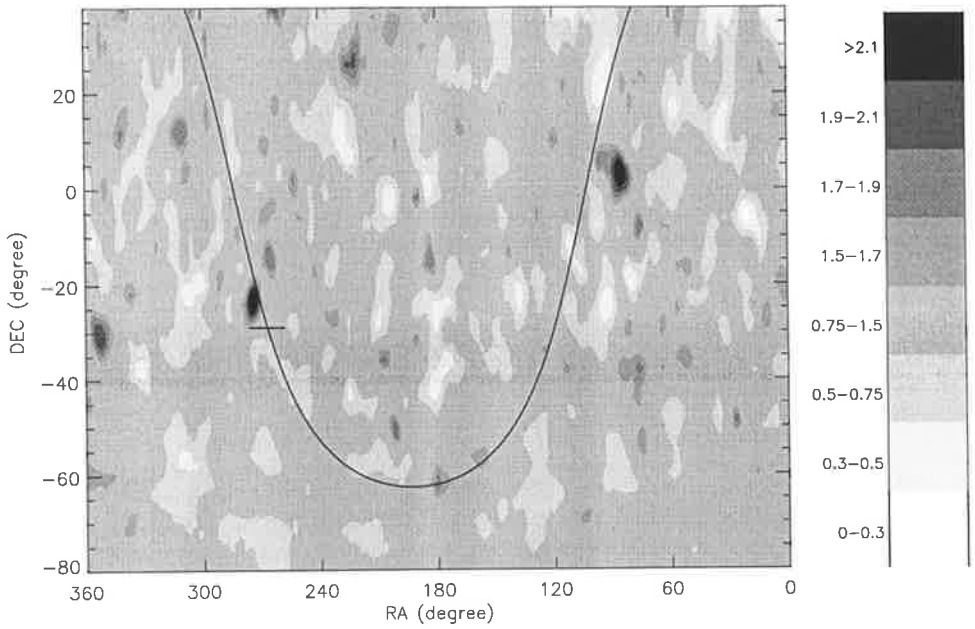

Figure 3.3: We compare Figures 3.1 and 3.2 and derive the fractional excess (or deficit) of the event density over the sky viewed by SUGAR. A value of 1 indicates that the measured density is in agreement with the expected density.

the significance sky map of the excess/deficit.

In principle, both excess regions in Figure 3.4 could be the result of statistical fluctuations. However, since we decided *a priori* that we would study only the region near the galactic center, the confidence level for the observed excess near the galactic center is higher than that for the excess observed at $(\alpha, \delta) = (85°, 3.3°)$ (B1950.0). This is despite the fact that the significance of both excess regions is similar (fig. 3.4). There are 432 regions in the SUGAR sky with sizes similar to the observed excess (10×10 degrees). Therefore, the chance probability of having an excess in any of these regions, is 432 times bigger than the chance probability of having an excess in a given 10×10 degree region (our *a priori* region).

Figure 3.5 shows in better detail the significance of the excess detected near the galactic center. The excess is centred at $(\alpha, \delta) = (274°, -22°)$ (B1950.0), close to the position of the AGASA excess. The contour level of the peak of the excess corresponds to 0.005, which is the probability of this excess happening by chance.

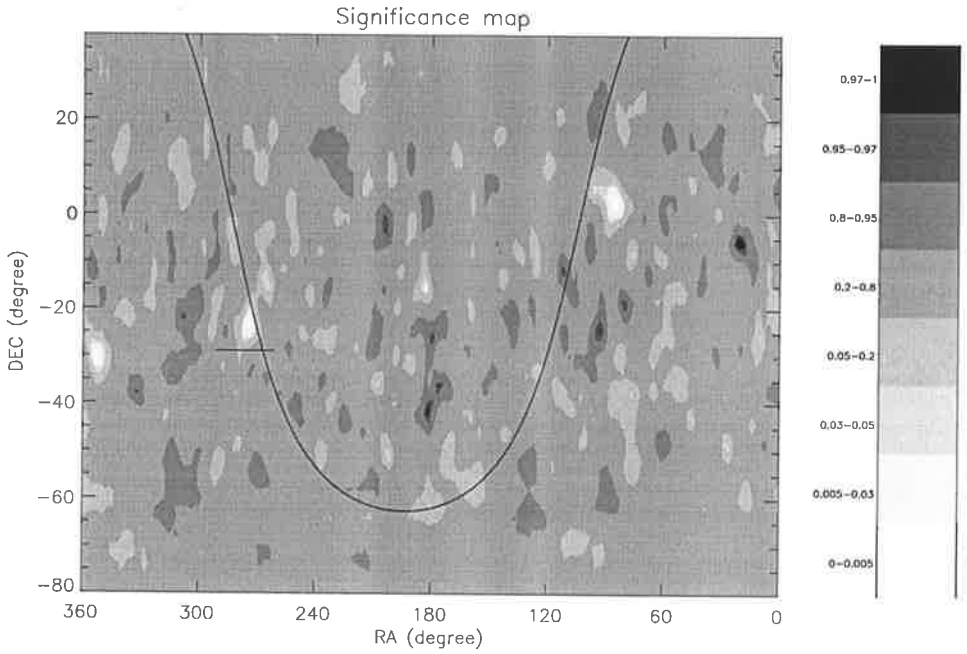

Figure 3.4: The significance sky map of the excess (or deficit) as calculated using synthetic data sets. The contours represent the chance probability of SUGAR detecting the observed density or greater. Thus, a contour level of 0.5 represents a measured density which is consistent with expectation.

We checked whether any excess from the Galactic Centre region was also observed at energies above or below the energy range selected for the SUGAR anisotropy study. We did not find any excess in these energy ranges.

3.2 Discussion

Two interesting features can be highlighted in figure 3.5,

- The SUGAR data do not show any excess from the true centre of the galaxy, even though SUGAR (unlike AGASA) had a clear view of this region. The peak of the signal region is 7.5° from the Galactic Centre.

- The size of the SUGAR excess region is consistent with the detector angular resolution, suggesting that the particle source is not an extended region, and that the particles have not experienced large direction deviations during propagation.

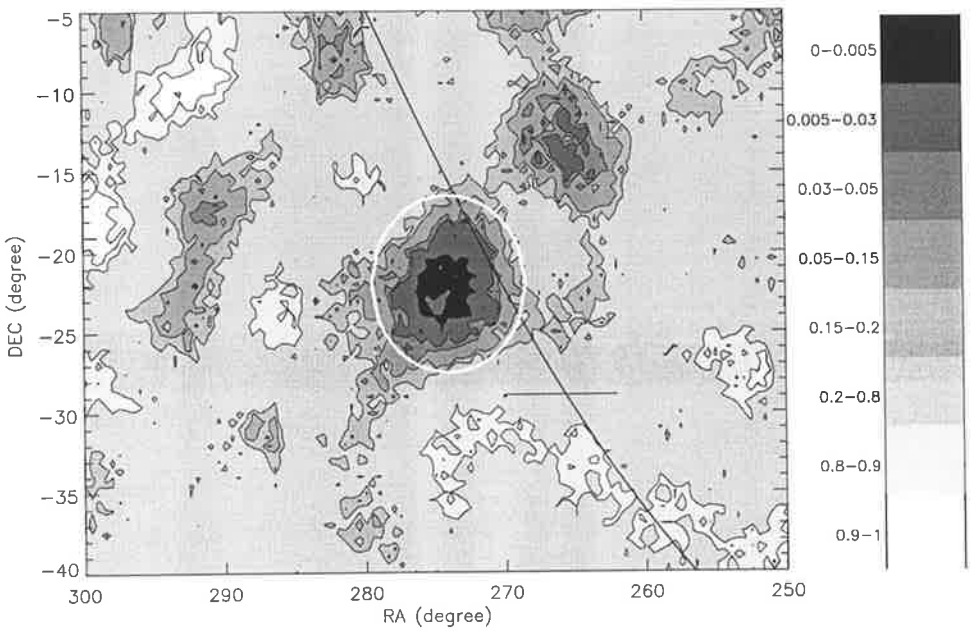

Figure 3.5: Significance of the excess detected in the Galactic Centre region. The peak of the signal region has a chance probability of 0.005. The galactic plane and Galactic Centre are indicated by the solid line and cross respectively. The white circle of radius 5.5° represents the region over the S/N would be maximum according with the SUGAR angular resolution. The excess therefore appears to be consistent with that from a point source.

The SUGAR angular resolution is indicated in figure 3.5 with a white circle around the excess region.

In Figure 3.6 we compare the SUGAR and AGASA significance maps. We plot over the SUGAR significance map the AGASA 2σ, 3σ and 4σ contours from reference [48] (fig. 2.2). The peaks of the signals are about 6° apart, and the size of the signal region is clearly different with AGASA seeing a much broader enhancement. There are several possible reasons for the differences, including

- The SUGAR data are, simply by chance, tightly clustered and offset from the AGASA signal.
- The SUGAR peak could be offset due to a systematic pointing error in local coordinates. This question has been thoroughly investigated by the SUGAR

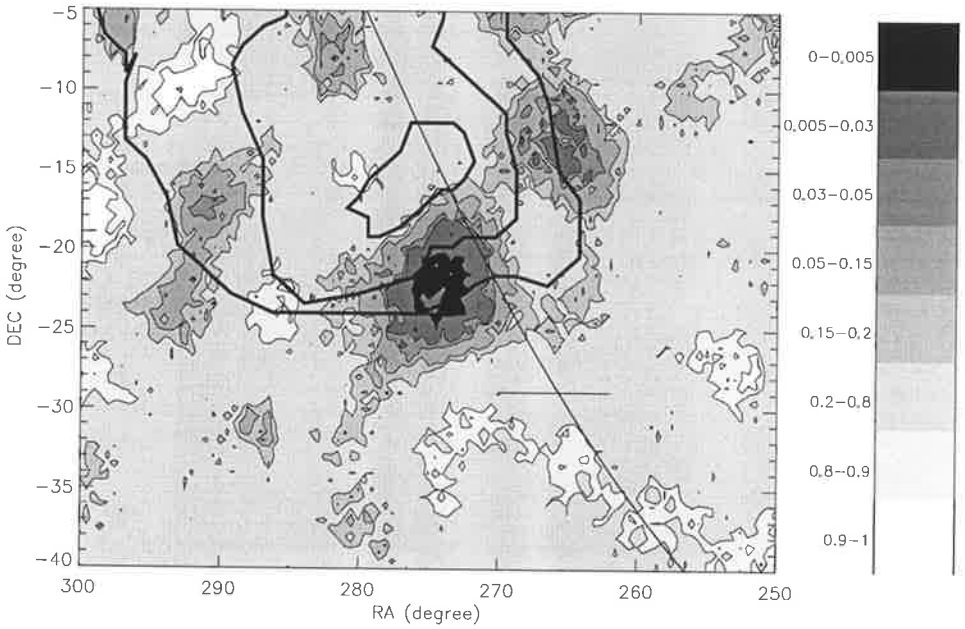

Figure 3.6: A comparison of the AGASA and SUGAR results. The SUGAR map from Figure 3.5 is overlaid with 2σ, 3σ and 4σ contours from reference [48] (fig. 2.2). Note that the limit of AGASA's view is close to $\delta = -24°$, indicated by the horizontal portion of the 2σ contour. The AGASA signal region size is significantly larger than seen by SUGAR. See the text for a discussion.

group [70]. Possible sources of systematic errors in pointing were investigated (array survey, curvature of the Earth, electronics, propagation of radio timing signals through a refractive atmosphere and vegetation, the effect of ghosting of these signals etc) and it was concluded that likely systematic errors were small compared with random errors. In any case, a systematic pointing error of reasonable magnitude would also cause a significant smearing of the signal in right ascension and declination.

- The AGASA angular resolution is poorer than expected at large zenith angles, and/or AGASA suffers from a systematic pointing error which manifests itself as a smearing and offset of the signal in right ascension and declination.

- The AGASA analysis technique, which uses signal averaging over 20° radius circles, has smeared out an otherwise point-like feature.

- Apparent excesses on the AGASA map further north along the galactic plane might have systematically shifted the peak of their main excess northward. No similar bias would have an opportunity to act southward, given their cutoff in declination at $\delta = -24°$.

We calculate the SUGAR source flux in the following way. Given our assumption that the size of the signal region is consistent with a point-spread function, we count the number of events inside a circle of radius 5.5° centred on $(\alpha, \delta) = (274°, -22°)$. The average zenith angle for events at this declination is approximately 30°, so the typical direction uncertainty would be $3° \sec(30°)$. Then, this uncertainty radius is multiplied by 1.59 in order to obtain a radius (5.5°) that maximizes the signal-to-noise ratio of our flux estimate. We find that the region enclosed by a circle of 5.5° radius centred at the SUGAR excess contains 21.8 equivalent events. This is compared with the background expectation of 11.8. The background expectation was calculated from the average number of events inside 27 circles of the same size arranged around same declination band. Thus the signal region is populated by approximately 10 signal events above an expectation of 11.8 background events. This is consistent with the chance probability of 0.005 derived above using shuffling and the sky maps. (The Poisson probability of observing 22 or more events when the expectation is 11.8 is 0.0050). Using the AGASA energy spectrum [68] as normalization, and assuming that the signal events have the same triggering efficiency as the background cosmic rays, this excess is equivalent to a point-source flux of $(9 \pm 3) \times 10^{-14}$ $m^{-2}s^{-1}$ or (2.7 ± 0.9) $km^{-2}yr^{-1}$ between $10^{17.9}$ and $10^{18.5}$eV. It was not possible to compare this flux with the AGASA result [48], since no flux is quoted and we do not know the procedure used by the AGASA group to estimate the signal and background counts within the large (20° radius) error circle used in their analysis. In particular, such a circle centred on the excess extends beyond the southern limit of the AGASA map.

The excess shown in Figure 3.5 is clearly not coincident with the Galactic Centre. At the declination of the Galactic Centre, the expected number of events between $10^{17.9}$ and $10^{18.5}$eV arriving within a circle of radius 5.5° is 13.4. The actual number of

events within 5.5° of the Galactic Centre is 12.5. Thus, we calculate a 95% upper limit [71] on the point source flux from the Galactic Centre of 2.2 $km^{-2}yr^{-1}$ (or roughly 70% of the cosmic ray flux) over this energy range.

The peak of the SUGAR excess does not appear to be centred on the galactic plane itself. However, at a galactic latitude of only about 3° south, it is still within the SUGAR angular uncertainty of the plane.

Melanie Johnston-Hollitt, a colleague from our Astrophysics group at Adelaide University, has examined astronomical data in the direction of the SUGAR peak to determine whether there might be any coincident objects of interest. She found that the direction is on the border of galactic plane surveys and many surveys have only statistically poor information. However, an 11cm Effelsberg 100m single dish radio survey (sensitive to broad scale structure) [72] and data from the COMPTEL gamma-ray telescope [73] do seem to be useful, based on their angular coverage and the apparent quality of the data.

The 10-30 MeV COMPTEL data set shows a large feature which arcs south of the galactic plane, from the Galactic Centre to an unidentified bright source in the galactic plane at 18° galactic longitude. That arc, with a radius of about seven degrees, is apparently centred on the direction of the SUGAR peak. The radio data show a bright region with a radius of about one degree in the direction of the peak and this appears to be surrounded by a roughly circular feature of much reduced radio intensity, again centred on the peak. There may be a brighter radio region outside that feature and coincident with the COMPTEL arc. The central radio source is polarised but there is no sign in the data for radio polarisation associated with the COMPTEL arc. If this feature was at the distance of the Galactic Centre, it would have a diameter of about 800pc.

It must be emphasised that these other astronomical data are within the SUGAR angular resolution and their apparently coincident directions may be a statistical artefact.

3.3 Conclusion

Data from the SUGAR array confirm the existence of an excess flux of cosmic rays from a direction near the Galactic Centre. While this result is not as statistically strong as that reported by the AGASA group, it is interesting in a number of ways. First, the SUGAR array consisted of buried scintillator detectors, with a muon energy threshold of 0.75 GeV for vertical showers. If the SUGAR flux we calculated above proves to be consistent with that measured by AGASA, it would imply that the signal particles are unlikely to be gamma-rays, unless our understanding of muon production in photon cascades is severely incomplete.

Secondly, the SUGAR array had a near overhead view of the true Galactic Centre, and found no signal from that direction. This, coupled with the observation that the SUGAR signal is point-like in character, raises the possibility that the source of these particles is unrelated to the centre of our galaxy. For example, it is conventional to think of the galactic magnetic field as a superposition of regular and turbulent components. It would be difficult to conceive of a field structure which would take a source of charged cosmic rays at the Galactic Centre and make it appear like a point source offset by 7.5° from the true source direction. Clay [74] has discussed propagation from such a source and has shown that a large diffuse region would result, a region much larger than the point spread dimensions observed with SUGAR.

The possibility of neutron primary particles cannot be ignored, especially as this could account for the turn-on of the signal at around 10^{18}eV (e.g. [49]) if the source were at a distance close to that of the galactic centre. It would also account for the point-like character of the excess as seen by SUGAR.

Chapter 4

The HiRes Detector

In this chapter I will summarize the main characteristics of the HiRes fluorescence detector. For greater detail about the HiRes detector the reader is referred to [75, 76]. I also discuss in this chapter a few aspects involved in the cosmic ray reconstruction process using the fluorescence technique.

The HiRes detector is a second generation fluorescence detector. It was built upon the experience gained in the Fly's Eye experiment. The HiRes detector was designed to optimize the detection and reconstruction of cosmic rays with energies above $10^{18.5}$ eV. The geometrical resolution and therefore the energy resolution were improved considerably. In chapter 5 and 6, I will present in more detail the HiRes geometrical resolution.

HiRes is located in the western desert of Utah (USA). HiRes consists of two sites (HiRes-1 and HiRes-2) located on the top of two mountains separated by 12.6 km. Each HiRes site consists of a set of mirror-cluster (mirror) modules. Figure 4.1 shows the configuration of a mirror module. The fluorescence light produced in the atmosphere by the EAS is reflected from a 2 m diameter mirror to the photomultiplier cluster which is located at the focal plane of the mirror ($\approx$ 2.3 m from the mirror centre). The photomultiplier cluster is formed with 256 hexagonal photomultipliers (PMTs). A UV-pass filter is mounted in front of the PMTs to improve the signal-to-noise ratio (see fig. 4.2). The PMT resolution is approximately 1°, and given the mirror-cluster

specifications, each mirror covers 16° in azimuth by 14° in elevation angle.

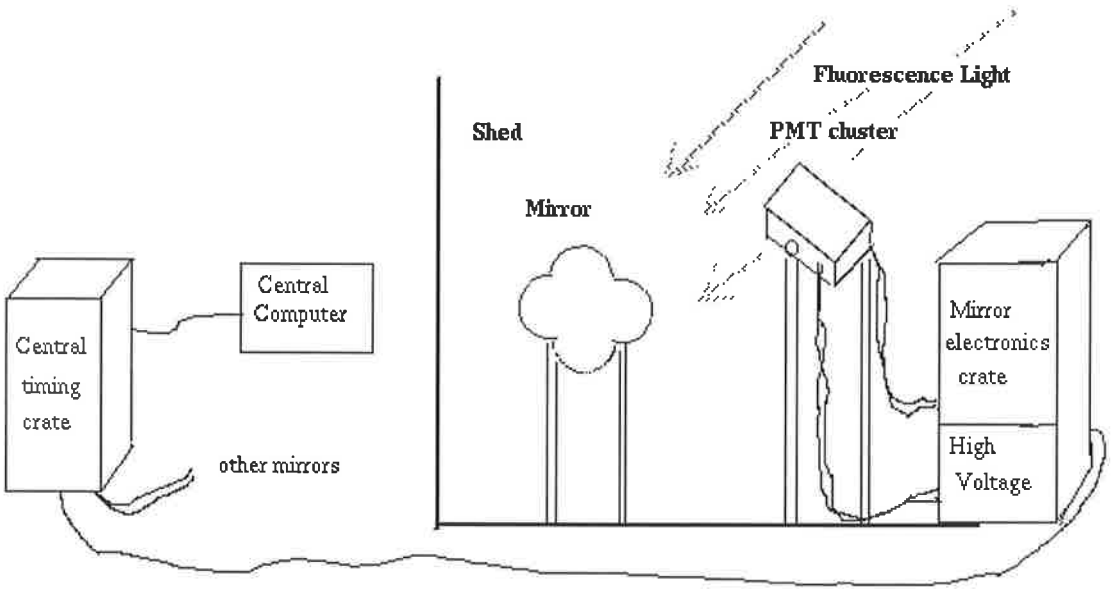

Figure 4.1: Schematic representation of a mirror-cluster module.

HiRes can see out to a distance of roughly 20 km before aerosols and other particles in the air scatter the light from the EAS and prevent us from detecting this light. The HiRes aperture is 9100 km^2sr for cosmic rays with energies above 10^{20} eV which helps us overcome the low flux rates that plague this area. The maximum distance that an EAS can be observed depends on how energetic a shower is. The more energetic it is the farther away HiRes can see it since more light reaches the detector. Thus, the actual aperture is very energy dependent. Considering that HiRes only operates during dark nights (a duty cycle of 0.1), the expected number of detected cosmic rays with energies above 10^{19} eV and 10^{20} eV (according to the AGASA cosmic ray flux) are approximately 300 and 9 particles per year respectively.

As the shower moves through the atmosphere, PMT tubes will progressively fire as the EAS passes through each photomultiplier field of view, and this defines the shower detector plane (SDP) which contains the shower axis and the detector (fig. 4.3). By using numerical and Monte Carlo fitting programs to analyze the amount

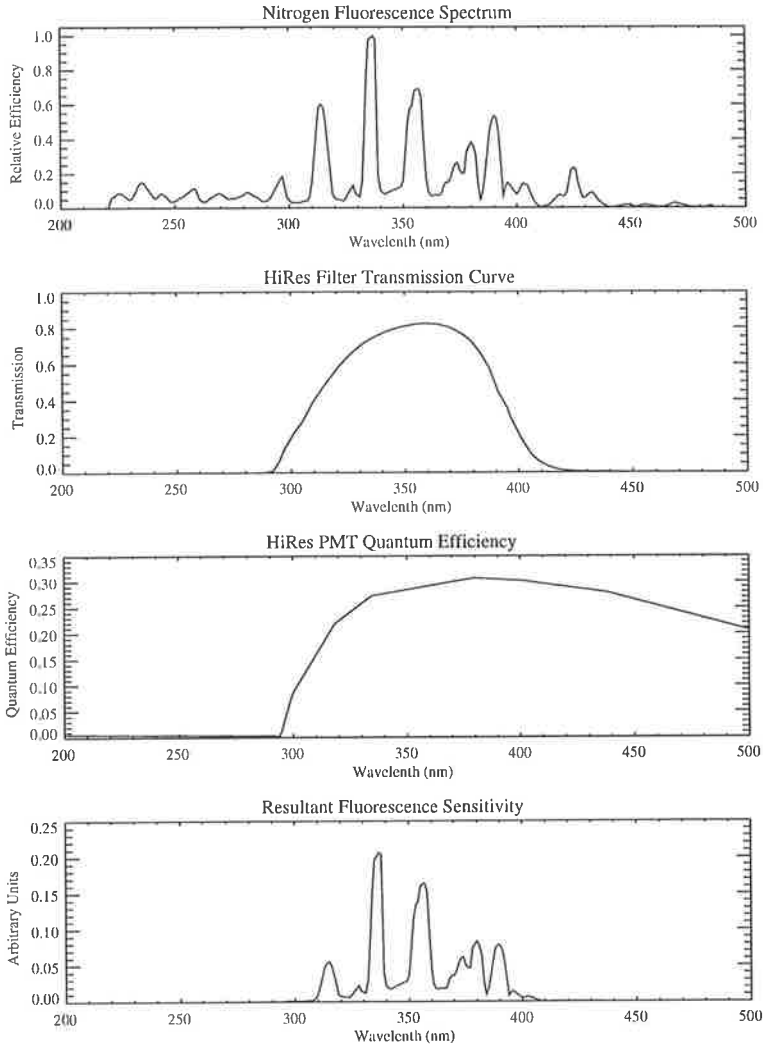

Figure 4.2: UV-pass filter process. The top plot shows the fluorescence spectrum as measured by Bunner[77] (the intensity scale is normalized to the peak at 337 nm), and the bottom plot shows the resultant fluorescence sensitivity taking into account the filter transmission curve and the PMT quantum efficiency.

of light received and the time it was seen, the arrival direction and the energy of the incoming particle is determined. Although this can be achieved with a single site, stereo observations of an EAS using two (or more) eyes improves the accuracy of the estimate of the direction, energy and mass of the originating particle.

The HiRes detector is now the detector with the biggest aperture and it has superior resolution in determining the arrival direction and energy of the primary cosmic ray. In addition, HiRes is able to estimate the mass of the cosmic ray. The time-averaged aperture of HiRes for energetic cosmic rays is four times bigger than the biggest ground

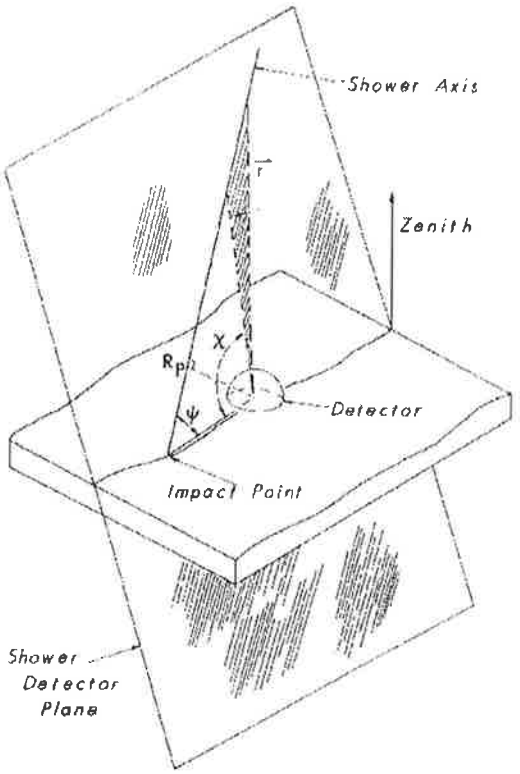

Figure 4.3: Geometry of the shower detector plane (SDP).

array detector (AGASA), and this means that in 3 years of full time operation HiRes would collect the same number of energetic cosmic rays that AGASA collected in 12 years.

4.1 Air fluorescence yield

The charged particles of the EAS excite the nitrogen molecules in the atmosphere. Most of the exited molecules come back to their ground energy states by emitting fluorescent light, some other exited molecules lose their energy through collisions with oxygen molecules. The latter mechanism makes the air fluorescence yield much lower than the fluorescence yield of pure nitrogen. The estimated nitrogen to air yield ratio is 20 in [78] and 5.6 in [79], the different results in both experiments are not well understood.

The fluorescence light is emitted isotropically, is more intense in the near UV-region

between 300 and 400 nm[77] (fig. 4.2 top plot) and is proportional to the number of charged particles in the EAS. The fluorescence yield per electron (photons/m/electron) depends weakly on the pressure and temperature of the atmosphere[79] (see figures 4.4 and 4.5). Figure 4.6 shows the air fluorescence yield at 760 mm Hg as a function of the incident electron energy as estimated by Kakimoto[79]. On the same plot it is shown the energy deposited in the air (dE/dx) by the same electron (the dE/dx scale is on the right hand side). These results indicate that the air fluorescence yield may be proportional to the electron dE/dx in that energy range.

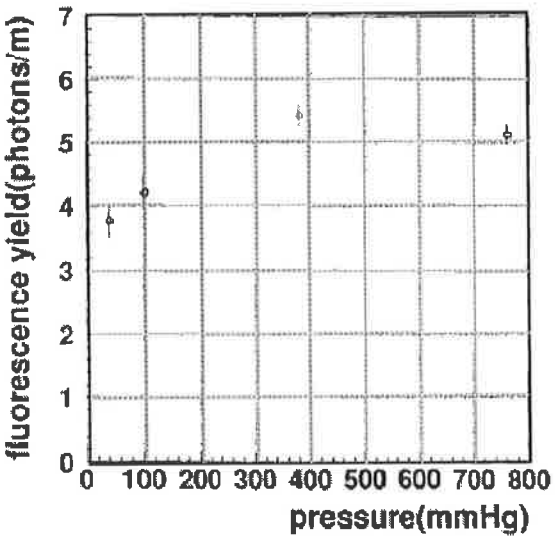

Figure 4.4: Nitrogen fluorescence yield between 300 and 400 nm as a function of pressure. This function was obtained using 1000 MeV electrons in dry air at 15°C.[79].

Bunner [77] showed that the fluorescence yield of a given wavelength peak is proportional to

$$yield \propto \frac{\rho}{1 + \rho B\sqrt{t}} \tag{4.1}$$

where B is a constant characteristic of the peak, t is the temperature, and ρ is the density. Therefore, Kakimoto *et. al.* [79] fitted their fluorescence yield results to a

function composed of two such terms

$$yield = \frac{\left(\frac{dE}{dx}\right)}{\left(\frac{dE}{dx}\right)_{1.4MeV}} \times \rho \left(\frac{A_1}{1+\rho B_1 \sqrt{t}} + \frac{A_2}{1+\rho B_2 \sqrt{t}} \right) \tag{4.2}$$

where dE/dx is the energy loss of the particle, ρ in kg/m^3, t in Kelvin (K), and $(dE/dx)_{1.4MeV}$ is the (dE/dx) evaluated for an electron at 1.4 MeV (table 4.1 shows the fitted value of the constants in equation 4.2). The first term in equation 4.2 accounts for the yields of the 337 and the 357 nm peaks, since they have the same pressure dependency. The other term accounts for the yield of the 391 nm peak, this peak did not show much pressure dependency.

A_1	$89.0 \pm 1.7 m^2 kg^{-1}$
A_2	$55.0 \pm 2.2 m^2 kg^{-1}$
B_1	$1.85 \pm 0.04 m^3 kg^{-1} K^{1/2}$
B_2	$6.50 \pm 0.33 m^3 kg^{-1} K^{1/2}$

Table 4.1: Constants used in equation 4.2 [79]

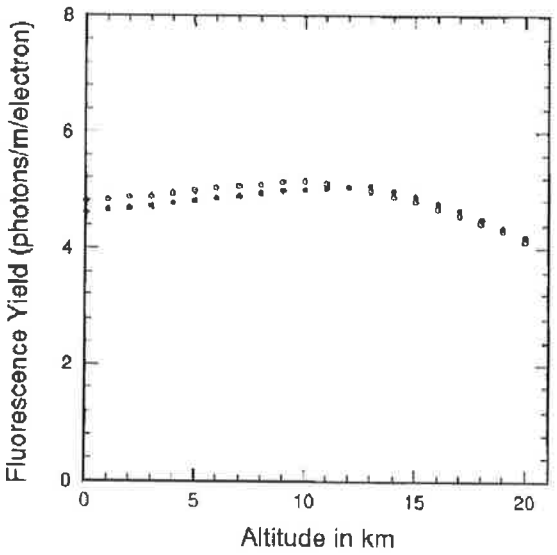

Figure 4.5: Fluorescence yield between 300 and 400 nm of an 80 MeV electron as a function of atmospheric altitude[79]. The slight temperature and density dependence of the fluorescence yield can be noticed when employing a typical mid-latitude summer atmospheric model with surface temperature 296 K (closed circles), and a similar winter model with a surface temperature of 273 K (open circles)[79].

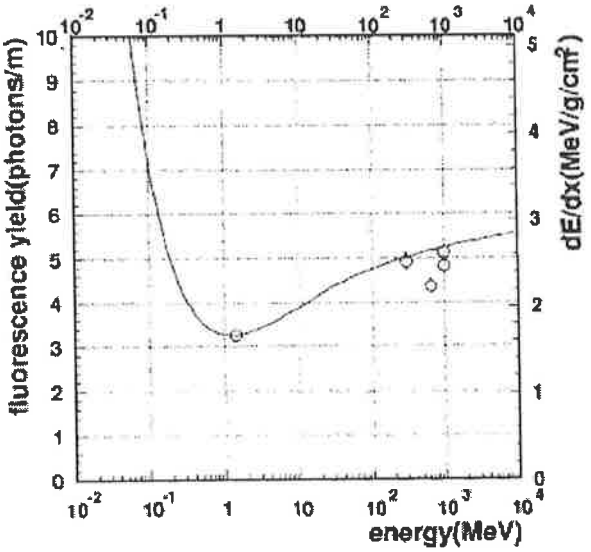

Figure 4.6: Energy dependence of nitrogen fluorescence between 300 and 400 nm in dry air at a pressure of 760 mm Hg. The dE/dx curve is shown as a solid line. The scale of the fluorescence yield is adjusted so that the 1.4 MeV point lies on the dE/dx curve[79].

4.2 HiRes-1 site

HiRes-1 is located at 40° 11' 43" latitude, 112° 50' 9" longitude and 1,457 m above sea level. It consists of a ring of 22 mirrors and covers $\sim$ 350° in azimuth and from 3° to 17° in elevation. Figure 4.7 shows the HiRes-1 site map. HiRes-1 records the triggering time and the integrated charge once the instantaneous tube current reaches some threshold level. The threshold is dynamically adjusted in order to keep the sky noise tube trigger rate at 200 Hz. This electronics is often called the Sample-and-Hold (S/H) electronics (more detail is given in section 5.2.1). HiRes-1 began taking data in May 1997, but the ring was only finished in March of 1998.

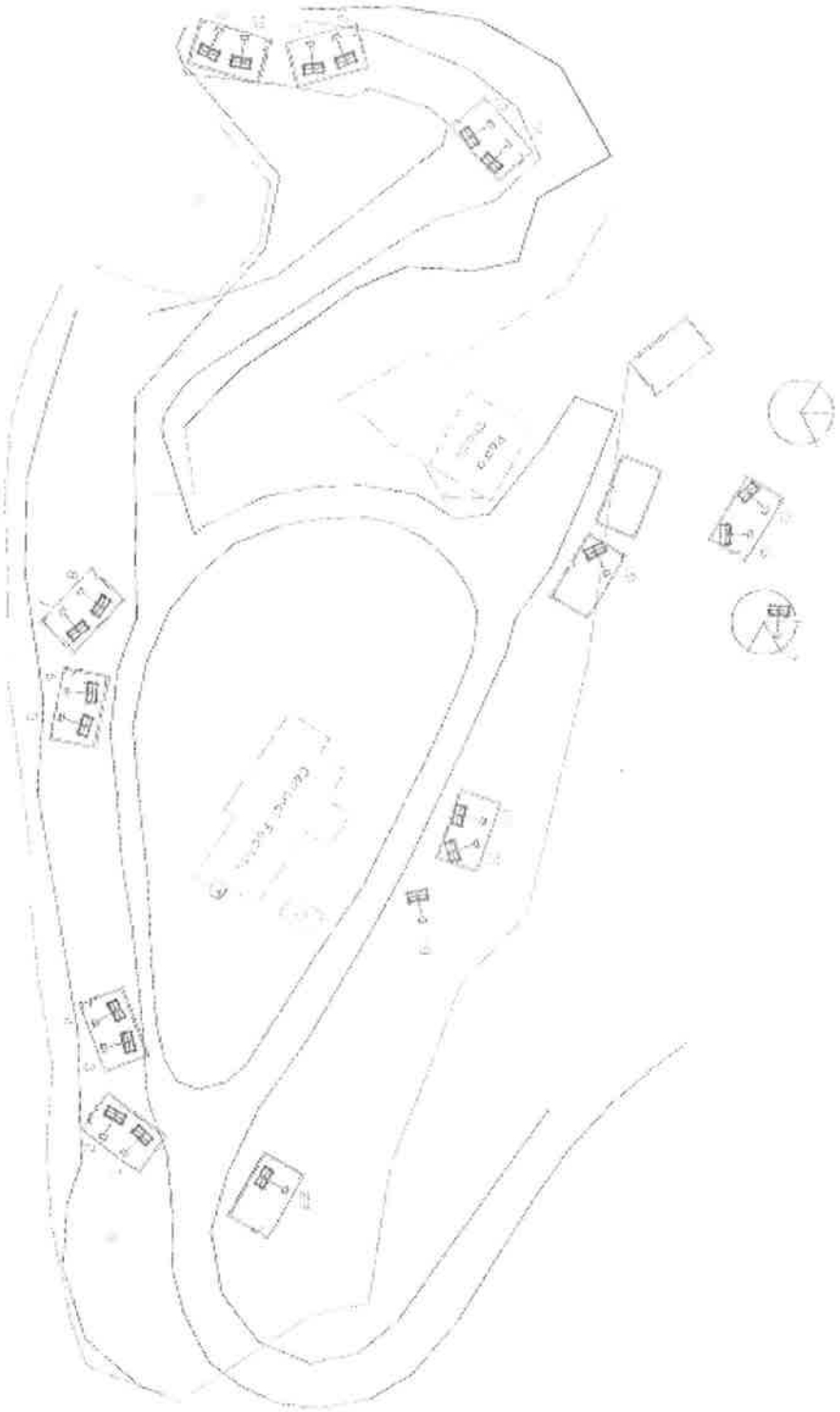

Figure 4.7: HiRes-1 site map.

4.3 HiRes-2 site

HiRes-2 is located 12.6 km South-West of HiRes-1. It consists of two rings of mirrors, covering almost 360° in azimuth. Figure 4.8 shows the HiRes-2 site map. The first ring covers from 3° to 17°, and the second ring from 17° to 31° in elevation. HiRes-2 uses Flash Analog to Digital Converter (FADC) electronics to record the pulse shape of the signal[80]. The incoming signal is digitized with a 100 ns sample rate by the FADC. The tube and mirror trigger specifications are different from HiRes-1. I will describe the HiRes trigger characteristics in section 5.2.1. HiRes-2 was completed and started operations in November of 1999.

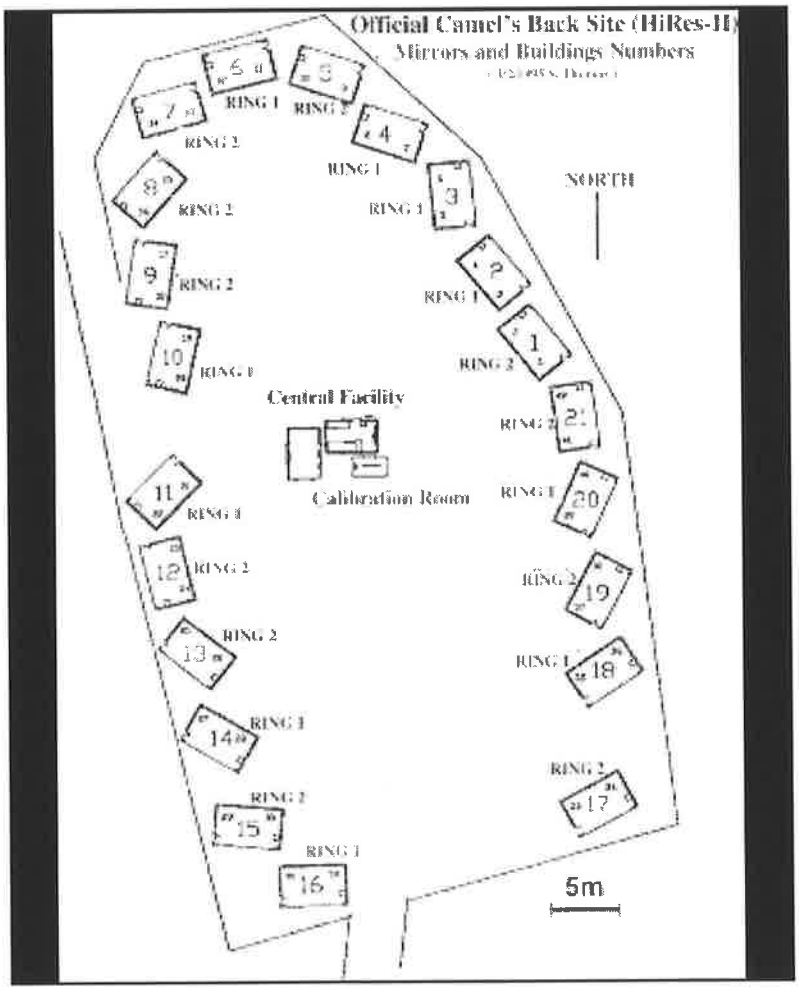

Figure 4.8: HiRes-2 site map.

4.4 Mirror-cluster calibration

In order to determine the number of fluorescence photons observed by each mirror, more specifically by each PMT, it is necessary to perform a careful and periodic mirror-cluster calibration. The number of photons collected by a PMT is obtained using a charge-to-digital convertor (QDC). The HiRes mirror-cluster calibration is described in good detail in [75]. I will now summarize the different steps of the calibration process.

Before placing the tubes in the clusters, they were calibrated one by one using a NIST-calibrated photodiode. Light at 325 nm from a He-Cd laser was passed trough a standard HiRes UV-pass filter and aimed at a beam splitter. One beam went to a second photodiode which continuously monitored the laser output. The other beam, with a 1 mm spot, illuminated the calibrated photodiode. Once the light delivered to the calibrated photodiode was defined by measuring the signal at the second photodiode, the calibrated photodiode was replaced by each tube. The measured responses over different regions of a PMT surface showed the response to be fairly homogeneous, and this behaviour did not change much from tube to tube. However, tubes with more than 20% nonuniformity across the surface, or an unacceptably low sensitivity or gain at a given voltage were discarded[81]. The result of this process were PMTs calibrated in an absolute sense.

The response of each tube is also checked periodically in HiRes using a Roving Xenon Flasher (RXF) and on a nightly basis using a YAG laser.

- **The RXF:** The RXF has a strong emission spectrum at between 300-400 nm, consistent with the atmospheric fluorescence light. The RXF is mounted in a portable housing. The housing is moved from cluster to cluster and placed in the centre of the mirror illuminating the cluster directly. The number of photo-electrons arriving at each PMT is estimated and the pedestal-subtracted QDC measurement is recorded. This procedure is repeated for different RXF intensities and the gain is determined from the slope of a plot of pedestal-subtracted

QDC counts vs number of photoelectrons. At HiRes-2, the response is adjusted to give one FADC count per photoelectron.

- **The YAG laser:** The frequency-tripled YAG laser delivers light at 355 nm to each mirror-cluster module via optical fibers. The mirror-mounted fibers illuminate the cluster directly allowing monitoring of tube response, while the cluster-mounted fibers illuminate the mirrors to allow tracking of the mirror reflectivity (see fig. 4.9). Teflon diffusers at the end of the fibers ensure uniform illumination of the cluster. Details of YAG systems can be found in [82] for HiRes-1 and in [83] for HiRes-2. The YAG calibration data are not used in the analysis yet.

In addition to the RFX and YAG calibrations, the gains of the PMT pre-amplifiers and electronics are measured nightly using a Programmable Pulse Generator (PPG). The PPG inserts a wave form pulse at the pre-amplifier at the base of each tube.

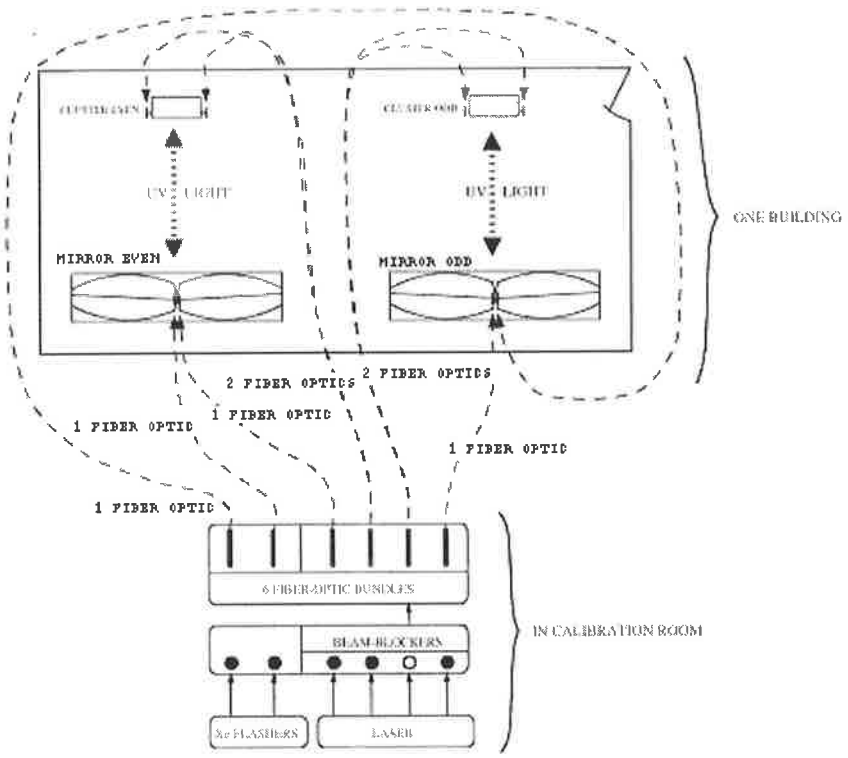

Figure 4.9: YAG mirror-cluster calibartion system[83].

4.5 Atmospheric calibration

The atmospheric calibration at HiRes is a crucial task for determining the primary energy of the cosmic ray. The atmosphere characteristics may be different for different nights, and they may even change during the same night. The HiRes detector needs especial care in characterizing the atmosphere because the EHECRs may be observed at distances of around 20 km. The effect of the atmosphere on the propagation of the fluorescence photons through such large distances is considerable[84].

To account for the atmosphere changing around the HiRes detector, several atmospheric monitoring tools have been deployed in the area. The aim of these tools is to determine the regions that contain clouds and to characterize the aerosols during the nightly run. Events detected in cloudy regions must be discarded from further analysis.

The atmospheric aerosol density can be parametrized using the horizontal attenuation length L^a and the scale height H_S. Typical values for the HiRes atmosphere are 25 km and 1.0 km respectively[84]. The horizontal attenuation length results from the aerosol density at that height, and the scale height describes an exponential aerosol density fall-off. The aerosols affect the propagation of the fluorescence photons because they generate Mie scattering (Mie scattering is described below).

The atmospheric monitoring tools include an Inter-Site Flasher, vertical flashers, steerable YAG lasers and cloud monitors.

4.5.1 Inter-Site flasher

The Inter-Site flasher (ISF) is an inclined Xenon flasher collimated by telescope optics and mounted at the old Fly's Eye-II site. The ISF track goes between HiRes-1 and HiRes-2. Eleven mirrors in HiRes-1 see light scattered by the ISF. This wide range of scattering angles allows one to investigate the amount of aerosols around the HiRes sites[85].

4.5.2 Vertical flashers

Ten vertical xenon flashers are deployed between HiRes-1 and HiRes-2 (fig.5.26). The flashers are fired during the run using radio signals. The vertical flashers are seen by both detectors on clear nights. During cloudy or too hazy nights the visibility is affected, and changes in the intensity and the shape of the tracks become notable in the detector event display. This gives an indication of periods with good and bad quality data. Vertical flashers were also used by the author to measure the inter-site time offset and to check the geometry reconstruction routines. This work will be discussed below.

4.5.3 Steerable YAG lasers

The steerable frequency-tripled YAG lasers[86, 87] are fired from HiRes-1 (HiRes-1 laser) and from HiRes-2 (HiRes-2 laser). The lasers are fired systematically with a variety of geometries and powers every hour to check the entire detectors aperture. The pointing directions of the lasers are programmable, and the possibility of shooting the lasers immediately after a high energy event candidate is detected is under consideration.

4.5.4 Cloud monitors

A cloud camera was recently (March 2001) installed by The University of Adelaide at HiRes[88]. The cloud camera consists of a 3° diameter resolution infrared camera. The camera is placed at HiRes-1 site to scan the sky continuously during the detector operation time. The cloud camera has a software that produces every 12 minutes (the time that the camera takes to scan the sky) a sky cloud picture. In reality the picture shows the temperature gradient across the sky, which is correlated with the presence of clouds (a warmer sky indicates the presence of clouds). A library containing the sky cloud pictures exists for future implementations of the cloud information in the analysis.

In addition to the cloud camera, The University of Adelaide previously installed 11 infrared sensors inside some of the buildings at HiRes-1[88]. The infrared sensors detect the sky temperature variations along fixed directions. The field of view of the infrared sensors are collimated to limit the field of view to 30° × 30°. A monitor shows the sky temperature variation as a function of time, alerting the operators to the presence of clouds.

4.6 Energy reconstruction

Once the PMTs are calibrated and knowing the atmosphere characteristics when a given event is detected, we can estimate the number of charged particles (N_e) that generated the fluorescence light observed in each PMT. Since each PMT visualizes a different stage of the EAS, we can reconstruct the longitudinal shower profile ($N_e(X)$), which is the number of charged particles in the shower as a function of the atmospheric depth (X). At HiRes, the observed longitudinal development of the shower is fitted to the Gaisser-Hillas function of the shower longitudinal profile[89]

$$N_e(X) = N_{max}\left(\frac{X - X_0}{X_{max} - X_0}\right)^{\frac{(X_{max}-X0)}{\lambda}} e^{\frac{X_{max}-X}{\lambda}} \tag{4.3}$$

where X_0 is a depth often interpreted as the depth of first interaction, $\lambda = 70$ g/cm^2, and N_{max} is the shower size at maximum.

Not all the light generated by the EAS is fluorescence light, there is also Cerenkov light. Fortunately, the Cerenkov light is not emitted isotropically. Instead, it is emitted within a narrow cone along the particle direction. The overall Cerenkov light is distributed within 25° of the shower axis[90]. The direct Cerenkov light does not often reach the detector because EHECRs are often observed far from the detector and, the detector ends up outside the Cerenkov light cone. However, some corrections are still necessary to account for the scattered Cerenkov light (Rayleigh and Mie scattering) that may reach the detector even when EHECRs are observed from large distances.

- **Rayleigh scattering:** Rayleigh scattering is an electromagnetic process well

understood and can be easily calculated since it only depends on the atmospheric density (ρ) and the photon's wave length (λ). The number of photons scattered out of the beam per unit length can be written as[90]

$$\frac{dN_\gamma}{dl} = -\frac{\rho N_\gamma}{X_R}\left(\frac{400nm}{\lambda}\right)^4 \tag{4.4}$$

where N_γ is the number of photons in the beam, and X_R is the mean free path for scattering (X_R at $\lambda = 400$ nm is 2970 g/cm^2).

The Rayleigh scattering angular distribution is given by[90]

$$\frac{d^2N_\gamma}{dld\Omega} = \frac{3}{16\pi}\left|\frac{dN_\gamma}{dl}\right|(1+cos^2\theta) \tag{4.5}$$

where θ is the scattered angle.

Figure 4.10 shows the estimated Rayleigh transmission factor for different tube elevation angles as a function of the horizontal distance.

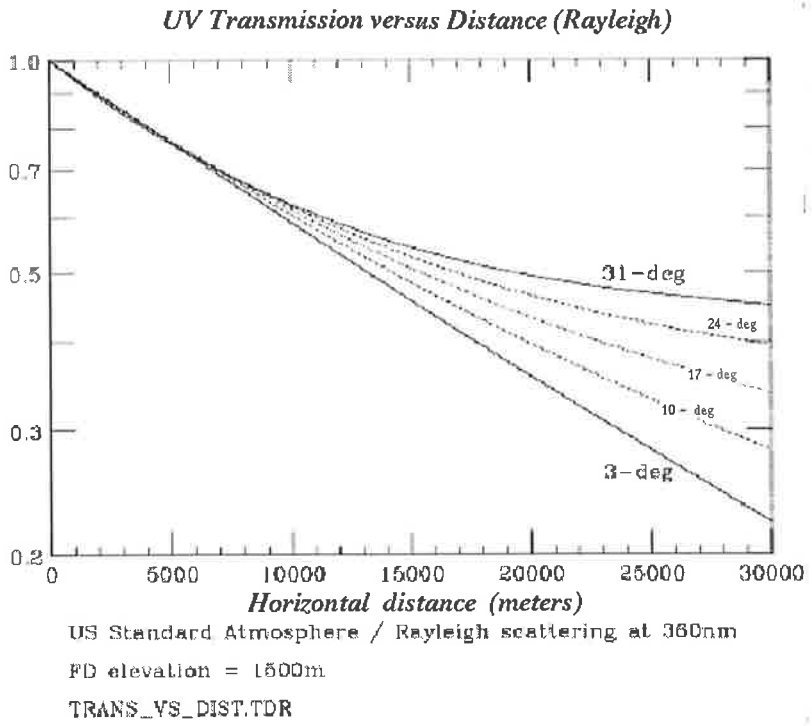

Figure 4.10: Transmission factor for Rayleigh scattering of 360 nm light by a molecular atmosphere. Curves shown are for tube elevation angles from 3 to 31 deg[91]. The assumed detector height above sea level is 1.5 km.

- **Mie scattering:** The Mie scattering or aerosol scattering is not easy to calculate, since it varies with the aerosol shape, aerosol size and aerosol dielectric constant. In addition, the aerosol contents are variable in the atmosphere. The aerosols may change as a function of altitude, composition of pollutants, and weather conditions.

  The Mie angular distribution depends on wavelength and aerosols characteristics. However it is strongly peaked in the direction of the photon. Therefore, Mie scattering will dominate over Rayleigh scattering at small scattering angles. Figure 4.11 shows the Mie transmission factor (for the UV range) as a function of the horizontal distance for tube elevation angles from 3^o to 31^o.

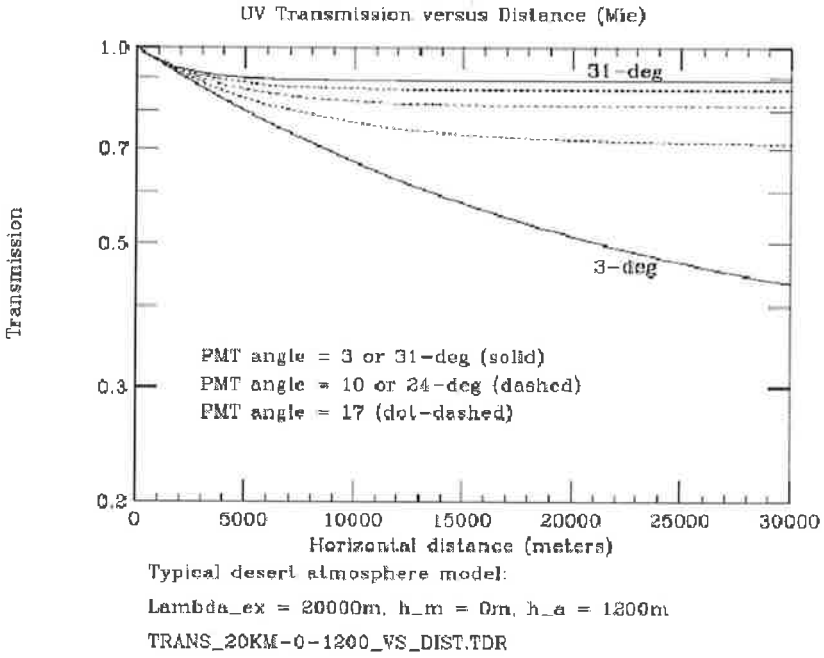

Figure 4.11: Transmission factor for Mie scattering on aerosols in the atmosphere. The aerosols are described by a horizontal attenuation length $L^a(360nm) = 20$ km, and a scale height $H_S = 1.2$ km. Curves shown are for tube elevation angles from 3 to 31 deg[91].

Only the fluorescence yield (not the scattered Cerenkov light) is proportional to the number of EAS charged particles in the PMT field of view. Thus, for calculating the shower longitudinal profile, a Monte Carlo simulation that parametrizes the scattered Cerenkov light is used to estimate the contamination of Cerenkov light in the

signal observed at the PMTs. Figure 4.12 (bottom right hand side plot) shows the reconstructed longitudinal shower profile for one energetic HiRes event.

The atmosphere is used as a big calorimeter. The total energy of the EAS is estimated by measuring the energy deposited in the atmosphere by the charged particles of the EAS (calorimetric energy, E_{cal}) which is given by

$$E_{cal} = \alpha \int N_e(X) dX \tag{4.6}$$

where α is the mean ionization loss rate per charged particle over the entire shower. The Monte Carlo estimated value for α is 2.19 MeV/(g/cm^2)[93]. It is approximately similar to $\frac{\epsilon_0}{X_0}$, where ϵ_0 is the electron critical energy (which is also the average electron energy at shower maximum, $\epsilon_0 = 86$ MeV[95]) and X_0 is the electron radiation length ($X_0 = 36.7$ g/cm^2[95]). The total energy of the EAS is a sum of this calorimetric energy and the undetected energy. The undetected energy can come from neutral particles that reach the ground without decaying (e.g. neutrinos), muons which lose most of their energy in the earth and from hadrons whose interactions do not produce fluorescence light. Using CORSIKA simulations Song *et. al.* studied the relation between the calorimetric energy and the cosmic ray primary energy[93]. Figure 4.13 shows the fraction of energy deposited in the atmosphere (E_{cal}/E_0, where E_0 is the primary energy) as a function of E_{cal}.

Figure 4.13 shows the average behavior for proton and iron initiated showers, this curve can be parameterized as

$$E_{cal}/E_0 = (0.959 \pm 0.003) - (0.082 \pm 0.003) E_{cal}^{-(0.150 \pm 0.006)}, \tag{4.7}$$

4.7 Energy spectrum

The differential cosmic ray energy spectrum $J(E)$ is calculated from

$$J(E) = \frac{dN/dE}{tA\Omega(E)} \tag{4.8}$$

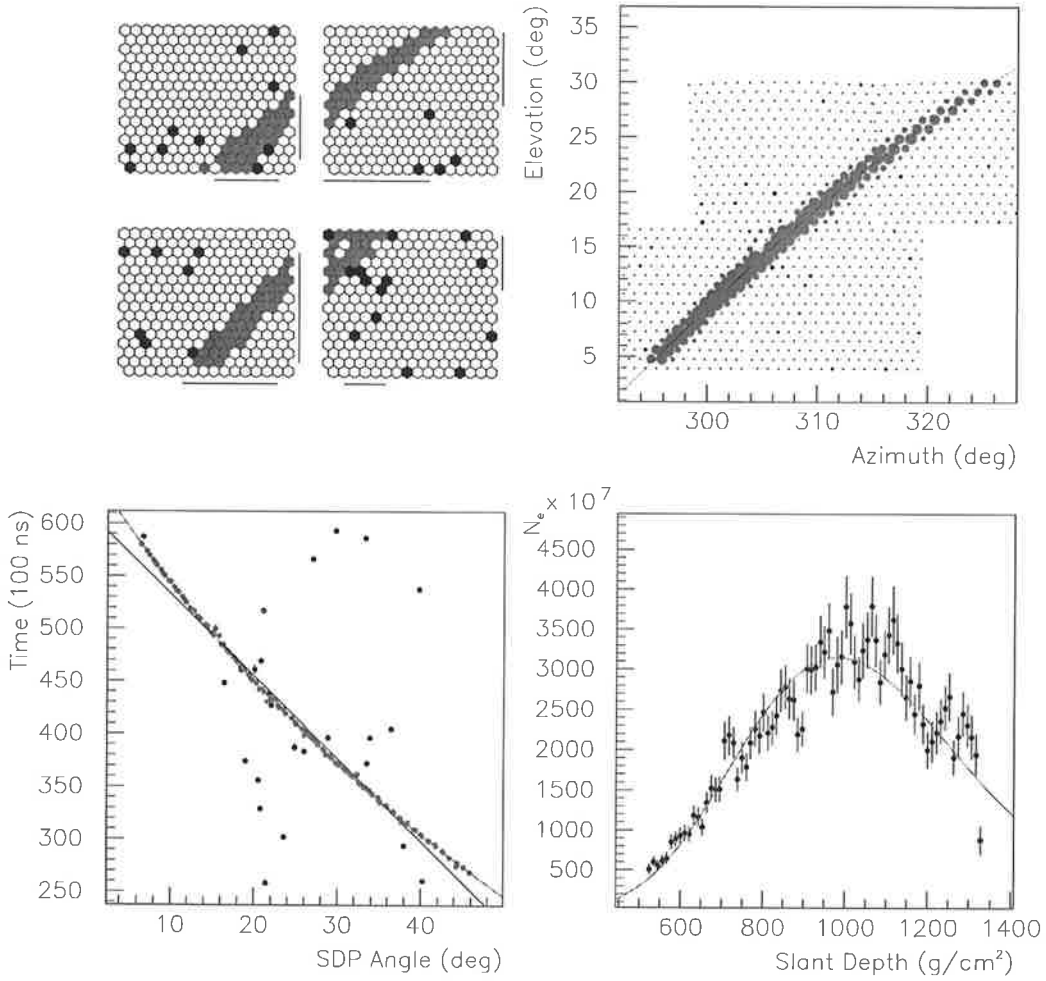

Figure 4.12: Display of an event with reconstructed energy of 52 EeV. The top left hand side plot shows the four mirrors that triggered for this event. The top right hand side plot shows the elevation vs. azimuthal angles of the triggered tubes. The bottom left hand side plot shows the time of the tube hits vs. the tube emission angle (angle between the shower axis and the tube direction), with two fits superimposed: a straight line and the result of a time fit. The bottom right plot shows the reconstructed shower longitudinal profile[92].

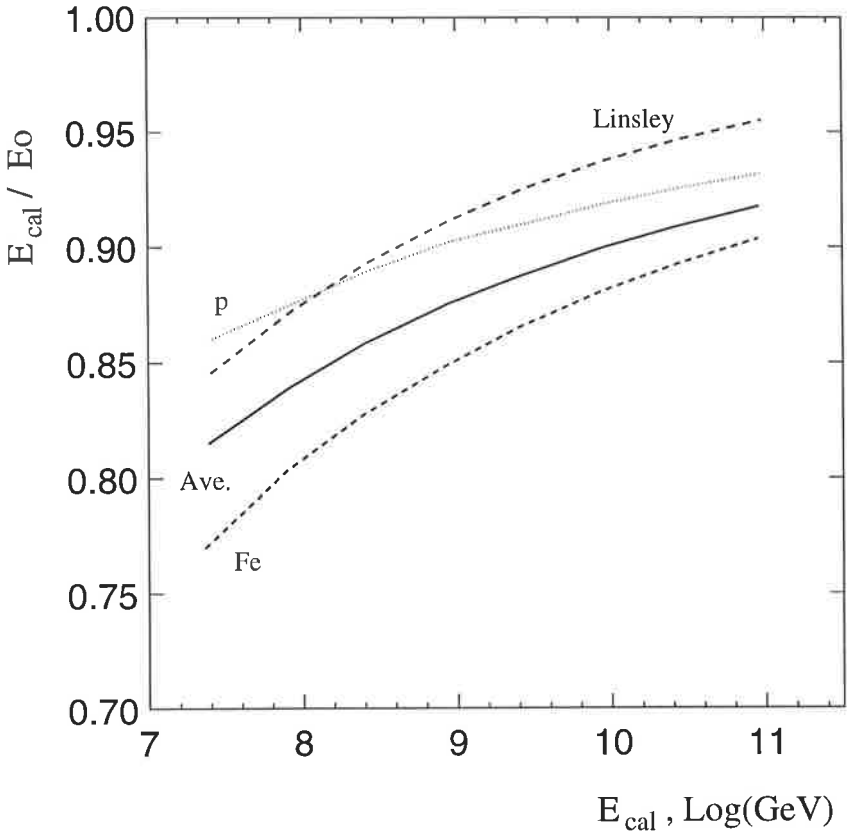

Figure 4.13: The functions for correcting the calorimetric energy to the primary energy, as a function of calorimetric energy. Shown are the corrections for proton showers (dotted line) and iron showers (short dashed line) and an average of the two (solid line). For comparison, Linsley's function[96] is also shown[93].

where dN/dE is the observed number of cosmic rays per energy bin, t is the exposure time and $A\Omega(E)$ is the aperture corresponding to that energy bin[90]. At HiRes the aperture is estimated using Monte Carlo simulations [76]. The energy and the exposure (therefore the cosmic ray flux) calculations for HiRes-1 and HiRes-2 mono events are performed independently by two different groups of the HiRes collaboration. The HiRes-1 and HiRes-2 cosmic ray flux calculations are described separately in [94] and [92] respectively. Figure 4.14 shows the estimated HiRes-1 and HiRes-2 differential cosmic ray energy spectra for events detected by each detector alone (i.e mono detection).

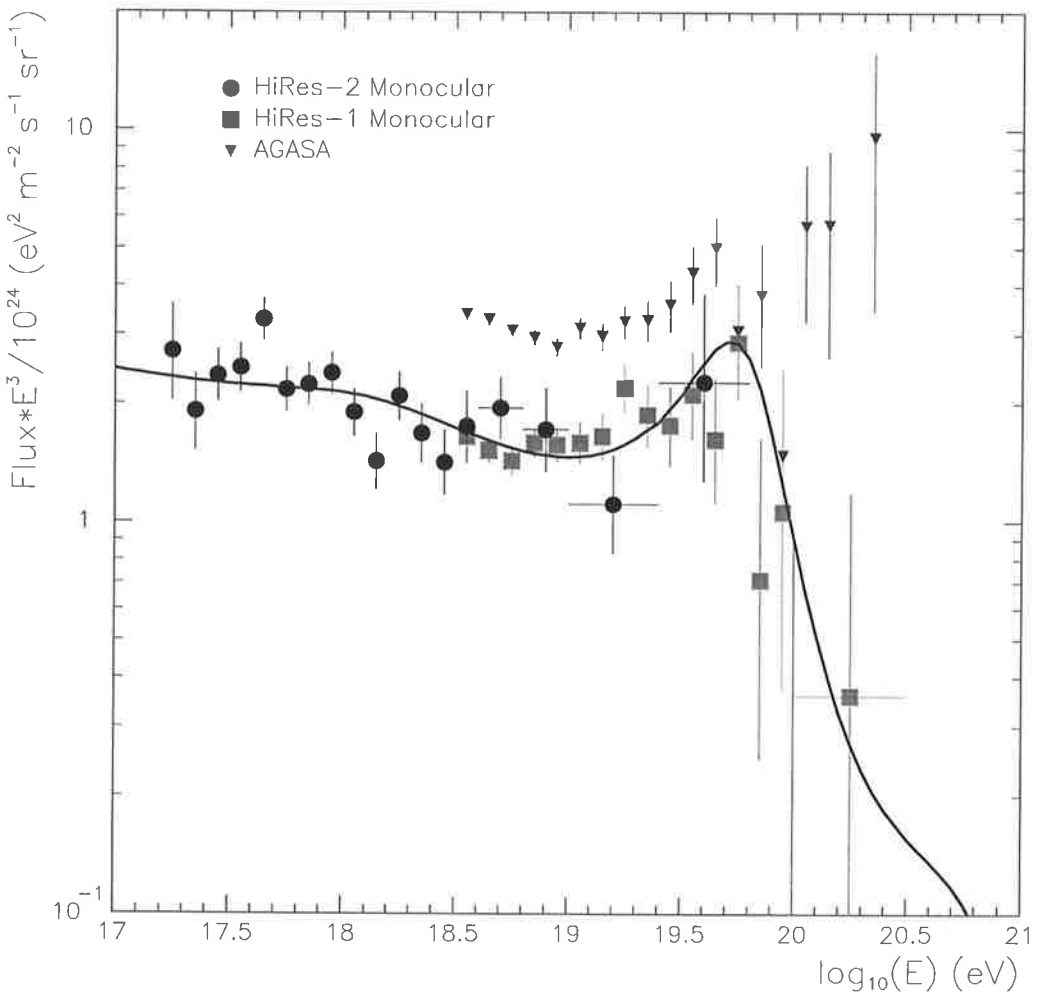

Figure 4.14: Estimated HiRes-1 and HiRes-2 cosmic ray flux. This plot also shows the cosmic ray flux estimated by AGASA[92]. The solid line is a fit to the data assuming a model, described in [92], of galactic and extragalactic sources.

Chapter 5

Preparing for geometrical reconstruction

For a successful or perhaps a better angular resolution of the geometrical reconstruction of a cosmic ray, it is necessary beforehand to cope with some important details. For a better stereo [1] reconstruction of a cosmic ray, especially when the opening angle [2] is small ($< 5°$), it is desirable to have both HiRes sites well synchronized in time (within 100 ns). HiRes-1 and HiRes-2 absolute timing is assigned using GPS clocks and 40 MHz scalers at each site. This system allows an intersite synchronisation of the order of 25-50 ns[97]. Also for a successful overall reconstruction of the cosmic ray, it is crucial to distinguish tubes that were fired by fluorescence light from tubes that were fired by fluctuations of the sky background noise.

[1] Stereo means that the shower is observed simultaneously by two sites (two fluorescence detectors placed in different locations).

[2] The smaller angle formed by the intersection of the SDPs is called in this thesis the opening angle.

5.1 Estimating the clock offset between HiRes1 and HiRes-2

It is desired to use the FADC timing information of HiRes-2 for a more accurate geometrical stereo reconstruction of events. I present here an analysis of the HiRes intersite clock offset performed using vertical flashers taken from January, February and March 2000. At that early stage of HiRes-2 operation, several timing problems were present. Then, detailed tracking of the intersite offset from day to day was necessary to identify potential timing problems. After being identified most of the timing problems reported in this section have been corrected.

In order to estimate the clock offset between sites, some dst[3] files with stereo events were recorded from Utah. The Fit_shower1 program (a program is described in Chapter 7) was used for the geometrical reconstruction of stereo events. The options selected for the reconstruction were amplitude weighted (-aw) and stereo only (-s). Time information was not used for the reconstruction. Events with core positions corresponding to the flasher positions were selected.

A program was written to read the stfit bank (this bank has the information of the reconstruction and is generated by the Fit_shower program) together with the fraw1, fpho1 and hraw1 banks which contain the HiRes-1 and HiRes-2 event information. This program estimates the distances from the fired mirror to the flasher axis along the fired tube direction. It also estimates the distance along the flasher axis from the ground to the intersection of the flasher axis with the fired tube direction.

Once we have the distance from the mirror to the flasher axis along the fired tube direction, and the distance from the intersection of the tube direction with the flasher axis to the ground, we read the tube trigger times (absolute time) from the hraw1 and fraw1 banks. With this information we can estimate the time when the flasher light was emitted at ground level (the flasher ground time "fgt"). In principle, for a given event this time should be the same for all tubes in HiRes-1 and HiRes-2.

[3] "dst", Data Storage Template is the structure used to store and manipulate the HiRes data [85].

Within a given fired mirror, we estimate the fgt according to each fired tube. Then the fgt averaged over all fired tubes will be the estimated mirror fgt. Tubes with fgt 500 ns away from the mirror fgt are more likely to be noise tubes, so they are not taken into account.

The intersite time offset is calcuted using the mirror fgt. If the flasher fired only one mirror at HiRes-2 the time offset between sites is,

$$\text{offset time} = \text{mirror fgt}_{\text{HiRes}-2} - \text{mirror fgt}_{\text{HiRes}-1} \tag{5.1}$$

and if there were two fired mirrors the time offset is,

$$\text{offset time} = (\frac{\text{mirror fgt}_{\text{HiRes}-2_A} + \text{mirror fgt}_{\text{HiRes}-2_B}}{2}) - \text{mirror fgt}_{\text{HiRes}-1}. \tag{5.2}$$

Since some flashers fire two mirrors at HiRes-2, we can use the same technique to estimate the time offset between these mirrors,

$$\text{mirror offset} = \text{mirror fgt}_{\text{HiRes}-2_A} - \text{mirror fgt}_{\text{HiRes}-2_B}. \tag{5.3}$$

If the system is working correctly, both the intersite time offset and the mirror time offset should be close to zero. In all plots to follow, we show results from vertical flashers.

5.1.1 Results of the time offset analysis

From the available stereo dst files we selected for the analysis the following nights: January 15, February 03, February 28 and March 05, 2000. The quality of the timing data appears to improve over this period.

5.1.1.1 January 15, 2000

The spread in the time offset between sites (fig 5.1) and the mirror time offset at HiRes-2 (fig 5.2) is because there were wrong values of the fraw1_it0 variable. The fraw1_it0 variable is the time of first digitization for each channel in units of 100 ns

since the last millisecond. So in principle fraw1_it0, should not be bigger than 10000. Looking at fraw1 bank, most of the fraw1_it0 values were bigger than 10000.

These features of timing problems were reported to our Columbia University collaborators[4]. They reported that they had found some processing problems. We were given access to some reprocessed dst files. Those reprocessed dst files contained information from HiRes-2 (fpho1 and fraw1 banks) only. We used the stereo dst files to match and extract the flasher events from the reprocessed banks, then the reprocessed banks were replaced in our version of the stereo files.

Using the stereo dst files with the replaced fraw1 and fpho1 banks we again estimated the time offset (fig. 5.3). The spread of the time offset distribution decreased from 0.9 msec to 322 nsec, but the offset was not centred at zero. The peak was at 0.819 msec. The variable fraw1_it0 now took reasonable values (less than 10000).

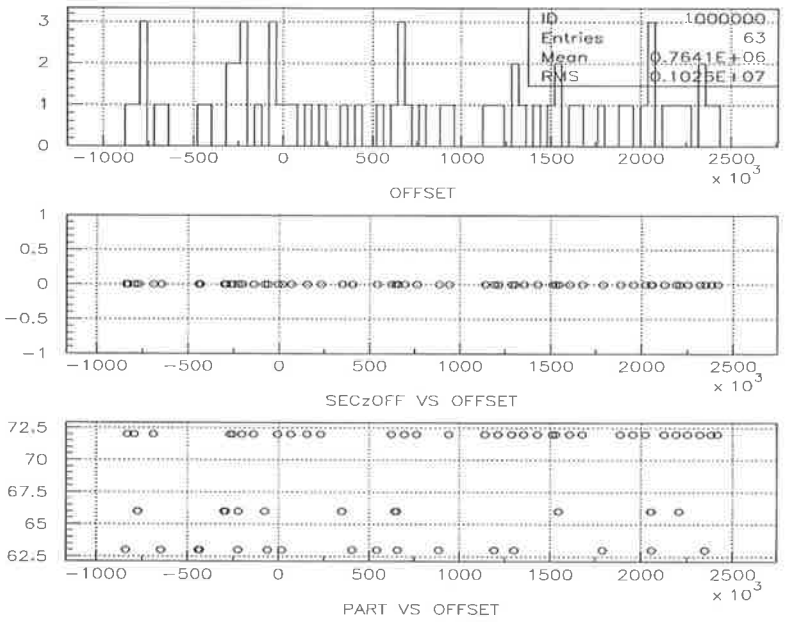

Figure 5.1: The histogram at the top is the nanosecond part of the time offset between sites. The middle plot shows the second part against the nanosecond part of the intersite offset. The bottom plot shows the data file part where the event was stored against the nanosecond part of the intersite offset. All time offsets are given in nanoseconds. January 15, 2000.

[4]The Columbia collaborators are the people in charge of the HiRes-2 electronics and processing system.

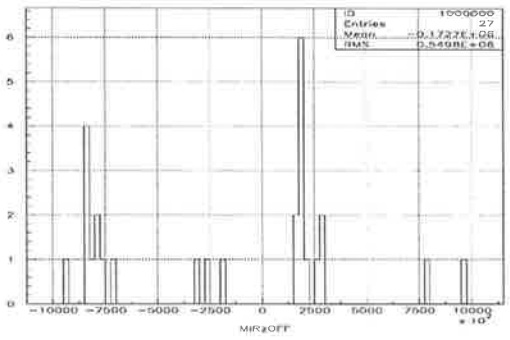

Figure 5.2: time offset between fired mirrors within HiRes-2. Units are nanoseconds. January 15, 2000 .

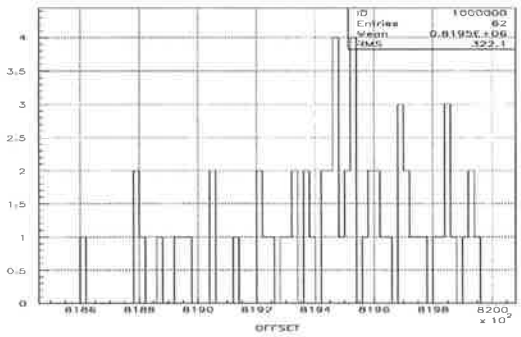

Figure 5.3: Plot generated using the reprocessed fraw1 and fpho1 banks. The histogram shows the distribution of the time offset between sites. Units are nanoseconds.

5.1.1.2 February 03, 2000

We begin with data from the original stereo files (reprocessed data will follow). Figure 5.4 shows that the distribution of the time offset is peaked at around zero (without considering the seconds offset shown in the middle plot). However there is some tail on the offset distribution (fig 5.4, top plot). There is a correlation between these events with large time offsets and the part number (fig5.4, bottom plot). Events belonging

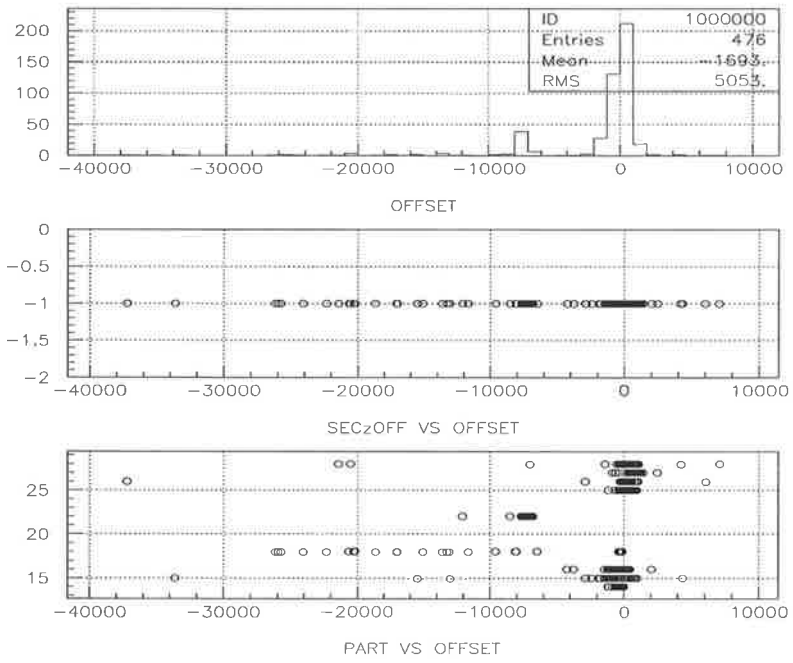

Figure 5.4: The histogram at the top is the nanosecond part of the time offset between sites. The middle plot shows the seconds part against the nanosecond part of the intersite offset. The bottom plot shows the the part where the event was stored against the nanosecond part of the intersite offset. All time offsets are in nanoseconds. February 3, 2000.

to part 22 have their time offset peaked at -7000 nsec, and events belonging to part 18 have their time offsets spread from -25000 to -6000 nsec. No event in part 22 has an time offset close to zero, but some events in part 18 do have time offsets peaked around zero. All events show an error in the seconds part of the offset (fig. 5.4, middle plot).

The peak of the time offset distribution (i.e. ignoring the tail in the top plot of fig 4) is centred at 97.02 nsec with an RMS of 622.3 nsec (fig 5.5).

The HiRes-2 mirror offset distribution is peaked at 89.28 nsec with a RMS of 205.7 nsec (fig 5.6). The problem present on the night of January 15 is not present any more.

Now we consider the reprocessed data from HiRes-2 for this night (see fig. 5.7 and fig. 5.8). Notice that apart from the peak around zero in the time offset distribution

(top plot), there appeared as well peaks centred at -0.45 sec and 0.55 sec. These peaks are separated by exactly one second (fig5.7, top plot).

The seconds part of the time offset now takes three values -1, 0 and 1. Notice that if we calculate the total time offset of the two peaks (-0.45 sec and 0.55 sec) by adding the second and the nanosecond part of the time offsets (fig5.7, middle plot), both peaks have almost the same value (0.55 sec) (i.e. 1-0.45=0+0.55 sec).

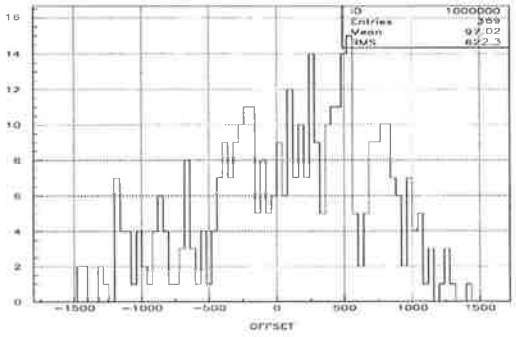

Figure 5.5: Zoom of the time offset between sites from fig. 5.4. time offset in nanoseconds.

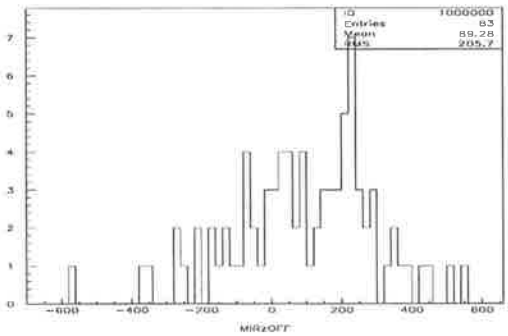

Figure 5.6: time offset between fired mirrors within HiRes-2 during night of February 3, 2000 . time offset in nanoseconds units.

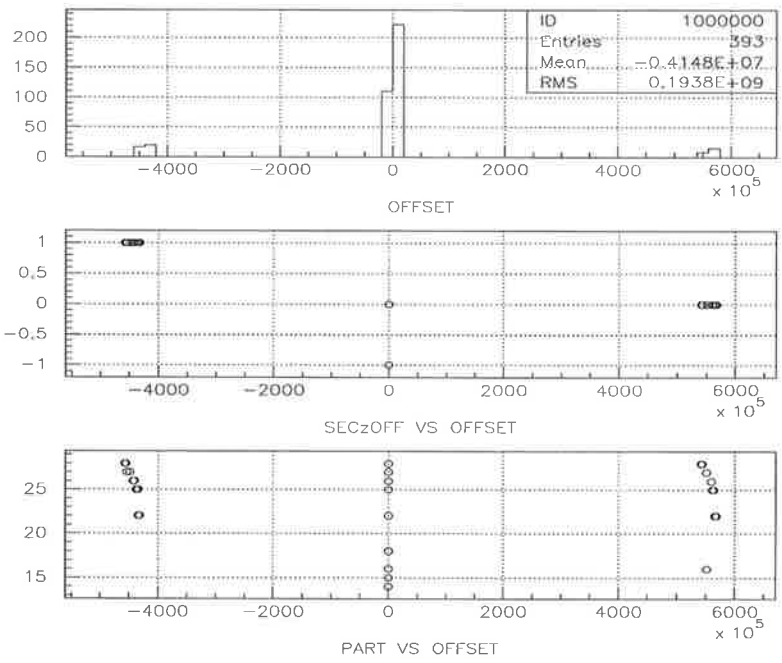

Figure 5.7: Plots generated using the reprocessed fraw1 and fpho1 banks. The histogram at the top is the nanoseconds part of the offset time between sites. The middle plot shows the seconds part of the time against the nanoseconds part of the intersite offset. The bottom plot shows the the part where the event was stored against the nanosecond part of the intersite offset. February 3, 2000.

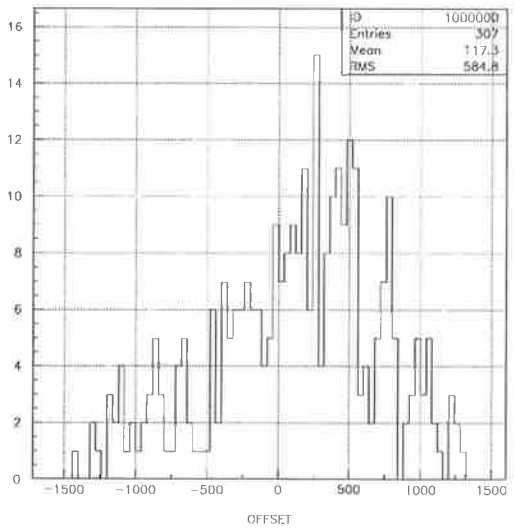

Figure 5.8: Zoom of the time offset distribution between sites from fig. 5.7, ignoring the events at -0.45 and +0.55 sec. Units of the offset are nanoseconds.

5.1.1.3 February 28, 2000

The time offset distribution for February 28 looked much better than previous nights. Almost all events are peaked around zero offset (fig 5.9, top plot). In the seconds part of the offset, all events show a time offset of -6 seconds (fig 5.9, middle plot).

In the mirror time offset within HiRes-2, there appears some spread (fig 5.11 top plot). It seems to be because in some stages of the night some clouds were present, and the light scattered in the clouds provoked mushrooming in the upper mirror. The bottom plot in figure 5.11 shows the mirror time offset against the time sequence of the events. Events between 1 and 38 have their time offsets around zero. Then events from 38 to 80 have their time offsets shifted to positive values (the cloudy stage). Events from 100 to 120 have their time offsets shifted to negative values (probably cloud at a different position). There are not reprecessed files for this night or for the night of March.

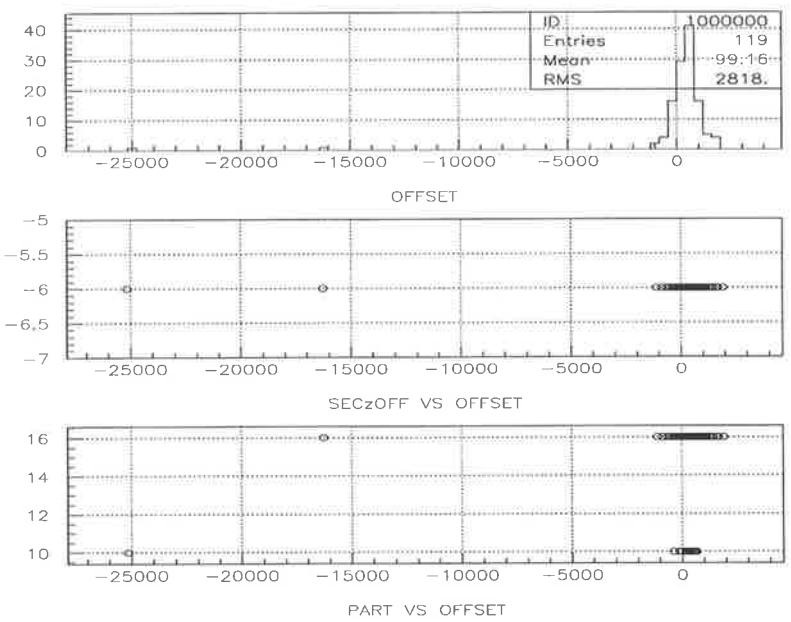

Figure 5.9: The histogram at the top is the nanosecond part of the time offset between sites. The middle plot shows the seconds part against the nanosecond part of the intersite offset. The bottom plot shows the the part where the event was stored against the nanosecond part of the intersite offset. All time offsets are given in nanoseconds. February 28, 2000 .

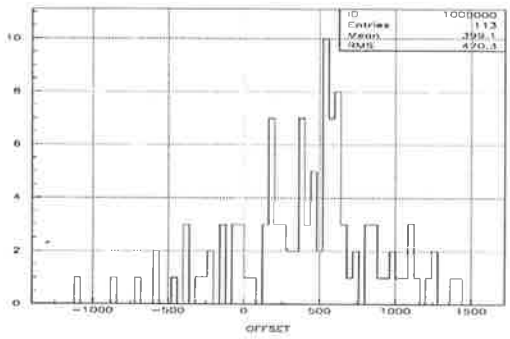

Figure 5.10: Zoom of time offset distribution between sites from fig. 5.9.

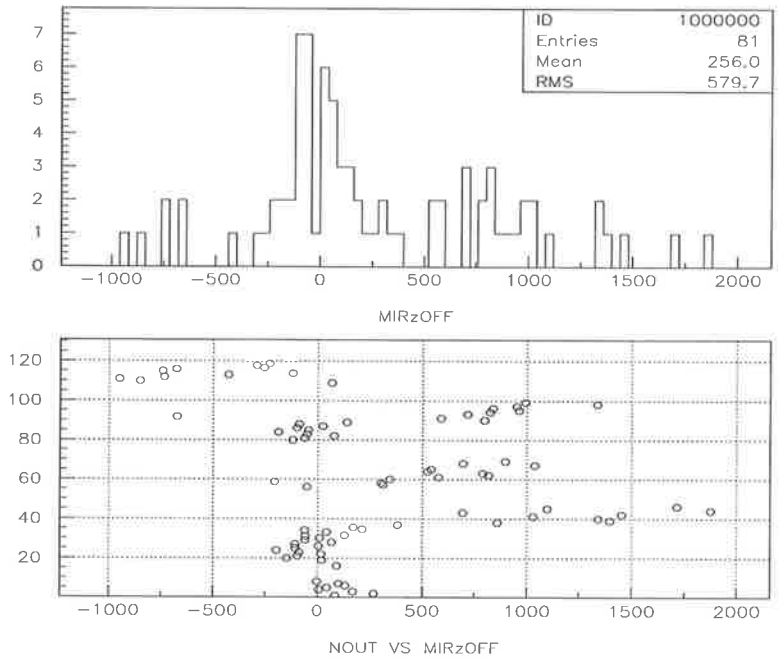

Figure 5.11: The histogram at the top is the distribution of mirror time offsets at HiRes-2. The bottom plot is the time sequence of the events against the mirror time offset . February 28, 2000.

5.1.1.4 March 05, 2000

The time offset distribution is peaked around zero (fig 5.12, top plot). There are some events with time offsets between -23000 and -3000 nsec, these events are from the 4 Km N flasher. The -6 seconds offset is still present on this night (fig. 5.12, middle plot).

Apart from the -6 seconds offset, the intersite offsets (fig 5.13) and the mirror offset within HiRes-2 (fig 5.14) seem to be reasonable.

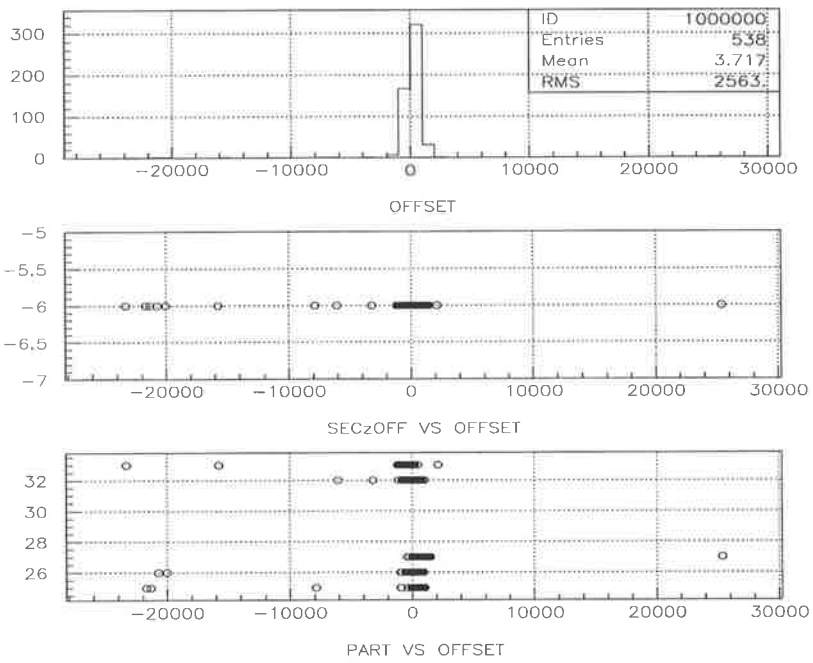

Figure 5.12: The histogram at the top is the nanosecond part of the time offset between sites. The middle plot shows the seconds part against the nanosecond part of the intersite offset. The bottom plot shows the part where the event was stored against the nanosecond part of the intersite offset. All time offsets are given in nanoseconds. March 05, 2000.

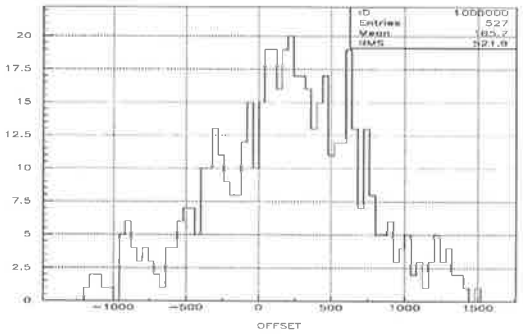

Figure 5.13: Zoom of time offset distribution between sites from fig. 5.12. Units are nanoseconds. March 05, 2000.

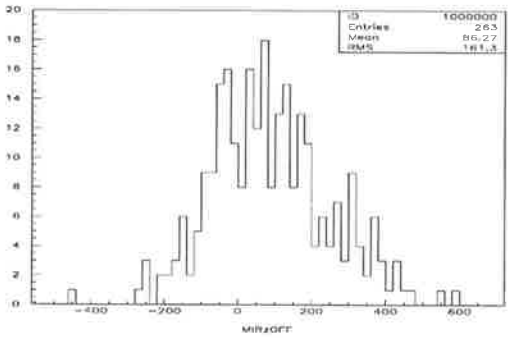

Figure 5.14: The histogram is the time offset distribution between mirrors within HiRes-2. Units are nanoseconds. March 05, 2000 .

5.1.2 Time slewing and the intersite time offset

It was discovered that the intersite time offset distributions, like that in Fig 5.13, were broadened by a systematic effect known as time slewing effect.

The FADC electronics at HiRes-2 allows us to measure the shape of the pulses within the tubes. Therefore we can associate the tube trigger time with the time of the middle of the pulse with good precision. At HiRes-1 the situation is slightly different. The S/H HiRes-1 electronics is designed to integrate the PMT signal over two fixed intervals of time (integration time), 1.5μs (Channel A) and 5.6μs (Chanel B). Chanel A is optimized for nearby air showers (short pulses) and Channel B for

distant air showers (wide pulses). When the PMT pulse reaches a certain threshold [5], the PMT triggers and the integration of the signal is started (for more details of the system see [98]). This electronics design does not record the time development of the PMT pulse, and we can not measure the time of the centre of the pulse. It only allows the recording of the PMT trigger time. At HiRes-1 the associated tube trigger time does not always correspond to the middle of the pulse. This is because for a given pulse width, more intense pulses will pass the threshold before less intense pulses. This is called time slewing. Narrow pulses have less of a problem with time slewing than broader pulses.

The intrinsic width of the flasher pulses (i.e. as emitted from the flash tubes) is of order 1 microsecond, a broad pulse compared to the intrinsic fluorescence pulses which relate to the thickness of the shower front. The flashers are placed at different distances from HiRes-1. So the intensities of the flashers seen at HiRes-1 will be different for each flasher, and the time slewing for each flasher will be different as well.

The trigger times of HiRes-1 tubes viewing a closer flasher (fig. 5.26 shows the locations of the vertical flashers), will be earlier (farther from the middle of the pulse) than tubes fired by more distant flashers. Fired tubes due to distant flashers will have their trigger times closer to the middle of the pulse. Figures 5.15 and 5.16 show the intersite time offset for different flashers. The 8 Km N and 10 Km N flashers are closer to HiRes-1 and we would expect early trigger times in that detector. Indeed in the figures we see that these flashers have more positive time offsets (time offset = HiRes-2 - HiRes-1). This is becauase HiRes-1 trigger times are earlier than the pulse centre.

In future, laser shots (which have shorter intrinsic pulse widths) could be used to reduce the time slewing effects (especially for close-by lasers) and allow an estimate of the intersite clock offset with much more precision. A tentative of using laser shots to study the time slewing effect is presented in section 7.1.3.1.

[5] Before comparing the PMT pulse with the threshold, the pulse passes through a low band pass filter to get rid of the frequent short pulses from sky noise

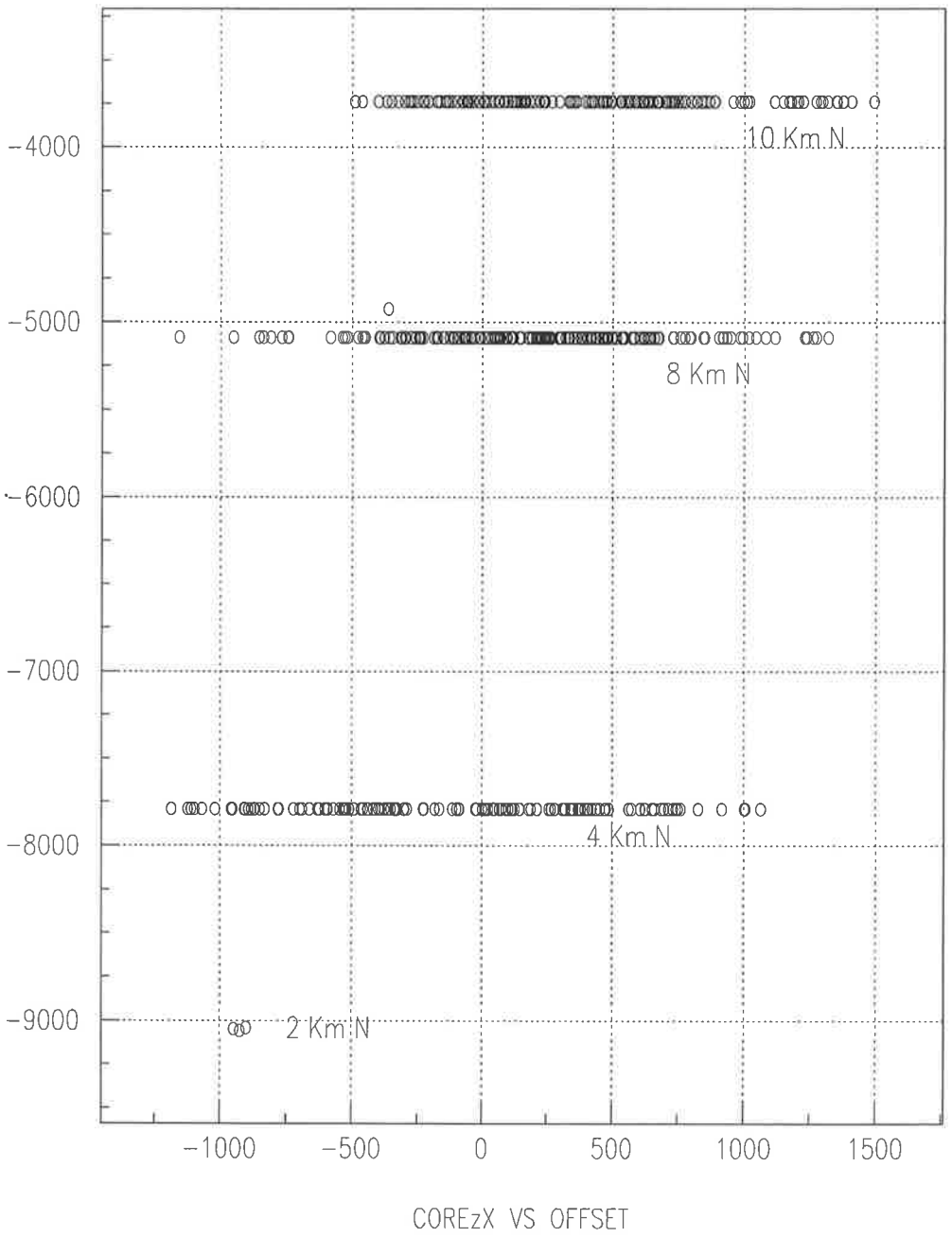

Figure 5.15: The x (east - west) coordinate of the flasher positions against the time offset. March 05, 2000 .

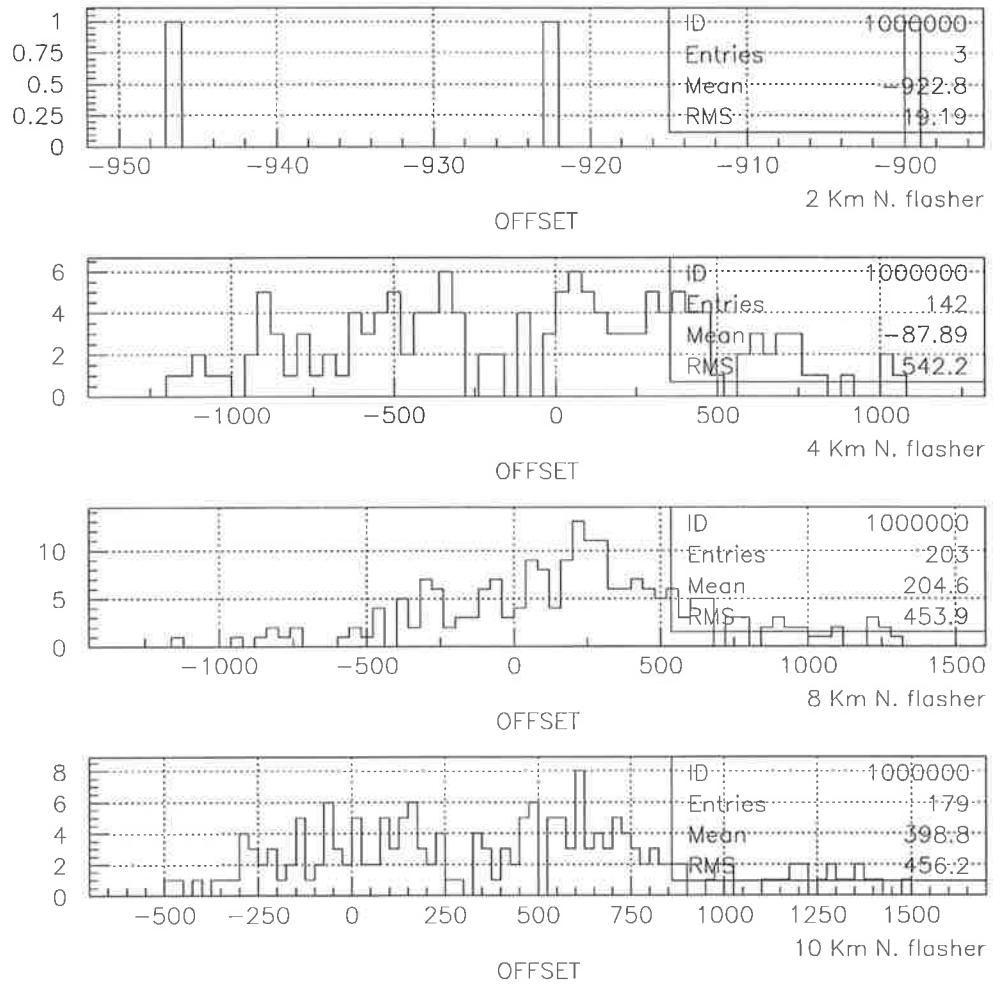

Figure 5.16: The histograms are the time offset distribution between sites for different flashers. March 05, 2000 .

5.1.3 Conclusion

A well known and stable absolute clock offset will allow stereo timing fits to be performed with much greater power than possible with unsynchronized clocks. In this section, I examined the absolute clock offsets between HiRes-1 and HiRes-2 using data collected from vertical flashers in January, February and March 2000. Results from January and early February show that the clock offset was large and varying in the stereo files produced by W.Springer. Subsequent reprocessing of HiRes-2 data has

improved the synchronization greatly. The resulting distributions of clock offsets seem reasonable, given that flashers with wide intrinsic pulse widths are being used for the study. The measured clock offset is also affected by some time slewing in HiRes-1. There remain some small problems, including an apparent discrepency in the seconds part of the absolute event time (in data from February 28 and March 5).

Later analysis showed that there was a time dependent systematic intersite offset. Figure 5.17 shows the intersite offset for the 10 km North flasher as a function of time. The periodic change in the intersite offset in Figure 5.17 was because the HiRes-2 GPS clock was operating in fixed position mode and the specified position was few kilometres away from HiRes-2. The specified position at the HiRes-2 GPS clock was then corrected and the RMS of the intersite offset distribution was considerable reduced from ~500 ns (Fig.5.13) to ~100 ns (Fig.5.18). A set of laser shots was planned to finally correct any small scale ($< 1\mu s$) systematic intersite time offset, but unfortunately after September 11 2001, the US army restricted access to the HiRes site. Since the intersite time offset problem is still present in the stereo data, the timing reconstruction algorithm (see section 7.1.3.2) will not require synchronization between sites.

The apparent scale of the time offset between HiRes-1 and HiRes-2 (≈ 0.7 μs, see Fig.5.18) does not reduce the number of coincidence events (stereo events). This is because the time coincidence window used in event matching is larger, 200 μs.

5.2 Algorithm to filter noise tubes at HiRes

The first step in the reconstruction of a cosmic ray at the HiRes detectors is to identify good[6] tubes and noise[7] tubes. The following steps of the reconstruction will only use

[6]good tubes are triggered by the fluorescence and Cerekov light produced at the cosmic ray air shower.

[7]noise tubes are often triggered by background light fluctuations.

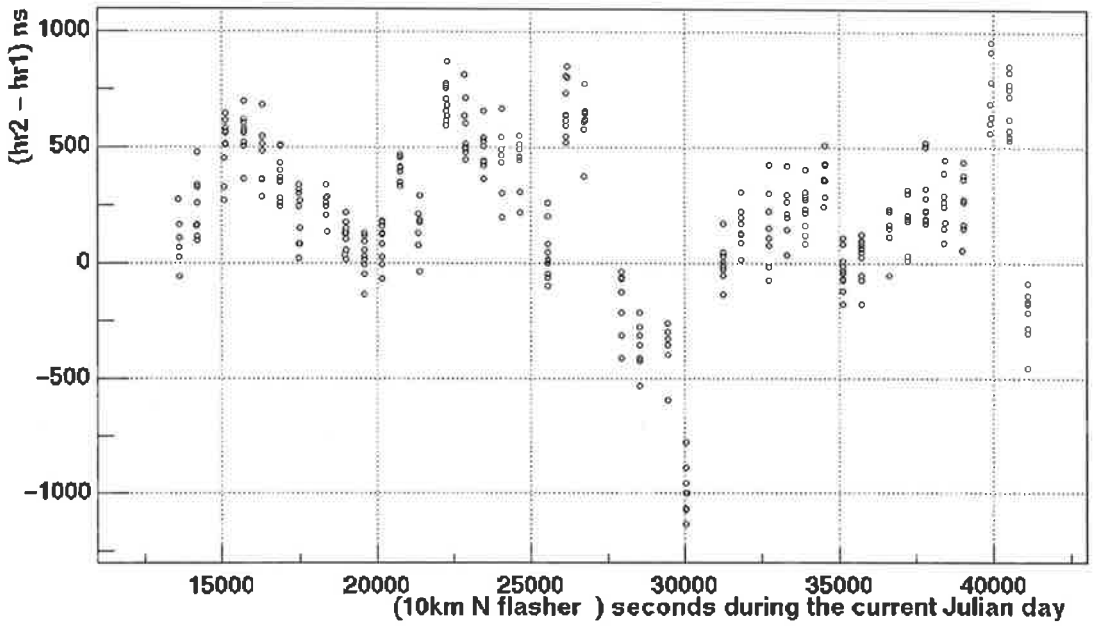

Figure 5.17: Estimated intersite time offset as a function of time using the 10 km North flasher. March 25, 2001.

the tubes identified as good ones to get the geometry and then the energy of the cosmic ray. This is the case for mono and also stereo reconstruction. So, if the algorithm that recognizes good tubes and noise tubes fails (i.e. a wrong identification of the good tube pattern), then the reconstruction of the cosmic ray will not be the best.

In this section, I give a detailed description of an algorithm used for filtering noise tubes at HiRes-1 and HiRes-2. This algorithm is used in Fit_shower1 (a stereo geometry reconstruction program described in chapter 7). Because of differences in the HiRes-1 and HiRes-2 event triggering conditions, an average of 84% of the triggered tubes at HiRes-1 are signal, while at HiRes-2 only 14% are signal tubes (fig.5.19). HiRes-2 requires special care to recognise signal tubes from noise tubes, because it is easy to find a very wrong pattern of signal tubes there.

The differences between HiRes-1 and HiRes-2 were taken into account for the design of the noise tube filtering algorithm. At HiRes-2 there are two rings of mirrors while at HiRes-1 there is only one. This implies that for a given event we often will have more good tubes at HiRes-2. On average for cosmic ray events there are 35 more signal tubes at HiRes-2 than at HiRes-1 (fig. 5.20), and we can afford to be more strict in

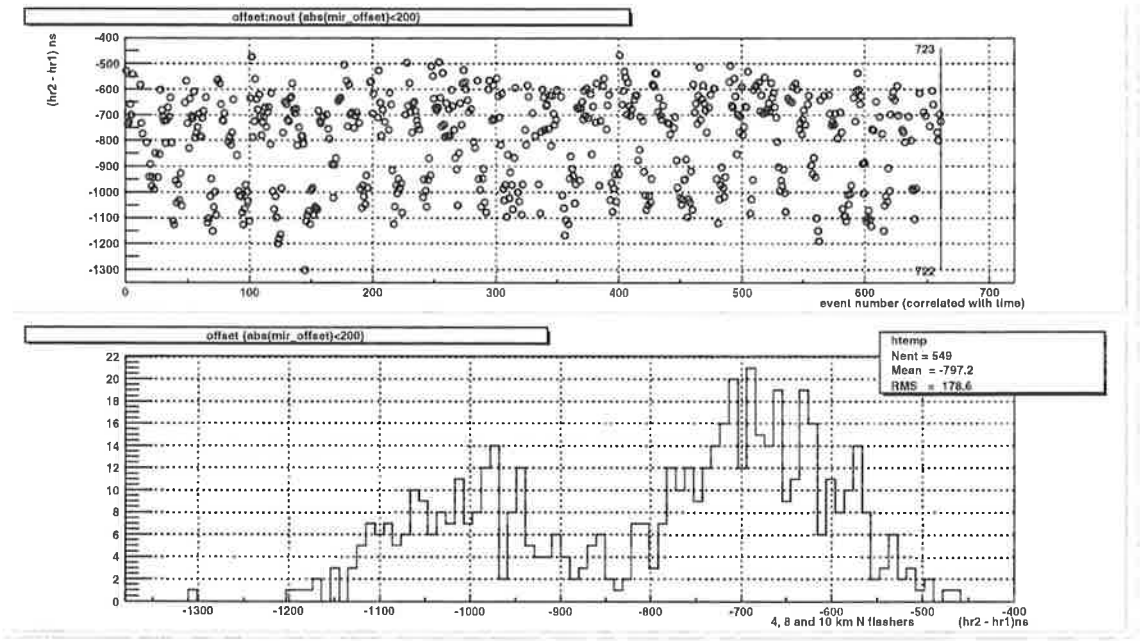

Figure 5.18: Estimated intersite time offset as a function of time using the 4, 8 and 10 km North flashers (top plot). Distribution of the estimated intersite time offsets (bottom histogram). Because of the different effects of the time slewing for the 4 km N flasher compared with the 8 and 10 km N flashers, the intersite time offset estimated using the 4 km North flasher appears centred at -980 ns, while the the intersite time offset estimated using the 8 and 10 km North flashers appear centred at -700 ns. These data was taken on July 23, 2001 and for this period the HiRes-2 GPS clock location was correct.

the filtering of HiRes-2. Note that in the case of both sites we readmit some tubes later in the process.

5.2.1 Event trigger requirements

- **HiRes-1:** At HiRes-1 the average individual tube trigger rate is kept at 200 Hz. So the required signal for triggering a tube changes according to the background light (the tube trigger threshold is dynamically adjusted every 4 seconds). A signal threshold of approximately four standard deviations above the mean background light keeps the tube trigger rate at 200 Hz.

  In HiRes-1 each mirror cluster is divided into 16 sub-clusters, with each sub-cluster having four columns and four rows (16 tubes). The next level of the trigger occurs in each sub-cluster. A sub-cluster triggers when there are at least

three triggered tubes with two of the tubes adjacent (within 25μs). Then a mirror trigger requires at least two sub-clusters to trigger within a 25μs window. If one mirror is triggered, then the neighbor mirrors will require a trigger in only one sub-cluster.

- **HiRes-2:** The HiRes-2 trigger is based on the analog sums of the 16 pmt's in each row and column. The analog sums are continuously digitized by the trigger channels. A 3-fold coincidence is formed between neighboring or next-to-neighboring rows or columns. Two 3-fold coincidences (row+row, row+col, or col+col) within 5 microseconds constitutes the primary trigger. At this point nothing is yet known about the signal in any individual tube.

  There is then a confirming scan performed. A search is performed for tube signals with at least 32 counts above pedestal after passing through a digital filter with a time constant of 1 microsecond. Thus, the threshold on the confirming scan is 32 pe for a delta function pulse, or about 50 pe for a 1 microsecond wide square

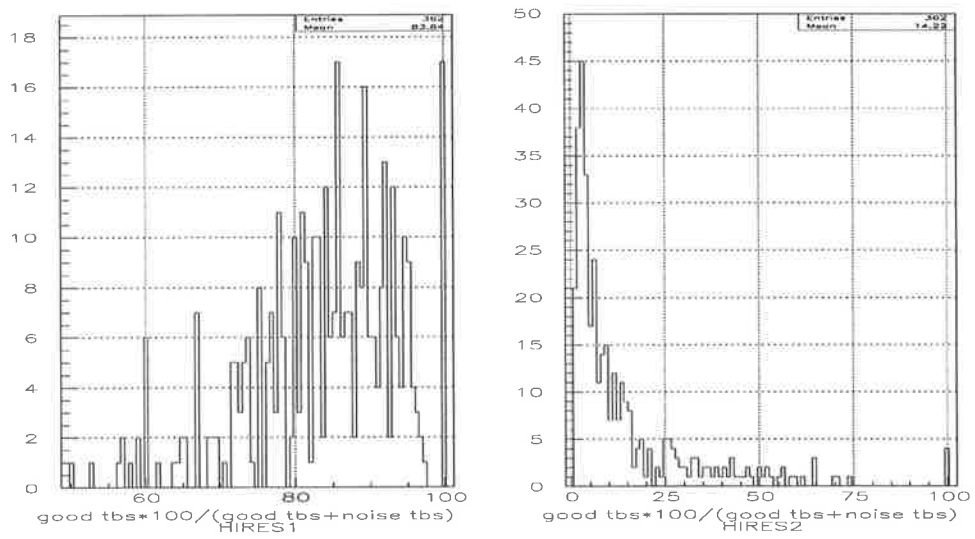

Figure 5.19: Distribution of the percentage of signal tubes triggered in an event in relation to the total number of triggered tubes. Here we use the noise filtering algorithm described in this section. This set of events corresponds to cosmic ray events. HiRes-1 left plot and HiRes-2 right plot.

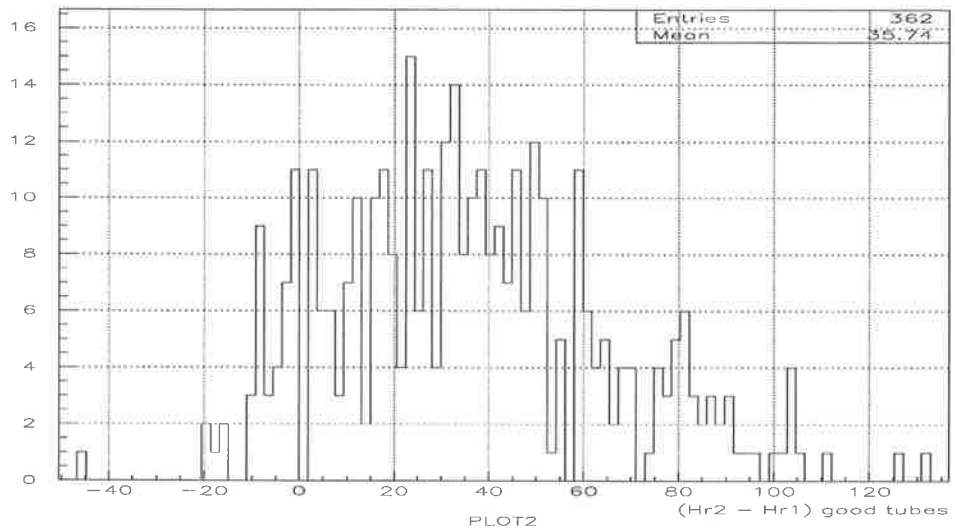

Figure 5.20: Distribution of the difference between the number of signal tubes triggered at HiRes-1 and HiRes-2 in an event. Figures 6.1 and 6.2 were generated using a set of 362 stereo cosmic ray events.

pulse. The secondary trigger requires a cluster of 3 tube hits from the confirming scan.

Finally there is a readout scan. This is the same as the confirming scan, but with a threshold of 24 instead of 32. All channels which pass the readout scan are read out. (Thanks to John Boyer for help with this description of the HiRes-2 triggering scheme).

5.2.2 Description of the noise tubes filtering algorithm

The following algorithm was designed to identify the tubes that will go on to the geometrical reconstruction process (i.e. good tubes).

1. The first step is to order the tubes sequentially according to their trigger times and also to estimate the average signal per tube at each site.

2. The dot product between each tube direction with its previous (dot1) and next (dot2) triggered tube will give the angular distance to the previous (*prev_theta*)

and next (*next_theta*) tube.

$$prev\_theta = acos(dot1) \tag{5.4}$$

$$next\_theta = acos(dot2) \tag{5.5}$$

At each site, *prev_theta* is zero for the first triggered tube and *next_theta* is zero for the last triggered tube.

In Fit_shower1, tubes are ordered in time regardless of whether they belong to HiRes-1 or HiRes-2. So it is necessary to check if the previous and next tube belongs to the correct site. Some noise tubes in one site can squeeze among the tubes from the other site. It is also necessary to check the mirror of the previous and next tubes, these tubes could belong to a neighbor mirror.

3. HiRes-1 tubes will be treated differently from HiRes-2 tubes. At HiRes-1, if a tube has signal lower than the average and its previous and next tubes are not neighbors (i.e. the *prev_theta* and the *next_theta* are greater than 2^o), It will be flagged as bad tube. However, none of the HiRes-1 tubes with signal greater than the average are flagged as bad tubes.

   At HiRes-2 regardless of the tube signal, all tubes for which their previous and next triggered tubes are not neighbors, will be flagged as bad tubes. This is because we often see noise tubes with signals comparable to good tubes. This process can throw out some good tubes, so we will check later if we need to readmit any tube.

4. All tubes with a signal lower than 25% of the site average signal are flagged as bad tubes.

5. A weight is assigned to each tube for a later linear regression fit of the tube zenith vs time. The weight is based on the angular distance to the previous and next good tubes (eq. 5.6). At this stage, most of the noise tubes may still be flagged as good tubes. Thus, noisy events may have many good tubes with big

angular distance to the previous and/or next good tubes. In such cases, the weight is based on the tube signal (eq. 5.7), see details below.

$$angular\_distance^2 = prev\_theta^2 + next\_theta^2$$
$$weight(angular) = \left(\frac{1}{angular\_distance^2}\right) \tag{5.6}$$

$$weight(signal) = \left(\frac{tube\_signal}{average\_signal}\right)^2 \tag{5.7}$$

The last triggered tube of the event (note that the last triggered tube of the event is not the last triggered tube with the status of good tube) will be automatically flagged as bad tube, this tube is often noise. It can be readmitted later.

We assign 5^o to *prev_theta* and *next_theta* for the first and last triggered tubes at each site. For good tubes the $angular\_distance^2$ is around 2. So, tubes with $angular\_distance^2$ greater than 37 *may* be flagged as bad tubes. (After a few trials 37 turns out to be a reasonable value). The decision is based on the following.

Sometimes with noisy events, some noise tubes are triggered between good tube triggering times. For this reason, several good tubes may have $angular\_distances^2$ greater than 37. We will flag all tubes with $angular\_distances^2$ greater than 37 as bad tubes only if after this cut there still remain at least 4 good tubes. Otherwise, we will only flag tubes as bad if as well as the $angular\_distances^2$ being greater than 37 they also had a signal lower than half of the average signal. This may increase the number of remaining good tubes. However, if the number of remaining good tubes is still lower than 4, none of the tubes are flagged as bad tubes at this step and the corresponding tube weight is calculated using equation 5.7.

6. A linear regression fit is performed of the tube zenith angles vs time. In this fit we only use the tubes that were not flagged as bad tubes before. The weight used for HiRes-1 tubes is the product of the square of the tube signal times the

weight estimated at step 5 (eq. 5.6 or eq. 5.7). The weight used for HiRes-2 tubes is only the weight estimated at step 5 (eq. 5.6 or eq. 5.7). At HiRes-2 noise tubes often have signals as large as good tubes.

$$weight(HiRes1) = tube\_signal^2 \times weight_{step5} \tag{5.8}$$

$$weight(HiRes2) = weight_{step5} \tag{5.9}$$

On average 84% of HiRes-1 tubes are signal (fig. 5.1). Thus, most of the time the $angular\_distance^2$ is small for HiRes-1 tubes and the $weight_{step5}$ will be calculated using equation 5.6. Very rarely $weight(HiRes1)$ will be equal to $tube\_signal^4/average\_signal^2$ (i.e. the $weight_{step5}$ being calculated using equation 5.7).

7. Once we have the linear fitting parameters of the tube zenith vs time curve, we use the slope, the zenith and the time of each tube to estimate the intercept of the curve at the tube zenith axis. A distribution of the intercepts is calculated. If any of the tubes at the extremes of this distribution are more than 8° from the peak, they are flagged as bad tubes. If all tubes successfully pass this condition we jump to the next step, otherwise we return to step 5.

8. With the remaining tubes a trial shower detector plane (SDP) is estimated for each site. Here, all tubes (including tubes that were flagged as bad tubes in previous steps) with an angular distance to the SDP smaller than 3^o are given the status of good tubes.

9. At this step we have identified all tubes close to the SDP. The last step is to check the time development of these tubes. We use again the fitting parameters calculated at step 6, this time to estimate the ground time distribution (the time expected for the shower to reach the ground). The RMS of this distribution varies according to the distance of the shower to the detector. For nearby showers

(around 4km) this RMS is around a few hundred nanoseconds, while for distant showers (more than 10 km) the RMS is around a few microseconds.

If the estimated ground time of a given tube is more than 5 times the mean deviation away from the peak, then the tube will be flagged as bad tube. The reason that we use the mean deviation and not the standard deviation (RMS), is because the standard deviation is strongly affected by tubes (noise tubes) with estimated ground times far from the peak.

Constraining the ground time distribution to be within 5 times the mean deviation could seem very generous. We keep this range large because we are approximating the zenith VS time curve to a straight line. Thus, if we make this range smaller we may throw out some good tubes that were at the extremes of a long angular track length event.

Step 3 could seem to be very strict (specially for HiRes-2) because it can throw out many good tubes. However as long as it does not throw out all good tubes there is no problem. The idea in step 3 is to throw out all noise tubes and to leave at least 3 good tubes. Only 3 good tubes are enough to construct a trial SDP, and with the SDP we can recover all good tubes that were initially thrown out.

5.2.3 Test of the algorithm

In order to test this algorithm we used vertical flashers. We chose for this test flashers from July 22, 2001 (1684 events). This was a clear night and both detectors operated without problems.

When using this filtering algorithm the reconstructed SDP could be very wrong (more than 10 degrees away) if the identified pattern of signal tubes is not the correct one. Also the reconstructed SDP can be slightly deviated due to some noise tubes close (within 3 deg) to the pattern of signal tubes that were not flagged as bad tubes. Figure 5.21 shows the differences between the reconstructed SDP and the expected SDP for each vertical flasher against the event number. In figure 5.21 we also compare

results from Fit_shower1 and results from other filtering algorithms used at HiRes-1 and HiRes-2. Results from other filtering algorithms are stored in dst banks called hpln1 (for HiRes-1) and fpln1 (for HiRes-2). In what follows I will refer as hpln1 and fpln1 results for the results stored in these banks.

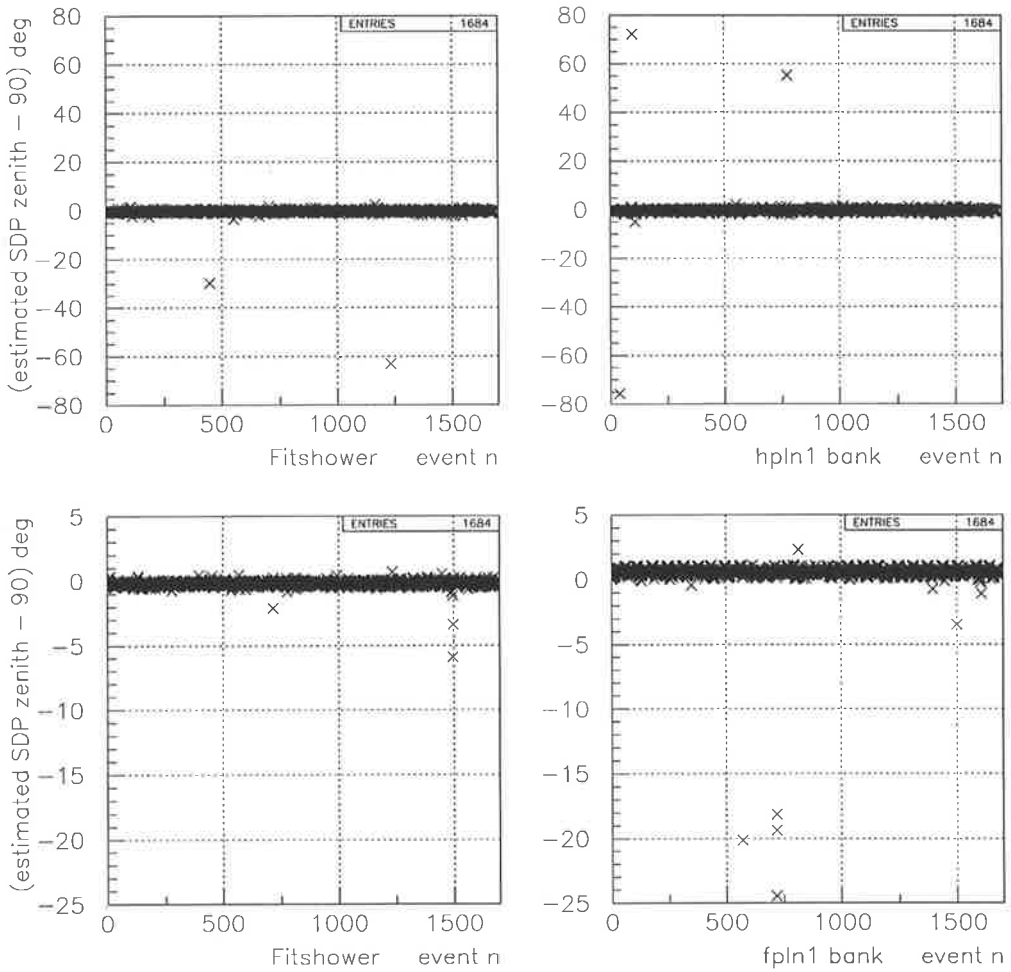

Figure 5.21: The normal to the SDP should have a zenith angle of 90o for these vertical flashers events. The plots show the deviation from this expectation versus event number (time ordered). The left plots are results from Fit_shower1 and right plots are for hpln1 and fpln1 results. The top plots correspond to HiRes-1 and the bottom plots correspond to HiRes-2.

There were two events with the reconstructed HiRes-1 SDP very wrong when using Fit_shower1, and three events when using the other program (hpln1 results). The

events which were poorly reconstructed by Fit_shower1 are not the same events that were poorly reconstructed according to the hpln1 results. Fit_shower1 poorly reconstructed the SDPs because it found wrong patterns of signal tubes. These events do not show a clear pattern of signal tubes (fig. 5.22). So, there was no way to distinguish between signal and noise tubes. It seems that both events were noise events.

The three events with wrong reconstructed SDPs in the hpln1 results (top right plot in fig 5.21) are due to some noise tubes not being flagged as bad. Only one noise tube flagged as a good tube could be enough to deviate the reconstructed SDP considerably (fig 5.23).

Figure 5.21 (bottom left plot) shows that when using Fit_shower1, none of the events had their HiRes-2 SDPs very poorly reconstructed. However a few events have their reconstructed HiRes-2 SDPs some degrees away (no more than 6 deg) from the expected direction. This is because some (probably only one) noise tubes close to the pattern of signal tubes were considered as good tubes (see fig. 5.24).

There are a few events (4 events) that according to the fpln1 results have their reconstructed HiRes-2 SDPs in error by 20 degrees. These events are close in time and it seems that at that time there was some background noise present. This background noise gave some of the noise tubes intense signals. In the fpln1 analysis these intense noise tubes were not flagged as bad (fig. 5.25) and they were used to estimate the SDP.

5.2.4 Interesting features

In figures 5.27, 5.28 and 5.29, I show some reconstruction results for vertical flashers. In terms of SDP resolution, it is noted that the HiRes-1 SDP becomes less well defined for more distant flashers, while the resolution in the HiRes-2 SDP remains rather constant. This is probably a reflection of the shorter track length at HiRes-1. For close by flashers the "fat" nature of the track helps with SDP resolution, but this is not the case for distant flashers. Figure 5.26 shows the location of the flashers.

It is also noted that a systematic shift exists in the HiRes-2 SDP, between that

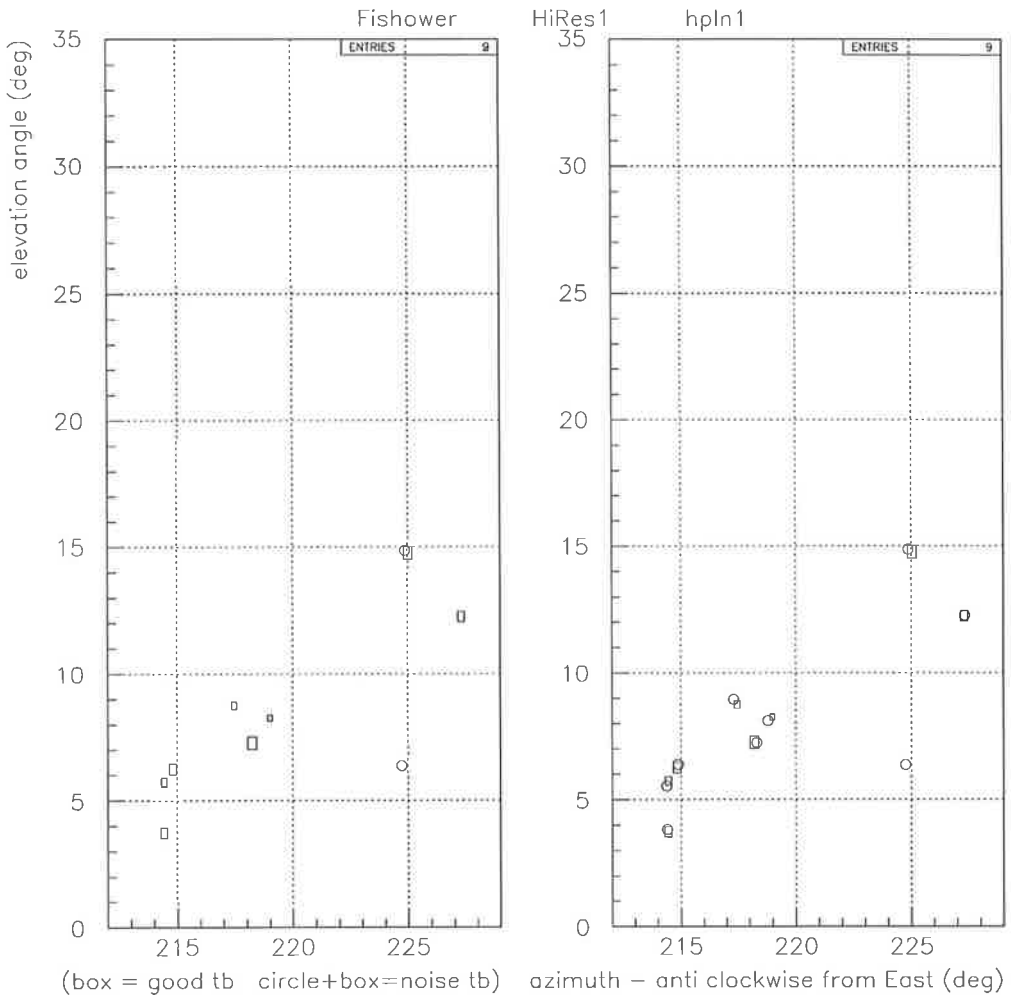

Figure 5.22: Event display showing an event which does not have a defined track (this is a noise event). The left plot shows noise tubes identified using Fit_shower1 and the right plot shows the noise tube identification coming from the hpln1 analysis. The estimated HiRes-1 SDP (using Fit_shower1) for this event is 60 deg away from the expected SDP for a vertical flasher. The size of the boxes indicate the relative tube signals.

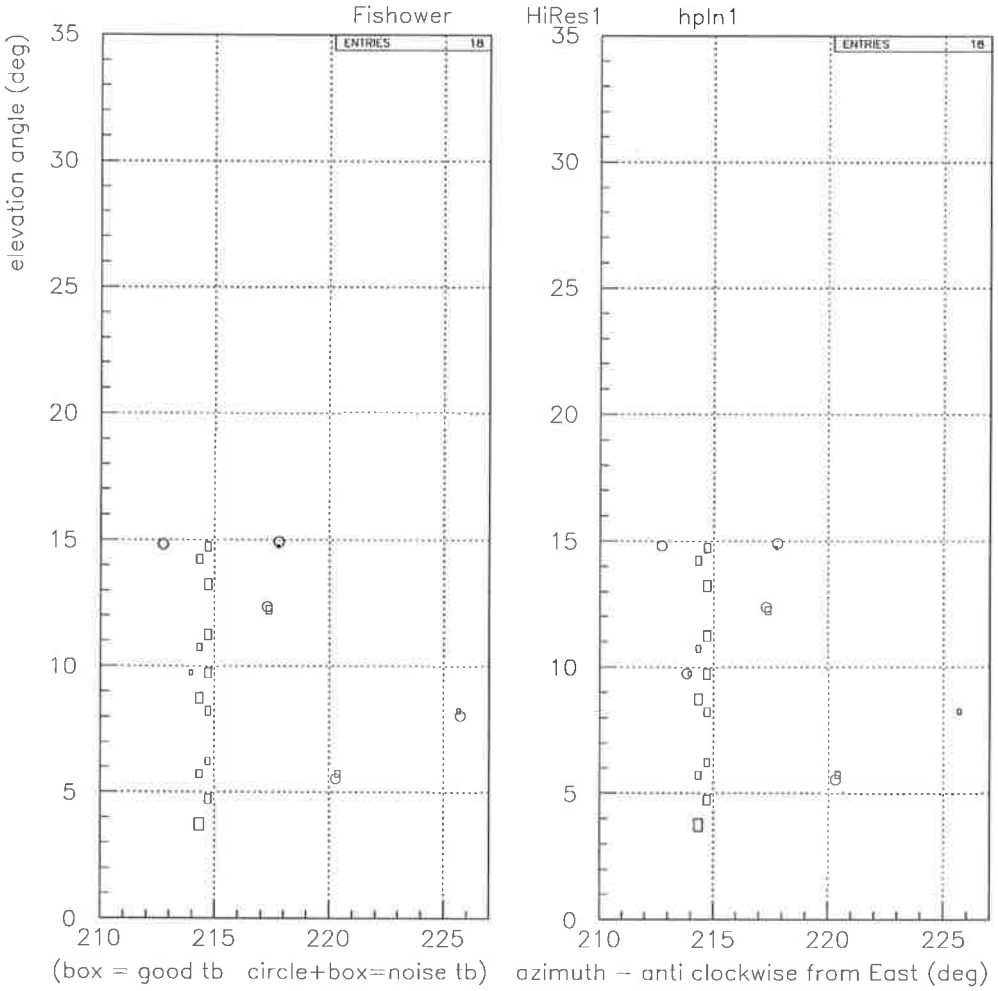

Figure 5.23: This event display shows a case where a noise tube far from the track was considered as good tube in the hpln1 analysis (right plot). This tube caused a deviation of 75 deg in the reconstructed SDP (see fig. 5.21).

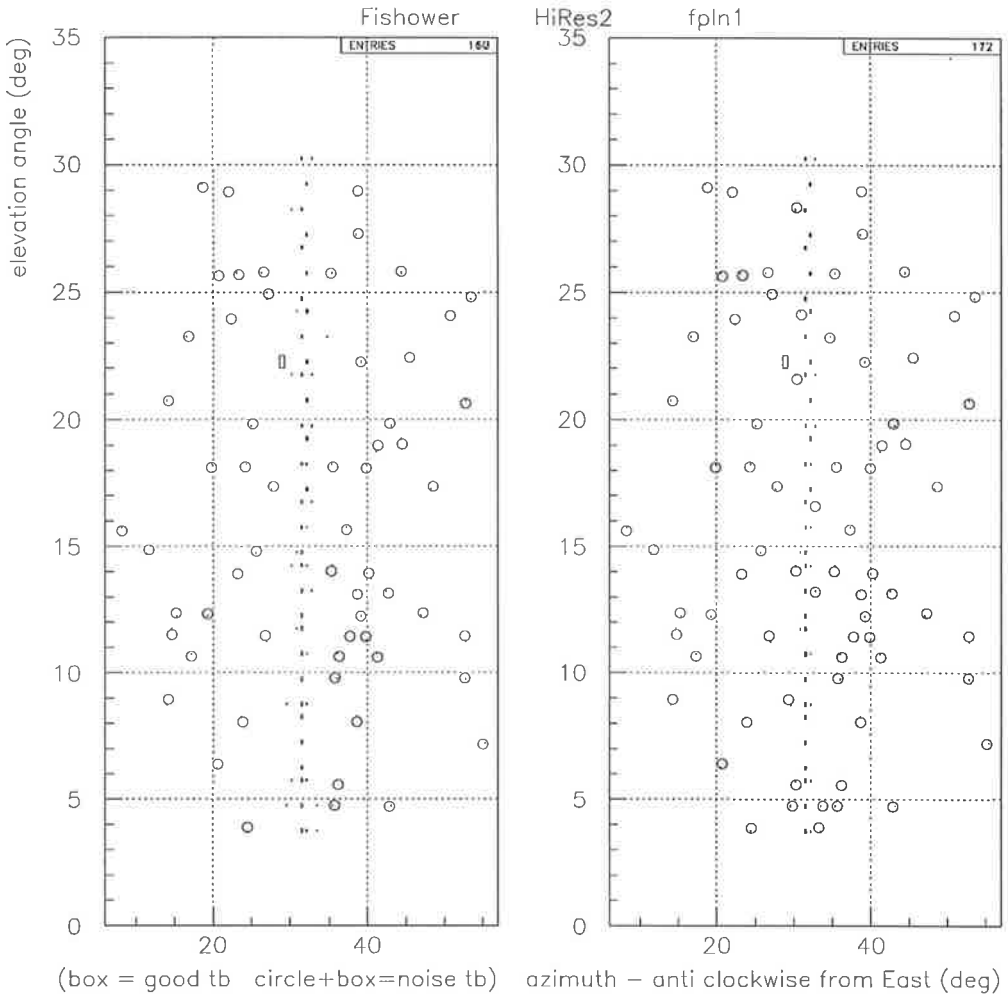

Figure 5.24: Event display showing a case where a noise tube close to the track (within 3 deg) was considered as good tube (using the Fit_shower1 algorithm). This tube with a signal bigger than the rest of the tubes caused a deviation of around 5 deg in the reconstructed SDP.

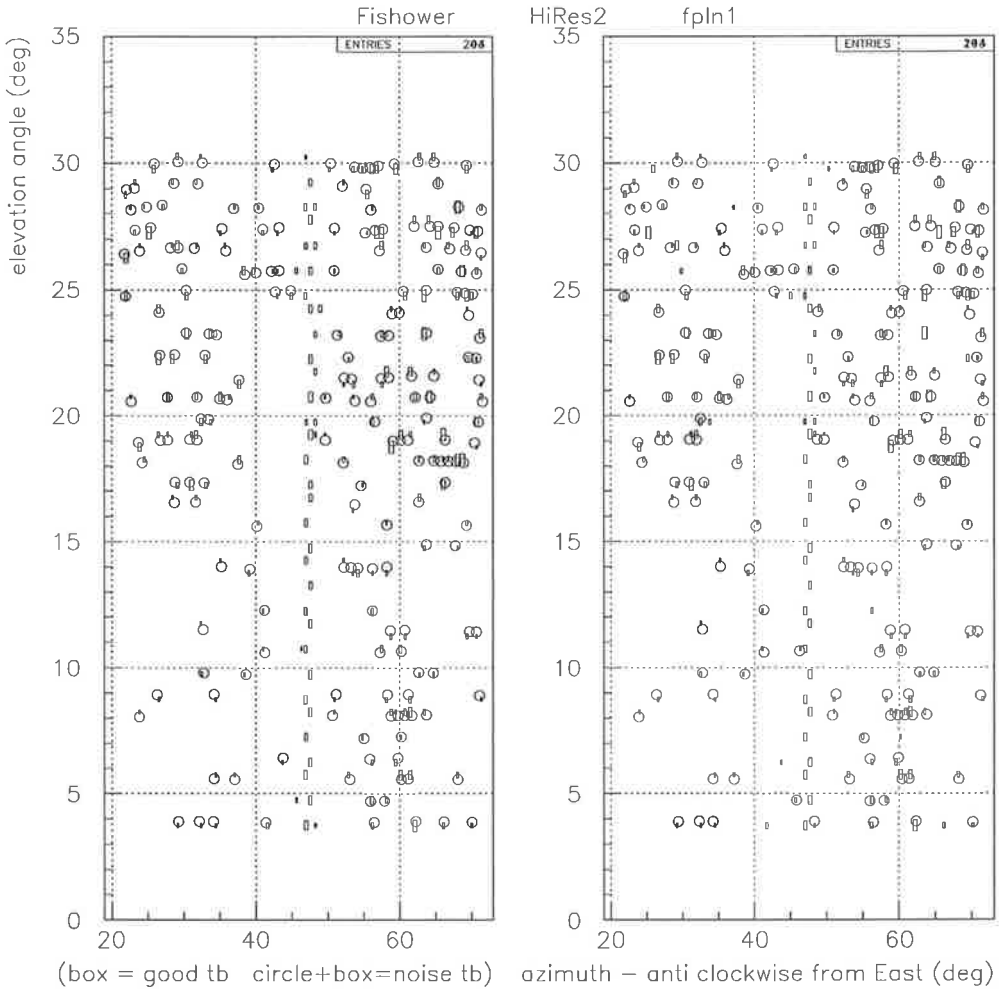

Figure 5.25: Event display showing an event with intense noise tubes. Some tubes with intense signals close to or far from the track were considered as good tubes in fpln1 (right plot). These tubes caused a deviation of around 20 deg in the reconstructed SDP.

determined by Fit_shower1 and that stored in the fpln1 bank (fig.5.28 and fig.5.29). The shift is around 0.25 deg for flashers far from HiRes-2, and 0.75 deg for close flashers. It was found that this shift appears in events that involved two mirrors. This happens when the different physical positions of the mirrors are not taken into consideration to estimate the SDP. Figures 5.28 and 5.29 (right plots) shows that the shift of the estimated HiRes-2 SDP in fpln1 is consistent with such parallax effects. For closer flashers the shift is larger.

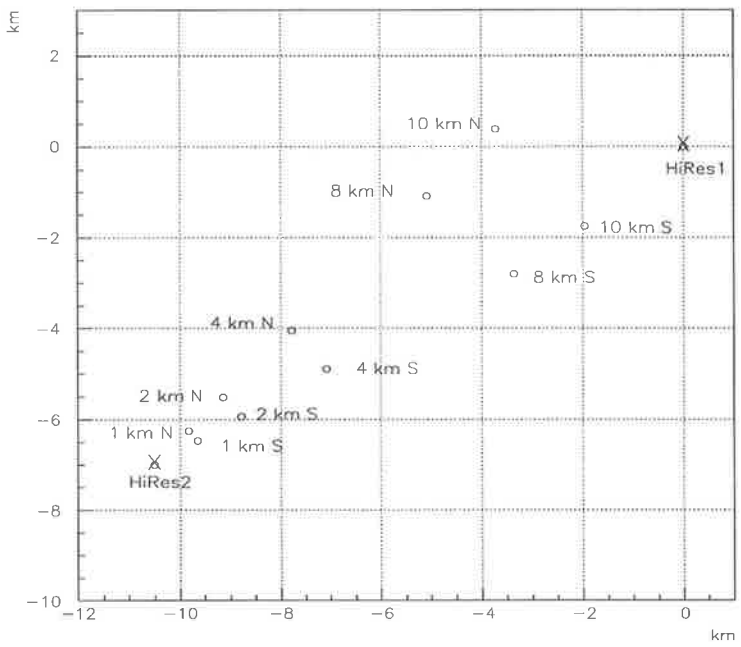

Figure 5.26: Locations of the radio controlled flashers.

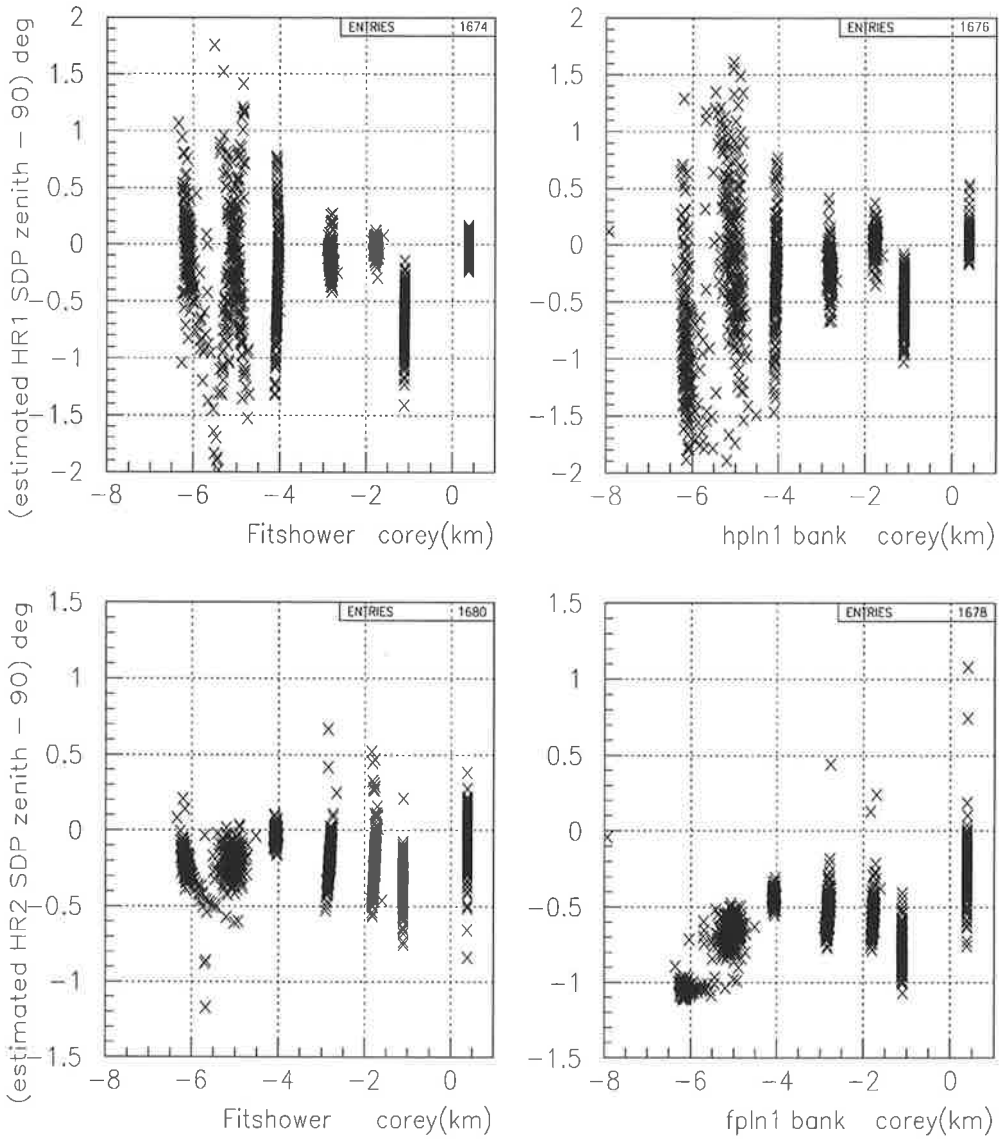

Figure 5.27: These plots show the deviation of the reconstructed SDPs from a vertical SDP vs the estimated flasher core positions, corey is the 'y' coordinate (HiRes-1 top plots and HiRes-2 bottom plots). The left plots are results from Fit_shower1 and the right plots arefrom hpln1 and fpln1 results. These data correspond to vertical flashers from July 22, 2001.

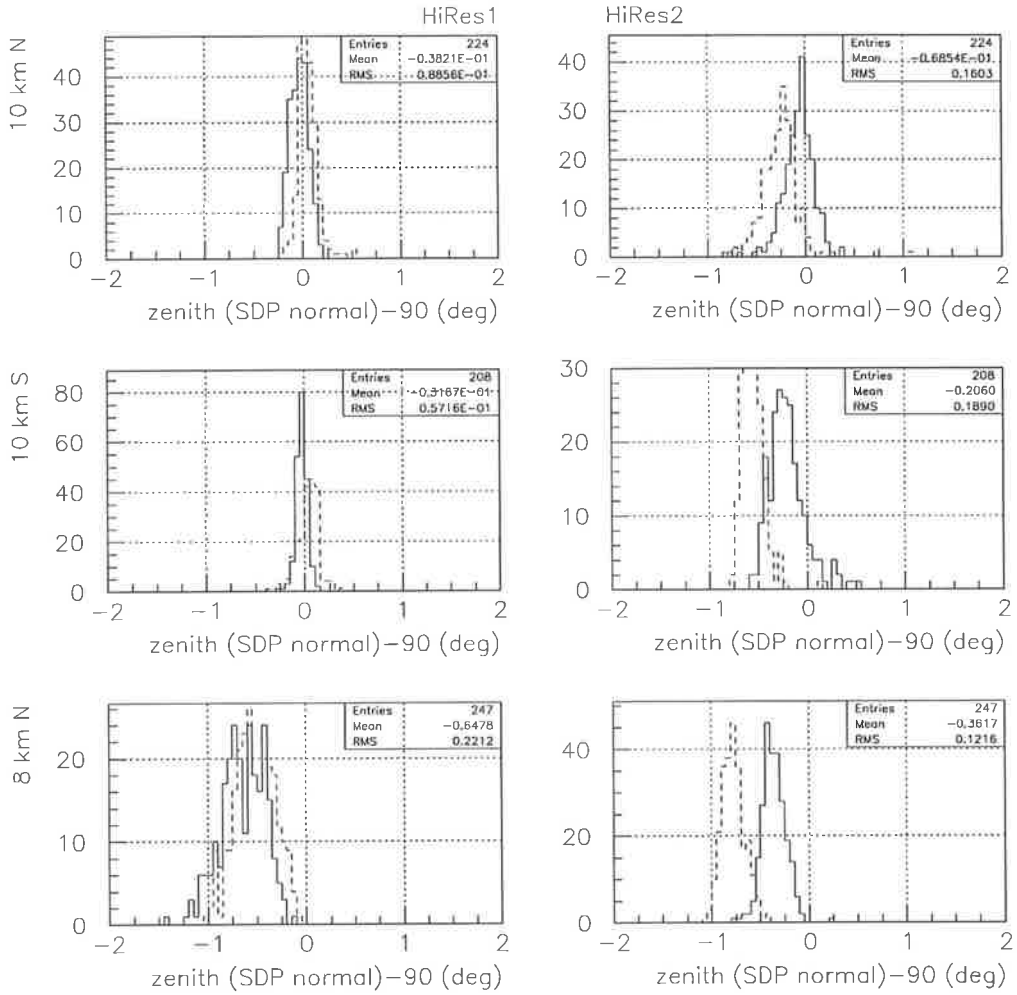

Figure 5.28: Distribution of the deviation between the zenith angle of the reconstructed SDP normals and the SDP normals expected for a vertical event. Plots on the left correspond to HiRes-1 and plots on the right correspond to HiRes-2. The flasher identification is on each plot. Solid lines correspond to results from Fit_shower1 and dashed lines correspond to hpln1 (HiRes-1) and fpln1 (HiRes-2) results.

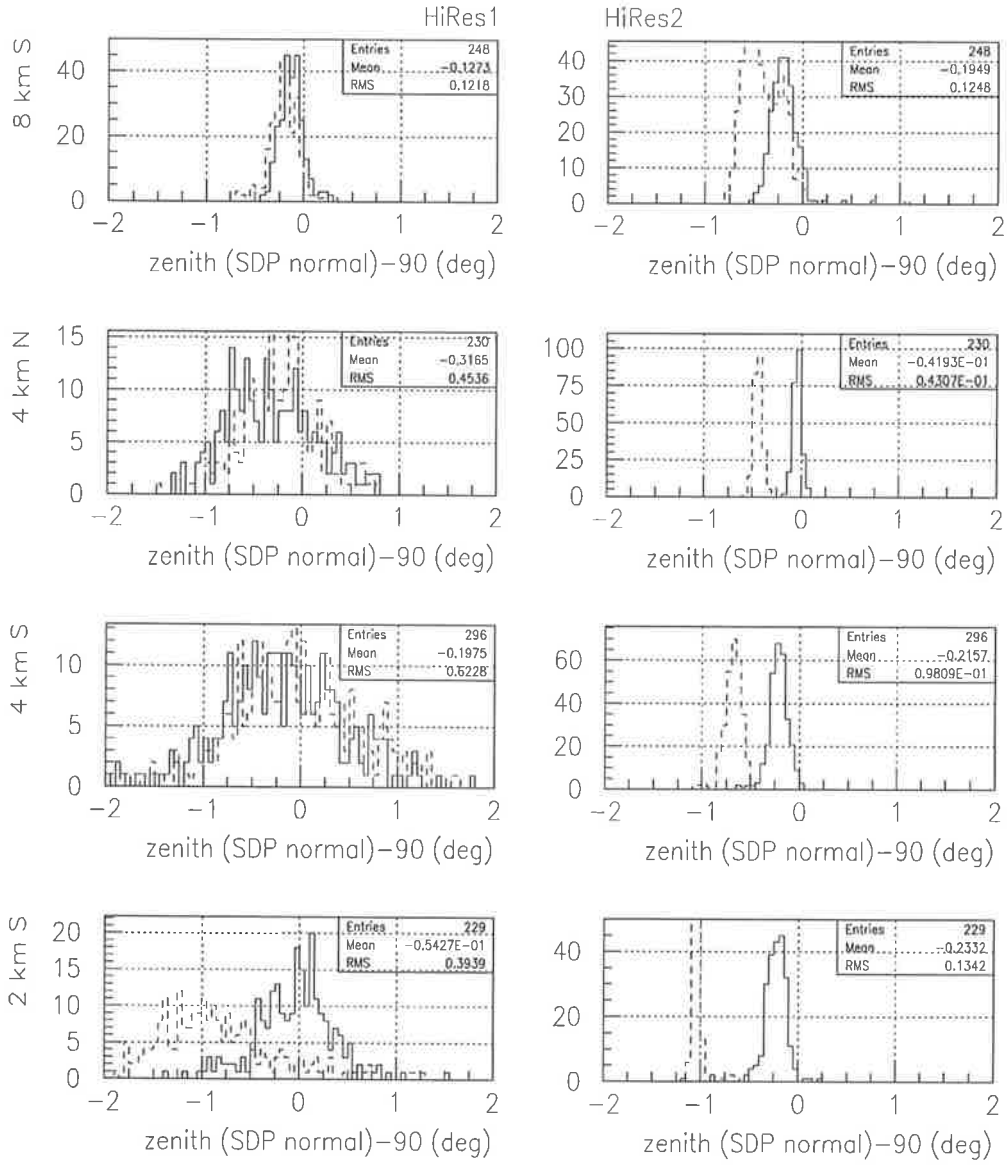

Figure 5.29: Same caption as figure 5.28.

Chapter 6

HiRes-1 monocular geometrical reconstruction

In this chapter I intend to characterize the accuracy of the 'Profile Constrained Geometry Fitting' (PCGF), the monocular geometrical reconstruction technique used in HiRes-1. For this purpose, I compare geometrical reconstruction results between monocular and stereo techniques. I also use a MC data set with energies above $10^{17.6}$ eV.

As mentioned above, the HiRes detector is a cosmic ray detector whose design optimizes the stereo detection of cosmic rays with energies above $10^{18.5}$ eV. Because of the 12.6 km separation between HiRes1 and HiRes2, most cosmic rays with energies below $10^{18.5}$ eV will only be seen by one site (monocular events). Although the aim of the HiRes collaboration is to study the highest energy cosmic rays ($> 10^{18.5}$ eV), it is valuable to use the large number of monocular events with energies around 10^{18} eV for specific anisotropy studies around this energy range. Other experiments, such as AGASA (see section 2.1.1) and SUGAR (see chapter 3) have found an excess of cosmic rays with energies between $10^{18.0}$ and $10^{18.5}$ eV coming from around the Galactic Centre. Also an excess from Cygnus X-3 around this energy range was observed by Fly's Eye and AGASA experiments (see section 2.1.2).

The HiRes-2 detector has two rings of detectors covering an elevation angle of 30°

(each ring covering $\sim 15^\circ$ of elevation). However the HiRes-1 detector has only one ring of mirrors and only covers $\sim 15^\circ$ of elevation angle. The geometrical reconstruction of monocular events by time fitting has a larger uncertainty when the observed track length of the cosmic ray is shorter. This fact makes the geometrical reconstruction a difficult task, especially for HiRes-1 where most of the monocular events have short track lengths.

In order to reduce the large uncertainties in the estimated arrival directions and energies of monocular events, a profile fitting method has been designed [99]. The PCGF method uses the expected form of the shower development to constrain the time fit to yield reasonable geometries. The shower profile is assumed to be described by the Gaisser-Gillas parameterization (eq. 4.3). The time fitting in conjunction with the profile fitting determine the cosmic ray arrival direction (see Apendix B for details).

For the analysis in this chapter, approximately 2.5 years of monocular observation, 1.2 years of stereo observation and a MC data set were considered. The uncertainty of the geometrical reconstruction of monocular events is estimated by comparing monocular results against stereo results for the same showers , and against the MC inputs.

6.1 Monocular data

HiRes-1 has been operating for 2.5 years alone. For this period of time all the data taken is monocular. The PCGF has been used to reconstruct the geometry of the events.

Figure 6.1 shows the energy, zenith, azimuth and psi angle distributions. The solid and dashed lines are distributions before and after applying pass4a cuts [1].The name of the file where these events are stored is 'y2001m05d13.a25sc10.ps4.dst'. The name of the file specifies the date that the data were processed and the kind of atmosphere used for the reconstruction. There are 9890 events in this file, and 5827 events passed the pass4a cuts.

[1]the pass4a cuts is a subset of the pass4 cuts, pass4a cuts are listed in section 6.3. All scatter plots in this chapter are after applying pass4a cuts.

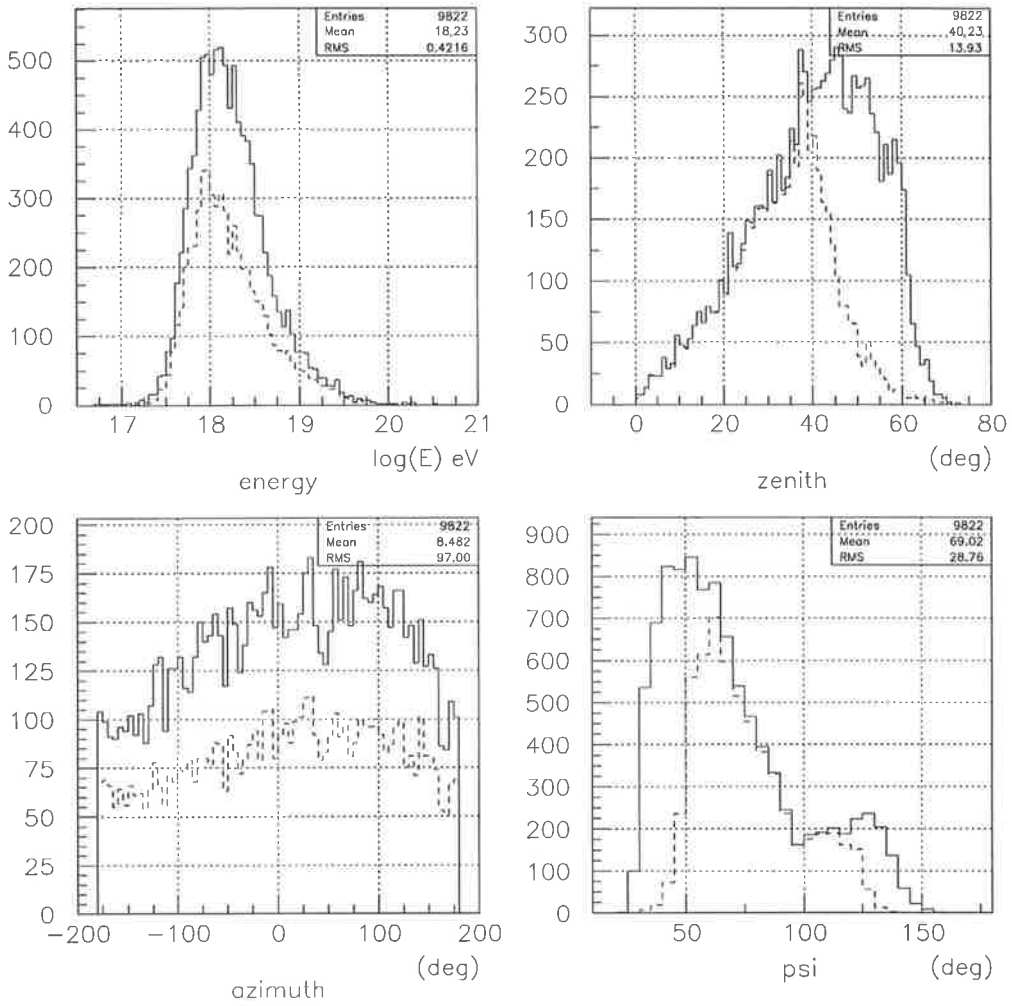

Figure 6.1: Estimated energy, zenith, azimuth and psi distribution of the entire monocular data set ('y2001m05d13.a25sc10.ps4.dst'). Solid and dashed lines are distributions before and after applying pass4a cuts.

6.2 Monocular results against stereo results

At the time of this analysis, there was available a small stereo data set containing 350 events. This allowed us to compare stereo and monocular reconstruction of the same events.

The arrival direction of monocular cosmic ray events is estimated in two steps. The first step is to estimate the shower detector plane (SDP). Given the high resolution pixels of the detector (1° resolution), the SDP normal is estimated with an uncertainty of approximately 0.3°. The second step is to estimate the shower axis direction within the SDP. The angle psi (ψ) defines the shower axis direction within the SDP (see fig. 4.3). The shower axis direction is estimated using the time (time fitting) and the longitudinal profile information (PCGF). In the case of stereo events the shower axis is estimated by intercept of both SDPs. The uncertainty of the stereo reconstruction is around 0.5° and varies with the geometry of the shower. In addition to this classic stereo method, we can use time information from both sites to improve the robustness of the results. For this to be useful, it is required to have HiRes-1 and HiRes-2 clocks well synchronized (better than 100 ns). As mentioned a in previous chapter, at this stage, the HiRes-2 time is reaching stability. Most of the detected problems have been understood and fixed. As soon as HiRes-1 and HiRes-2 be well synchronized, the time information would be used for a more accurate stereo reconstruction.

Because of the small uncertainty of stereo reconstruction compared with monocular reconstruction, it will be assumed that the stereo reconstruction is the true geometry. Figure 6.2, top left hand plot, shows the energy distribution of the stereo data set, where the solid and dashed lines show the distribution before and after pass4a cuts. The dotted lines show events that passed pass4a cuts but their monocular reconstructed psi angles are more than 20° away from the stereo value. Figure 6.2, top right hand plot shows the stereo reconstructed psi angle (only events that passed pass4a cuts) against the monocular reconstructed one. The bottom plots in figure 6.2 show the viewed track length in kilometers (the "longitudinal track length") (left hand

plot) and the number of good tubes (right hand plot) against the monocular-stereo psi deviation. Here also there are only events that passed pass4a cuts.

Because of the small statistics of stereo events (353 events) at the moment, and because of the triggering bias in the stereo events, we can not be conclusive with the stereo-monocular comparison. However we can point out some interesting features. Those features can then be studied by analysing a larger MC data set of monocular events.

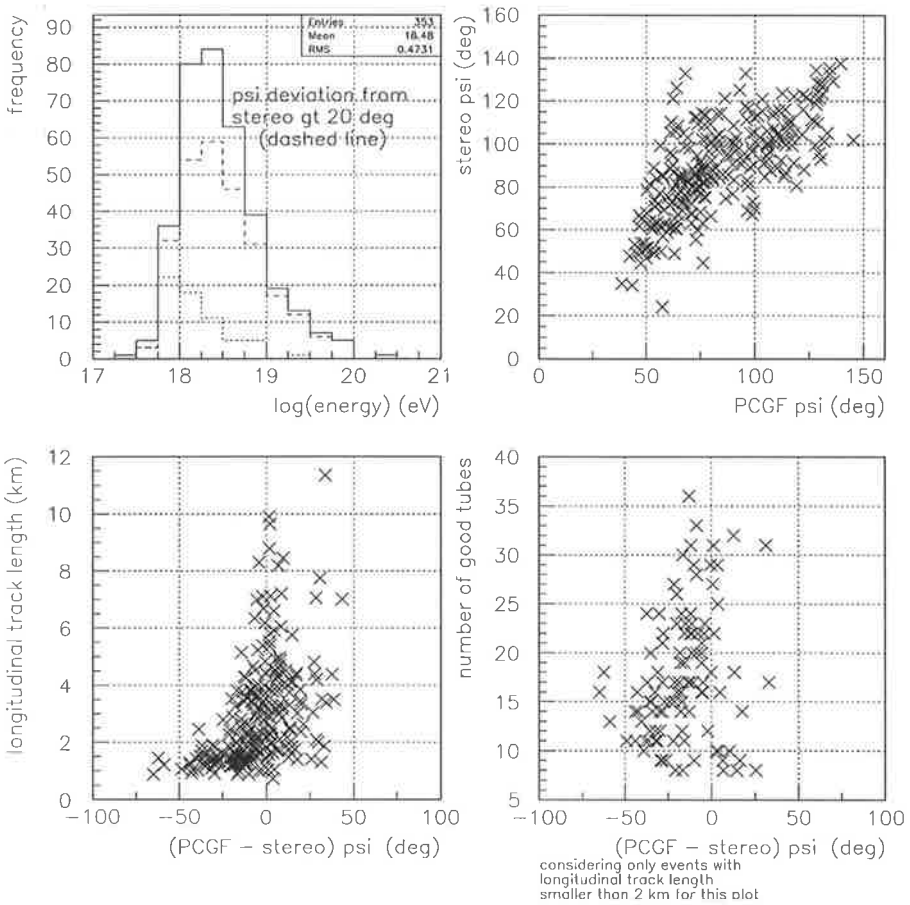

Figure 6.2: The top left plot shows the energy distribution of the stereo data set. Solid and dashed lines are before and after applying pass4a cuts. The dotted line represents the energy distribution of events where the monocular reconstructed psi angle deviates more than 20° from the stereo one. The top right plot shows the stereo reconstructed psi angle against the monocular reconstructed psi angle. The bottom plots show the longitudinal track length and the number of good tubes against the monocular-stereo psi deviation. The scatter plots are only considering events that passed pass4a cuts.

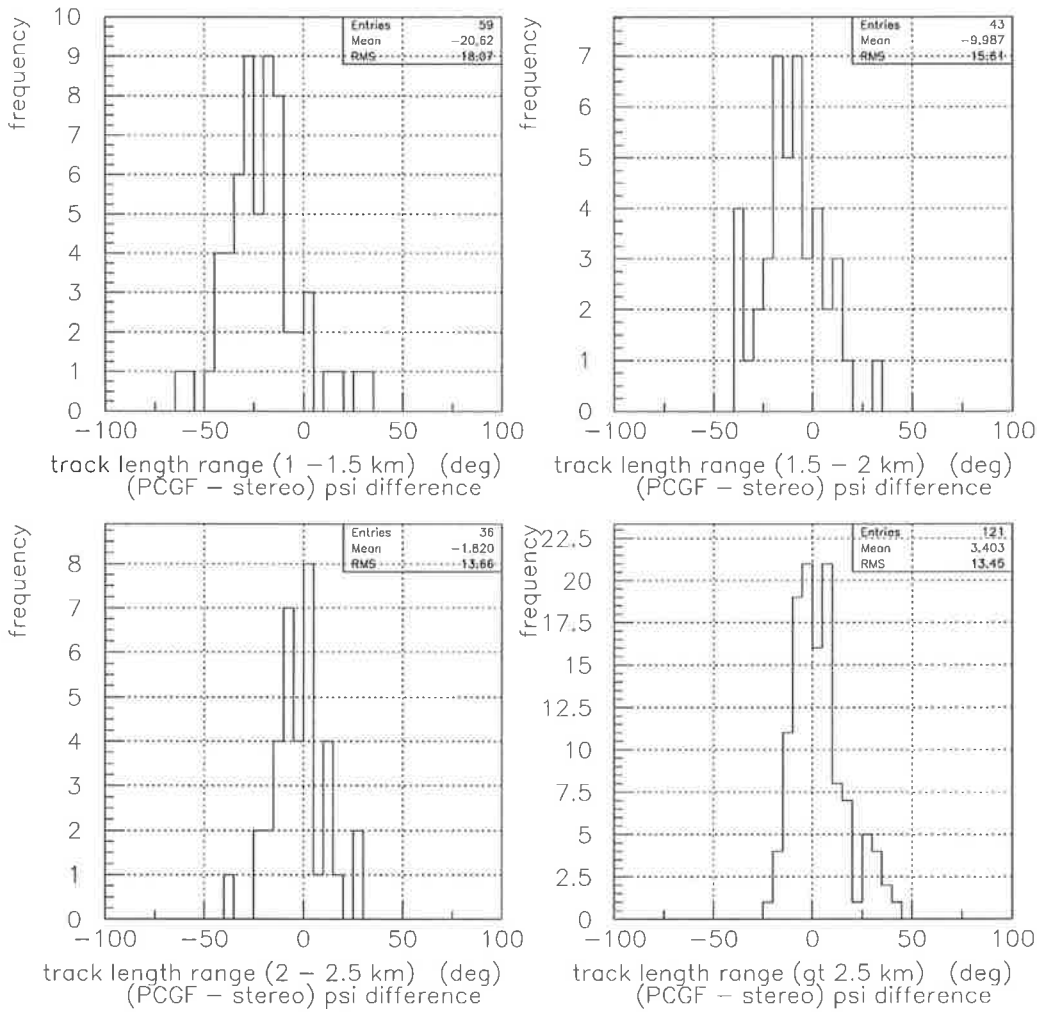

Figure 6.3: monocular - stereo psi deviation distributions for different longitudinal track length ranges (after pass4a cuts).

6.2.1 Interesting features

The monocular reconstruction appears to be shifting the psi angle to smaller values. Figure 6.3 shows the monocular-stereo psi deviation distributions for different longitudinal track length ranges. The shift is significant only when the longitudinal track

length is smaller than 2 km. However, when the number of tubes fired (good tubes) is bigger than approximately 20, the shift is smaller (figure 6.2 bottom right plot).

6.3 Monocular results against MC inputs

A Monte Carlo data set of 96268 monocular events (prot***.bigh22.a25sc10.new.ps4.dat) was used for this study. The input energy of the MC events starts from $10^{17.6}$ eV and follows an energy spectrum with differential index of 2.6 (the Fly's Eye estimated spectral index for protons).

It was noticed that before applying pass4 cuts (pass4 is a step of the HiRes reconstruction process), that the MC psi angle distribution (figure 6.4 solid line distributions) was not consistent with the real monocular data psi distribution (figure 6.1 bottom right plot). However after applying a subset of the pass4 cuts described below (pass4a cuts), the MC and real data psi distribution are consistent (see dashed distributions in figure 6.4). The stereo psi distribution is shown as a reference in figure 6.4 (top plots). The reason for having a different MC psi distribution is not clear. However, it could be related with the Cerenkov light simulation, because the MC data (before applying pass4a cuts) has an excess of events with large psi angles with large core distances (20 to 40 km) that in reality do not trigger the detector. Some of the pass4 cuts (pass4a cuts) have been applied *a priori*. We cut an event if it satisfies any of the following conditions:

1. Events with at least 2 bins with more than 25% of direct Cerenkov light.

2. Events with an average correction factor [2] per bin lower than 0.55 m^2.

3. Events with the depth of first observed bin greater than 1000 g/cm^2.

[2]The correction factor is a measure of the light collection efficiency in terms of effective area. The effective area of a HiRes mirror (considering effects such as the shadow of the cluster, the non-reflecting area of the mirror, edges of the mirror pieces and cracks between tubes) is approximately 2.2 m^2. The shower track is divided into 1° bins. Each bin may involve more than one PMT. Therefore each PMT can be thought of as having a specific effective area (a correction factor) for a particular shower. The sum of the effective areas of the PMTs involved in a bin is in most cases approximately 2.2 m^2.

4. Events with reconstructed energy lower than 1 eV. Some events that experimented problems in the reconstruction process have energies below 1 eV.

These cuts have shown correlation with poorly reconstructed events, except for the cut to events with a high level of direct Cerenkov light contamination. However, this cut was applied for two reasons - to avoid any problem that could be introduced by a different MC psi distribution (this cut eliminates most of the events with psi angles greater than 120°) and because we are not sure about the energy resolution of events with high Cerenkov light contamination.

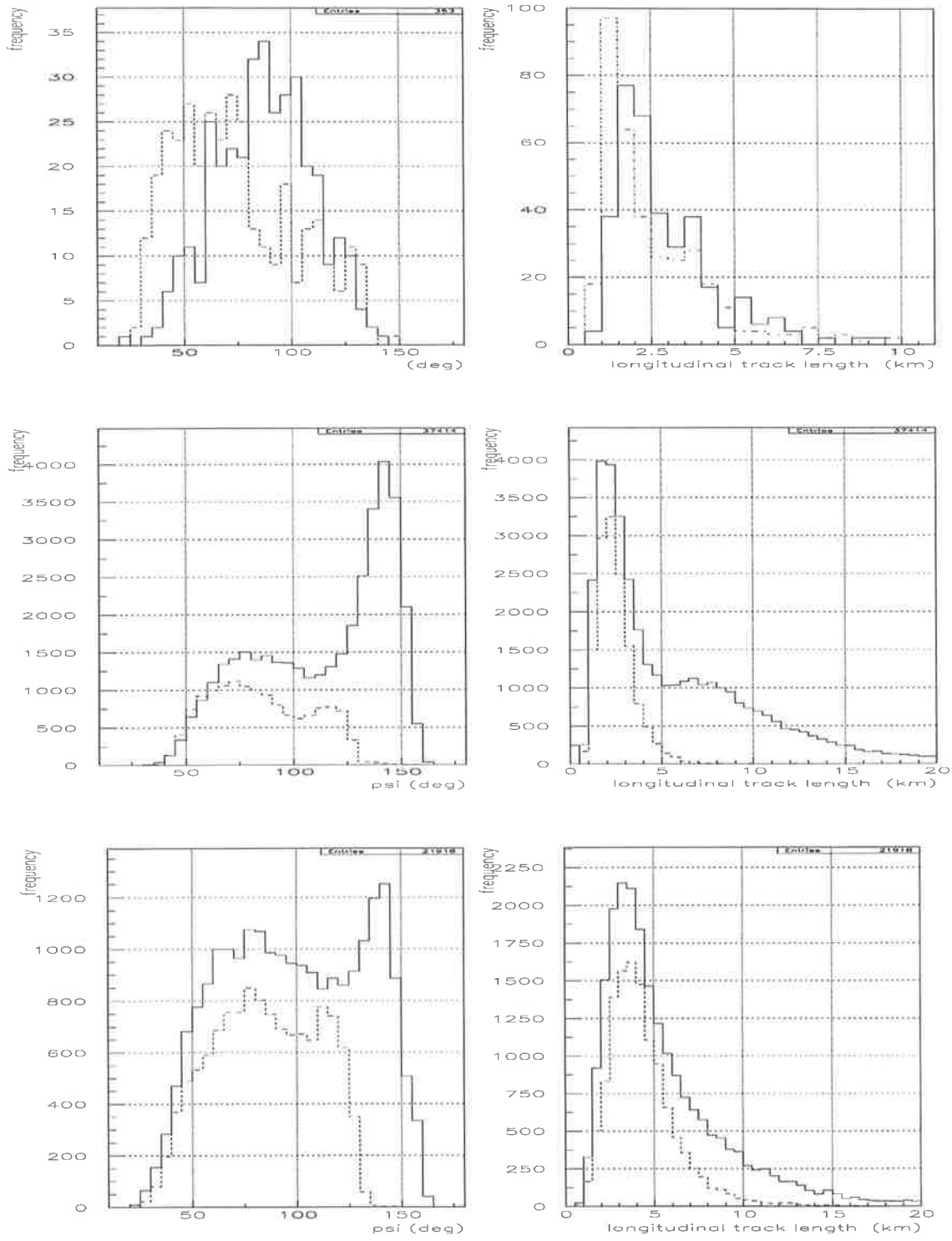

Figure 6.4: Psi angle (left plots) and longitudinal track length (right plots) distributions. Solid lines refer to stereo (top plots) and MC input values (middle and bottom plots) geometries and the dashed lines to the monocular reconstructed geometries. Middle plots are for reconstructed energies between 10^{18} and $10^{18.5}$ eV. Bottom plots are for reconstructed energies $> 10^{18.5}$eV (pass4a cuts have been applied to the monocular reconstructed distributions).

Figures 6.5 (10^{18} eV < reconstructed energies < $10^{18.5}$ eV) and 6.6 (reconstructed energies > $10^{18.5}$ eV) show the reconstructed energy distribution, the MC psi angle against the PCGF psi angle, the longitudinal track length and the number of good tubes against the PCGF-MC psi angle deviation. At this stage we have applied the pass4a cuts.

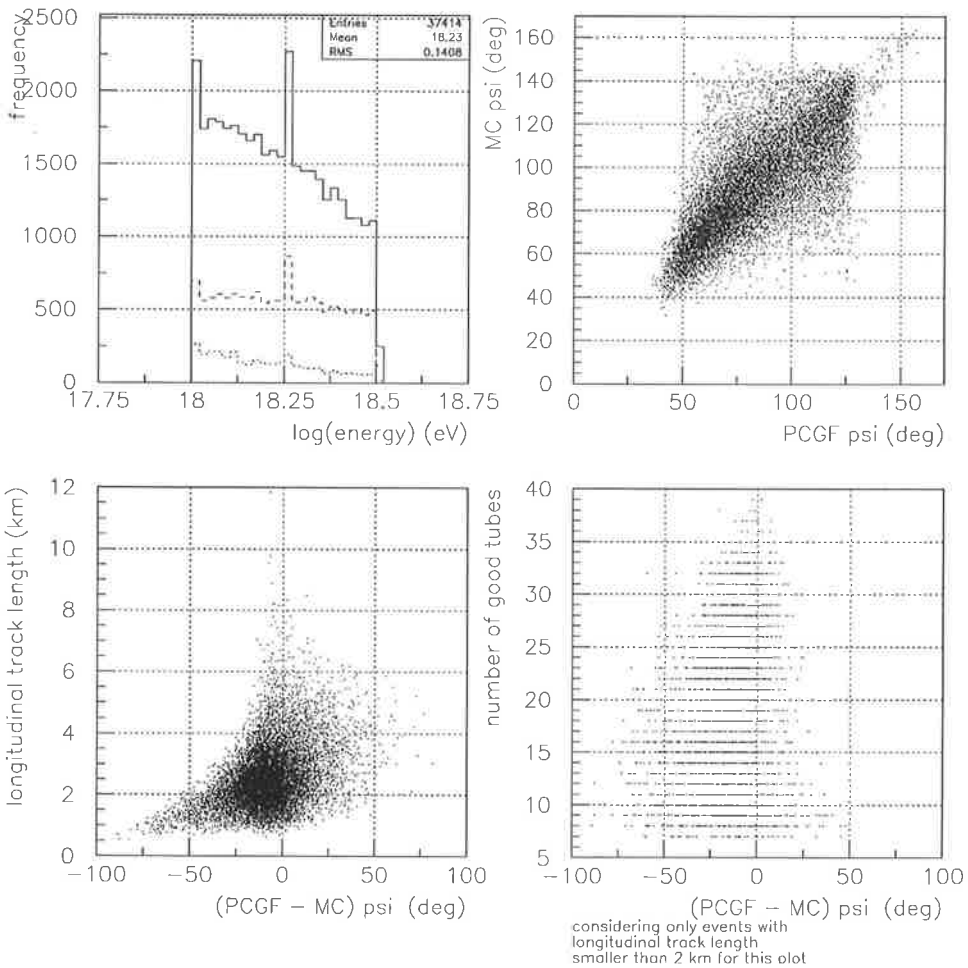

Figure 6.5: The top left plot shows the reconstructed energy distribution of the MC data set before (solid line) and after (dashed line) applying pass4a cuts. The dotted line represents the energy distribution of events where the monocular reconstructed psi angle deviates more than 20° from the MC psi angle. The top right plot shows the MC psi angle against the monocular estimated psi angle. The bottom plots show longitudinal track length and the number of good tubes against the PCGF-MC psi deviation. Scatter plots are after pass4a cuts.

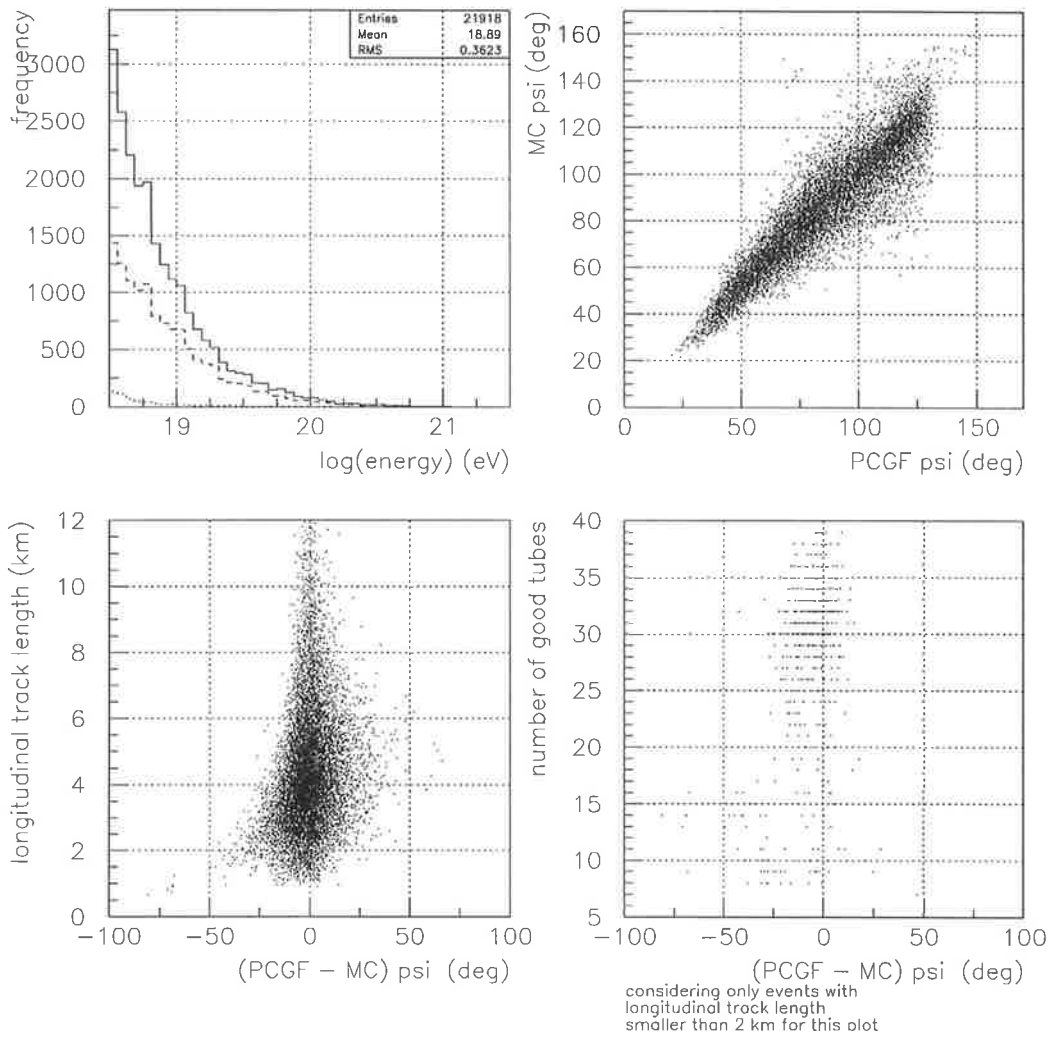

Figure 6.6: Same as figure 6.5 but for events with reconstructed energies $> 10^{18.5}$ eV.

The angular track length was a variable traditionally used to identify events with bad monocular geometrical reconstruction. This was the case when pure timing information was used in the fitting process. Figure 6.7 shows the angular track length against the psi angle deviation. Notice that the angular track length is not as well correlated with the psi angle deviation as is the longitudinal track length (bottom left plot in figures 6.5 and 6.6). This is probably due to the influence of the profile fitting, where seeing a larger part of the shower development profile is a real advantage.

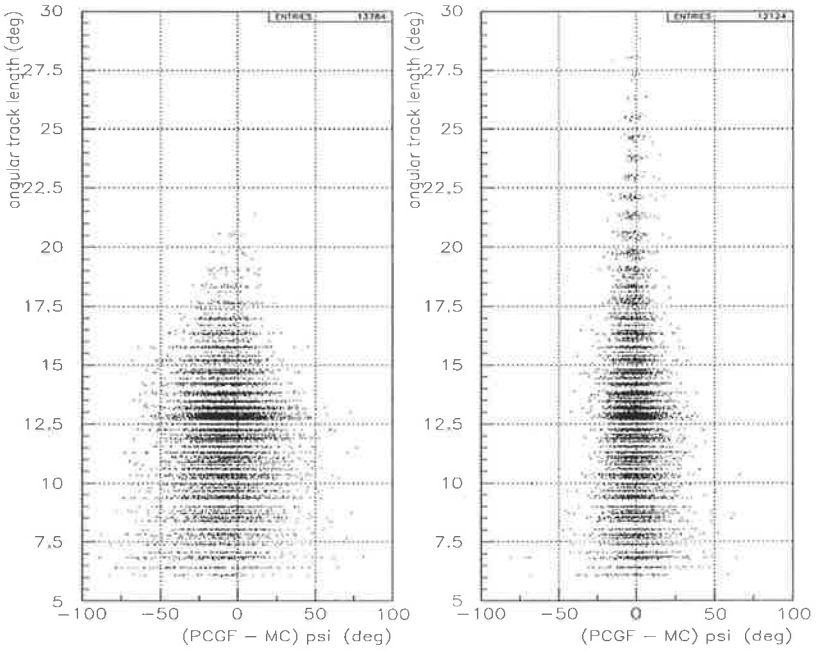

Figure 6.7: Angular track length against the monocular - MC psi deviation. Left hand plot is for reconstructed energies lower than $10^{18.5}$ eV and the right hand plot is for energies greater than $10^{18.5}$ eV. Only events that passed the pass4a cuts are shown.

The features pointed out in section 6.2.1 from the monocular-stereo comparison are also present here (figure 6.5 and figure 6.6). This agreement gives us certain confidence in using MC and stereo events for studying the PCGF reconstruction technique. Figures 6.8 (10^{18} eV < reconstructed energies < $10^{18.5}$eV) and 6.9 (reconstructed energies > $10^{18.5}$eV) show the monocular-MC psi angle deviation for different longitudinal track length ranges.

From the monocular-MC comparisons, we note that the monocular reconstructed psi angle is only systematic shifted to smaller values when the the reconstructed energy is smaller than $10^{18.5}$ eV (figure 6.8).

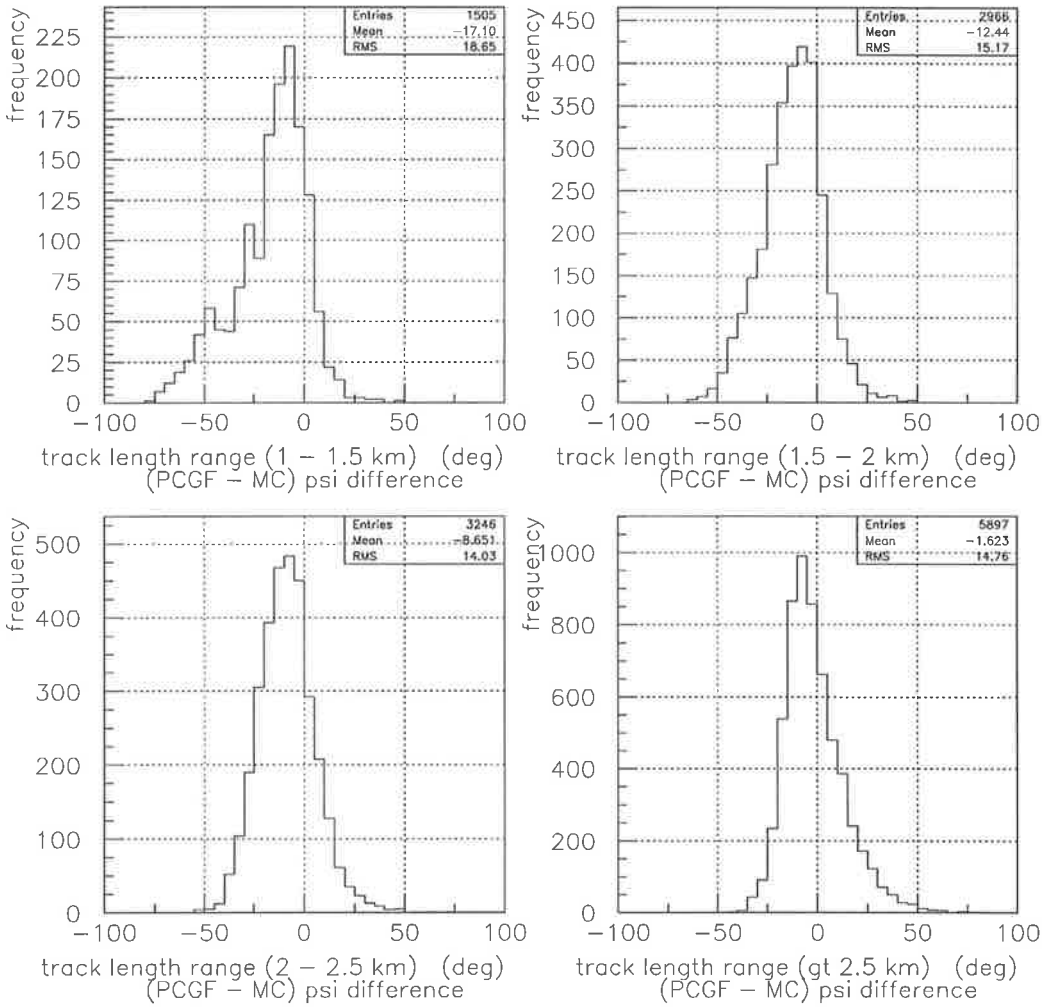

Figure 6.8: monocular - MC psi deviation distributions for different longitudinal track length ranges (10^{18} eV < reconstructed energies < $10^{18.5}$eV) after applying pass4a cuts.

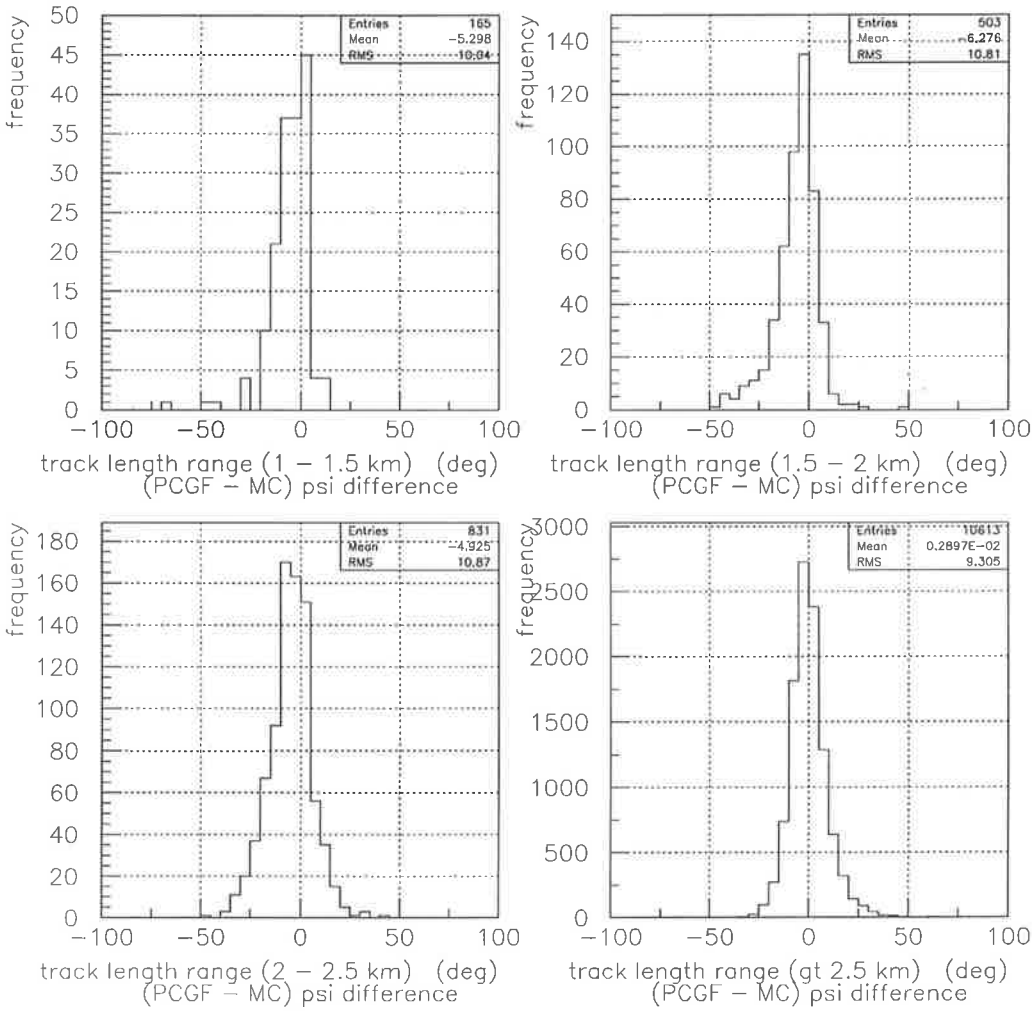

Figure 6.9: monocular - MC psi deviation distributions for different longitudinal track length ranges (reconstructed energies $> 10^{18.5}$eV) after applying pass4a cuts.

6.4 Quality cuts

In this section the possibility of using parameters from the profile and time fitting for quality cuts is studied. The minimum χ^2 value of a fit is the usual parameter used for applying quality cuts. The minimum χ^2 should tells us the uncertainty level of the fitted parameters. For a larger minimum χ^2 the uncertainties are generally larger. Figure 6.10 shows the time and profile χ^2 against the monocular-stereo psi deviation, and figures 6.11 and 6.12 against the monocular-MC psi deviation for two different energy ranges (pass4a cuts were applied).

From figures 6.10, 6.11 and 6.12 we notice that the estimated minimum χ^2 (time and profile fit) values are not correlated with the psi angle uncertainty. A number of events with estimated psi angles that deviate more than 20 degrees from the true values have small χ^2 values (left plots on figures 6.11 and 6.12). Also a number of the events that deviate less than 20 degrees have very large χ^2 values (right plots on figures 6.10, 6.11 and 6.12).

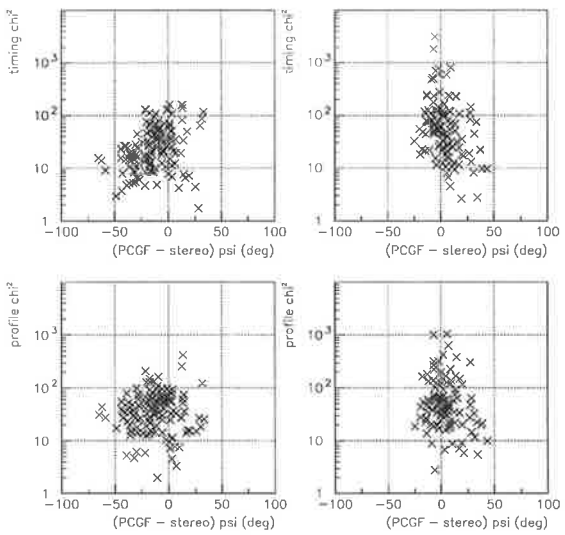

Figure 6.10: Estimated minimum χ^2 for time (top plots) and profile fitting (bottom plots) against the **monocular-stereo** psi angle deviation. The left plots only consider events with longitudinal track lengths shorter than 2.5 km and the right plots only longer than 2.5 km (after pass4a cuts).

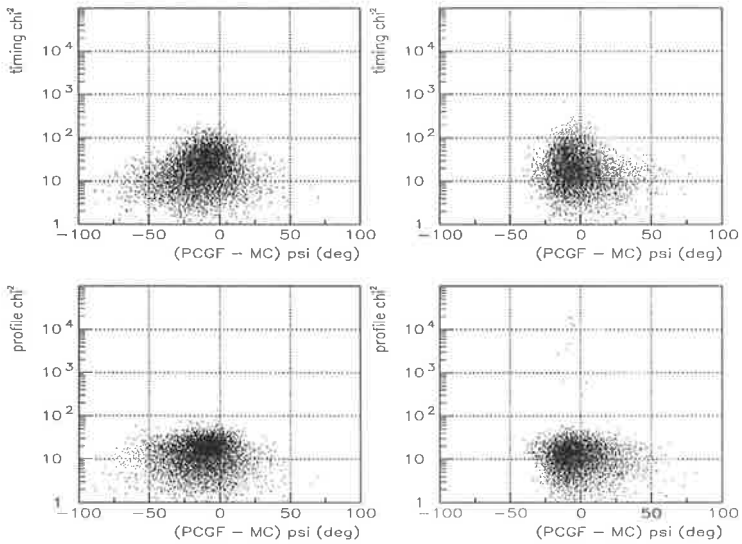

Figure 6.11: Estimated minimum χ^2 for time (top plots) and profile fitting (bottom plots) against the **monocular-MC** psi angle deviation. The left plots only consider events with longitudinal track lengths shorter than 2.5 km and the right plots only longer than 2.5 km (10^{18} eV < reconstructed energies < $10^{18.5}$eV) (after pass4a cuts).

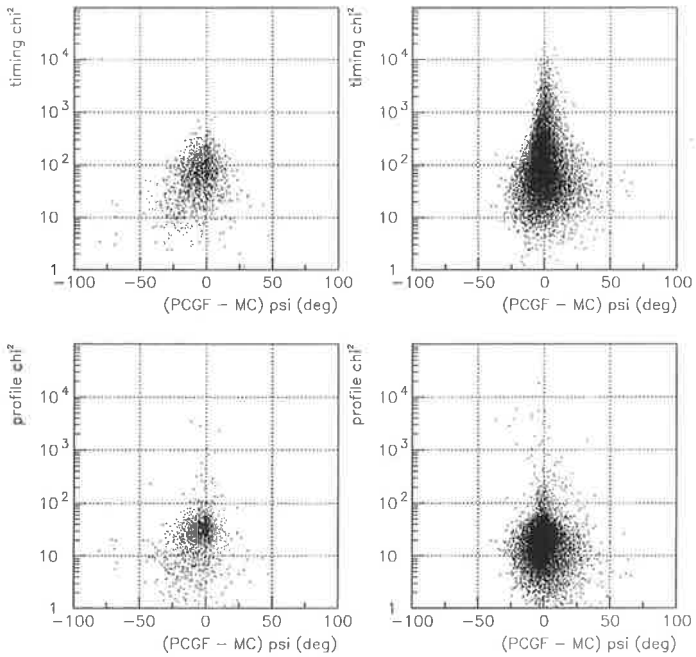

Figure 6.12: Estimated minimum χ^2 for time (top plots) and profile fitting (bottom plots) against the **monocular-MC** psi angle deviation (after pass4a cuts). The left plots only consider events with longitudinal track lengths shorter than 2.5 km and the right plots only longer than 2.5 km (reconstructed energies > $10^{18.5}$eV).

6.5 Estimated uncertainty in psi

The PCGF estimates the uncertainty in the reconstructed psi. A left (lpsi) and a right (rpsi) uncertainty is given for every estimated psi (mpsi). It is desirable that these uncertainties be correlated with the monocular-stereo and monocular-MC deviations. Figure 6.13 (monocular-stereo) and figures 6.14 and 6.15 (monocular-MC) do not show deviations correlated with the estimated left and right uncertainties.

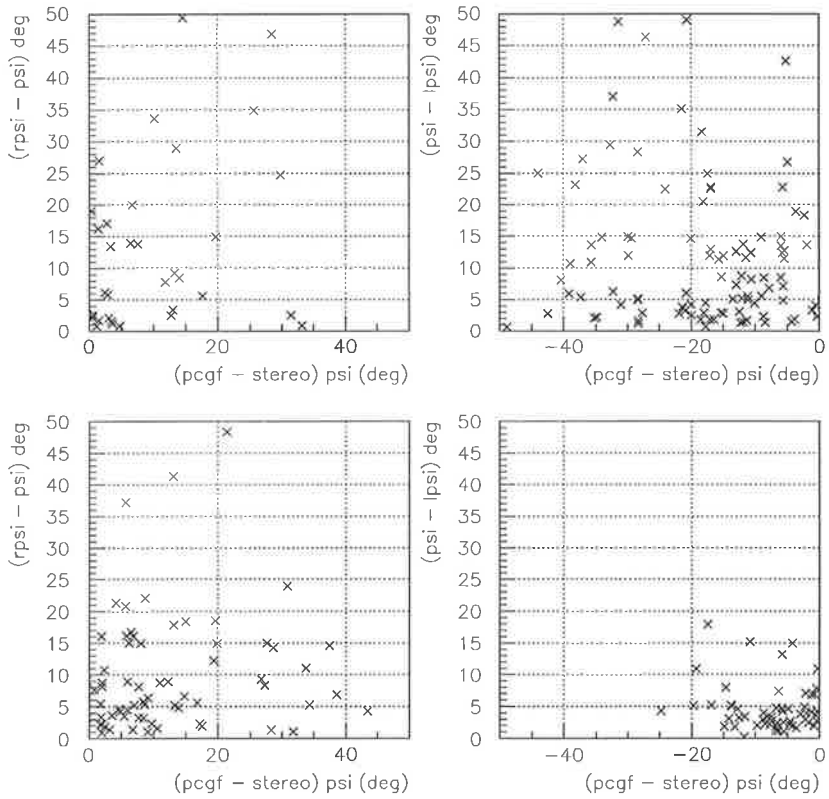

Figure 6.13: The figure shows the estimated right (left plots) and left (right plots) psi angle uncertainty against the **monocular-stereo** psi angle deviation. The top plots only consider events with longitudinal track lengths shorter than 2.5 km and the bottom plots longer than 2.5 km (after pass4a cuts).

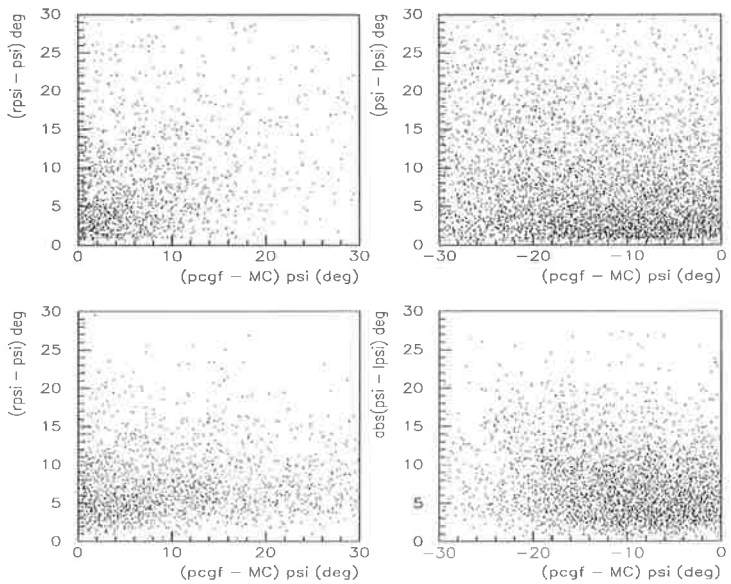

Figure 6.14: The figure shows the estimated right (left plots) and left (right plots) psi angle uncertainty against the **monocular-mc** psi angle deviation (after pass4a cuts). The top plots only consider events with longitudinal track lengths shorter than 2.5 km and the bottom plots longer than 2.5 km (10^{18} **eV** < **reconstructed energies** < $10^{18.5}$ **eV**).

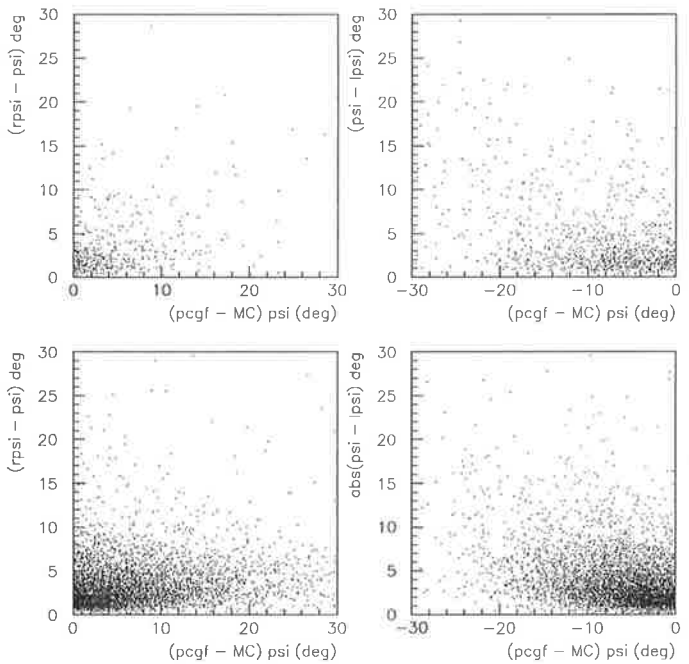

Figure 6.15: The figure shows the estimated right (left plots) and left (right plots) psi angle uncertainty against the **monocular-mc** psi angle deviation (after pass4a cuts). The top plots only consider events with longitudinal track lengths shorter than 2.5 km and the bottom plots longer than 2.5 km (**reconstructed energies** > $10^{18.5}$ **eV**).

6.5.1 Quality code

Some of the variables already seen in previous sections could help us to identify events with poor geometrical reconstruction even after the application of pass4a cuts. These variables are rpsi, lpsi (figures 6.13, 6.14 and 6.15), longitudinal track length, time and profile χ^2 (figures 6.10, 6.11 and 6.12) and the number of good tubes fired. We will impose some conditions on these variables. If the event does not satisfy any of the conditions it will be considered a bad quality event.

1. The value $abs(rpsi - mpsi)$ should be smaller than 40° (**code=3**).
2. The value $abs(lpsi - mpsi)$ should be smaller than 40° (**code=5**).
3. The longitudinal track length should be longer than 1 km (**code=1000**).
4. The profile χ^2 should be smaller than 1000 when the longitudinal track length is shorter than 2.5 km (**code=20**).
5. The number of good tubes fired should be greater than 25 when the longitudinal track length is shorter than 2 km (**code=100**).
6. The number of good tubes fired should be greater than 20 when the longitudinal track length is between 2 and 2.5 km (**code=200**).

We assigned a code to each condition. A given event may fail more than one condition and the respective codes will be added. We call this final number the quality code number. The codes are chosen in such a way that it should be easy to see which of the conditions failed by looking at the quality code number. Events that satisfied all the conditions will have a quality code equal to zero. Figures 6.16, 6.18 and 6.20 show the events that failed any of the good quality conditions, and the resultant quality code against the psi angle deviation. From these figures we see that some conditions or combination of conditions are selecting the very poorly reconstructed events (5,8,20,23,25,120,123,203,220, and quality codes above 1000) and others are selecting events with a broader psi angle deviation distribution (3,20,100,103,200 and

quality code 1000). Given that most poorly reconstructed events have quality codes of 100 or 200 we will only plot error histograms for these codes. Figures 6.17, 6.19 and 6.21 show the psi angle deviation distribution for events with these codes.

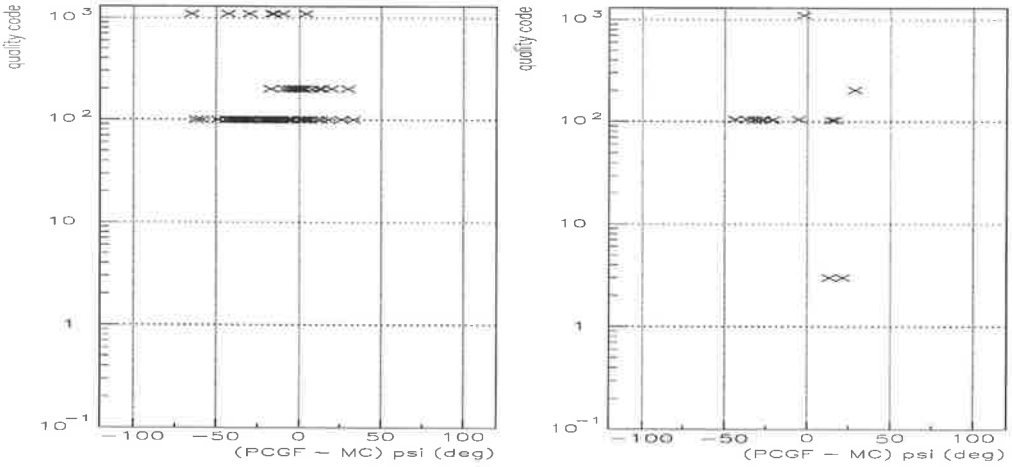

Figure 6.16: Scatter plot of the quality code number against the (**monocular - stereo**) psi deviation (after pass4a cuts). In the left plot are quality code numbers ending in zero (20, 100,120, 200, 220, 1000, 1100 and 1120). In the right plot are quality code numbers not ending in zero (3, 5, 8, 23, 25, 103, 105, 123, 203, 1003 and 1103).

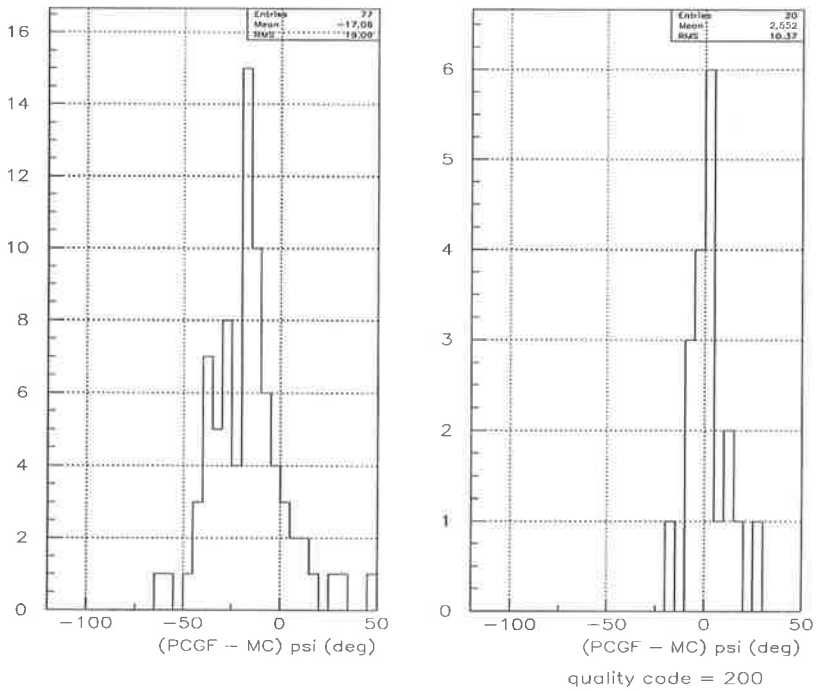

Figure 6.17: (**monocular - stereo**) psi distribution for events with quality code equal to 100 (left plot) and 200 (right plot).

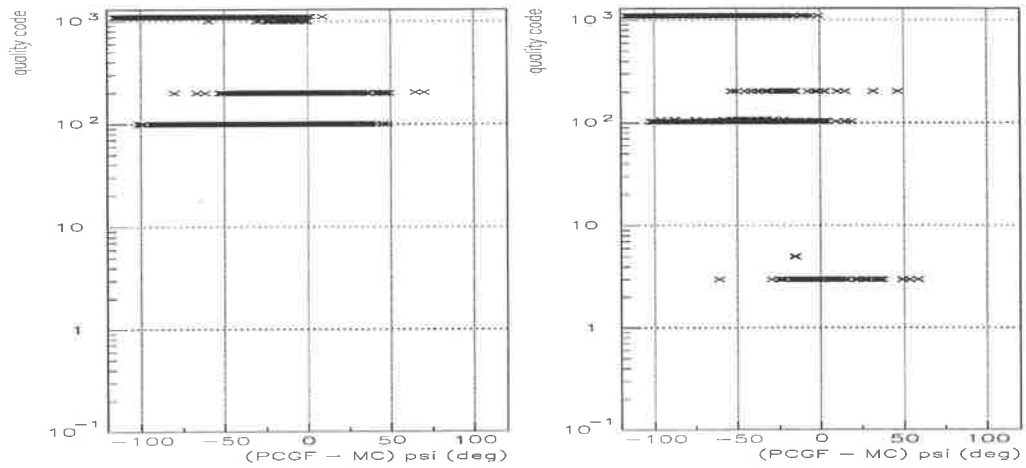

Figure 6.18: Scatter plot of the quality code number against the (**monocular - MC**) psi deviation (after pass4a cuts). In the left plot are quality code numbers ending in zero (20, 100,120, 200, 220, 1000, 1100 and 1120). In the right plot are quality code numbers not ending in zero (3, 5, 8, 23, 25, 103, 105, 123, 203, 1003 and 1103). Reconstructed energies between 10^{18} and $10^{18.5}$ eV.

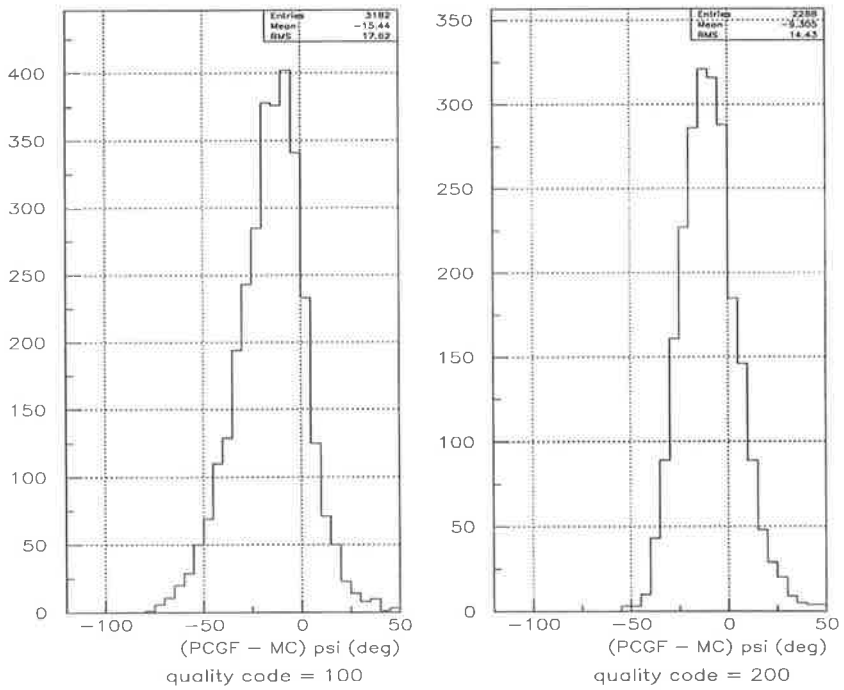

Figure 6.19: (**monocular - MC**) psi distribution for events with quality code equal to 100 and 200 (10^{18} eV < energies < $10^{18.5}$eV).

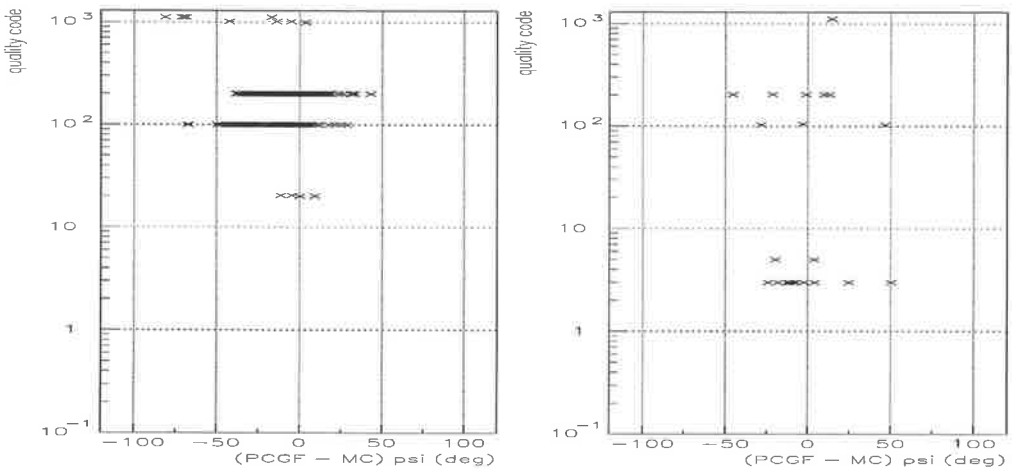

Figure 6.20: Scatter plot of the quality code number against the (**monocular - MC**) psi deviation (after pass4a cuts). In the left plot are quality code numbers ending in zero (20, 100,120, 200, 220, 1000, 1100 and 1120). In the right plot are quality code numbers not ending in zero (3, 5, 8, 23, 25, 103, 105, 123, 203, 1003 and 1103). Reconstructed energies greater than $10^{18.5}$ eV

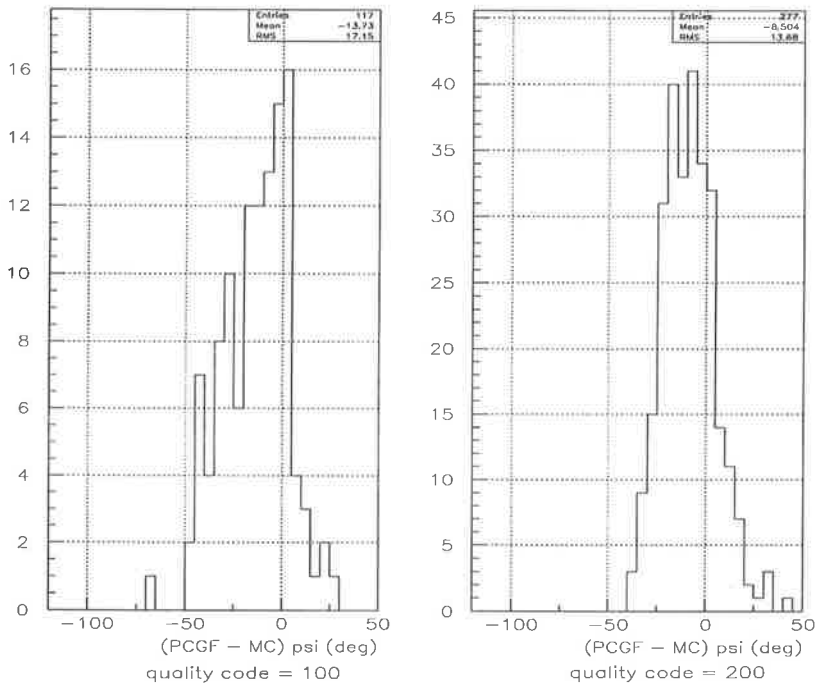

Figure 6.21: (**monocular - MC**) psi distribution for events with quality code equal to 100 (left histogram) and 200 (right histogram) (energies> $10^{18.5}$eV).

Figure 6.16 shows the estimated quality code number of the events against the psi angle deviation for the stereo data set. Figure 6.16 shows the same features as figures 6.18 and 6.20 (MC data set), except for events with quality code 200. In the MC data set, events with quality code 200 (figure 6.19 and figure 6.21) have the reconstructed psi angle distribution shifted to the left by approximately 9 degrees with broad distributions. The stereo data set (figure 6.17) shows a centered psi error distribution which is narrower. The reason for this difference is not clear, perhaps it is because of the bias in the stereo data set. Events detected in stereo may have favorable features for monocular reconstruction.

6.6 Good quality events

In this section I will show how the good quality conditions help to improve the angular resolution of the data set. Figures 6.22, 6.23 and 6.24 show the stereo and MC psi deviation distributions for different longitudinal track length ranges and different energy ranges. For these plots we are only considering events that passed pass4a cuts and have a quality code equal to zero. Compare these figures with figures 6.3, 6.8 and 6.9 respectively (before applying quality cuts). Note that the psi uncertainty (RMS of the distribution) has decreased after applying the quality cuts. Figure 6.25 shows the reconstructed energies against the stereo and MC psi deviation before and after applying the quality cuts.

Figure 6.26 shows the energy distribution of the real monocular data. The total number of monocular events analysed is 9890, as a result, 5827 events passed pass4a cuts (solid line figure 6.26) , 5014 events passed pass4a cuts and have quality codes equal to 0, 100, or 200 (dashed line figure 6.26), and 2345 events passed pass4a cuts and have quality codes equal to 0 (dotted line figure 6.26).

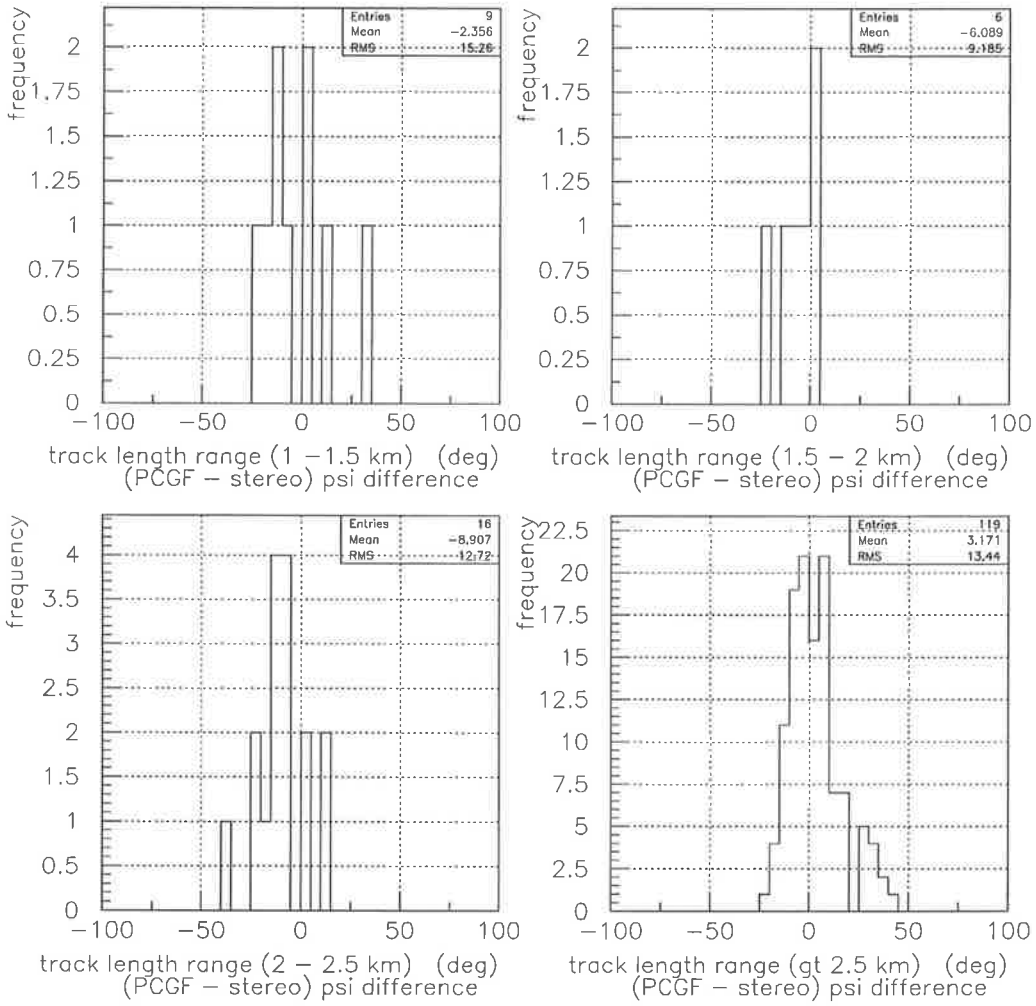

Figure 6.22: **(monocular - stereo)** psi deviation distributions for different longitudinal track length ranges after applying pass4a and quality cuts .

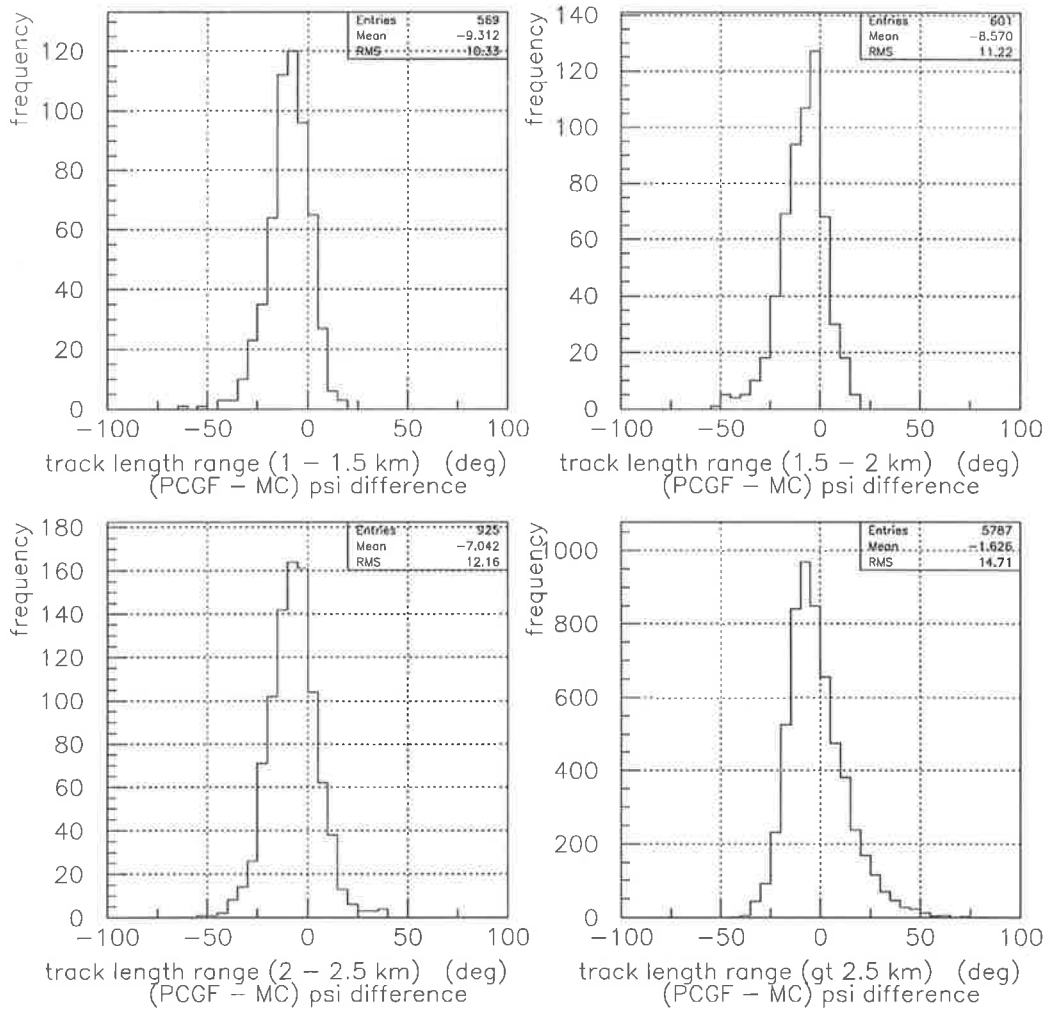

Figure 6.23: **(monocular - MC)** psi deviation distributions for different longitudinal track length ranges after applying pass4a and quality cuts (10^{18} eV < energies < $10^{18.5}$eV).

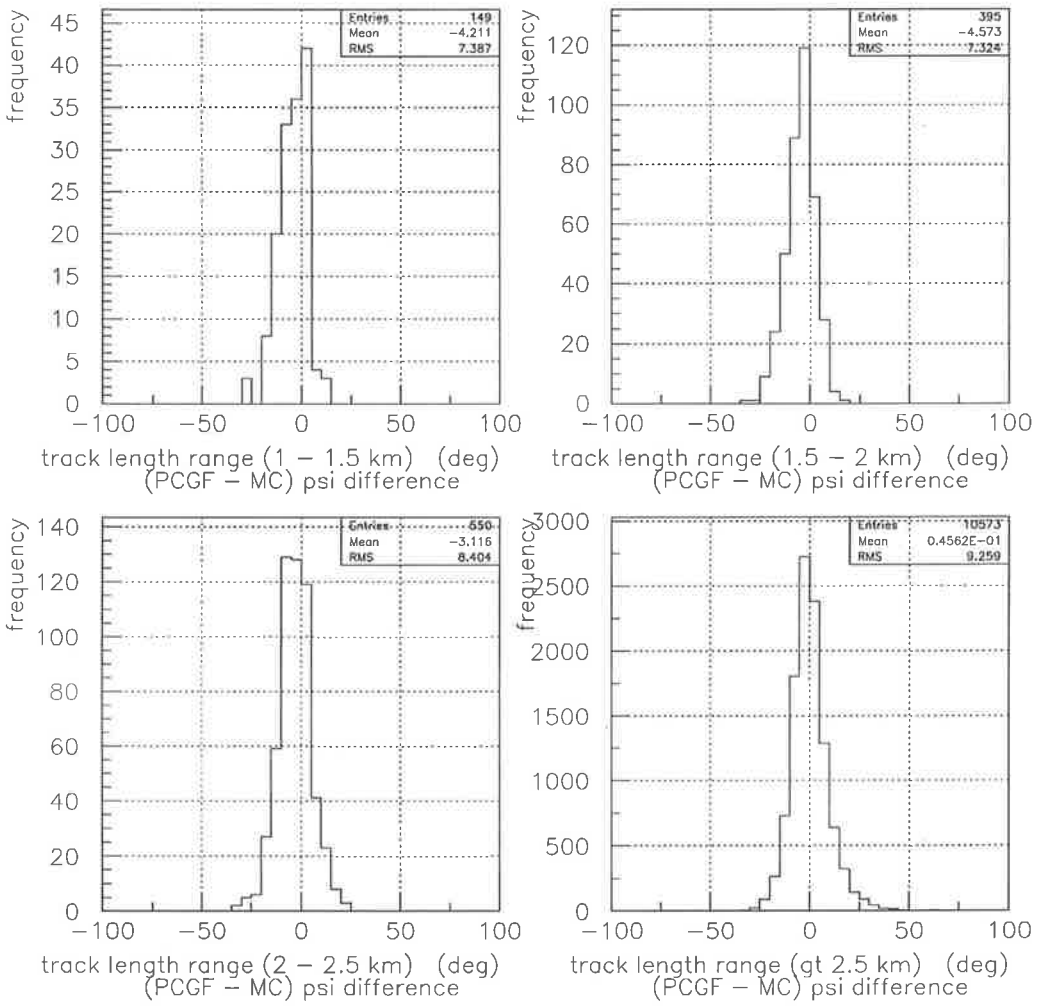

Figure 6.24: **(monocular - MC)** psi deviation distributions for different longitudinal track length ranges after applying pass4a and quality cuts (energies $> 10^{18.5}$eV).

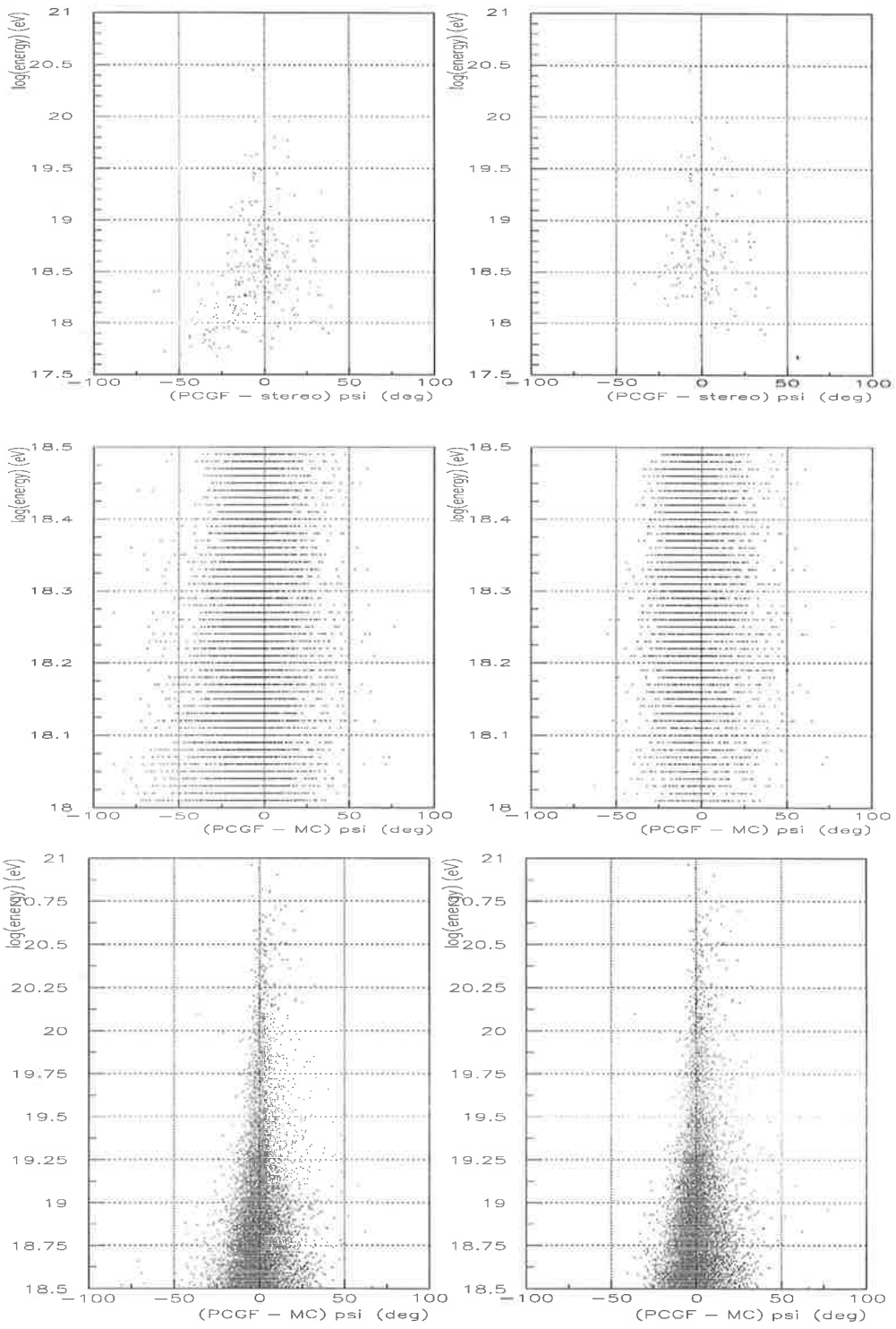

Figure 6.25: Scatter plot of the monocular reconstructed energy against the psi deviation from the true value. The top plots use real events and assume the stereo reconstructed geometry is the true value. The middle and bottom plots are using MC events with energies between 10^{18} - $10^{18.5}$ eV and energies above $10^{18.5}$ eV respectively. The left and right hand side plots are before and after applying all the quality cuts respectively.

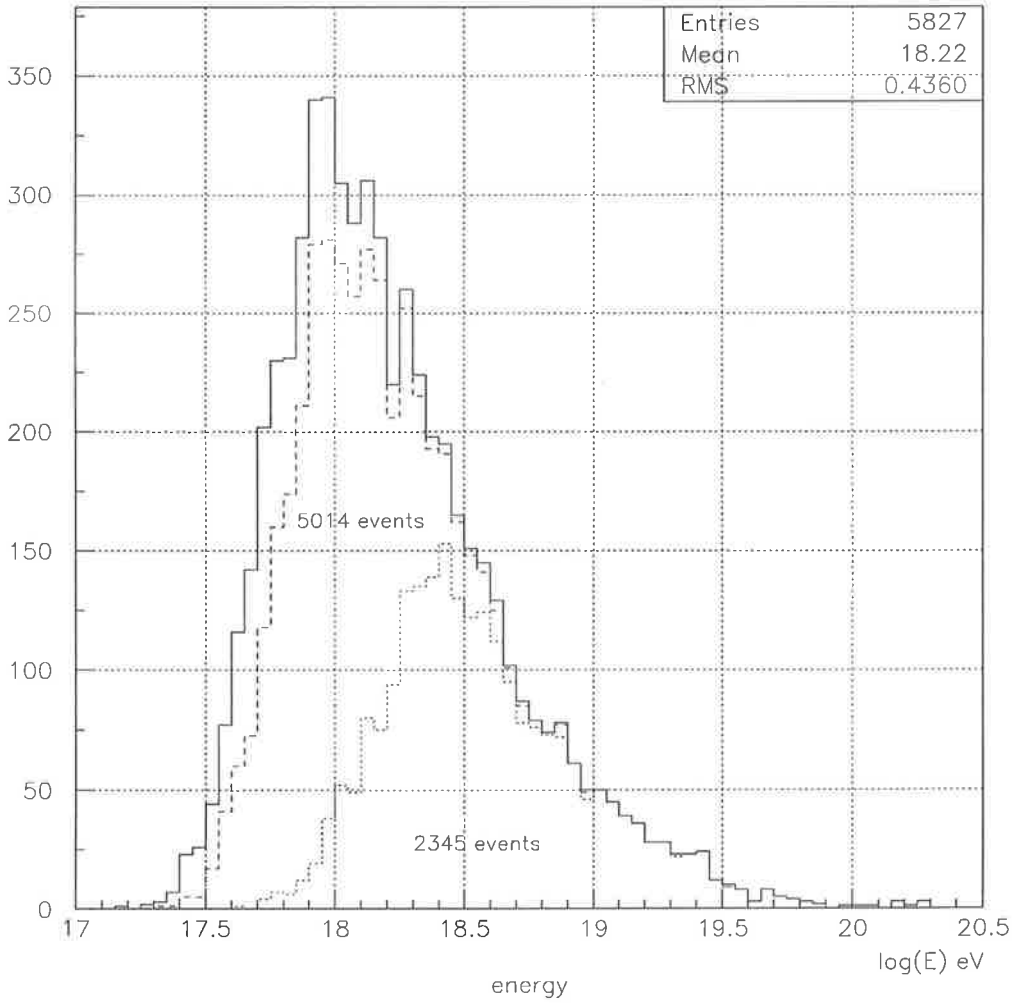

Figure 6.26: Energy distribution of real monocular data set. The solid line is for events that passed pass4a cuts. The dashed line is for events that passed pass4a cuts and have quality codes equal to 0, 100 or 200. The dotted line distribution is considering only events passing pass4a cuts with quality codes equal to 0.

6.7 Conclusions

In this chapter the HiRes-1 PCGF geometrical reconstruction was analyzed. For the anisotropy study purpose, it is necessary to know how accurately the arrival directions are estimated, and also whether the estimated psi angle uncertainties are truly correlated with the deviations from the true values.

After comparing the monocular reconstruction results with the stereo results and with the MC parameters, we can enumerate the following conclusions.

1. Events with energies lower than $10^{18.5}$ eV present a systematic shift and a broad error distribution for the reconstructed psi angle (figure 6.23).

2. The estimated right and left uncertainties of psi are not correlated with the psi deviation observed from stereo and MC comparisons (figure 6.13, figure 6.14 and figure 6.15).

3. A combination of quality cuts based on the estimated left (lpsi) and right (rpsi) psi error, longitudinal track length, profile χ^2 and to the number of good tubes fired remove most of the events with poor geometrical reconstruction. These quality cuts reduce the width of the psi error distribution (figure 6.22, figure 6.23 and figure 6.24). However a systematic shift in psi is still present in low energy events.

We suggest a correction in psi for events with energies lower than $10^{18.5}$ eV. The corrections will be taken from the distributions of the MC psi deviation for different longitudinal track length ranges (figure 6.23). The suggested psi angle correction and uncertainty values are summarized in table 6.1.

In the table longer longitudinal track length events have been assigned a larger uncertainty in psi. This is only because more quality cuts were applied to shorter longitudinal track length events.

The majority of events that failed the quality cuts have quality codes equal to 100 and 200. The stereo and MC data in the energy range $10^{18} - 10^{18.5}$ eV have

Energy(eV)	longitudinal track length range(km)	psi angle correction(deg)	psi uncertainty (deg)
$E < 10^{18.5}$	1 - 1.5	7	12
	1.5 - 2	7	12
	2 - 2.5	7	12
	> 2.5	7	15
$E > 10^{18.5}$	1 - 1.5	0	7
	1.5 - 2	0	7
	2 - 2.5	0	8
	> 2.5	0	9

Table 6.1: Suggested psi angle corrections and uncertainties according to MC comparisons for events that successfully passed the suggested quality cuts.

quite consistent psi deviation distributions for events with quality codes equal to 100 (figure 6.17 and figure 6.19), both distributions are shifted by more than 15 degrees and the RMS of their distributions (psi uncertainty) are close (around 18 degrees). This suggests that we can apply a special correction to such events in order to include them for anisotropy studies. Despite the differences between the stereo and MC psi deviation distributions for events with quality codes equal to 200, we can also apply a special correction to these events, but this correction must have a larger psi uncertainty than the RMS of the distributions, because the mean values do not match with the stereo distributions (right plots in figures 6.17, 6.19 and figure 6.21). It is important to keep in mind that even though the psi uncertainty can be large for certain events, they can still be useful for monocular anisotropy studies because the uncertainty is only distributed along the SDP. The special corrections suggested for events with quality cuts 100 and 200 are in table 6.2.

Note that the psi angle corrections and uncertainties are a function of energy. This is well illustrated in figure 6.25 (bottom plots). For pure timing reconstruction (i.e. not using shower profile information) we would not expect a strong correlation between the quality of reconstruction and the event energy. Instead, we would expect a direct correlation with the event angular track length. However, in the PCGF method the profile gains importance, and the length of the track in g/cm^2 or kilometres, and the

curvature of the viewed shower profile, become relevant. A higher energy event is likely to fall further from the detector, so it will typically have a long track within the detector's field of view, and importantly it will probably have a shower profile with nice curvature. This assists the PCGF method to converge, and better reconstruction results.

Energy(eV)	quality code	psi angle correction(deg)	psi uncertainty (deg)
$E < 10^{18.5}$	100	15	18
	200	9	25
$E > 10^{18.5}$	100	10	18
	200	9	25

Table 6.2: Special psi angle corrections and uncertainties suggested for events with quality codes 100 and 200.

Chapter 7

HiRes stereo geometrical reconstruction

Fit_shower is a program that reconstructs the shower geometry of stereo events which was originally used with the HiRes prototype detector. The author adapted Fit_shower to work with the characteristics of the current stage of the HiRes detector. In addition, some changes were made in order to better represent the uncertainty region around the reconstructed arrival directions. Fit_shower1 is the name of the new version of Fit_shower.

In this chapter the methods available in Fit_shower1 to reconstruct the geometry of the air shower axis are described. Here is also described the technique used to estimate the uncertainty associated with the reconstruction process. Vertical flashers and Monte Carlo data were used to check the reconstructed results and the estimated uncertainties.

When we have stereo data there are two methods to determine the geometry of the air shower axis, the stereo and the hybrid method.

The stereo method does not use time information of the fired tubes. This method reconstructs the shower detector planes (SDP) related to each site. Then the intersection of both SDPs will determine the air shower axis.

The good angular resolution of HiRes allows for the determination of the SDP

normal with less than 0.5° of uncertainty and therefore the reconstructed shower axis is determined with an approximately similar uncertainty . However when the opening angle is smaller than approximately 10 degrees, the uncertainty of the reconstructed shower axis increases as the opening angle gets smaller. For opening angles smaller than 3 degrees, the uncertainty of the reconstructed shower axis is about 15 degrees (see fig. 7.4).

The hybrid method uses the SDP information, plus time information of the fired PMTs. In principle, a hybrid reconstruction should be more accurate than the stereo method. However small imprecisions in the timing may increase the uncertainty of the hybrid reconstruction. In order to get the best results from the hybrid reconstruction, it is desirable to have the clocks at both sites (HiRes-1 and HiRes-2) well synchronized within 100 ns. To reach this synchronization level, it is necessary to correct any systematic time shifts that could be present as a result of the electronics and cabling. It is also desirable to have FADC systems for recording the time development of the signal pulse at each PMT. The FADC system determines with good precision (less than 100 ns) the time when the PMT recorded the peak of the pulse.

Unfortunately only the HiRes-2 site uses a FADC system. HiRes-1 uses S/H electronics and the time of the peak of the pulse is determined with a larger uncertainty due to the time slewing effect. The time slewing error is related to the amplitude and width of the pulse. Tests using laser shots (equipped with GPSY clocks) showed that the time slewing at HiRes-1 introduced a time offset of about 1 μs when comparing the 'true - estimated' laser firing time distributions from different laser geometries (fig. 7.3). Different laser geometries produce different pulse shapes because of different orientation with respect to the detector. Thus, we have different magnitudes for the slewing effect.

In order to minimize the effect of the HiRes-1 time slewing, we used a hybrid geometry reconstruction technique which does not require a time synchronization between HiRes-1 and HiRes-2. This technique reduces considerably the arrival direction uncertainty for small opening angle events (compared with the stereo uncertainty) from

approximately 15° to 3° (fig. 7.4). However synchronized HiRes-1 and HiRes-2 clocks may reduce even more the uncertainty for small opening angle events.

7.1 Geometry reconstruction techniques

The geometry reconstruction techniques (stereo and hybrid) used in Fit_shower1 are described below. The very first step, common to both methods, is to estimate a "first guess" of the shower axis. So before describing the stereo and hybrid technique I will describe the processes followed to estimate a trial shower axis. This technique is also described in [100, 101].

7.1.1 First Guess:

- Using the fired tube pointing directions ($tb\_\hat{dirn}$) and the tube signals (integrated photoelectrons, tb_pho), the centroid vector is estimated (eq. 7.1).

$$c(k) = \frac{\sum_{i=0}^{i=N} tb\_dirn[k]_i * tb\_pho_i}{|\vec{c}|} \tag{7.1}$$

- The unit vector $\hat{h}$ perpendicular to the centroid and parallel to the horizontal (h(z)=0) is defined.

$$h(x) = c(y)/|\vec{h}| \; ; \quad h(y) = -c(x)/|\vec{h}| \; ; \quad h(z) = 0 \tag{7.2}$$

- The cross product between the centroid ($\hat{c}$) and the vector $\hat{h}$ will determine the vector $\hat{u}$ (eq. 7.3). Then the vectors $\hat{c}$, $\hat{h}$ and $\hat{u}$ will define an orthogonal basis.

$$\hat{u} = \hat{c} \times \hat{h} \tag{7.3}$$

- The projection of the tube directions into a plane defined by the vectors $\hat{h}$ and $\hat{u}$ is estimated (eq. 7.4). This plane is perpendicular to the centroid, $\hat{c}$.

$$\begin{aligned} xxx(i) &= tb\_\hat{dirn}_i \cdot \hat{h} \\ yyy(i) &= tb\_\hat{dirn}_i \cdot \hat{u} \end{aligned} \tag{7.4}$$

where $xxx(i)$ and $yyy(i)$ are the projected coordinates of tube 'i'.

- The projected points ($xxx(i)$ and $yyy(i)$) representing the triggered PMTs fall close to a straight line which passes near the centroid direction. A straight line can be fitted to these points. The projected points are weighted by their respective PMT amplitudes. The orientation of the fitted line can be expresed in terms of the unit vectors $\hat{h}$ and $\hat{u}$ (eq. 7.5).

$$\vec{r} = \hat{h} + slope * \hat{u}, \tag{7.5}$$

  the parameter 'slope' in equation 7.5 is obtained from the line fitting.

  In events where two or more mirrors were involved a parallax effect is introduced at this stage. This is because of the different physical location of the mirrors. The projection of the tube directions from different mirrors in the plane perpendicular to the centroid (note that the centroid is common for all mirrors involved) will fall near to slightly different straight lines. Then the fitted line will correspond to a line in between. This has stronger effects for nearby showers. This parallax effect shifted the estimated HiRes-2 SDP by 0.8° for a 2 Km distance vertical flasher (see fig. 5.29).

- The trial SDP normal vector direction is obtained from the vector product of $\vec{r}$ and $\hat{c}$ (eq. 7.6).

$$\hat{normal} = \frac{\vec{r} \times \hat{c}}{|\vec{r} \times \hat{c}|} \tag{7.6}$$

- The shower axis must be perpendicular to the HiRes-1 and HiRes-2 SDP normal vectors. Thus the vector product between both SDP normal vectors will define the trial shower axis direction.

7.1.2 Stereo geometry reconstruction

The idea of stereo reconstruction is to determine the SDP related to each site, then the interception of the planes will determine the shower axis. In Fit_shower1 there are

two methods to determine the SDPs, the amplitude weighted (aw) and the amplitude fitted (af) methods.

A different χ^2 function is built for each method. The best shower geometry is obtained by minimizing the χ^2 by varying 4 parameters (the zenith and azimuth angles of both SDP normal vectors). The χ^2 minimization is done using the Downhill Simplex Method (program amoeba from Numerical Recipes). Previously, the fitting parameters were the zenith and azimuth angles, and the core location of the shower. However using the zenith and azimuth of the SDP normal as fitting parameters, we can easily estimate the uncertainties in these parameters. The uncertainties in these parameters reproduce better the uncertainty region around the reconstructed shower axis.

- **Amplitude Weighted Method:**
  - The first guess for the shower axis is used to estimate the SDP for *each mirror*. This procedure takes into account the different locations of neighboring mirrors. In this way it fixes any parallax effect that may have been introduced when estimating the first guess.
  - The offset angle between each tube and the SDP of the tube's mirror is estimated. The offset angle of tube 'i' is given in equation 7.7.

$$offset\_angle_i = \hat{tb\_dirn_i} \cdot \hat{mir\_norm_i} \tag{7.7}$$

    where $\hat{mir\_norm_i}$ is the normal direction of the SDP for the mirror that holds the 'i' tube.
  - The amplitude weighted χ^2_{aw} function is built based on each tube offset angle. (eq. 7.8). Each tube contribution to the χ^2_{aw} is weighted with the tube signal (in photoelectrons) over the average tube signal of the site.

$$\chi^2_{aw} = \sum_{i=0}^{i=N} \frac{tb\_pho_i}{average\_signal} * \frac{(offset\_angle_i)^2}{sigma^2_{aw}} \tag{7.8}$$

    $sigma_{aw}$ is the expected error for the estimated tube offset. For HiRes, an appropriate error is taken to be 0.3°.

- **Amplitude Fitted Method:**

The PMT amplitudes have a dependence on the angular separation, p, of the PMT off the track. The amplitude is at a maximum value, α, for a PMT which is centred on the track and the amplitude distribution behaves approximately like a Gaussian distribution as a function of p [100, 102]. The value of α is determined based on the amplitudes of neighboring PMTs along the track, and assuming the PMT is at an angle p off the track (p is obtained using the trial geometry). Then, the amplitude of the PMT ($expect\_pe$) is predicted. The best geometry is obtained by minimizing χ^2_{af} (eq. 7.9).

$$\chi^2_{af} = \sum_{i=0}^{i=N} \frac{tb\_pho_i}{average\_signal} * \frac{(tb\_pho_i - expect\_pe_i)^2}{sigma^2_{af}} \tag{7.9}$$
$$sigma^2_{af} = tb\_pho + sky\_noise + (0.15 * expect\_pe)^2$$

where $sigma^2_{af}$ takes into account the Poisson fluctuations in the PMT amplitude ($\sqrt{tb\_pho_i}$), the sky noise fluctuation during the PMT integration ($sky\_noise = 40 photoelectrons^2$) and an arbitrary 15% error in the estimated amplitude. The magnitude of the last term is in order to have an average reduced χ^2_{af} equal to 1. This is a crucial requirement for calculating the uncertainties on the reconstructed parameters.

We define $st1$ and $st2$ as the HiRes-1 and HiRes-2 stereo χ^2 functions. They could be estimated using either the χ^2 expression for the 'aw' (eq. 7.8) or 'af' (eq. 7.9) technique. The minimization process can be done by minimizing $st1 + st2$ together, or by minimizing independently $st1$ and then $st2$. It was noticed that sometimes minimizing $st1 + st2$ does not remove efficiently the SDP shifts introduced by the parallax effect. However when independently minimizing independently $st1$ and then $st2$ we find that the SDP shifts were corrected. So, Fit_shower1 minimizes $st1$ first and then $st2$.

7.1.3 Hybrid geometry reconstruction

The best results of the hybrid method are obtained when the intersite time is synchronized to better than 100 ns. However, despite having both sites well synchronized, the time slewing effect can introduce an apparent intersite time offset which may affect the results.

Time slewing is not a problem at HiRes-2 since it uses a FADC system to record the pulse of the PMTs. However HiRes-1 may have time slewing problems.

7.1.3.1 Time slewing

We use vertical flashers and lasers equipped with GPSY clocks[1] to measure the range of the PMT trigger time variations. Figure 5.26 shows the location of HiRes-1, HiRes-2 and the vertical flashers. This section should be a complement of an earlier time offset analysis presented in section 5.1.2.

Figure 7.1 shows the estimated intersite time offset as a function of the flasher distance to HiRes-1. Time slewing causes this distribution not to be flat. For flashers closer to HiRes-1 the time slewing effect is bigger, because they produce bigger amplitude pulses at HiRes-1. So, the apparent intersite time offset introduced by the time slewing effect would be bigger for flashers close to HiRes-1. The fact that in figure 7.1 the estimated intersite time offset using nearby flashers is closer to zero, is the result of a systematic intersite time offset.

The estimated intersite time offset using nearby flashers differs by approximately 500ns from the intersite time offset estimated using the most distant flashers (fig. 7.1). The wide intrinsic pulse of the flashers ($1\mu s$), increases the time slewing effects.

We do not have the firing time of the flashers (at least not to within 100 ns), so we can only measure the relative intersite time offset, without identifying any systematic time offset at HiRes-1 or HiRes-2. However, a laser equipped with a GPSY clock can record the laser firing time with better than 100 ns precision [103]. In this way we

[1] GPSY stands for Global Position System for Yag lasers. The GPSY is a clock system which enables the laser to fire precisely ($\approx$25 ns) at programmable times.

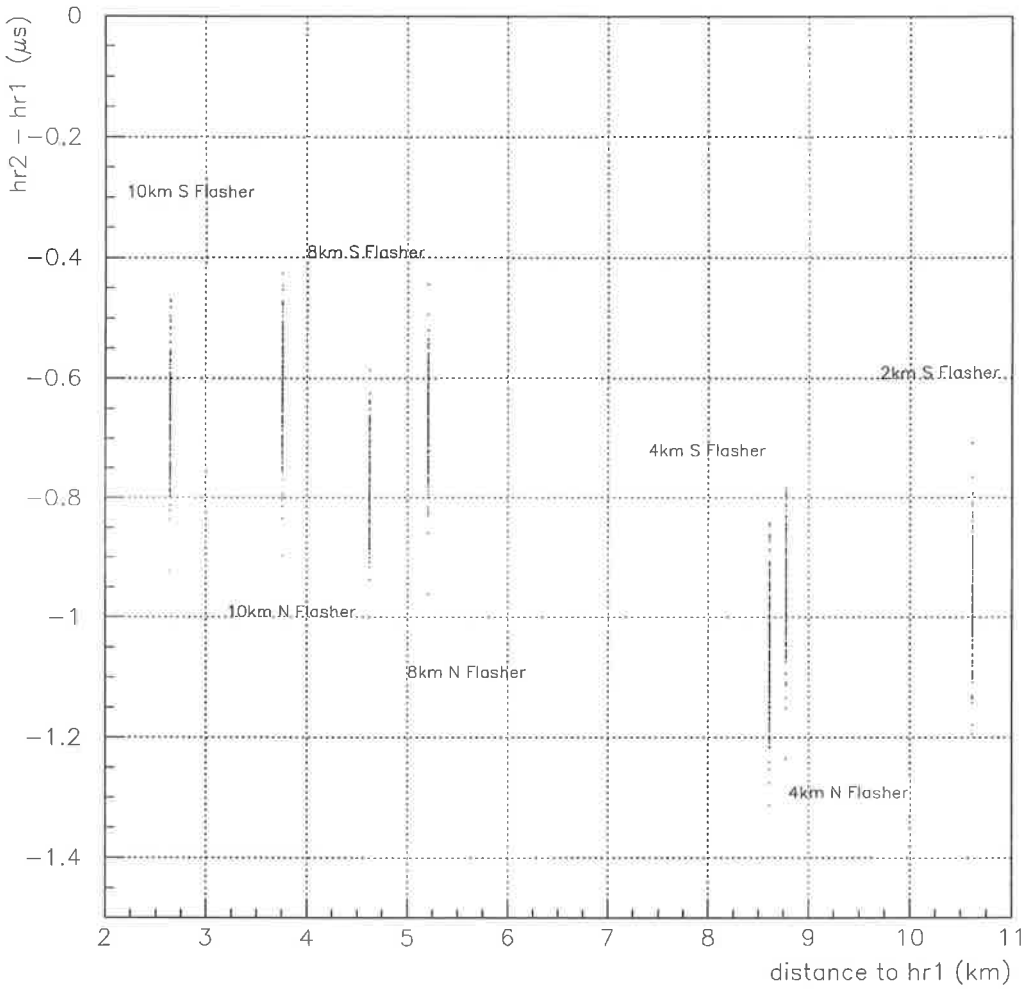

Figure 7.1: Estimated intersite time offset as a function of the flasher-HiRes-1 distance. Perfect vertical orientated flashers were assumed.

can measure any systematic time offset present in HiRes-1 or in HiRes-2, and then the magnitude of the time slewing effect at HiRes-1.

We used a set of laser shots fired by a mobile roving steerable laser system (rsls) on July 17, 2001. The reconstructed geometry of the laser shots and the PMT trigger times were used to estimate the laser firing time [2]. Then this time was compared with

[2]The laser orientations recorded in the log file were uncertain. That is because these laser shots were only engineering shots. These engineering shots were meant to set the rsls (orientation and timing) for later laser tests. Unfortunately soon after, the army indefinitely closed access to the detector, and no more laser tests were possible.

the programmed laser trigger time at the GPSY clock. The GPSY clock was programmed to trigger the laser 0, 250, 500 and 750 ms after every UT second (4Hz rate). Figure 7.2 shows the rsls position and orientation. Figure 7.3 shows the distribution of the difference between the GPSY firing time and the estimated firing time using HiRes-1 time information. Two different laser shot geometries were analysed.

The laser shots directed away from HiRes-1 (see fig. 7.2) have a distribution $(estimated\ fired\ time - GPSY\ time)$ centred in the negative direction at -236 ns (HiRes-1 PMTs triggered earlier than expected). This is related to the high intensity of the laser shots and the fact that events going away from the detector produce wider pulses. So, the time slewing effect is bigger for this laser orientation.

The distribution $(estimated\ fired\ time - GPSY\ time)$ for the laser shot which is almost going towards HiRes-1 is centred at +804 ns. It is approximately $1\mu s$ different from the distribution obtained using the laser fired away from the detector. This means that the time slewing effect has introduced an apparent time offset of at least $1\mu s$ to the laser shots going away from the detector.

The time slewing effect should produce early PMT triggers. So, the laser firing times estimated using the PMT time would be earlier than the real laser firing time. Then, the distribution (tb(i) estimated fired time - GPSY time) should be centred on the negative axis and centred at zero when no time slewing is present.

The reason for one of the distributions being centred at +804 ns may be because we have used the GPSY trigger times instead the GPSY escape times [103] (we do not have the GPSY escape times). The GPSY unit triggers the laser at the specified times, but the emission of the laser pulse may be delayed with respect to the trigger. Our results imply that the GPSY escape times are $\approx 1\mu s$ after the GPSY trigger times, unless a systematic time offset exists between the HiRes-1 GPS clock and the GPSY clock.

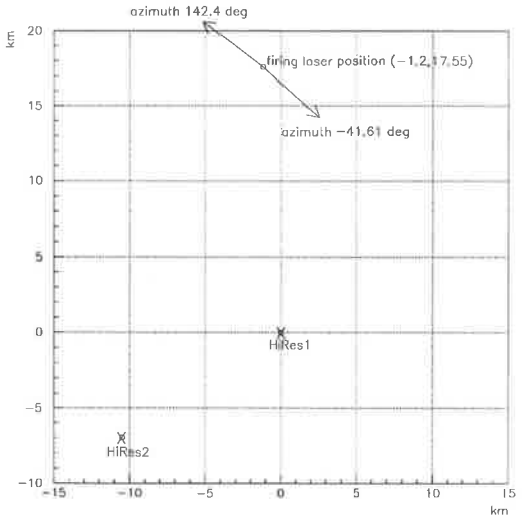

Figure 7.2: Firing laser position. The arrows show the azimuth direction of the fired lasers. The zenith angle of both laser shots is 21°.

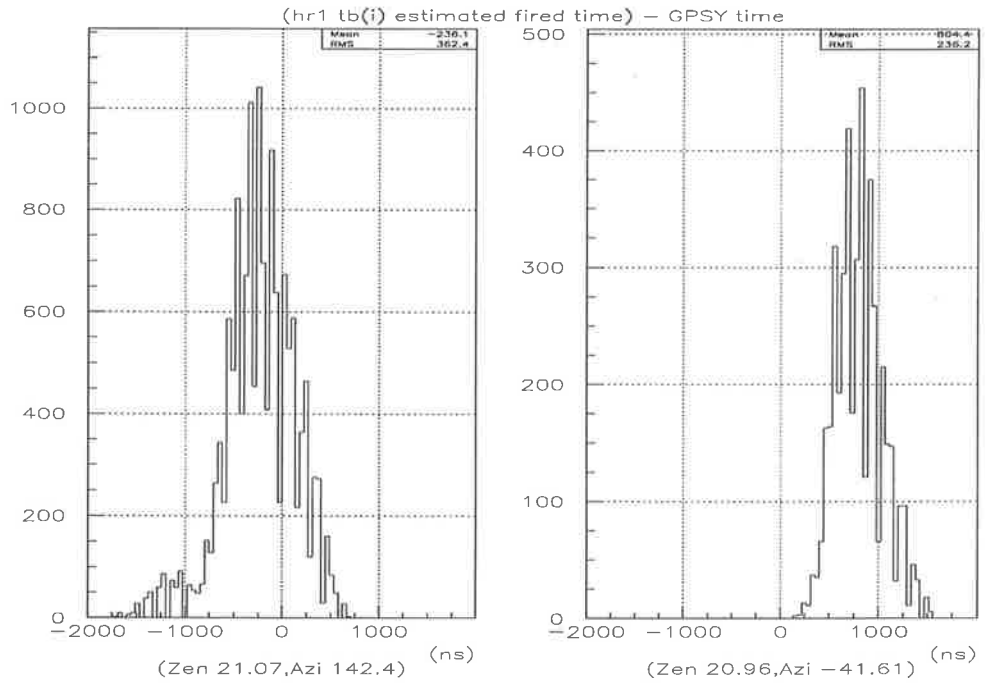

Figure 7.3: The above distributions show the difference between the estimated laser firing time using *HiRes-1* and the programmed firing time at the GPSY clock. Two different laser orientations were analysed .

7.1.3.2 Timing χ^2 function (χ^2_{time})

The idea of timing reconstruction is to use a trial orientation of the shower axis to estimate an expected PMT trigger time. Then, this time is compared with the recorded PMT trigger time. To estimate the expected PMT trigger time, we use information from each PMT (trigger time and PMT orientation) to calculate the time when the air shower was at its closest point to the first triggered mirror (the Rp time). Alternatively we can calculate the ground time (the time when the air shower reaches the ground).

From each PMT we obtain one Rp time (or ground time), and the average Rp time (or ground time) is used as a reference time to calculate each expected PMT trigger time (eq. 7.10).

$$expected\_time_i =< Rp\_time > + \frac{Rp}{c} tan(\frac{\theta_i}{2}) \tag{7.10}$$

where θ is the PMT emission angle and Rp is the distance to the shower closest point.

In Fit_shower1 we estimated an Rp time independently for HiRes-1 (Rp_1 time) and for HiRes-2 (Rp_2 time). The Rp_1 and Rp_2 times were obtained from the average over the HiRes-1 and the HiRes-2 PMT Rp times respectively. We use independent reference times for HiRes-1 and HiRes-2 (Rp_1 and Rp_2) because of the problem of the intersite time offset (Section 5.1). On the positive side, this reduces the influence of time slewing in the reconstruction, but it has the negative effect of reducing the overall constraining power of stereo timing information. Equation 7.11 shows the timing χ^2 function,

$$\chi^2_{time} = \sum_{i=0}^{i=N} \frac{(expected\_time_i - tube\_time_i)^2}{sigma^2_{time_i}} \tag{7.11}$$

where $sigma_{time_i}$ is the trigger time uncertainty of PMT 'i'. This time is 30% of the average time that the reconstructed shower takes to cross 1° (1° is the field of view of a PMT).

We define $tm1$ and $tm2$ as the HiRes-1 and HiRes-2 timing χ^2 functions. The best hybrid reconstructed geometry is obtained by minimizing $st1 + st2 + tm1 + tm2$. Here $st1 + st2 + tm1 + tm2$ is the sum of four reduced χ^2 values (i.e. the total χ^2 has been divided by the number of degrees of freedom). In this way all four χ^2 components have

similar weights in a hybrid reconstruction. The author has checked carefully that the mean values of the reduced χ^2 are approximately 1. The variance term in each χ^2 has been adjusted (within reasonable bounds) to produce reduced χ^2 distributions with a mean value of 1.

7.2 Test of the reconstruction techniques

The direction of the vertical flashers described in figure 5.26 were reconstructed. Figure 7.4 shows the reconstructed zenith angles for each flasher (fig 7.4 left hand side plot) and the RMS values of the reconstructed zenith distributions (fig 7.4 right hand side plot), both as a function of the opening angle between the HiRes-1 and HiRes-2 shower detector planes.

Figure 7.4 shows that for events with opening angles bigger than 30° the reconstructed orientation of the flashers are similar (within approximately 0.2°) when using any of the reconstruction techniques. However for flashers with opening angles smaller than 30° the difference between hybrid and stereo results are notable. Hybrid results are more accurate and precise, especially for opening angles smaller than 3°.

Only flashers with small opening angles had some reconstructed zenith angles far from the vertical direction. Some of these events were correlated with high χ^2 values. Thus, based on flasher reconstruction results, Fit_shower1 assigns a failmode value different to zero (zero is for successful reconstructed events) to events with $tm1$ or $tm2$ larger than 20 and $st1$ or $st2$ larger than 15. These values should be checked when stereo MC data is available. Figure 7.5 shows the reconstruction efficiency for each method, where only events with a failmode value equal to zero were considered as successfully reconstructed.

All flashers, except the 10 km N flasher (the one with the largest opening angle, 56°), had hybrid reconstruction results with narrower distributions than stereo results. Figure 7.6 shows the reconstructed zenith angle distribution for the 10 km N and 2 km S flashers (the 2 km S flasher is the one with the smallest opening angle 2.5°).

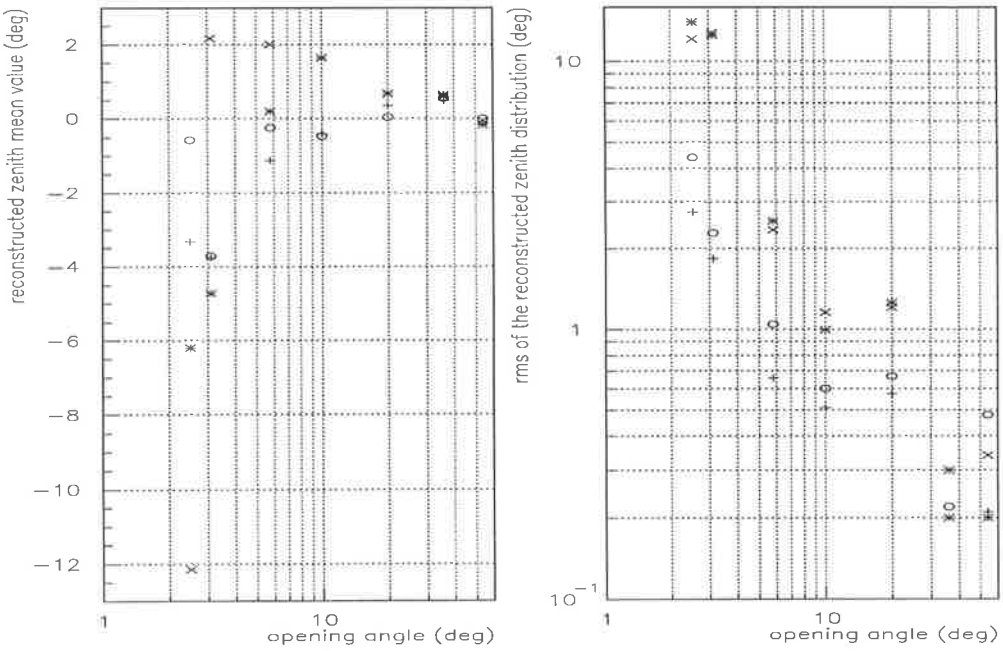

Figure 7.4: Reconstructed zenith angle (mean value) and the RMS of the reconstructed zenith angle distribution as a function of the opening angle. A different mark is used for each reconstruction method. The circle 'o' is for hybrid aw, plus '+' is for hybrid af, asterisk '$*$' is for stereo af and times '$\times$' is for stereo aw.

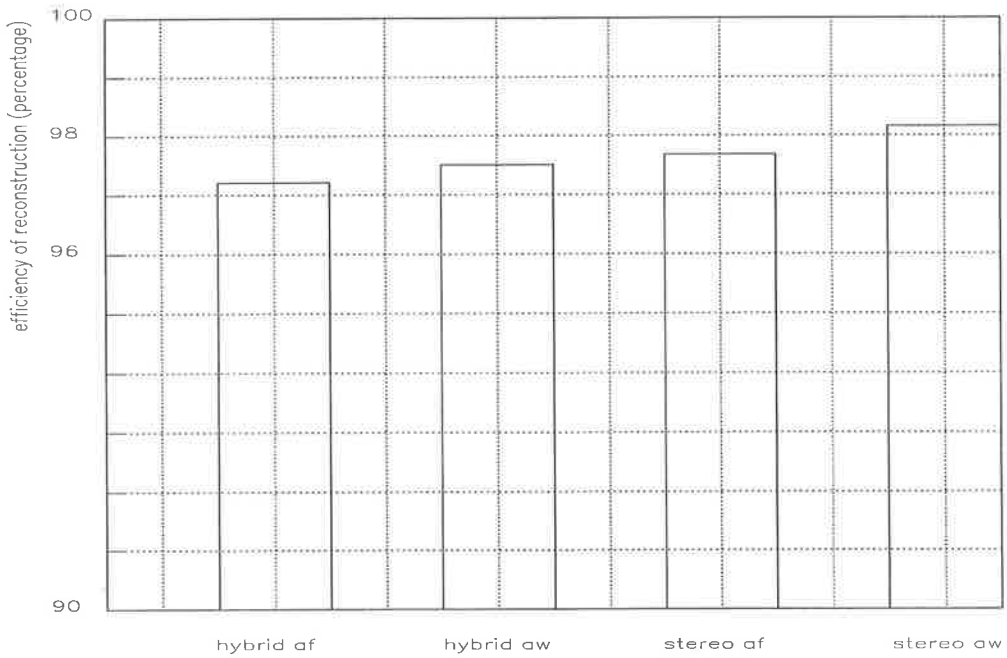

Figure 7.5: Reconstruction efficiency.

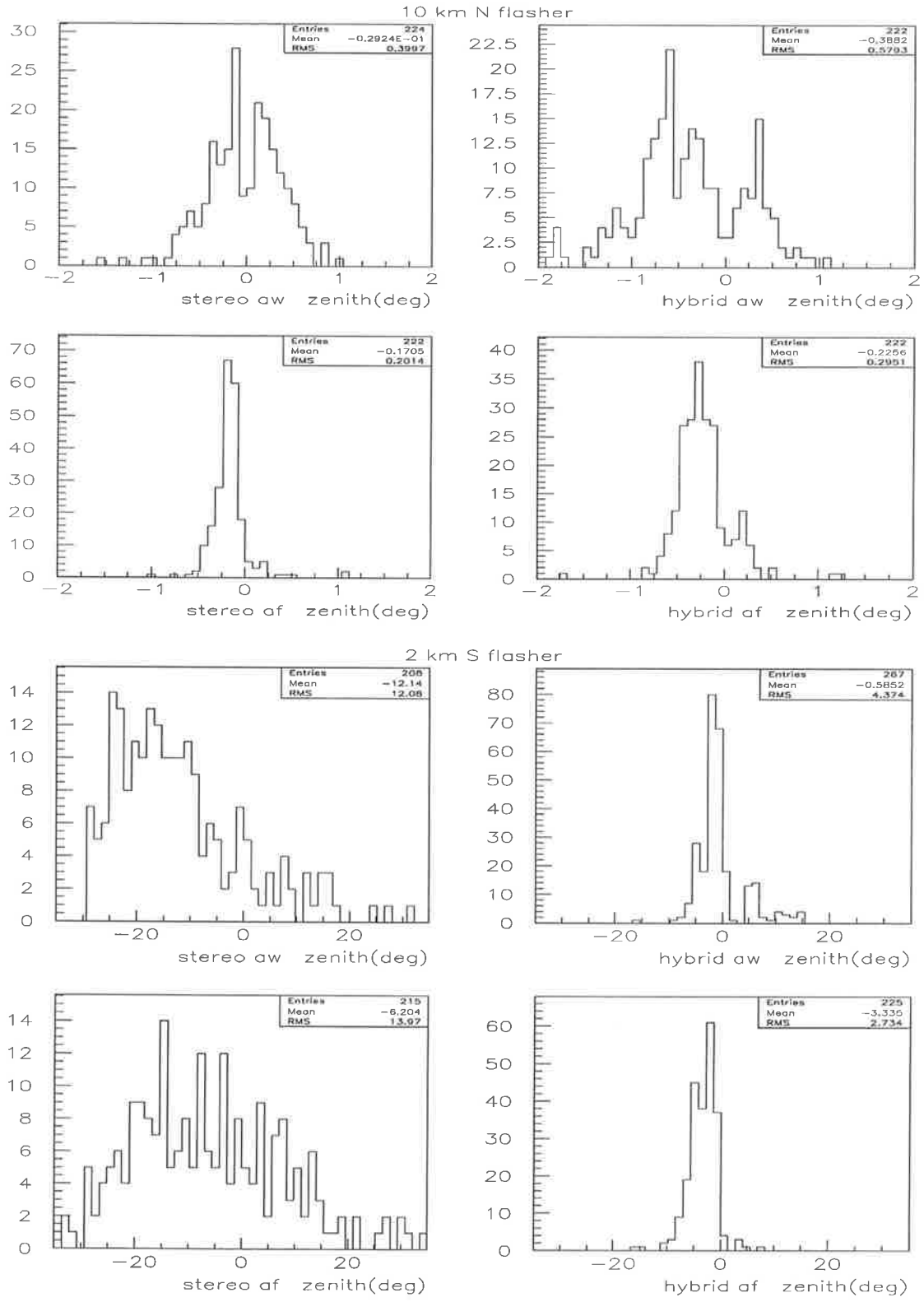

Figure 7.6: Stereo and hybrid reconstructed zenith angle distribution for the 10 km N, and 2km S flashers. The 10 km N and the 2 km S flashers have opening angles 56° and 2.5° respectively

The slightly broader distributions in the hybrid results for the biggest opening angle flasher (figure 7.6 top plots), may be reduced by giving more weight to the χ^2 plane components ($st1$ and $st2$). The extra weight will only be necessary for events with opening angles larger than approximately 45°. For small opening angles the hybrid reconstruction is much better than the stereo reconstruction. The RMS of the reconstructed zenith of the 2 km S flasher has been reduced from 13° to 3° (figure 7.6 bottom plots).

7.2.1 Uncertainty of the reconstructed orientation

Previously, the uncertainty of the reconstructed orientation was obtained from the estimated uncertainties on the reconstructed zenith and azimuth angles of the shower axis. Fit_shower1 uses as fitting parameters the zenith and azimuth of the SDP normal for each eye. Therefore the uncertainty of the reconstructed shower axis will be determined by the uncertainties on the SDP normals.

It was found that by having uncertainties based on the SDP normal directions, we can reproduce better the uncertainty region (size and shape) around the reconstructed shower axis orientation.

To estimate the uncertainty of each fitted parameter, we vary the value of each parameter, keeping the other parameters fixed (fixed to their best estimated values). The parameter is varied until the total χ^2 is increased by certain amount [3]. The appropriate increment in the total χ^2 ($\Delta\chi^2$) was determined using MC data, so that the variation in each parameter represents one sigma errors. A complete description of this technique can be found at [104].

Figure 7.7 shows the estimated error size as a function of $\Delta\chi^2$. The estimated error represents one sigma uncertainty when the distribution of the error size has an RMS equal to one. We define error size as the difference (absolute value) between the reconstructed parameter and the true parameter (MC input) over the estimated error.

[3] An increment of one in the total χ^2 corresponds to one sigma confidence (for one degree of freedom). However when the errors are not normal distributed, or small systematics errors are present, an increment in the total χ^2 bigger than one may be required.

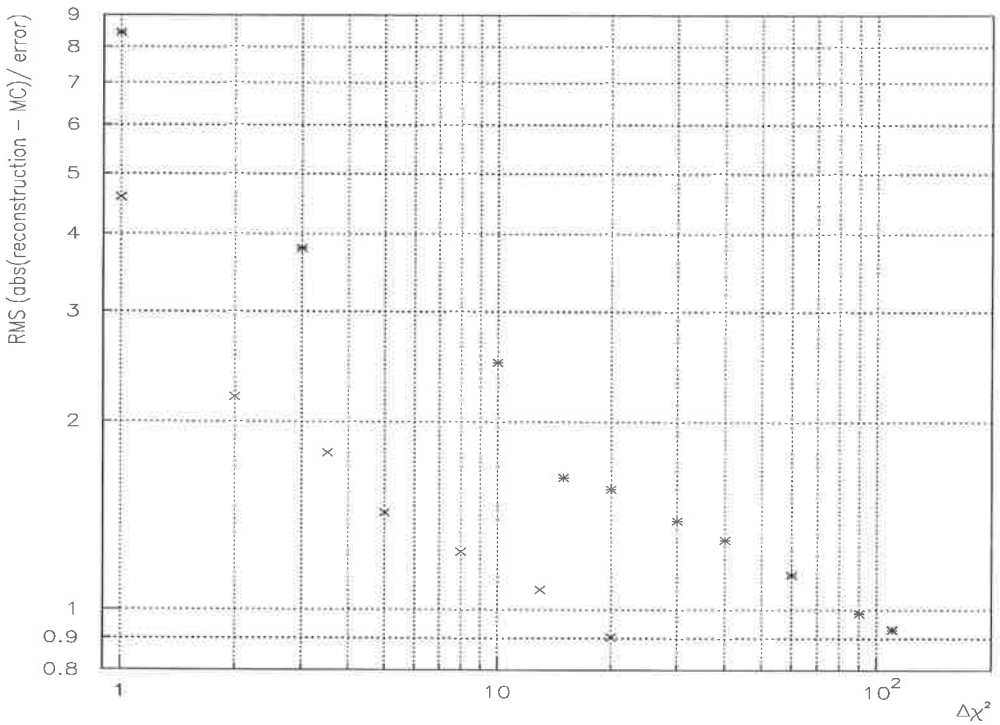

Figure 7.7: Error size as a function of the χ^2 variation ($\Delta\chi^2$). These values were calculated using MC data. The asterisks are for stereo af and the crosses are for stereo aw (see text for details).

From figure 7.7 we determined that the best $\Delta\chi^2$ for stereo aw is 15 and for stereo af is 90. Then we used these values to estimate the errors.

To check the estimated errors of the reconstructed directions, we used again vertical flashers (fig. 5.26). Figure 7.8 shows reconstructed directions for the North flashers using the stereo aw and af techniques. And figure 7.9 shows the estimated uncertainty regions.

The uncertainty regions were built by choosing randomly one reconstructed flasher event for each flasher position. Each point from figure 7.9 comes from a random combination of SDP normal orientations (zenith and azimuth) around the reconstructed parameters. The distributions of the SDP normal orientations follow Gaussian distributions, where the mean values are the reconstructed SDP normal orientations, and the sigmas are the estimated errors.

The estimated uncertainty regions (figure 7.9) are bigger than the actual reconstructed direction distributions (figure 7.8). This may be because the MC data used to estimate the appropriate $\Delta\chi^2$ did not take into account the different location of the mirrors, introducing some parallax effects. Fit_shower1 does take into account the different mirror locations. Soon, new MC data, which does take into account the different locations of the mirrors should be available and the appropriate $\Delta\chi^2$ could be re-estimated.

The MC data also had some timing problems, so we could not use it for estimating the appropriate $\Delta\chi^2$ for the hybrid technique.

Figure 7.10 shows the estimated error size as a function of $\Delta\chi^2$, calculated using vertical flashers and laser shots for which the geometry is known. The appropriate $\Delta\chi^2$ values in order to get one sigma errors are 1 and 3.5 for stereo aw and af respectively. These values are much smaller than the ones estimated using MC data (from statistical theory $\Delta\chi^2 = 1$ is necessary to get 1 sigma errors). Figure 7.11 shows the stereo-aw and stereo-af reconstructed uncertainty regions for the North flashers using $\Delta\chi^2 = 1$ and $\Delta\chi^2 = 3.5$ respectively. The uncertainty regions are consistent with the reconstructed direction distributions (figure 7.8).

For hybrid-aw and hybrid-af fitting methods the appropriate values for $\Delta\chi^2$ are 4.5 and 4 respectively (fig. 7.10). The reconstructed orientation of the North and South vertical flashers using the hybrid-af and hybrid-aw techniques are shown in figures 7.12 and 7.13 respectively. The estimated uncertainty regions for hybrid-af reconstruction is shown in figure 7.14. These uncertainty regions are also consistent with the reconstructed direction distributions (fig. 7.12), except for the 2 km and 4 km South flashers.

We obtained consistent values for the appropriate $\Delta\chi^2$ when using flashers and laser shots. However, the estimated uncertainty regions for the small opening angle ($< 5°$) flashers (2 km S and 4 km S flashers, fig. 7.14) seem to be smaller than the reconstructed direction distribution (fig. 7.12). The reason may be because flashers have larger intrinsic pulses (1μs) that increase the hybrid reconstruction uncertainty.

For comparison purposes figures 7.15 and 7.16 show the reconstructed orientations and uncertainties for the South vertical flashers using the stereo-af and stereo-aw techniques respectively. Stereo reconstruction of these small opening angle events ($< 10°$) is definitely not recommended.

When a shower is closer to one site, the uncertainty is mainly distributed within the SDP relative to that site. This is because it was assigned to each PMT a weight proportional to its signal, and PMTs that belongs to the closest site will have greater weights. This is the reason why the 4 km North flasher (closer to HiRes-2) and the 10 km North flashers (closer to HiRes-1) have their reconstruction uncertainties distributed within the HiRes-2 and HiRes-1 SDPs respectively (see fig. 7.8).

Considering the uncertainty distributions of the 4 km and 10 km North flashers (fig. 7.8), the 10km North flasher has a smaller distribution. This is because HiRes-2 has two mirrors involved in every vertical flasher event. Therefore it has a longer track which defines with a better resolution the SDP.

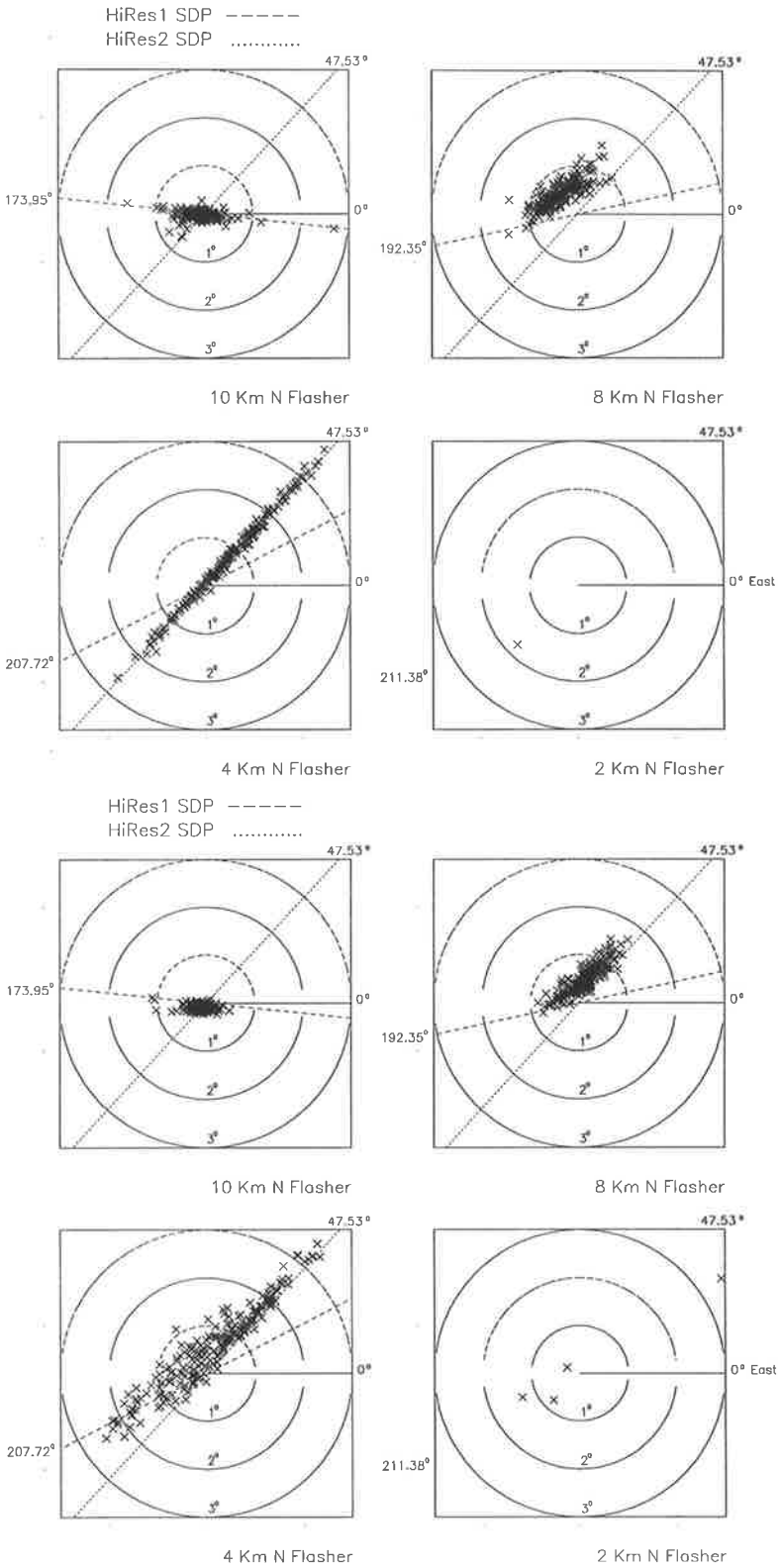

Figure 7.8: Reconstructed orientation of the North vertical flashers. The upper and lower plots are for stereo-aw and stereo-af respectively. The radial distance represents the zenith and the polar angle represents the azimuth of the reconstructed axis. The lines represent the HiRes-1 and HiRes-2 SDP projections on the sky.

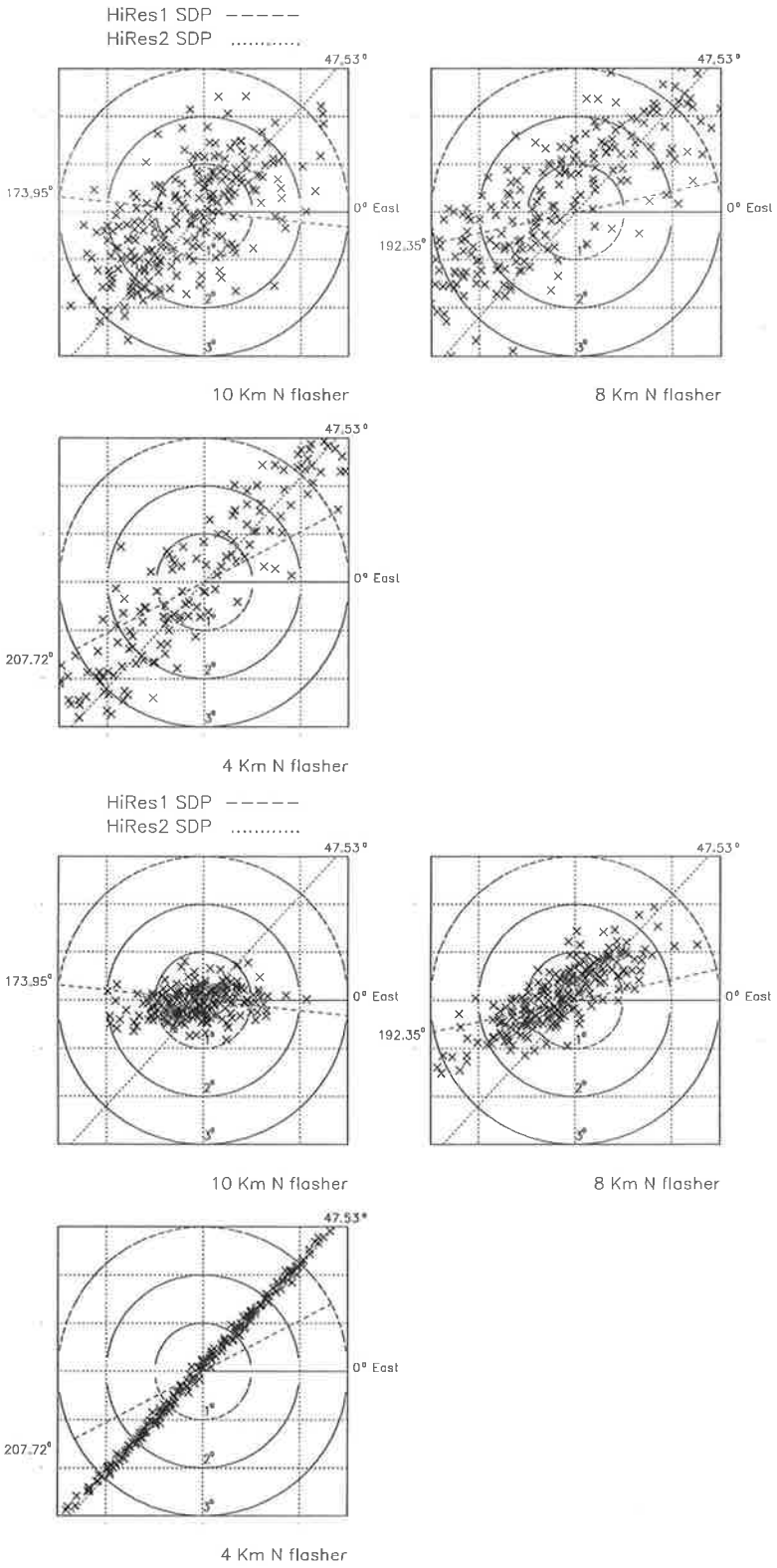

Figure 7.9: Reconstructed uncertainty region of the North vertical flashers (see caption in fig. 7.8). For stereo-aw the errors were estimated using $\Delta\chi^2 = 15$ (upper plots) and for stereo-af the errors were estimated using $\Delta\chi^2 = 90$ (lower plots). The values of $\Delta\chi^2$ are assigned **according to MC data**.

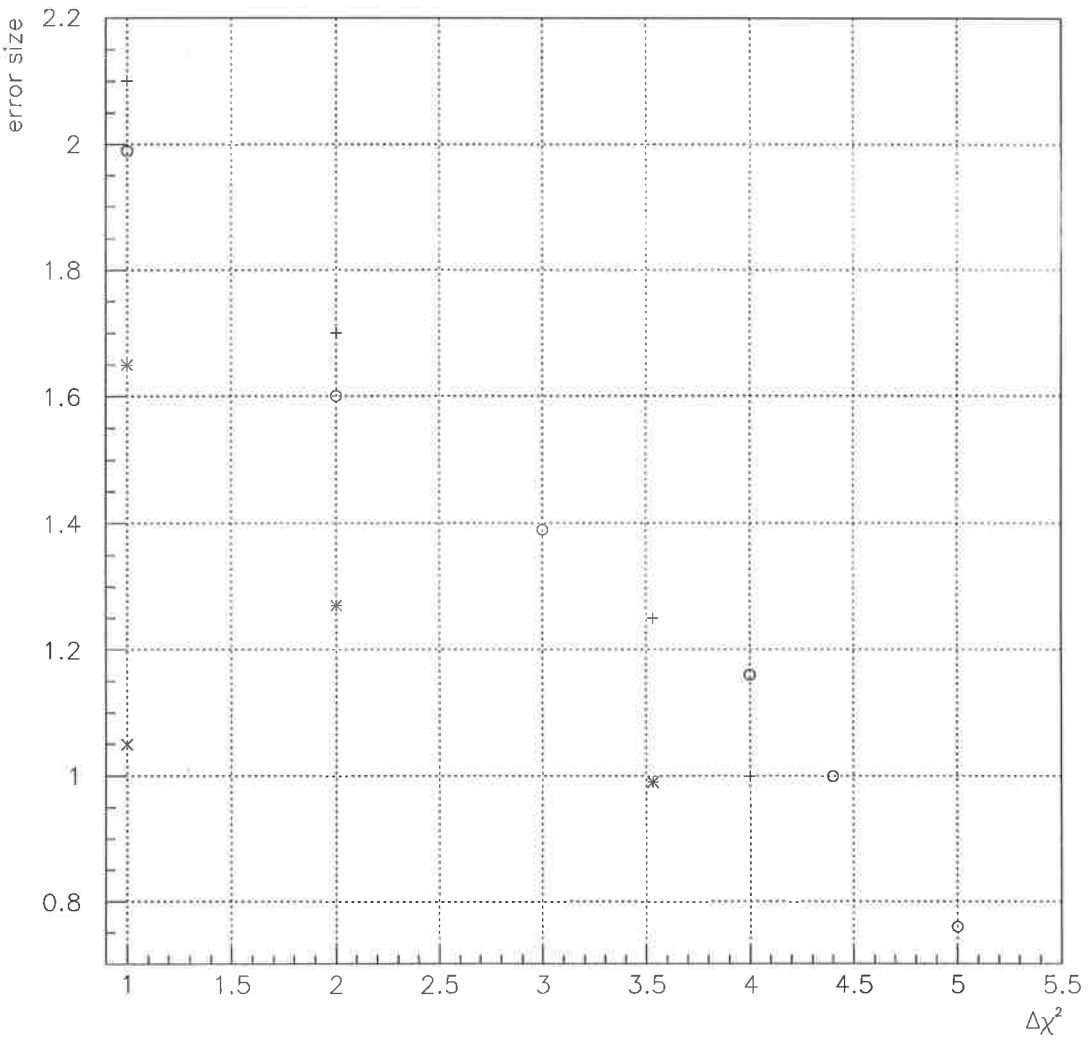

Figure 7.10: Error size as a function of the χ^2 variation ($\Delta\chi^2$). The error size is defined as $|(reconstructed\ \ parameter - expected\ \ value)|/(estimated\ \ error)$. These values were calculated using vertical flashers and laser shots. The circle '$\circ$' is for hybrid aw, plus '$+$' is for hybrid af, asterisk '$*$' is for stereo-af and times '$\times$' is for stereo aw.

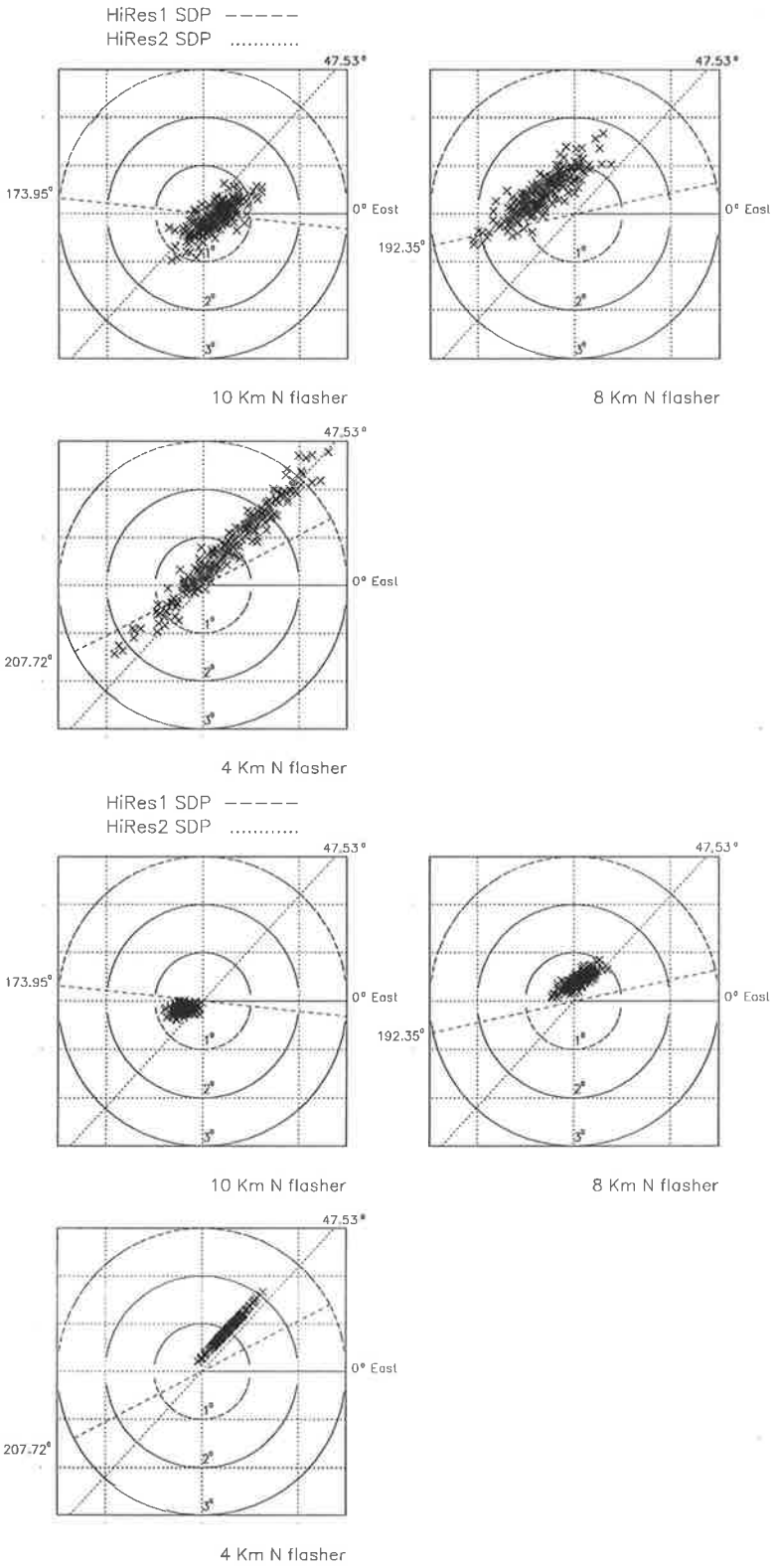

Figure 7.11: Reconstructed uncertainty region of the North vertical flashers (see caption in fig. 7.8). For stereo-aw the errors were estimated using $\Delta\chi^2 = 1$ (upper plots) and for stereo-af the errors were estimated using $\Delta\chi^2 = 3.5$ (lower plots). The values of $\Delta\chi^2$ are assigned **according to flasher and laser shot** events (see fig. 7.10).

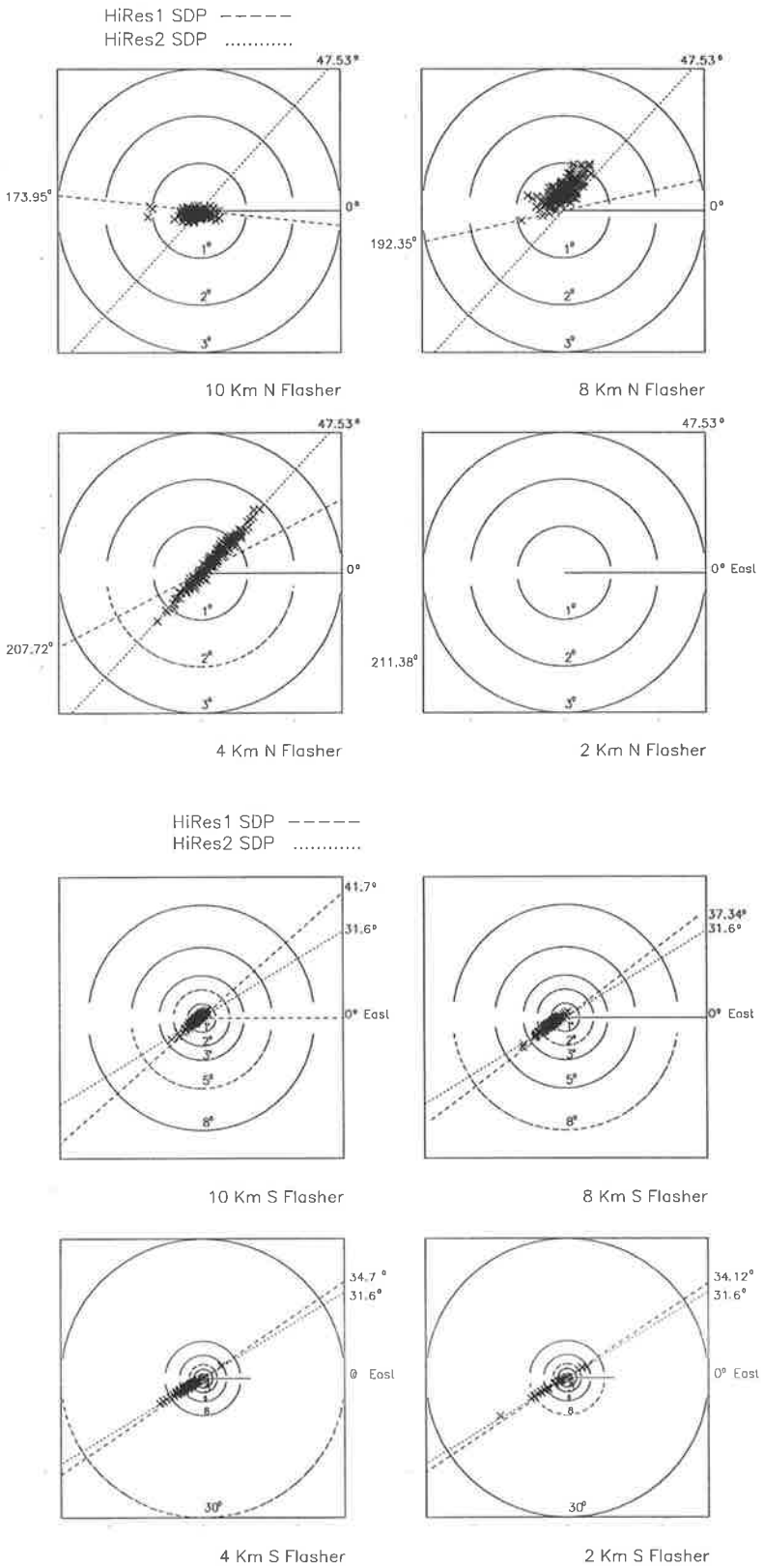

Figure 7.12: Reconstructed orientation of the North and South vertical flasher, using the **hybrid-af** technique. The radial distance represents the zenith and the polar angle represents the azimuth of the reconstructed axis.

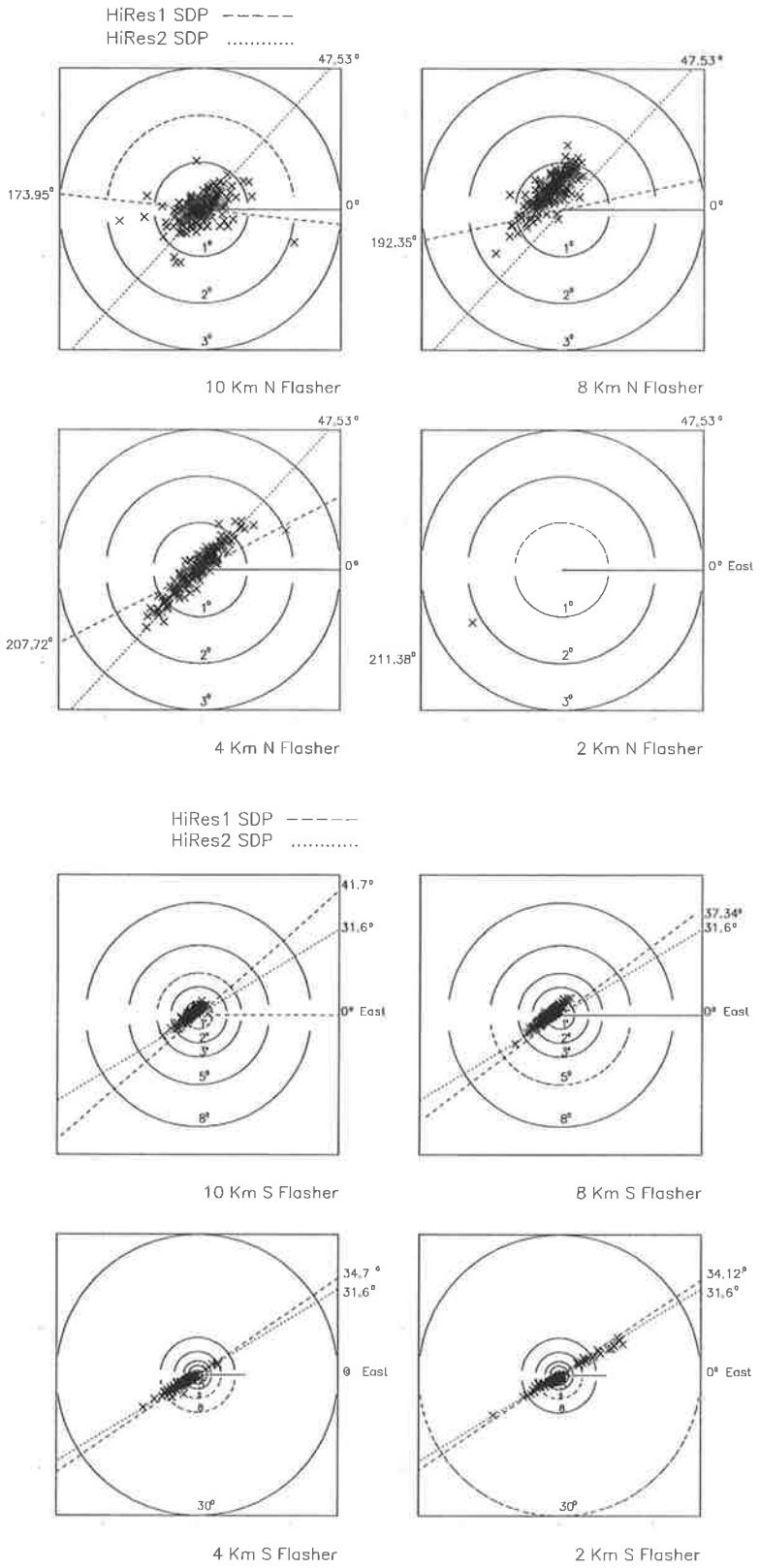

Figure 7.13: Reconstructed orientation of the North and South vertical flasher, using the **hybrid-aw** technique. The radial distance represents the zenith and theta represents the azimuth of the reconstructed axis.

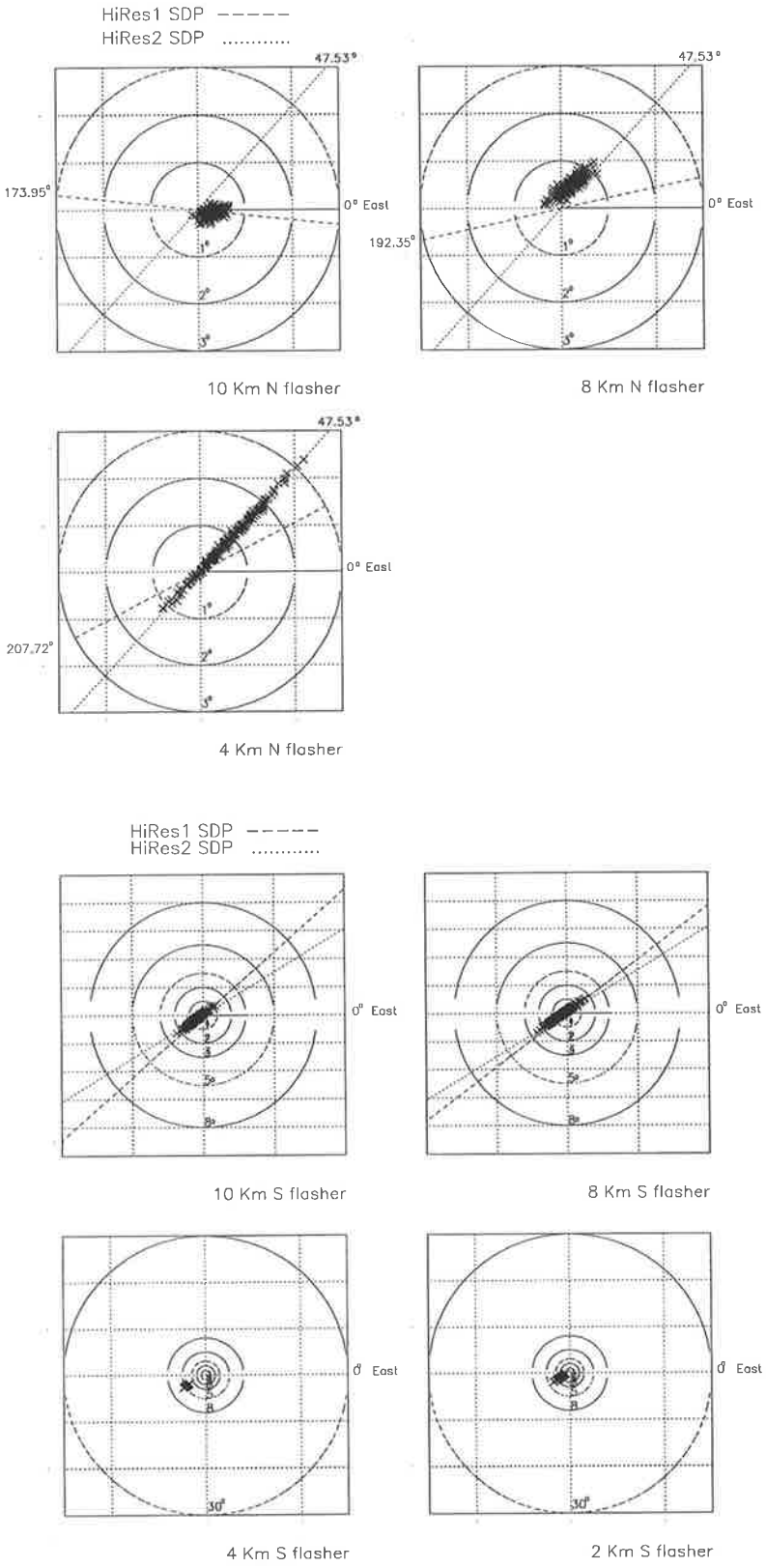

Figure 7.14: Reconstructed uncertainty region of the North and South vertical flashers using the **hybrif-af** technique. The errors were estimated using a $\Delta\chi^2 = 4$. The value of $\Delta\chi^2$ is assigned **according to flasher and laser shot** events (see fig. 7.10).

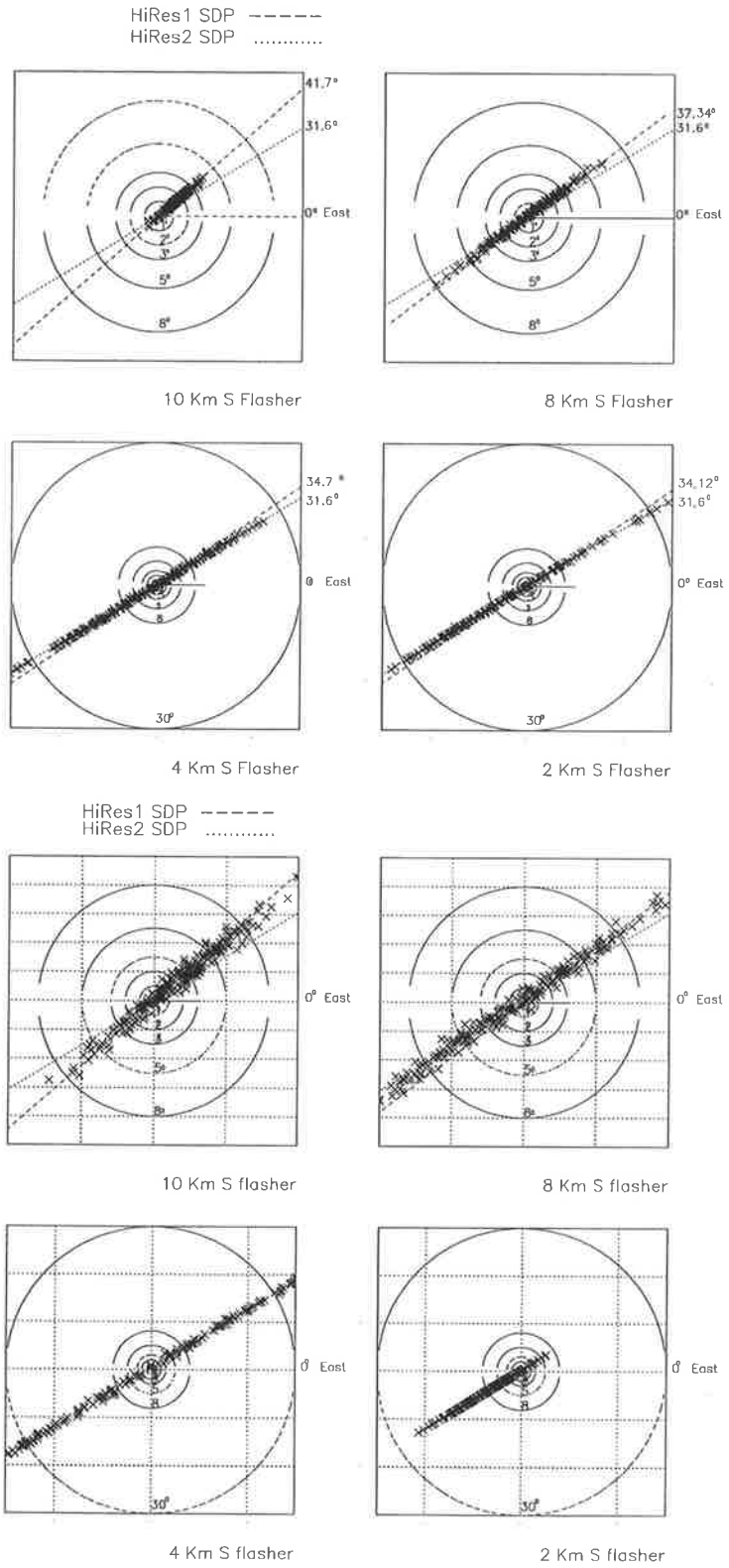

Figure 7.15: Reconstructed orientation (upper plots) and uncertainty (lower plots) of the South vertical flashers using the **stereo-af** technique (upper plots). The errors were estimated using a $\Delta\chi^2 = 3.5$. The value of $\Delta\chi^2$ is assigned **according to flasher and laser shot** events (see fig. 7.10).

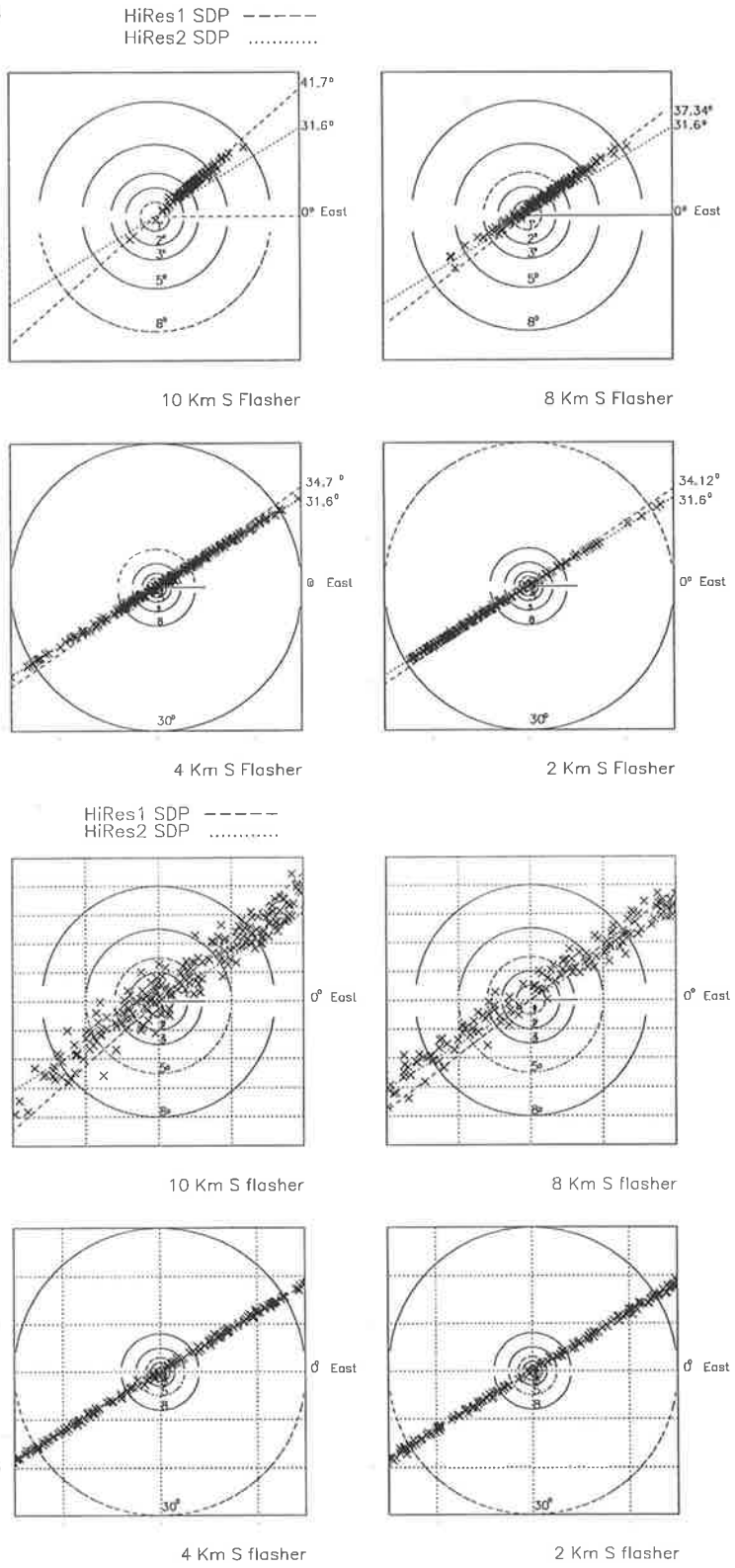

Figure 7.16: Reconstructed orientation (upper plots) and uncertainty (lower plots) of the South vertical flashers using the **stereo-aw** technique. The errors were estimated using a $\Delta\chi^2 = 1$. The value of $\Delta\chi^2$ is assigned **according to flasher and laser shot** events (see fig. 7.10).

Chapter 8

HiRes anisotropy studies

In chapter 2, I presented a review containing the anisotropy results of other groups. These previous results were considered for the selection of *a priori* source candidates and energy ranges for the HiRes anisotropy studies. Such *a priori* selections reduce the number of trials involved in source searches. Therefore, the statistical significance of an observed source is greater. The HiRes *a priori* cosmic ray source candidates are Cygnus X-3 ($E \geq 10^{18}$ eV), the AGASA triplet ($E > 4 \times 10^{19}$ eV), the galaxy M-87 (Virgo A) ($E > 4 \times 10^{19}$ eV) and the supergalactic plane ($E > 4 \times 10^{19}$ eV)[105]. For the HiRes anisotropy analysis using skymaps three energy ranges were selected *a priori*. These energy ranges are 10^{18} eV $< E < 10^{18.5}$ eV, $10^{18.5}$ eV $< E < 10^{19}$ eV and $E > 10^{19}$ eV.

In previous chapters, I have also presented studies of the resolution of the reconstructed cosmic ray arrival directions. In chapter 6, I estimated the geometry resolution for HiRes-1 mono events, and in chapter 7 for HiRes stereo events. It was shown that the uncertainty regions of the reconstructed arrival directions have elliptical shapes. These elliptical errors have their larger axis oriented parallel to the SDP projection on the sky. For HiRes-1 mono events the elliptical errors are very elongated (see table 6.1), and for stereo events the ellipses are much smaller, and in some cases the uncertainty regions are almost circular (see fig. 7.8). I start this chapter studying how these characteristics of the reconstruction may affect an anisotropy analysis using

shower density contour plots, and how we can deal with them.

The HiRes detector has a great exposure toward the North Celestial Pole. However, the traditional time shuffling technique used to estimate the cosmic ray background flux has some difficulties around the pole region. I present in this chapter an alternative way to estimate the cosmic ray background flux using Monte Carlo data. This new technique does not present any problems in estimating the expected background around the pole. Finally in this chapter the HiRes anisotropy results are presented. The techniques described early in this chapter are used for the anisotropy analysis.

The sky density maps method is the prime analysis method used by the author for the HiRes anisotropy analysis. There are other methods available [105], but they are being studied by others [106, 107].

8.1 Shower density contour plots technique

The shower density contour plots technique used here for the HiRes anisotropy analysis is basically similar to that used for the SUGAR analysis (see chapter 2 for a description). At HiRes, the Gaussian probability functions around each reconstructed direction have elliptical shapes determined by the orientation of the SDPs. This is in contrast to SUGAR where the errors had circular shapes. The reconstruction of the uncertainty regions (Gaussian probability functions) for the mono and stereo reconstruction are explained in chapters 6 and 7 respectively.

Depending on the energy and the source distance of the cosmic rays, their paths are deflected by magnetic fields. Because of this effect we do not expect point sources at lower energies ($< 10^{19}$ eV), unless they are sources of neutral particles. At this lower energy range we expect "smeared" out sources, that is point sources made more diffuse by astrophysical effects (magnetic bending).

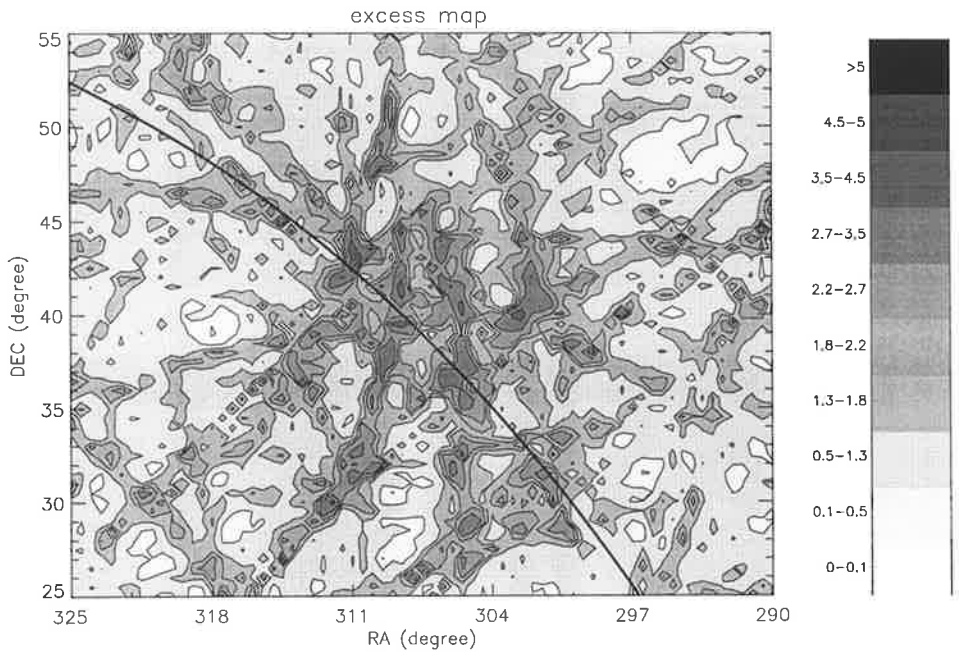

Figure 8.1: Excess map calculated after having introduced 49 artificial events into the HiRes-1 mono data set. The artificial events are randomly distributed within a 5° radius circle centred at Cygnus X-3. The excess represents the ratio of the observed signal over the expected signal assuming an isotropic cosmic ray flux. The solid line represents the galactic plane.

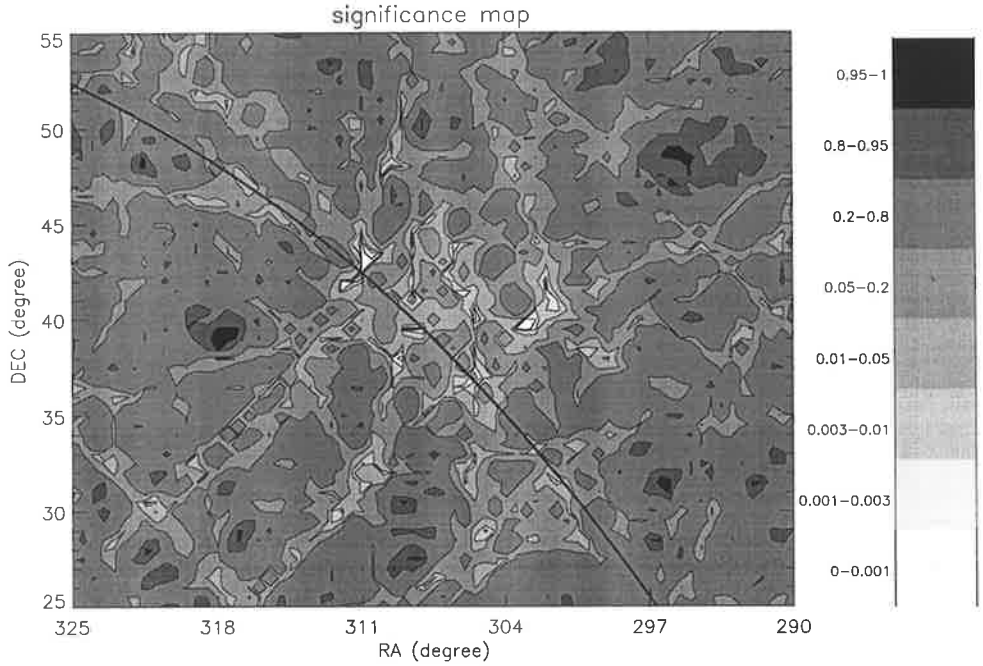

Figure 8.2: Significance of the excess observed in figure 8.1. The significance represents the chance probability of having an excess similar to or greater than the observed excess at the particular bin.

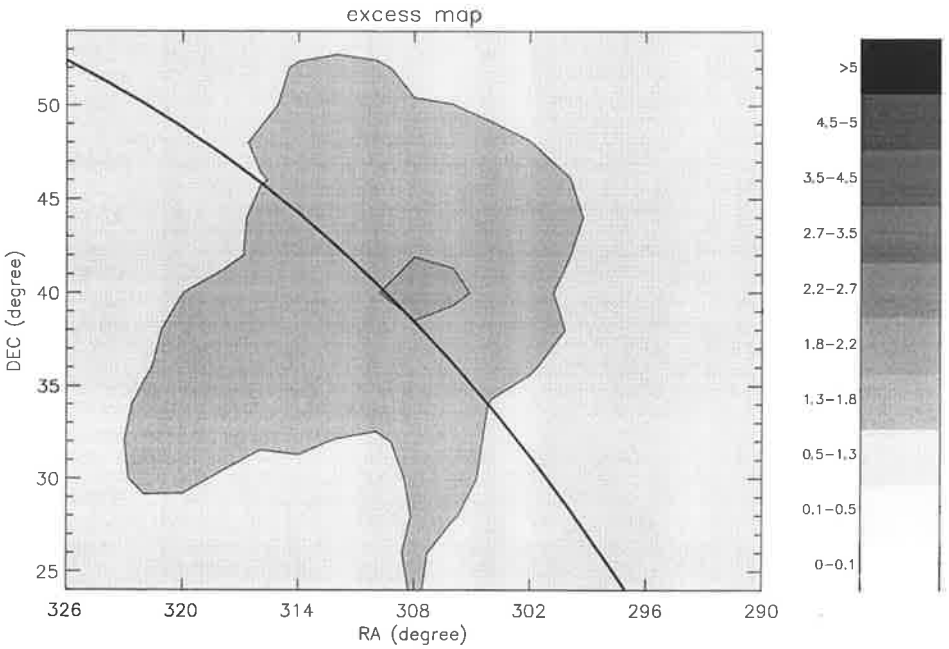

Figure 8.3: Excess map after having introduced 49 artificial events into the HiRes-1 mono data within a circle centred at Cygnus X3 with approximately 5° radius. The number of events within a circle of 5° radius centred on each bin was counted. Then, this number of events was compare with the number expected from an isotropic arrival direction distribution.

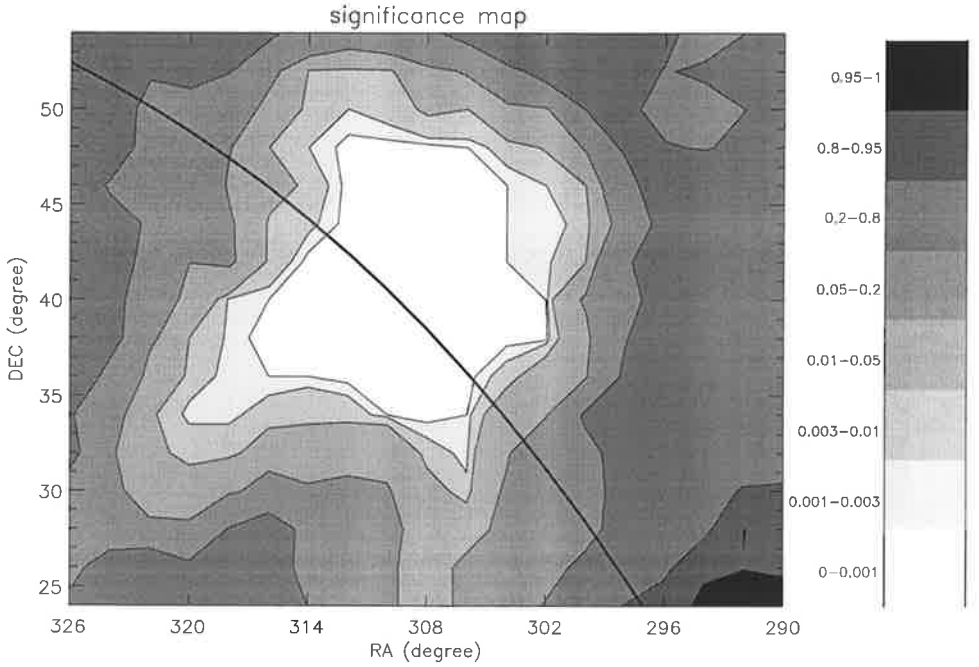

Figure 8.4: Statistical significance of the excess region in fig. 8.3.

8.1.1 Astrophysically smeared sources

Because of this astrophysical smearing and the elongated elliptical errors for HiRes-1 mono events, our sensitivity to smeared sources is dramatically reduced. Figures 8.1 and 8.2 show the excess and significance maps calculated after introducing to the real data set (energy range $10^{18} - 10^{18.5}$ eV) a strong artificial smeared source centred in the direction of Cygnus X-3. The 49 artificial arrival directions are randomly distributed within a 5° radius circle centred at Cygnus X-3 (49 corresponds to 7 times the expected background within a 5° radius circle centred at Cygnus X-3). These 49 events were randomly selected from real events within the corresponding declination band. Their arrival times were modified in order to have them randomly distributed within the desired region around Cygnus X-3.

From figure 8.1 we notice that the excess ratio exhibits only small peaks with excess ratios between 3.5 and 4.5. Note that this excess is only half of that expected according to the artificial source magnitude. Despite the strong artificial source introduced, figure 8.2 barely shows the presence of a smeared source.

Figures 8.3 and 8.4 show an alternative way to identify smeared sources. The sky maps were divided in bins with intrinsic sizes of 2° in RA by 2° in DEC. The equivalent number of events inside circles centred at each bin was calculated and assigned to the respective bin (density map). The sizes of the circles are related with the astrophysical effects (magnetic bending). Therefore we refer to the radius of the circles as 'smearing size'.

For the excess map (fig. 8.3) we compare bin by bin the density map with a density map estimated assuming an isotropic cosmic ray flux (a background map). For the significance map (fig. 8.4) we count how many background maps (out of 1000) had in each bin an event density similar or greater to that in the corresponding bin in the density map. This technique, using smearing circles, may reduce the resolution in determining the source direction, but increases the sensitivity to smeared sources.

It was noticed that approximately only 20 to 25 percent of the artificial signal

ended up within the 5° of Cygnus X-3. The reason for this is the large uncertainties in the arrival directions represented by elongated ellipses. Even though the nominal arrival directions of the 49 artificial events were inside the 5° radius circle, only a signal equivalent to 10 events was effectively inside the circle (apart from the background). Therefore, the estimated excess estimated in figure 8.3 is only ≈2.2 (value of the peak). The statistical significance of this excess is shown in figure 8.4.

8.1.2 Point Sources

Anisotropy analysis of HiRes-1 mono events is sensitive to point sources despite the large uncertainties. This is because although the reconstructed directions of the point source events are broadly distributed around the source direction, their elliptical errors should be oriented toward the true point source direction. As a result the ellipses overlap at the point source direction increasing the signal from this region. Figure 8.5 shows the density distribution for an artificial point source containing 49 events (same number of events used to simulate a smeared source).

The artificial point source shown in figure 8.5 was added to a real density distribution. Like the smeared source simulation above, this real density distribution corresponds to an energy range between 10^{18} - $10^{18.5}$ eV. Figures 8.6 and 8.7 show the resulting excess and significance maps. The excess ratio peak (fig. 8.6) corresponds to an excess of 8 times. This number agrees with that expected from a source with intensity 7 times the background. The estimated significance of the excess (fig. 8.7) certainly suggests the presence of a very significant point source. Notice that the resolution of the estimated point source direction is better than 1°. This is a remarkable result considering the large uncertainties (more than 12°, see table 6.1 for details) of the HiRes-1 mono reconstruction. This good resolution for point sources is related to the good resolution in determining the SDP.

8.1.3 Summary

This analysis shows that despite the poor monocular reconstruction resolution, the shower density contour plots technique may still be sensitive to point sources. The point source region may be determined with a resolution better than 1°. However because of the poor monocular resolution, the standard shower density contour plots technique is less sensitive to astrophysically smeared sources. A variation of the technique (using smearing circles) may increase the sensitivity to astrophysically smeared sources.

If we expect a smeared source it is better to do an analysis with a smeared circle. However if we expect a point source, it is better not to use a smearing circle.

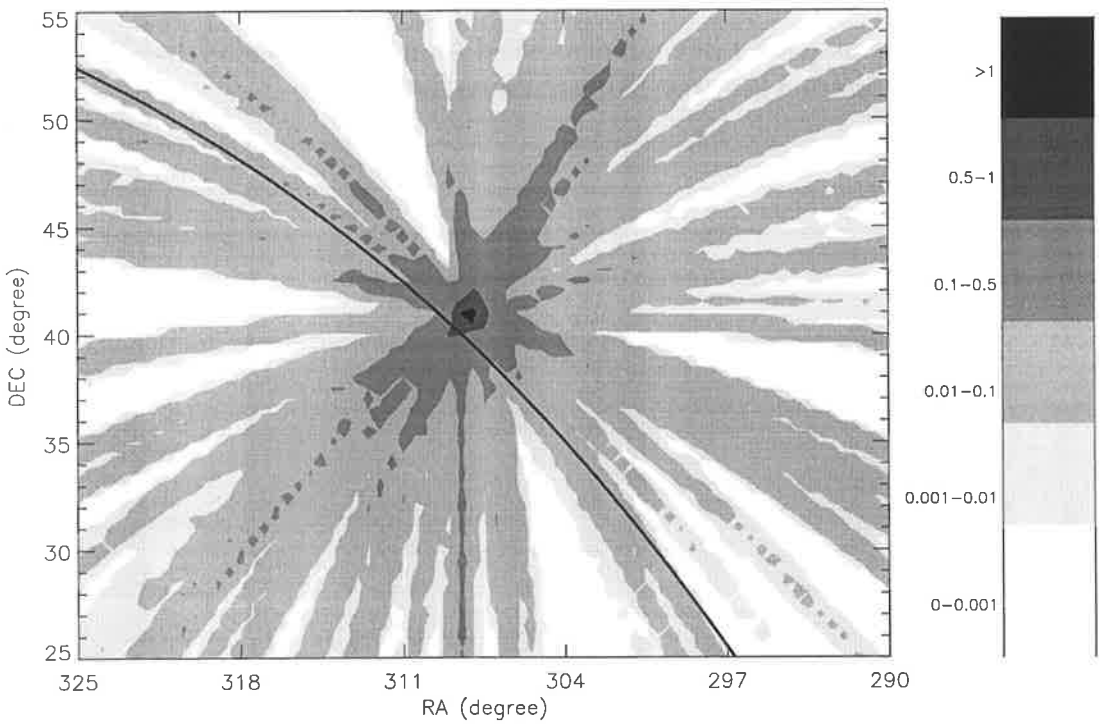

Figure 8.5: Artificial events simulating a point source. The plot show the event density (events per square degree) of 49 artificial events distributed around Cygnus X-3 (see text for details). The elliptical error of each event is oriented toward Cygnus X-3. No background is included in this particular plot.

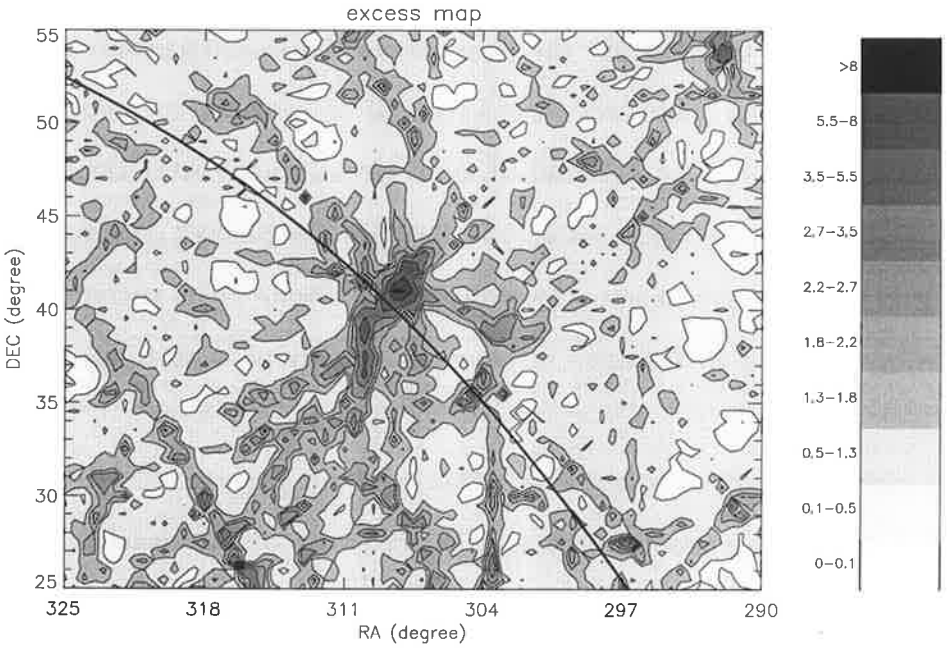

Figure 8.6: Excess map after having introduced 49 artificial events (simulating a point source) shown in figure 8.5 to the HiRes-1 mono data.

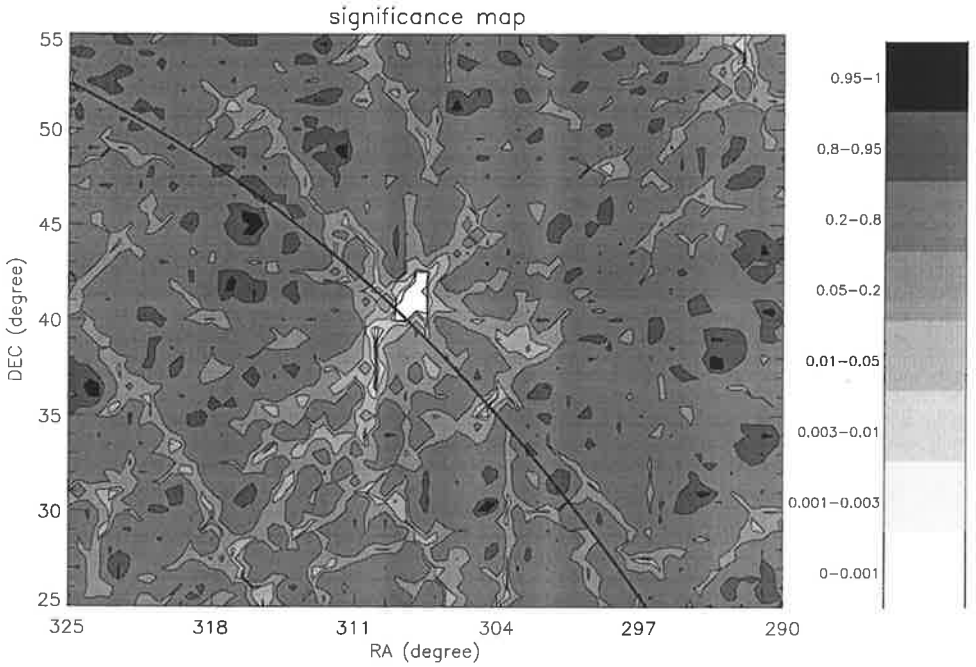

Figure 8.7: Statistical significance of the excess region in figure 8.6.

8.1.4 Calculating the background density

The anisotropy features of a given data set are obtained by comparing the observed shower density distribution with the background. The background is the expected density distribution of cosmic rays assuming an isotropic flux. Calculation of the background must take into account the operation time periods, the detection efficiency for different shower zenith angles and primary energies, and the cosmic ray spectrum.

A traditional technique used to estimate the background is the time shuffling technique (this technique was described in chapter 2). This technique relies on real event information to estimate the background. Each event arrival direction is randomly paired with another event arrival time. By doing so, the right ascension (RA) of the resultant event is randomized according to the detector operation time periods. The declination (DEC) is not affected when the arrival time of an event is changed. The estimated background using the time shuffling technique has similar distributions for the arrival times, the zenith angles and the primary energies as the real data set.

The HiRes detector has permanent exposure to the North celestial pole. Because of this, the time shuffling technique has some difficulties in estimating the background at this region. At the pole, the estimated background would always be similar to the observed signal. Therefore a possible excess or deficit of cosmic rays from the pole region would always be masked. To illustrate this point, a density map containing 3571 events was generated using MC events (see below for a description), and three artificial sources at RA 60° and declinations 0°, 45° and 90° were introduced. The magnitudes of the artificial sources are 7 times the expected number of events within 5° radius circles in the corresponding regions. Figures 8.8 and 8.9 show the estimated excess and significance maps respectively using the traditional time shuffling technique. Notice that neither the excess map nor the significance map show the source at the pole region, but they do show the other two sources.

The author designed an alternative technique to estimate the expected cosmic ray background. This technique uses a large MC data set with similar zenith and azimuth

distributions as the real data set. Note that lower energy events have a different zenith angle distribution to higher energy events (higher energy events would tend to have higher zenith angles). In order to generate the celestial coordinates for the MC data, each MC arrival direction is paired with a real event arrival time.

For anisotropy studies of events with energies below and above 4×10^{19} eV two different monocular MC data sets with 10968 and 10466 events were generated respectively. The zenith and azimuth angle distributions of these MC data sets are consistent with those observed at energy below and above 4×10^{19} eV respectively.

A total of 2309 and 920 cosmic rays with energies between 10^{18} and $10^{18.5}$ eV and between $10^{18.5}$ to $10^{18.0}$ eV were observed in the mono data set (after quality cuts) respectively. Therefore, in order to generate a particular background density map for these energy ranges, 2309 and 920 events were randomly selected from the entire MC data set respectively. Each of these events was randomly associated with a real event arrival time. The event uncertainty region was assigned according to the geometry of each MC event and according to table 6.1. Note that the number of events in any declination band of a background map may fluctuate, including at the pole region. This feature allows the determination of any excess or deficit at the pole.

Considering again the synthetic data set with three artificial sources, figures 8.10 and 8.11 show the excess and significance maps. This maps were estimated using MC events and real arrival times to produce each of the 1000 density background maps used in the analysis. Notice that the significance map (fig. 8.11) does show the excess at the pole region.

For the HiRes anisotropy analysis, the author will use this alternative technique to produce the expected shower density background maps.

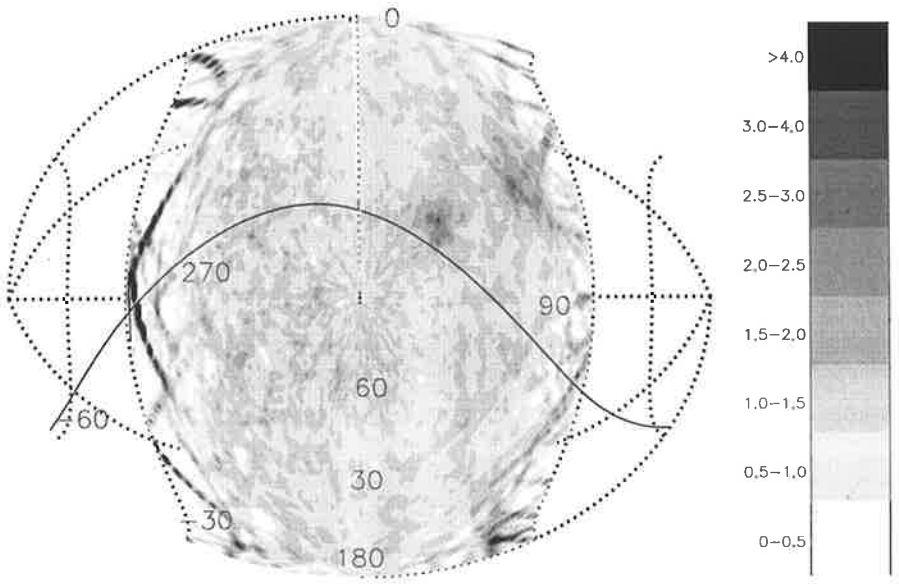

Figure 8.8: Estimated excess map using the traditional time shuffling technique. Three artificial sources were introduced at declinations of 0, 45 and 90 degrees. The number of artificial events at each source is 7 times the background at each declination level. The coordinates are projected over an Aitoff projection map. The celestial North pole is located at the centre of the map.

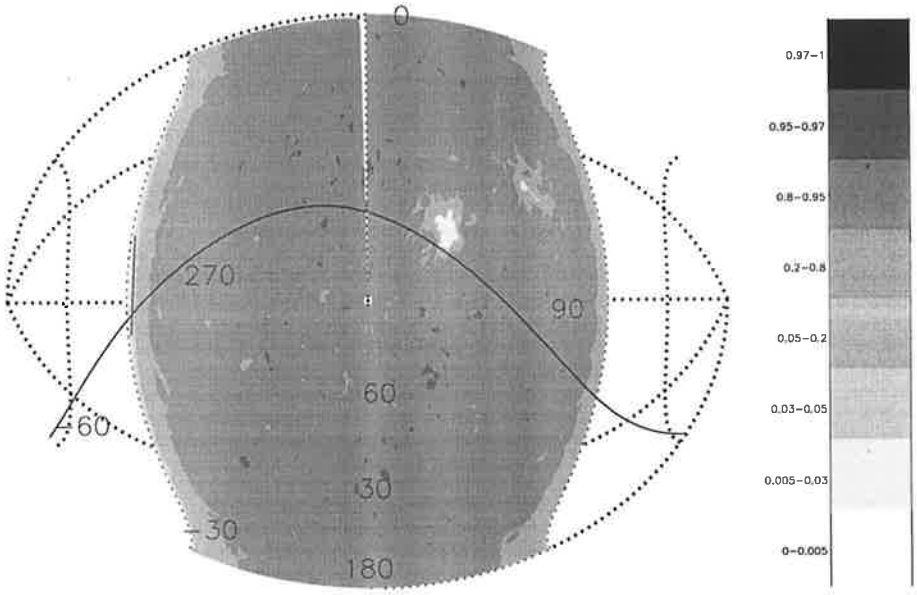

Figure 8.9: Chance probability of having in each bin an excess greater than or equal to that in figure 8.8 (Significance map). The 1000 isotropic background maps used in the analysis were estimated using the traditional time shuffling technique.

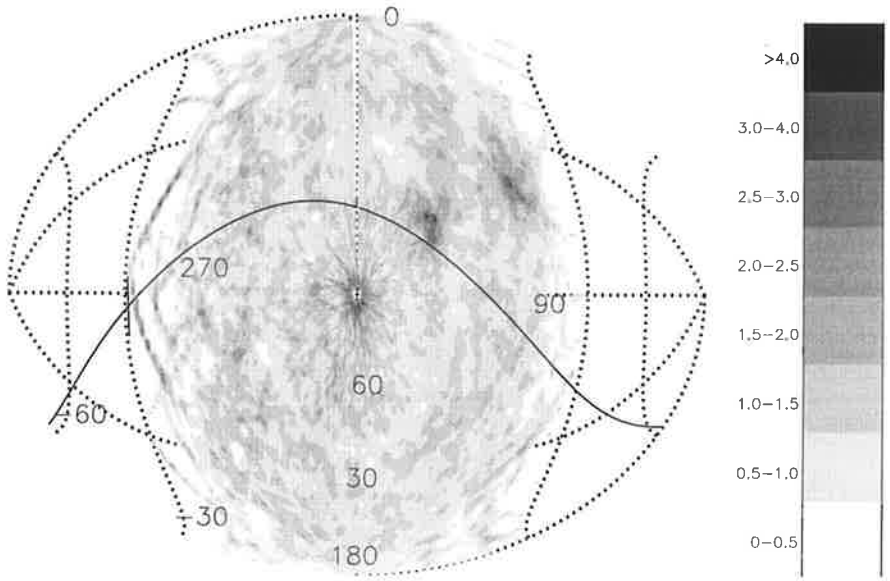

Figure 8.10: Estimated excess map using MC events (MC geometry) combined with real arrival times to produce the background maps used in the analysis (see text for details).

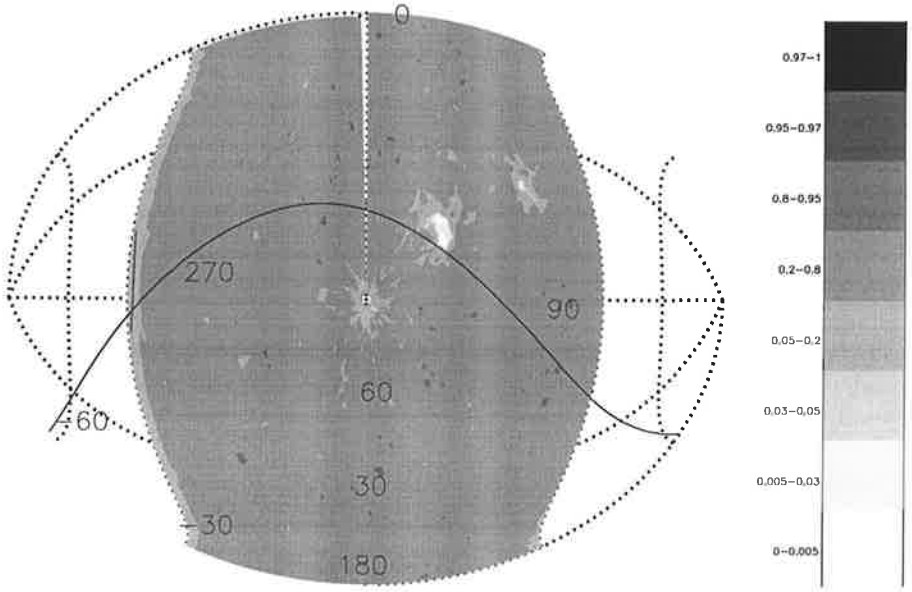

Figure 8.11: Chance probability of having in each bin an excess greater than or equal to that in figure 8.10 (Significance map). The 1000 isotropic background maps used in the analysis were estimated using MC events (MC geometry) associated with real event arrival times. Compare this map with figure 8.9.

8.2 HiRes-1 anisotropy results

As seen in chapter 2, there may be different anisotropy features expected for different energy ranges. Any HiRes confirmation of previous observations would have higher statistical significance than any new source candidate this analysis may point out. In this section we study the HiRes anisotropy features.

8.2.1 Cosmic rays with energies above 10^{18} eV

The HiRes-1 mono data set has 3571 events above 10^{18} eV after applying quality cuts (see chapter 6 for details). First we will search for point sources, and then for astrophysically smeared sources.

8.2.1.1 Searching for point sources

Figures 8.12 and 8.13 show the shower density and expected background maps. The expected background is the average of 1000 backgrounds maps generated using MC event geometries and real event arrival times (see description above), and we will apply this method for all energy ranges. The excess ratio and the statistical significance of the excess are shown in figures 8.14 and 8.15. In figure 8.15 and in all significance maps, a small value (lighter colors) indicates a low probability of having the observed excess by chance. A significance value around 0.5 means that the observed signal was consistent with the expected one. A significance value close to 1 (darker color), means a high probability of having a greater signal than the observed one. Therefore, darker regions indicate a deficit of cosmic rays.

Figure 8.15 does not show significant evidence of any point source. However, it shows a region with a few excess peaks around RA=130°, DEC=40°. The biggest peak is located at RA=130°, DEC=50°, and has a chance probability between 0.03 and 0.05. No excess is observed from the region of Cygnus X-3, one of our *a priori* sources.

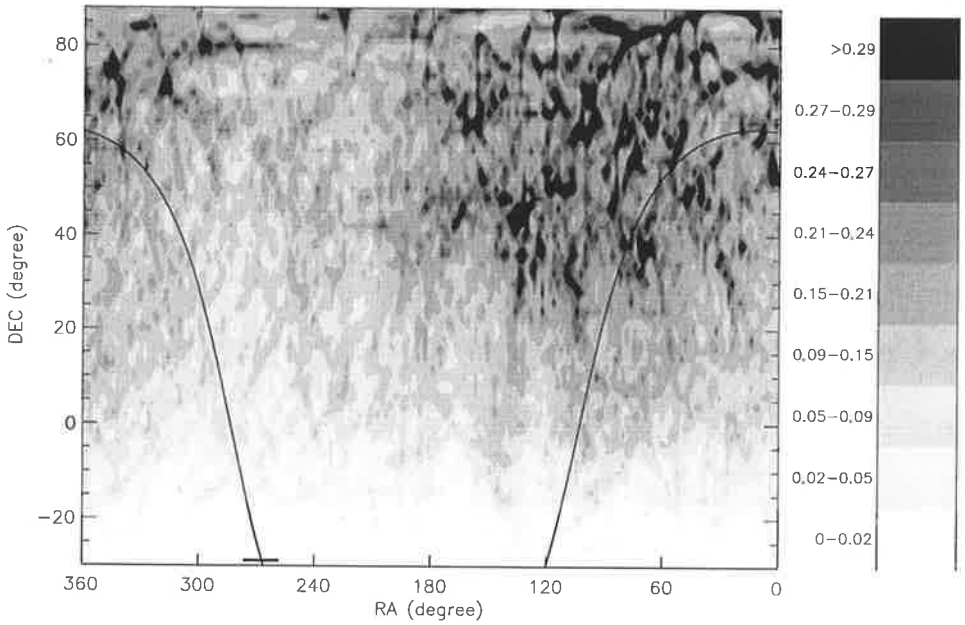

Figure 8.12: Cosmic ray event density for the 3571 events above 10^{18} eV (HiRes-1 mono events). The density scale represents the number of events viewed per true square degree of sky. A three dimensional ellipsoid with total volume equal to one represents the angular uncertainty of each event.

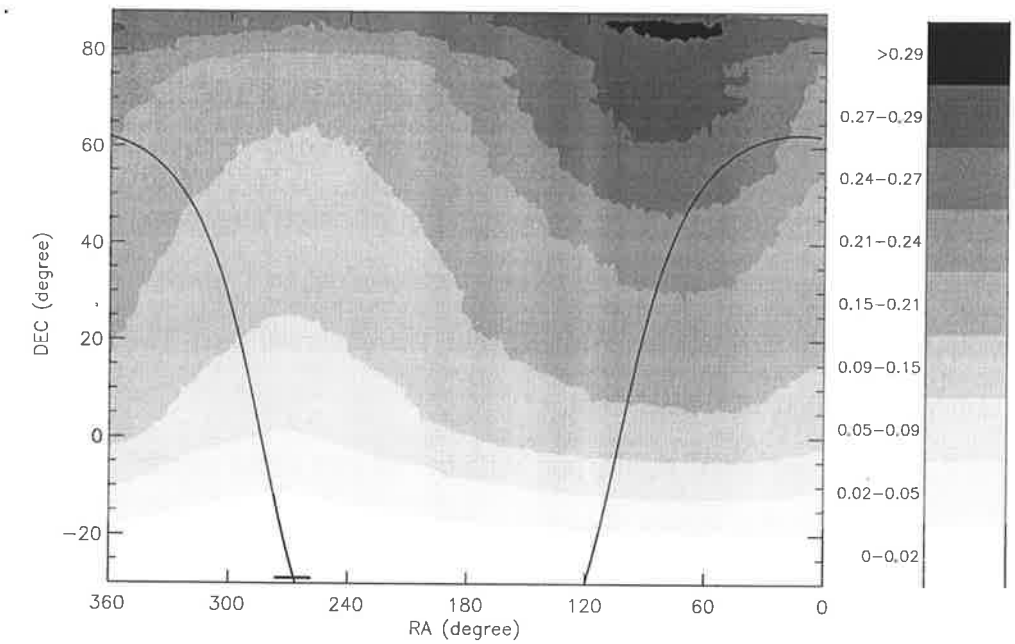

Figure 8.13: The expected density of events for an isotropic flux of cosmic rays above 10^{18} eV. The density is given in units of events per true square degree. The solid line indicates the galactic plane.

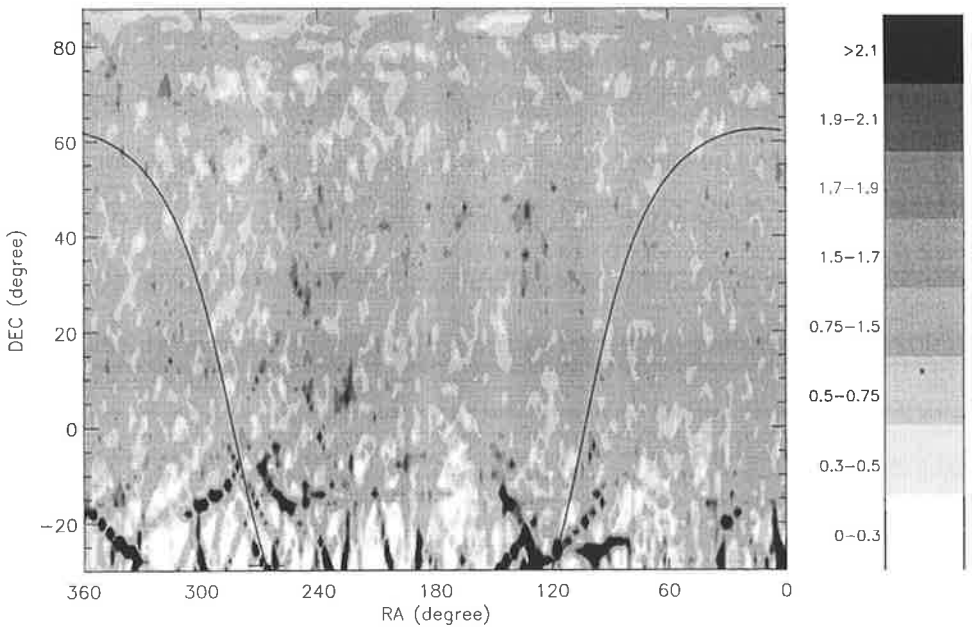

Figure 8.14: Fractional excess map. This map is obtained by comparing Figs. 8.12 and 8.13. A value of 1 indicates that the measured density is in agreement with the expected density.

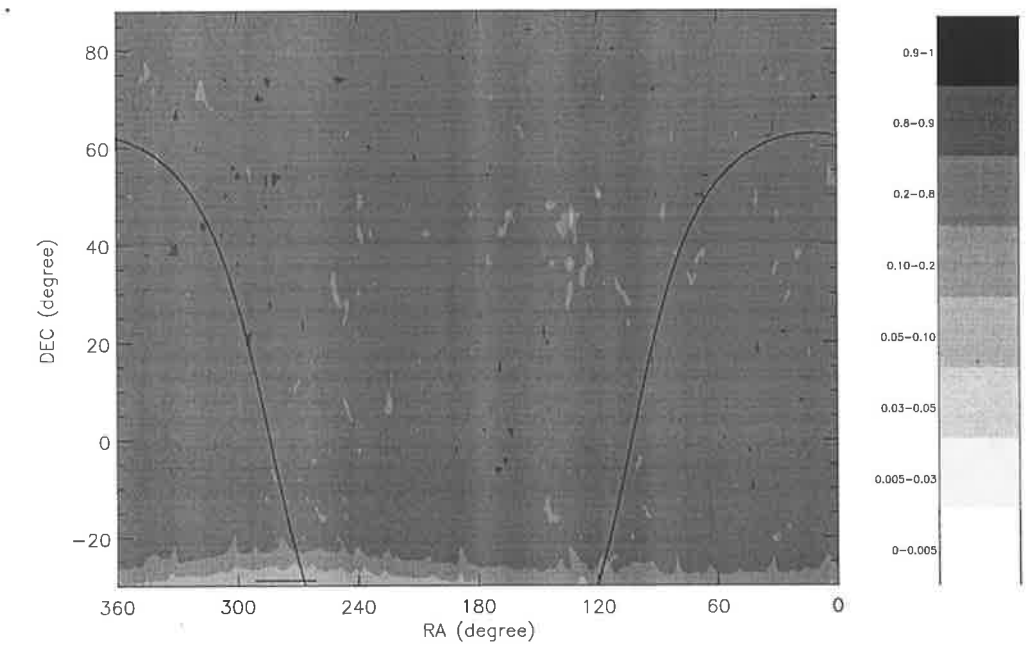

Figure 8.15: The Significance of the excess regions (events above 10^{18} eV). The contours represent the chance probability of detecting the observed density or greater. This map is constructed using the 1000 background maps derived from MC data and real event arrival times.

Given the large number of bins 0.5° × 0.5° (172,800 bins) in the significance map (figure 8.15), one would expect a few bins with the lowest possible chance probability value. The reason for not observing such bins in figure 8.15 is partly due to the algorithm that defines the contour levels, and partly due to the elongated Gaussian probability function representing each arrival direction. The elongated Gaussian probability functions mean that neighboring bins are statistically correlated. This reduces the number of independent bins in the map. Figure 8.16 shows the bins that had a chance probability value lower than or equal to 0.005.

Figures 8.17 to 8.24 show the results considering events between $10^{18.0}$ and $10^{18.5}$ eV and events between $10^{18.5}$ and 10^{19} eV independently. At lower energies, the significance map (fig. 8.20) shows two fairly big regions with a few significant excess peaks. These excess regions are approximately at RA=130°, DEC=40° and at RA=260°, DEC=40°.

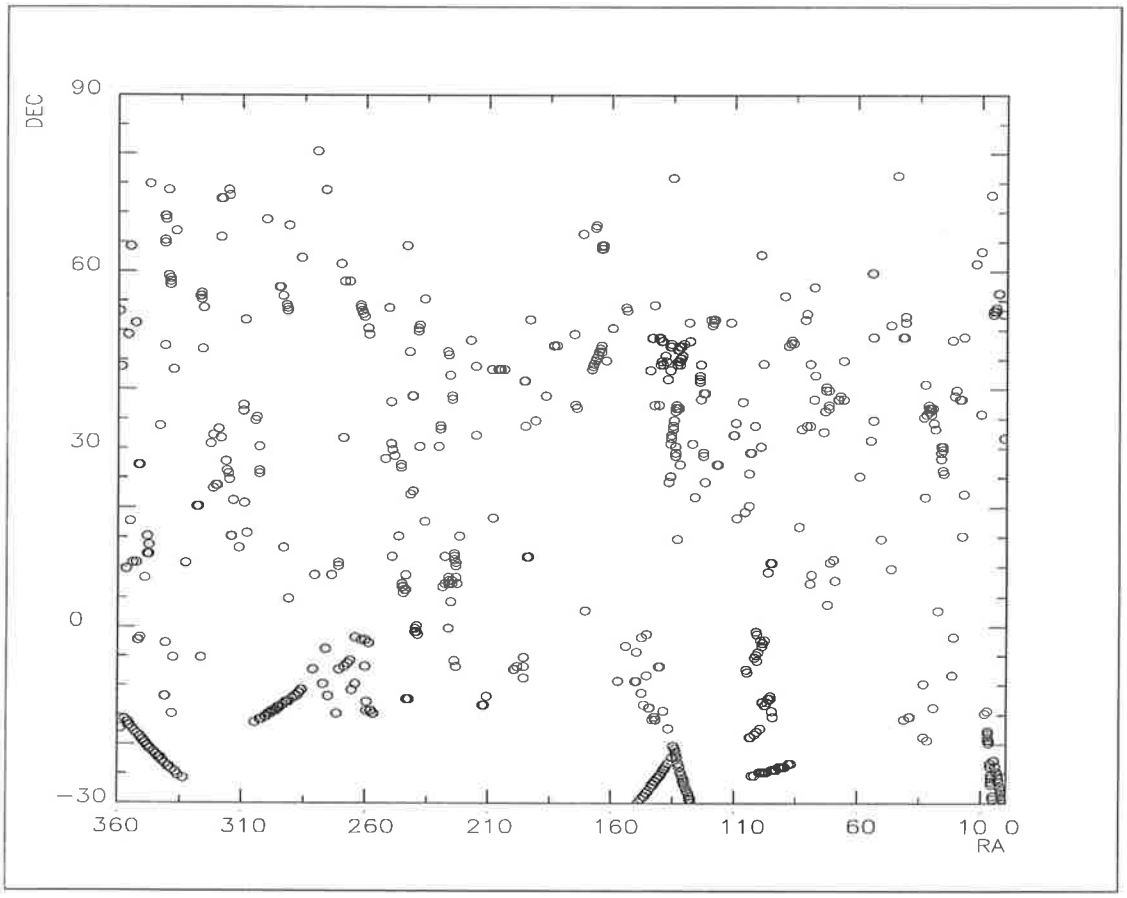

Figure 8.16: This plot shows the bins that had a chance probabilty value lower than or equal to 0.005 in figure 8.15.

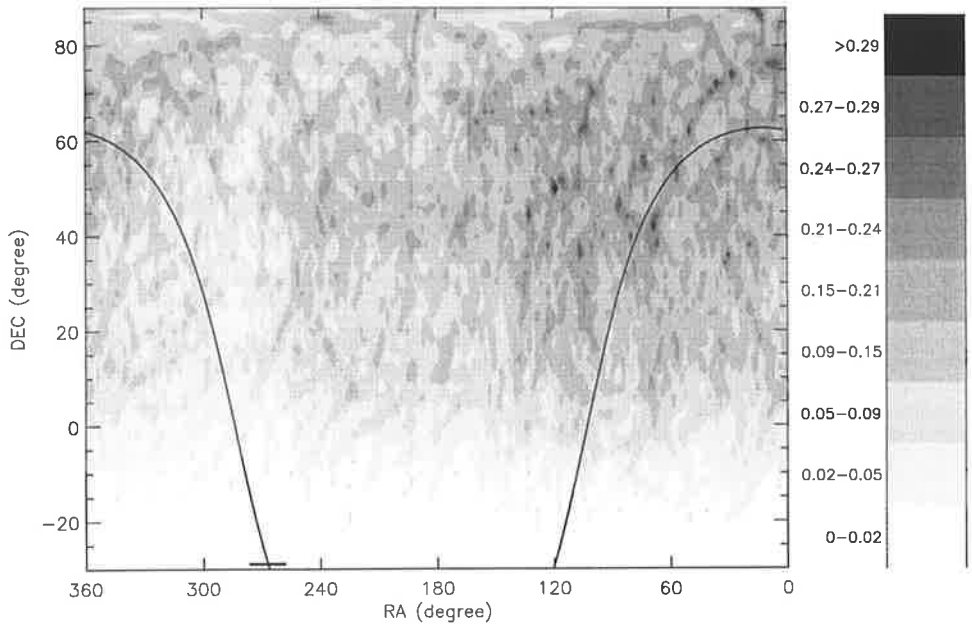

Figure 8.17: Cosmic ray event density for the 2309 events between $10^{18.0}$ and $10^{18.5}$ eV (HiRes-1 mono events). The density scale represents the number of events viewed per true square degree of sky. A three dimensional ellipsoid with total volume equal to one represents the angular uncertainty in each event.

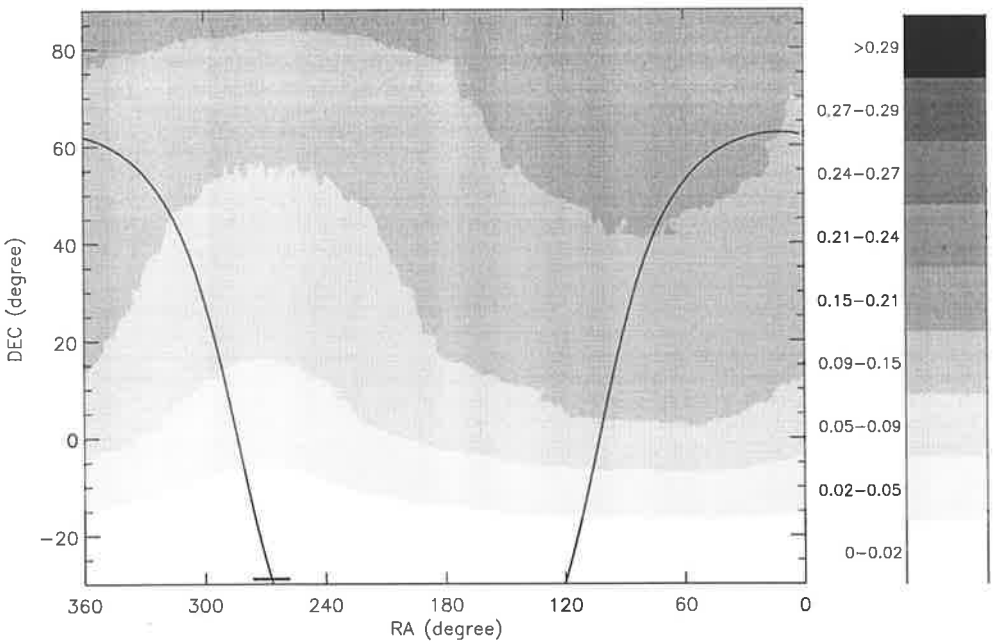

Figure 8.18: The expected density of events for an isotropic flux of cosmic rays between $10^{18.0}$ and $10^{18.5}$ eV. The density is given in units of events per true square degree.

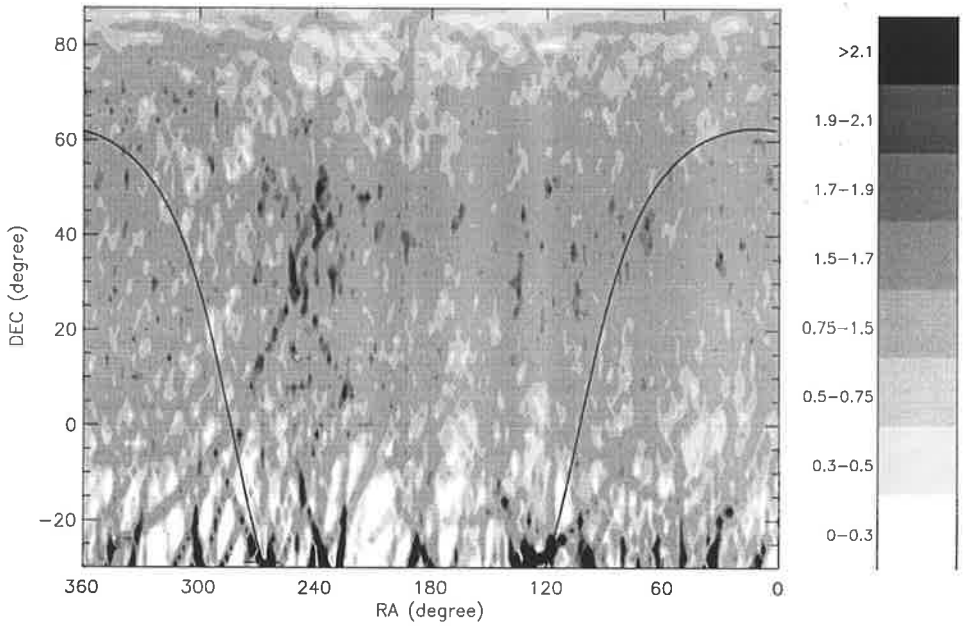

Figure 8.19: Fractional excess map. This map is obtained by comparing Figs. 8.17 and 8.18. A value of 1 indicates that the measure density is in agreement with the expected density.

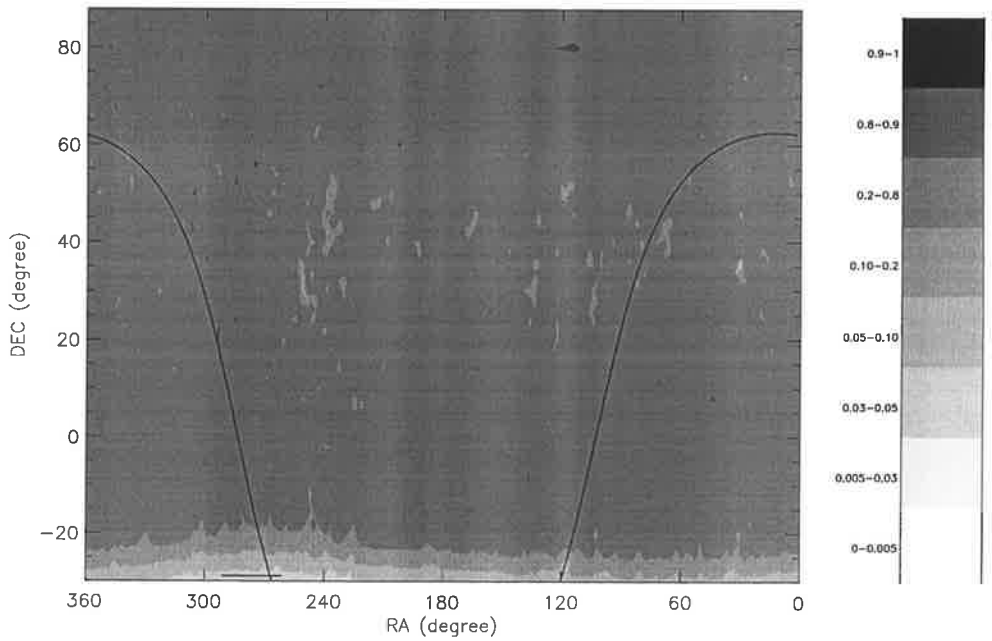

Figure 8.20: The Significance of the excess regions (events between $10^{18.0}$ and $10^{18.5}$ eV). The contours represent the chance probability of detecting the observed density or greater.

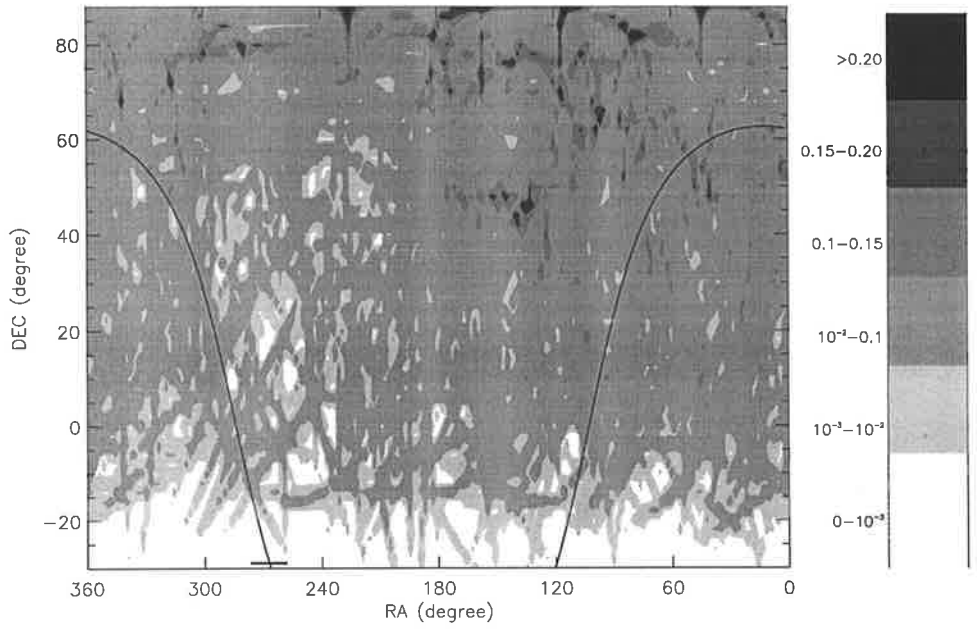

Figure 8.21: Cosmic ray event density for the 920 events between $10^{18.5}$ and $10^{19.0}$ eV (HiRes-1 mono events). The density scale represents the number of events viewed per true square degree of sky. A three dimensional ellipsoid with total volume equal to one represents the angular uncertainty in each event.

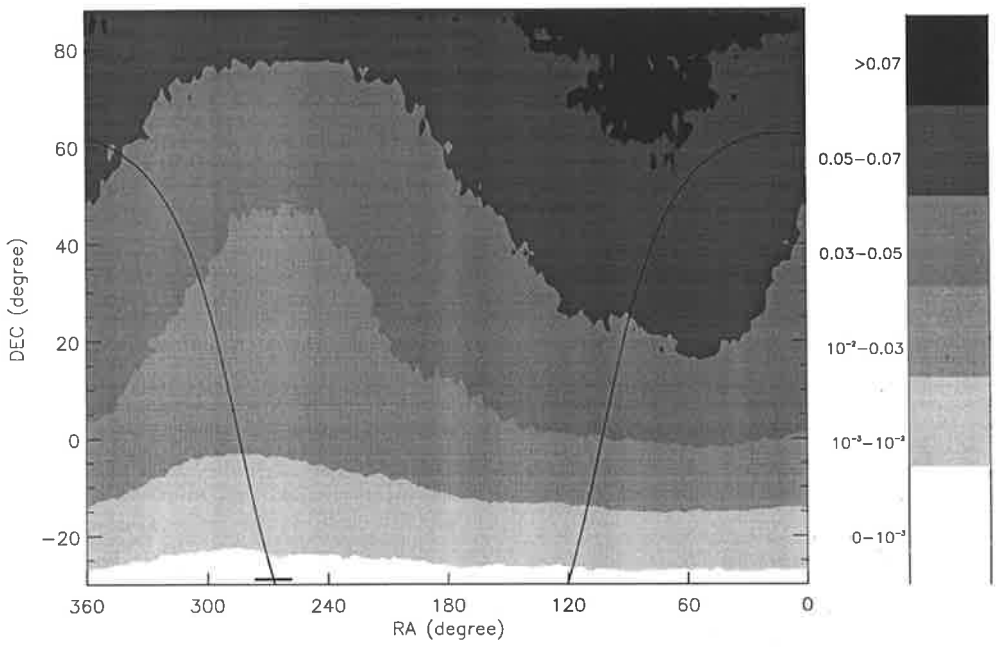

Figure 8.22: The expected density of events for an isotropic flux of cosmic rays between $10^{18.5}$ and $10^{19.0}$ eV. The density is given in units of events per true square degree.

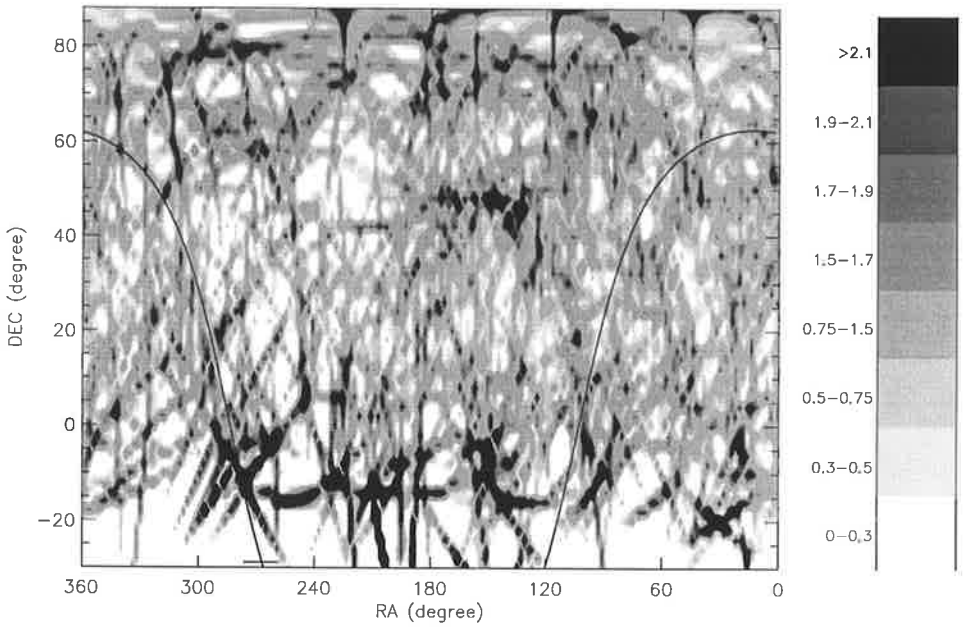

Figure 8.23: Fractional excess map. This map is obtained by comparing Figs. 8.21 and 8.22. A value of 1 indicates that the measure density is in agreement with the expected density. However, due to the small number of events (920 events), the magnitude of the excess becomes less meaningful.

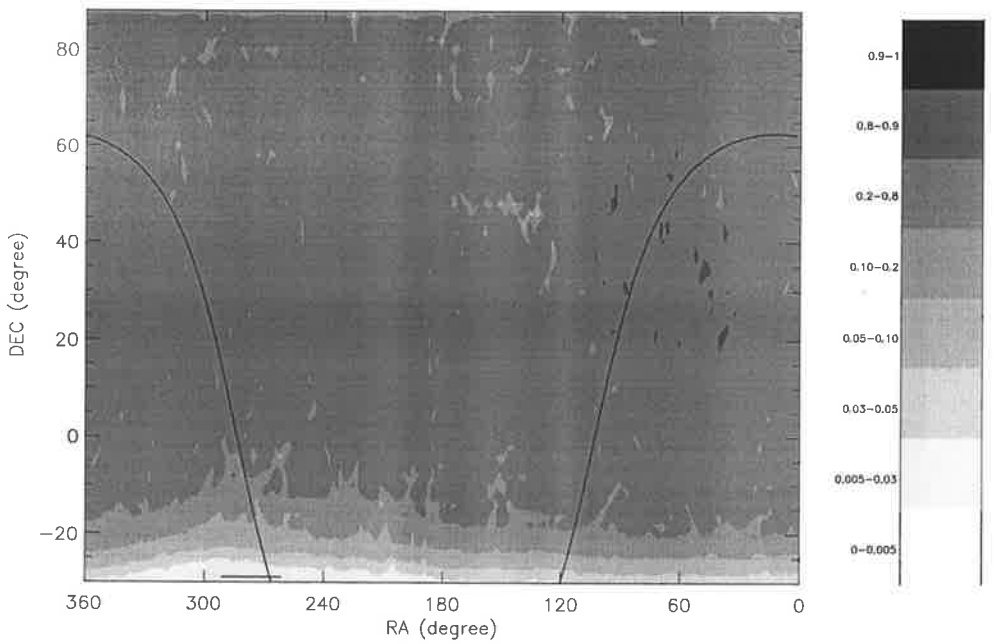

Figure 8.24: The Significance of the excess regions (events between $10^{18.5}$ and $10^{19.0}$ eV). The contours represent the chance probability of detecting the observed density or greater.

At energies between $10^{18.5}$ and $10^{19.0}$ eV the significance map (fig. 8.24) shows a region with a few bins of significant excess. This excess region is located at around RA=138°, DEC=47°. A zoom of this region is shown in figure 8.25. The peak corresponds to a contour level between 0 and 0.005. The source of this excess is more likely to be poor statistics or an astrophysically smeared source (see below for details). It does not look like a point source because there are a few significant peaks a few degrees apart.

Figure 8.25 does not look as smooth as figure 8.24. This is because the contour plot resolution for full sky maps is 2° in RA by 2° in DEC, and the resolution for the zoom plot is 0.5° in RA and DEC.

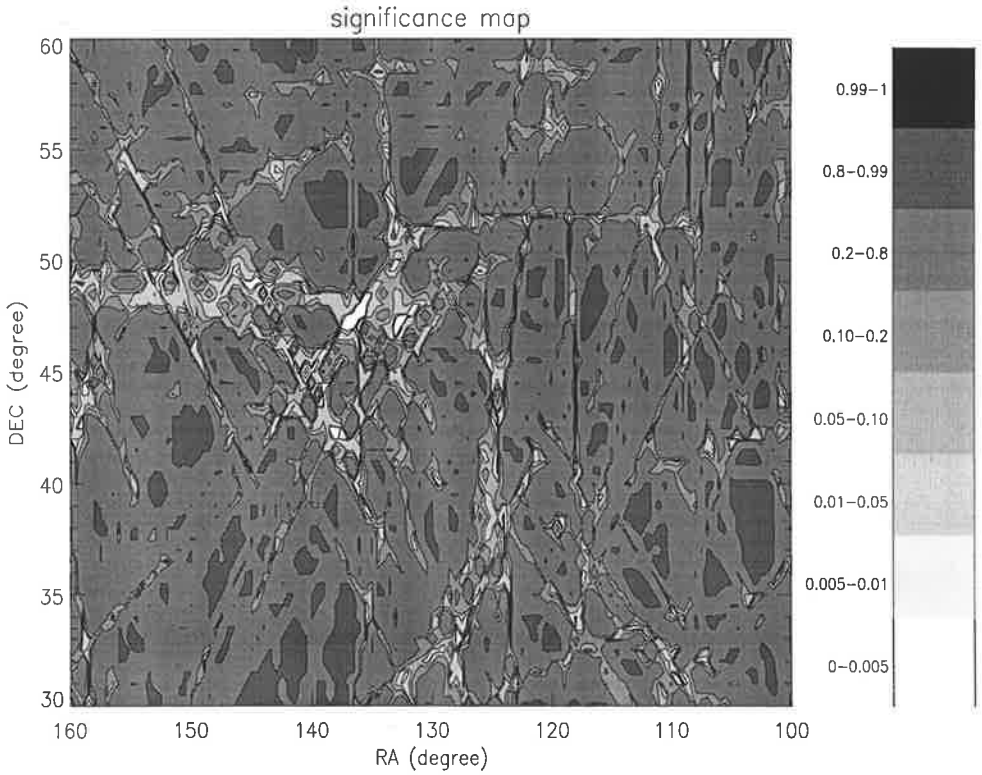

Figure 8.25: Zoom of the significance map (fig.8.24) around the region RA=138°, DEC=47°.

8.2.1.2 Searching for astrophysically smeared sources

Figures 8.20 and 8.24 show some regions that contain a few excess peaks. In this section we apply the technique described in section 8.1.1 to see whether these excess regions are consistent with astrophysically smeared sources. Note that we have already explored the sky map above 10^{18} eV as defined in our pre-published strategy [105]. We did not observe any outstanding excess in that "raw" map. Thus we are now free to apply a few more trials to see whether any excess is enhanced by considering a smearing hypothesis.

In order to check whether these excess regions are consistent with astrophysical smeared sources we tried different smearing circle sizes. For every $2^\circ \times 2^\circ$ bin on the skymap, we calculate the total shower density within the smearing circle centred at that bin. This produces the "smeared" density map. Considering only bins around the excess regions, figure 8.26 shows the distribution of the number of sigmas of excess for different smearing sizes. In the energy range between $10^{18.0}$ and $10^{18.5}$ eV there are two excess regions. They are located around RA=130°, DEC=40° and around RA=240°, DEC=40° . In the energy range between $10^{18.5}$ and 10^{19} eV there is only one excess region. This excess region is around RA=138°, DEC=47°.

The number of sigmas of excess is defined as the difference between the observed signal and the background divided by the square root of the background. The signal and the background represent the sum of events within a circle with radius equal to the smearing size. The circle is centred at the respective bin. The background is the average of 1000 synthetic data sets produced using MC geometries and real arrival times. Figure 8.26 shows that smearing sizes of 20° and 10° maximize the excess region observed around RA=130°, DEC=40° and RA=138°, DEC=47° at energies between $10^{18.0}$ and $10^{18.5}$ eV and between $10^{18.5}$ and $10^{19.0}$ eV respectively. The excess region observed at RA=240°, DEC=40° at energies between $10^{18.0}$ and $10^{18.5}$ eV, is maximized with a smearing size of 15°. The criteria adopted to select the optimum smearing sizes from figure 8.26 is that the distribution should be peaked at a high

excess, and it should have fewer bins with a lower excess.

Figures 8.27 and 8.28 show the significance sky maps using 20° and 10° smearing sizes respectively for the two different energy ranges. The significance maps were generated as described in section 8.1.1.

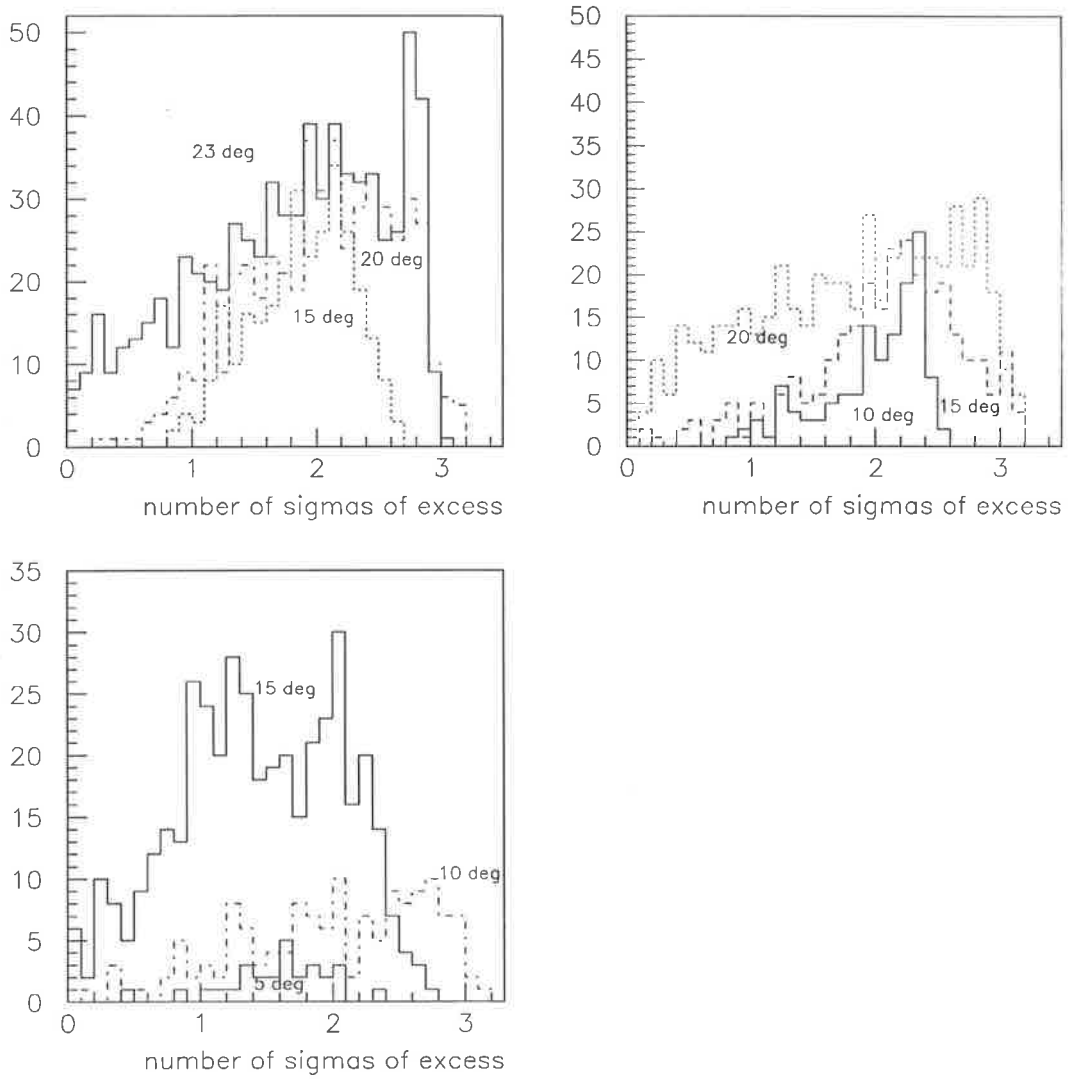

Figure 8.26: Distribution of the number of sigmas of excess for different smearing sizes (see text for details). The smearing sizes are indicated in the plots. The upper plots correspond to the excess regions observed at energies between $10^{18.0}$ and $10^{18.5}$ eV. The upper left and right hand side plot are for the regions around RA=110°, DEC=39° and RA=242°, DEC=40° respectively. The bottom plot corresponds to the excess region observed at energies between $10^{18.5}$ and 10^{19} eV around RA=139°, DEC=47°. The bins inside the respective circle smearing size around each excess region were included in the histograms.

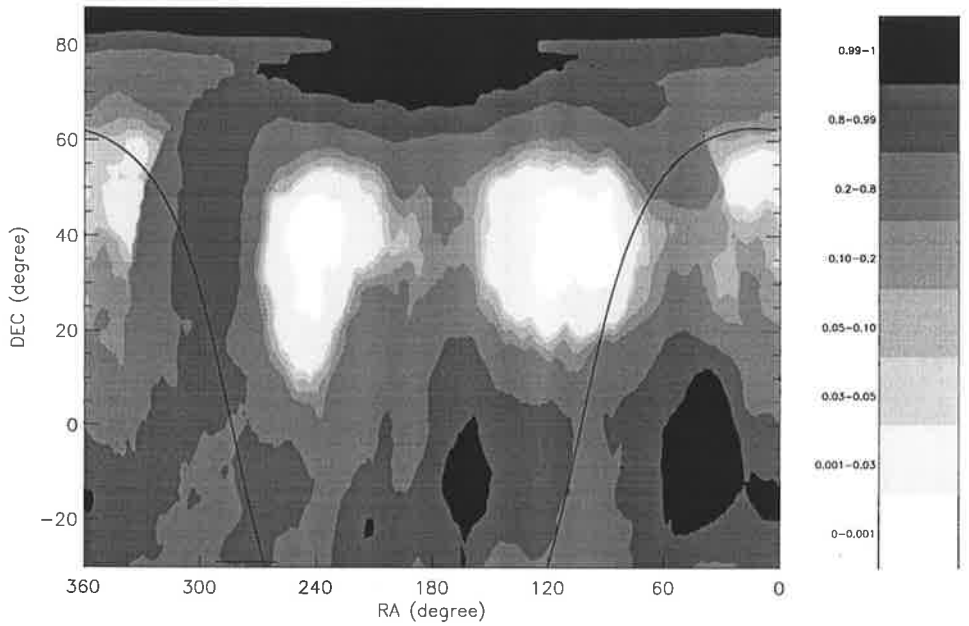

Figure 8.27: Probability of having by chance a greater or equal number of events (events between $10^{18.0}$ and $10^{18.5}$ eV) than that expected in the respective bin (Significance map). The computed signal in each bin corresponds to the number of events within 20° radius (20° maximizes the excess at this energy range, see fig. 8.26).

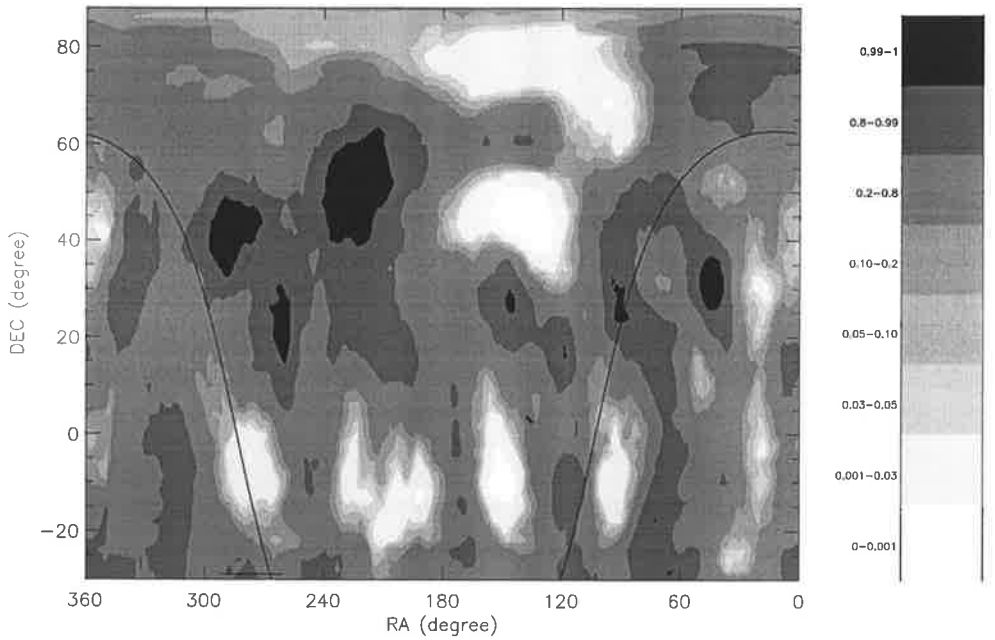

Figure 8.28: Probability of having by chance a greater or equal number of events (events between $10^{18.5}$ and $10^{19.0}$ eV) than that expected in the respective bin (Significance map). The computed signal in each bin corresponds to the number of equivalent events within 10° radius (10° maximizes the excess at this energy range, fig. 8.26).

The significance maps (fig. 8.27 and fig. 8.28) indicate the chance probability of having the observed excess *at those particular regions.* Considering the center of one of the excess regions (RA=110°, DEC=39°) in figure 8.27, the computed signal per bin is $S = 199.4 \pm 9.2$ events, and the estimated background is $B = 166.4 \pm 9.1$ events. The errors correspond to one standard deviation of the signal and background distributions considering only bins with chance probability lower than 0.001. The Poisson probability of having a signal $S = 199$ or higher when the expected background is $B = 166$ is 0.0076. If we consider the quoted uncertainties in S and B, the Poisson probability can be as low as 0.00064. Therefore, the estimated significance (< 0.001) is consistent with that expected for Poisson fluctuations.

None of the excess regions in figures 8.27 and 8.28 were quoted as '*a priori*' source candidates. Therefore, the chance probability of these excesses should be higher than the estimated significance. The estimated significance would only be meaningful for '*a priori*' source candidates. For excesses that are not correlated with any '*a priori*' source candidate, we should take into account that these excess may happen by chance anywhere on the sky map.

In order to determine the chance probability of having an excess anywhere in the sky map like those observed in figures 8.27 and 8.28, we use the expected background density map. The expected background density map is the average of 1000 backgrouns maps. Each background map was generated using a synthetic data set with isotropic distribution of arrival directions and using smearing circles. The synthetic data sets with isotropic distribution were produced using MC geometries and real event arrival times. The expected background density map is the same density map used to estimate the excess map.

Five series of 1000 synthetic data sets (like those used to generate the expected background density map) were generated. The density map (generated using smearing circles) generated by each synthetic data set was compared with the expected background density map. The number of data sets that produced excess regions (anywhere) with *magnitudes and sizes* similar to or more significant than those observed in figures

8.27 and 8.28 were counted.

The magnitude of the excess in figures 8.27 and 8.28 is indicated by its estimated significance. For strong excesses the estimated significance should be close to 0. Note that the significance values quoted in figures 8.27 and 8.28 were obtained using 1000 synthetic data sets. We would like to avoid going through this process for every trial map in this study. Hence, we have determined a simpler method for assigning a significance, that is to calculate the number of standard deviations of any excess (see fig. 8.26).

The weakness of this procedure is that we do not know precisely the fluctuation of the background signal that corresponds to 1 sigma deviation. However, we can use the approximation that a fluctuation equal to the square root of the background signal corresponds to 1 sigma deviation.

Figure 8.29 shows the relation between the number of sigmas of excess (or deficit) and the estimated significance values in figure 8.27. The bottom right hand side plot shows that a significance value of 0.001 or lower corresponds approximately to bins with 2.5 sigmas of excess. Figure 8.27 has 132 bins with at least 2.5 sigmas of excess in each of the two excess regions. Considering that 1° in RA corresponds to $1° \times cos(DEC)$ (true size) in the sky, each bin has been assigned a weight equal to $cos(DEC)$. Thus, the weighted sum of the 132 bins is 104.

In 5 series of 1000 synthetic data sets, an average of 7.4 out of 1000 data sets produced excess regions with magnitudes ($\geq 2.5\sigma$ of excess) and sizes (≥ 104 weighted bins) similar to or greater than those observed in figure 8.27. However, none of the 5000 data sets produced a map with two such excess regions.

Figure 8.30 shows the results of 1 of the 5 series of 1000 synthetic data sets. The top plot shows the DEC distribution of bins (without weighting) with at least 2.5 sigmas of excess. This distribution shows a higher chance probability of having significant excesses at lower latitudes. The apparent peak around 70° declination may be related with the fact that near the pole region the true size of the bins becomes smaller. Therefore any excess in that region involves a larger number of bins. The bottom plot

shows the weighted sum of bins with at least 2.5 sigmas of excess in each data set.

The probability of having by chance (anywhere in the sky) an excess like that in figure 8.28 is estimated in a similar way. Coincidentally, an average of 7.4 synthetic data sets out of 1000 produced excess regions with magnitudes ($\geq 2.2\sigma$ of excess) and sizes (≥ 57 weighted bins) similar to or greater than the one observed in figure 8.28.

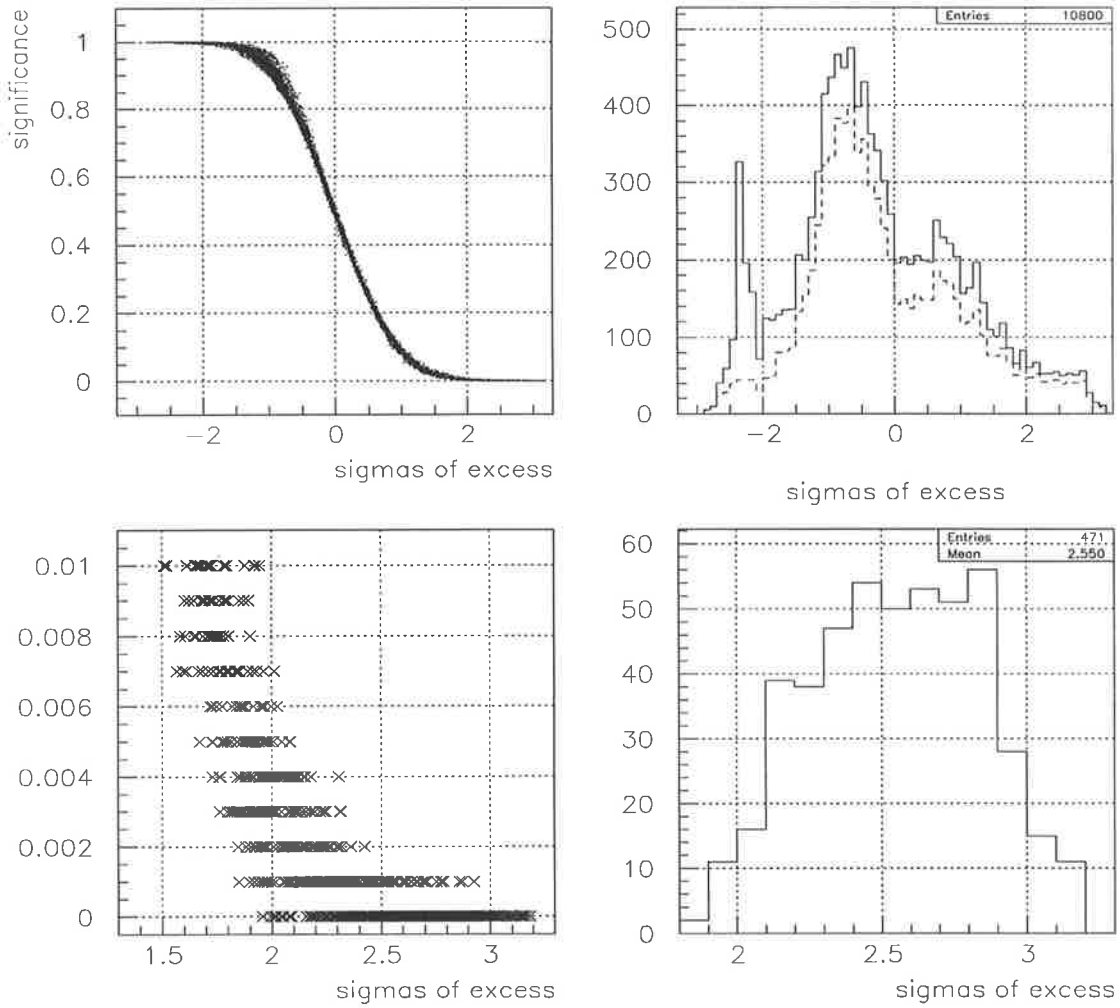

Figure 8.29: Data derived from figure 8.27. The top left hand side plot shows the estimated significance against the observed excess/deficit (in terms of sigmas of excess). The top right hand side plot (solid line) shows the distribution of the observed sigmas of excess in all bins (2° bins in RA and in DEC). The peak present at -2.5 is because a deficit region is located at the pole region (see fig.8.27) and the true size of these bins (in terms of solid angle) are smaller. Thus, the deficit region involved more bins. The dashed lines shows the same distribution assigning to each bin a weight of $cos(DEC)$. The bottom left hand side plot is a zoom of the significance against the observed excess/deficit plot. The bottom right hand side plot shows the number of sigmas of excess distribution for bins with estimated significance 0.001 or lower.

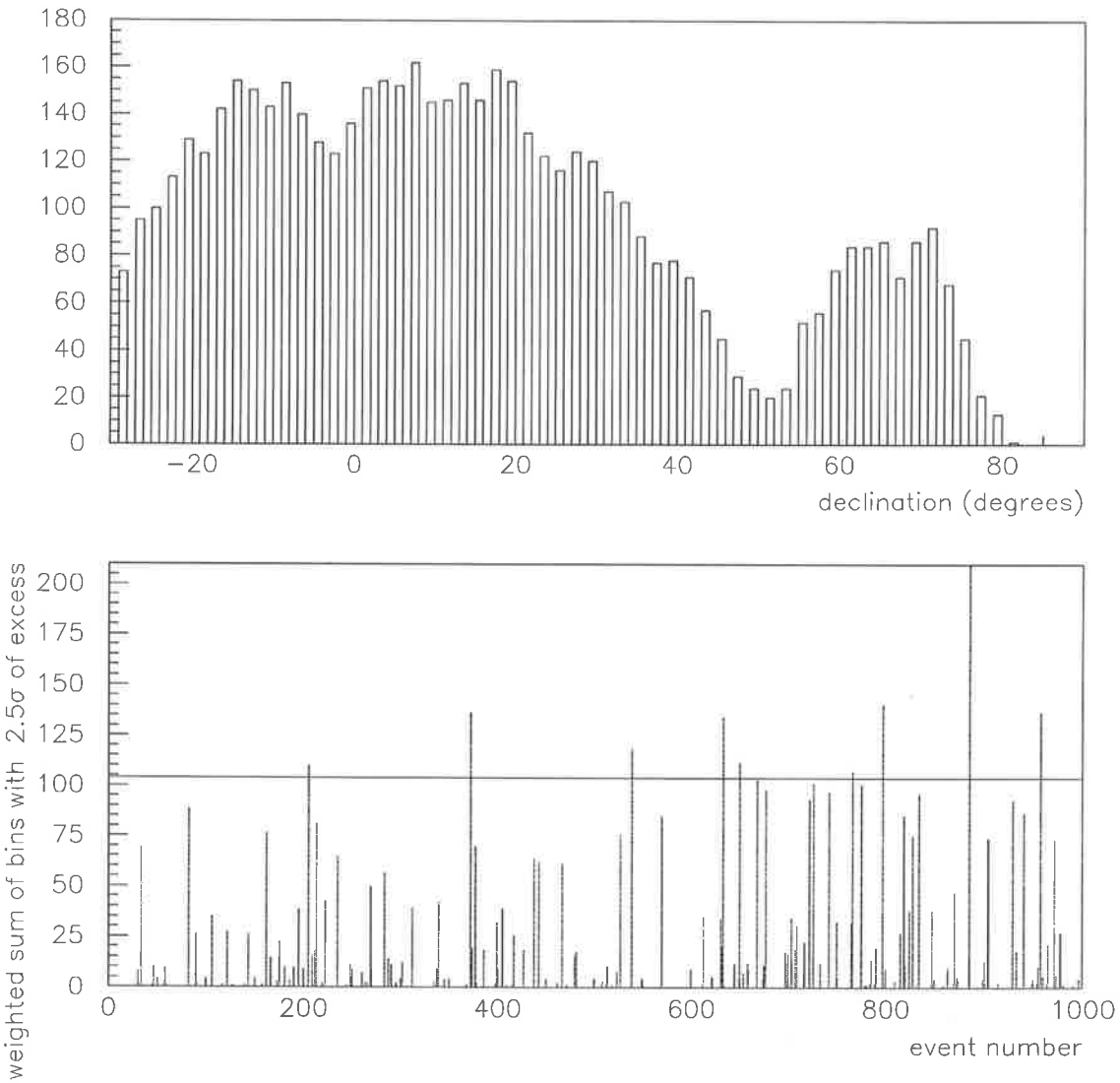

Figure 8.30: Declination distribution of bins having at least 2.5σ of excess in 1000 synthetic data sets (top plot). The lower plot shows the weighted sum of bins having at least 2.5σ of excess in each of the synthetic data sets. The horizontal line indicates the weighted sum of bins having at least 2.5σ of excess in one of the excess regions in figure 8.27.

8.2.1.3 Cygnus X-3

For the HiRes anisotropy analysis, Cygnus X-3 (RA=308°, DEC=40.7°) has been indicated as an *a priori* source candidate of cosmic rays in the $\geq 10^{18}$ eV range [105]. Figure 8.15 does not show evidence of any excess from Cygnus X-3. Recently a systematic energy shift was found in the HiRes-1 monocular reconstruction [108]. The systematic energy correction will raise the actual energies. So, events that actually have energies just below 10^{18} eV, should be considered for this analysis.

8.2.2 Cosmic rays with energies above 10^{19} eV

Anisotropy analysis of cosmic rays above 10^{19} eV becomes complicated because of the lower statistics. The HiRes-1 monocular data set has only 341 events (after quality cuts) above 10^{19} eV. As for lower energies we will search first for point sources, and then for smeared sources.

8.2.2.1 Searching for point sources

Figures 8.31 to 8.34 show the density, background, excess and significance sky maps. The significance map (fig. 8.34) shows several regions with an 'excess' of cosmic rays. Most of them may be due to statistical fluctuations, especially those at lower latitudes where the background is not well defined. Of especial interest are the excesses observed at RA=170°, DEC=62° and at RA=140°, DEC=36°. The first region is $\approx 5°$ away from the AGASA triplet (see table 2.3) one of our *a priori* source regions. The second region is consistent with the excess region observed at energies between 10^{18} and $10^{18.5}$ eV (fig. 8.27) and between $10^{18.5}$ and $10^{19.0}$ eV (fig. 8.28). Because of the low statistics, it is not possible to define whether these excesses correspond to point sources. The chance probabilities of having greater excesses at these regions are 0.05 to 0.1 and 0.03 to 0.05 respectively (from fig. 8.34).

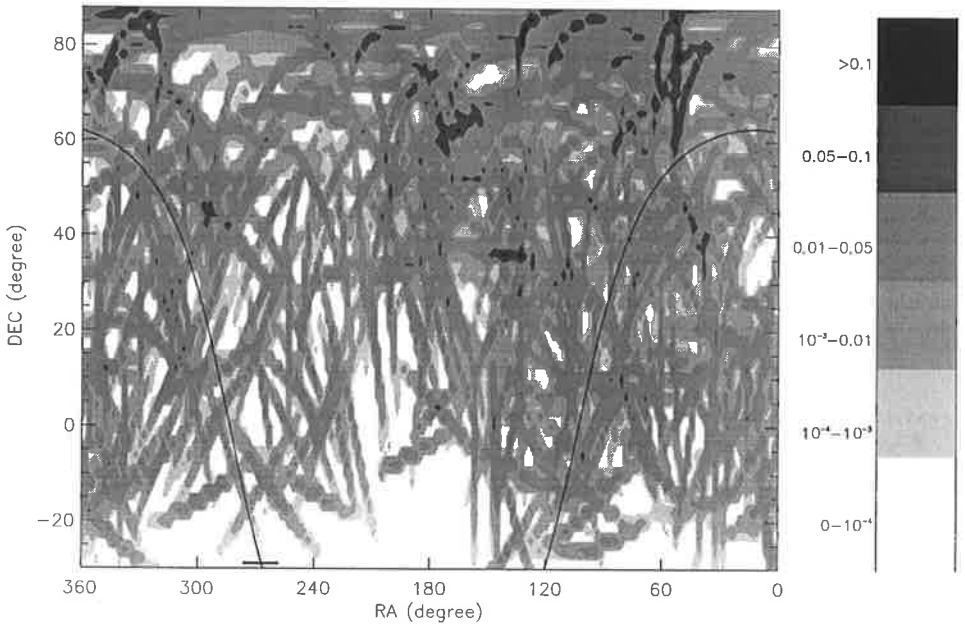

Figure 8.31: Cosmic ray event density for the 341 events above $10^{19.0}$ eV (HiRes-1 mono events). The density scale represents the number of events viewed per true square degree of sky. A three dimensional ellipsoid with total volume equal to one represents the angular uncertainty in each event.

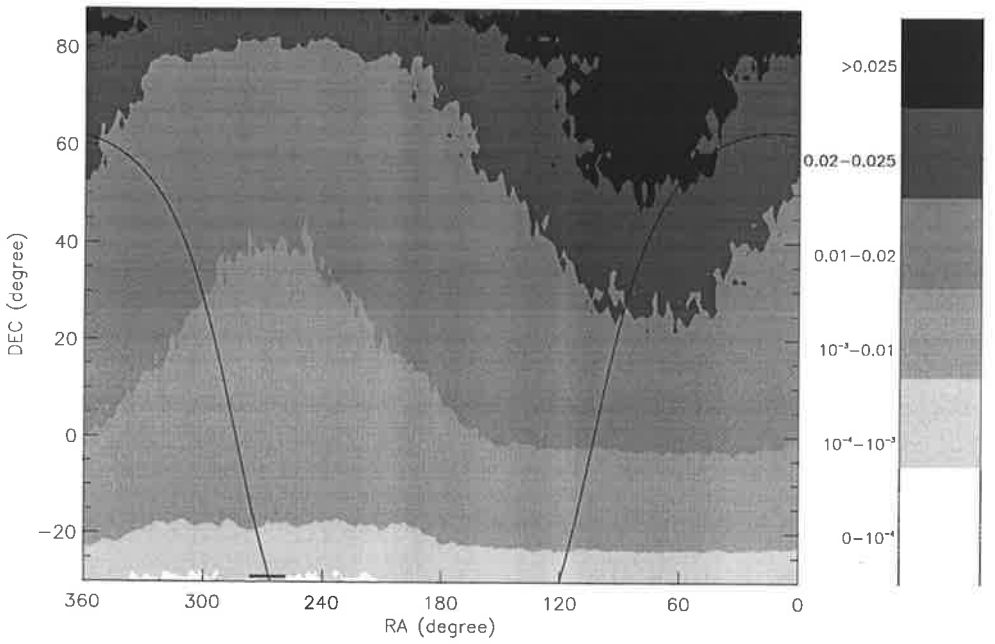

Figure 8.32: The expected density of events for an isotropic flux of cosmic rays above $10^{19.0}$ eV. The density is given in units of events per true square degree.

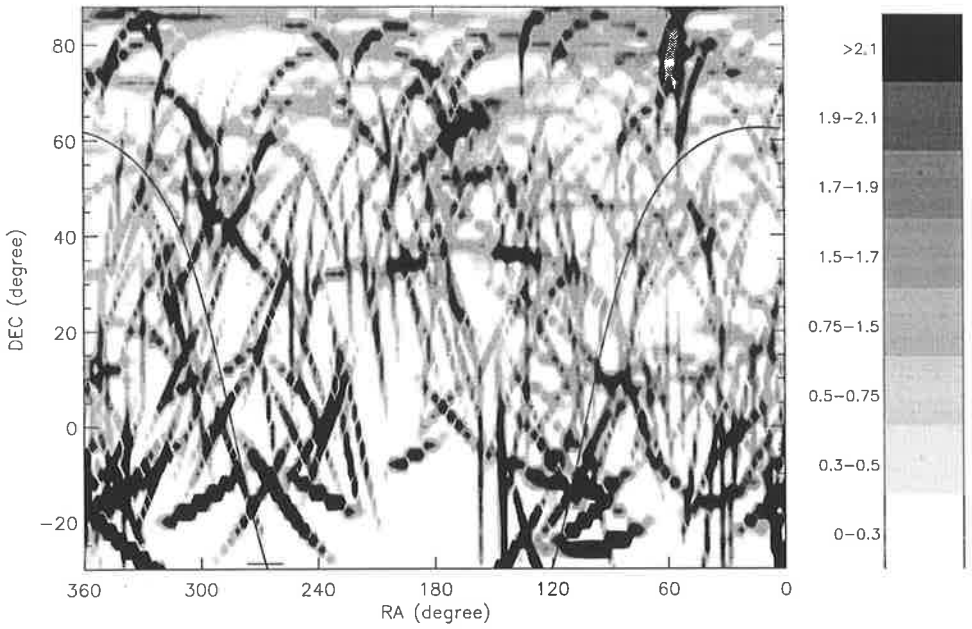

Figure 8.33: Fractional excess map. This map is obtained by comparing Figs. 8.31 and 8.32. A value of 1 indicates that the measure density is in agreement with the expected density. However, due to the small number of events (341 events), the magnitude of the excess becomes less meaningful.

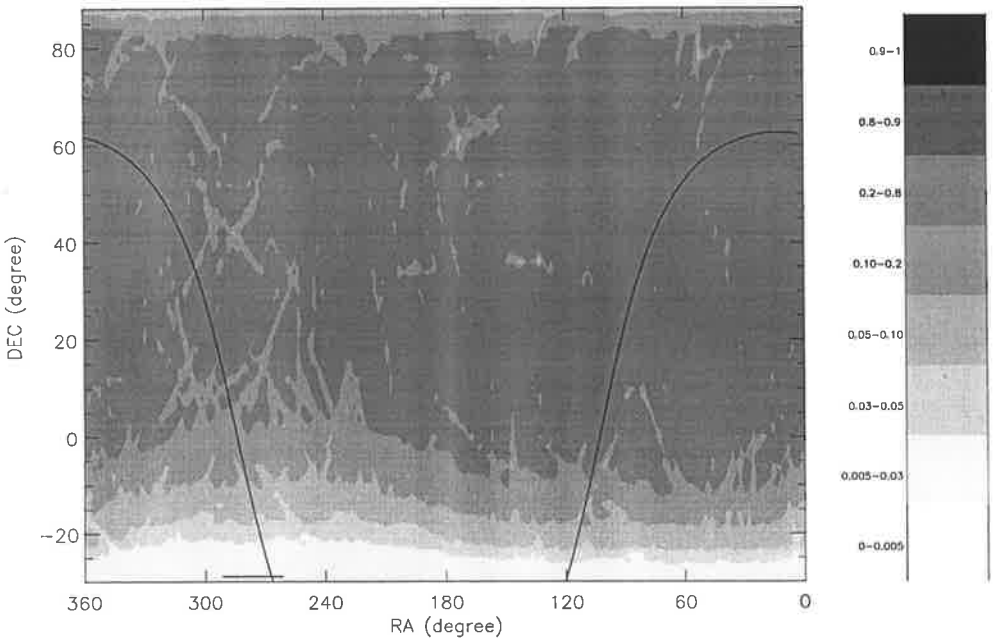

Figure 8.34: The Significance of the excess regions (events above $10^{19.0}$). The contours represent the chance probability of detecting the observed density or greater.

8.2.2.2 Searching for astrophysical smeared sources

Using a similar technique to that described in figure 8.26, an optimum smearing size was estimated. The optimum smearing size maximizes the excess regions of interest in figure 8.34 (RA=170°, DEC=62° and RA=140°, DEC=36°). It was found that both excess regions are maximized with a smearing size of 5°. Figure 8.35 shows the significance map using a smearing size of 5°.

The estimated probability of having by chance a similar or greater excess than that observed at the regions of interest is lower than 0.001.

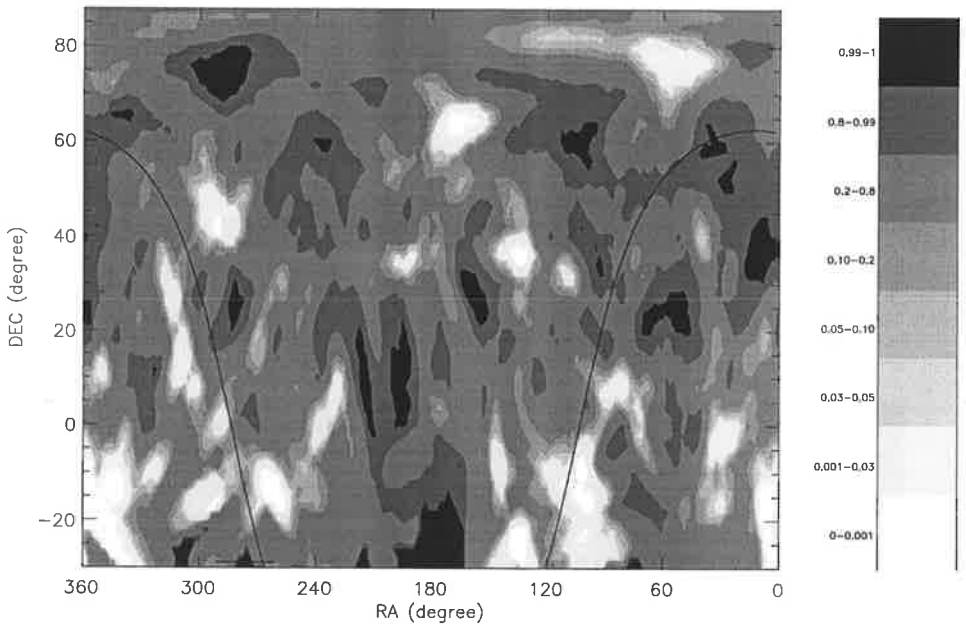

Figure 8.35: Probability of having by chance a greater or equal number of events (events above 10^{19} eV) within each bin (Significance map). An smearing size of 5° was used. This smearing size maximizes the excess regions of interest (RA=170°, DEC=62° and RA=140°, DEC=36°).

8.2.3 Cosmic rays with energies above 4×10^{19} eV

Only 30 events were detected by HiRes-1 in this energy range. With these low statistics there is not much we can conclude. However, there are a few things we can do:

1. Look to see if there is any clustering of events (especially triplets).
2. Check whether any of the events are consistent with the '*a priori*' source candidates for this energy range - the AGASA triplet and the galaxy M-87 (Virgo-A) [105].
3. Look whether the events show any broad correlation with the supergalactic plane, also an *a priori* target. (see chapter 2 for details).

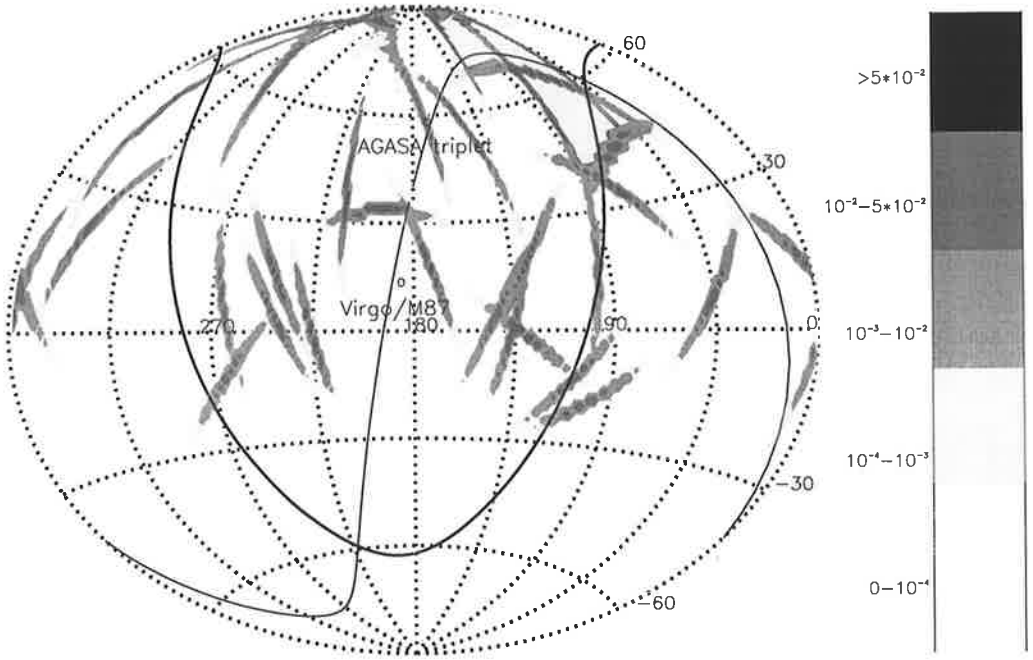

Figure 8.36: Event density map for the highest energy ($> 4 \times 10^{19}$ eV) HiRes-1 monocular events (30 events). The map is in equatorial coordinates. The small circles show the '*a priori*' source candidates (the AGASA triplet and the galaxy M-87). The solid lines show the galactic (thicker line) and supergalactic (thinner line) planes.

The reconstructed directions of the HiRes-1 monocular events are well defined within the respective SDPs. Figure 8.36 shows the reconstructed arrival directions of the 30 events with energies above 4×10^{19} eV. Each arrival direction is represented by a two dimensional Gaussian probability function. The projection of each Gaussian probability function on the RA, DEC plane has an elliptical shape. The bigger axis of the ellipse corresponds to the SDP projection on the sky. Note that despite the poor angular resolution of an individual event, the intersection of three ellipses would define with good resolution a clustering region. However, due to the elongated nature of the ellipse errors, several intersections of two ellipses are expected to happen by chance. Therefore, we will not look for doublets.

In figure 8.36 approximately at RA= 130°, DEC= 20° three ellipses intersect. One of the ellipses happens to correspond to the only event with an energy above 10^{20} eV. The intersection of ellipses near the pole region is not considered. This is because at that region more intersections are expected by chance.

Figure 8.36 also shows that the arrival direction of one HiRes-1 monocular event is consistent with the AGASA triplet. Considering the HiRes exposure, the probability of having by chance one event (out of 30 events) consistent (within 2.5°) with the AGASA triplet is 0.04. None of the HiRes-1 events show evidence of coming from the galaxy M-87 (Virgo A).

The same technique used by Stanev [57] and Kewley [58] (see page 33 for details) was used to evaluate any correlation with the galactic or supergalactic planes.

To calculate $<| b^G |>$ and $<| b^{SG} |>$, each arrival direction in the real data (data) and in a MC simulated data (MC) was represented by 100 points. The points were distributed around the reconstructed arrival direction following an elliptical Gaussian probability function. Then, each point was considered as one independent event. In this way we consider in the analysis the errors on the reconstructed arrival directions. The calculation of "P" is explained on page 33.

Table 8.1 shows the evaluation for HiRes-1 events ($E > 4 \times 10^{19}$ eV) clustering toward the galactic and supergalactic planes. Considering table 8.1, a value of P

close to 0 indicates a correlation and a value close to 1 indicates an anti-correlation. The calculation of "P" is explained on page 33. The HiRes-1 data do not show any significant correlation or anti-correlation with the galactic or supergalactic planes.

no. of events	b^G_{rms}			b^{SG}_{rms}			$<\mid b^G \mid>$			$<\mid b^{SG} \mid>$		
	data	MC	P	data	MC	P	data	MC	P	data	MC	P
30	36.6	38.3	0.31	41.3	37.54	0.84	29.8	32.1	0.26	34.6	30.98	0.83

Table 8.1: Tests for HiRes-1 energetic events ($> 4 \times 10^{19}$ eV) clustering toward the galactic and supergalactic planes. The calculation of P is explained on page 33.

8.3 Preliminary HiRes stereo results

In this section the author will present a preliminary anisotropy analysis of the HiRes stereo events. The reason it is considered preliminary is that the stereo data may be incomplete. The stereo data set provided by colleagues at the University of Utah was used.

In a recent HiRes collaboration meeting, it was pointed out that the University of Columbia had an stereo data set approximately twice as large as the stereo data set available at the University of Utah. The reason for having a different number of stereo events in the two data sets may be related to different quality cuts and to different stereo event matching processes. Currently there is an ongoing job of reviewing the stereo data set at the University of Utah [109].

The data set used for the current analysis has 998 events with energies above 10^{18} eV that passed successfully the reconstruction process (no extra cuts were applied). Figure 8.37 shows the density sky map of the reconstructed arrival directions. From the monocular analysis we learnt that, if the density map has many regions with no events, the excess and significant maps become less useful. The stereo density sky map has many regions with no events. Therefore, the stereo significance map (fig. 8.38) mainly shows the reconstructed arrival directions.

In order to look for regions with possible excesses of cosmic rays, we have used a smearing circle of 15° radius. This smearing size was not selected to maximize a particular excess region. It was selected in order to reduce the regions with no events at the density sky map. Figure 8.39 shows the significance map using the 15° smearing size. This map shows the regions with possible excesses of cosmic rays. A dataset with better statistics would be necessary to decide whether those excess regions are consistent with a point source, an astrophysically smeared source or with statistical fluctuations. Note that both excess regions observed in figure 8.27 (mono events between $10^{18.0}$ and $10^{18.5}$ eV) are also present in figure 8.39. This is remarkable since the mono and stereo data sets are quite different. The stereo data set is not completely a subset of the mono dataset. This is because there are different trigger requirements and quality cuts for stereo events (less demanding). Therefore, 80% of the stereo events are not part of the HiRes-1 monocular data set.

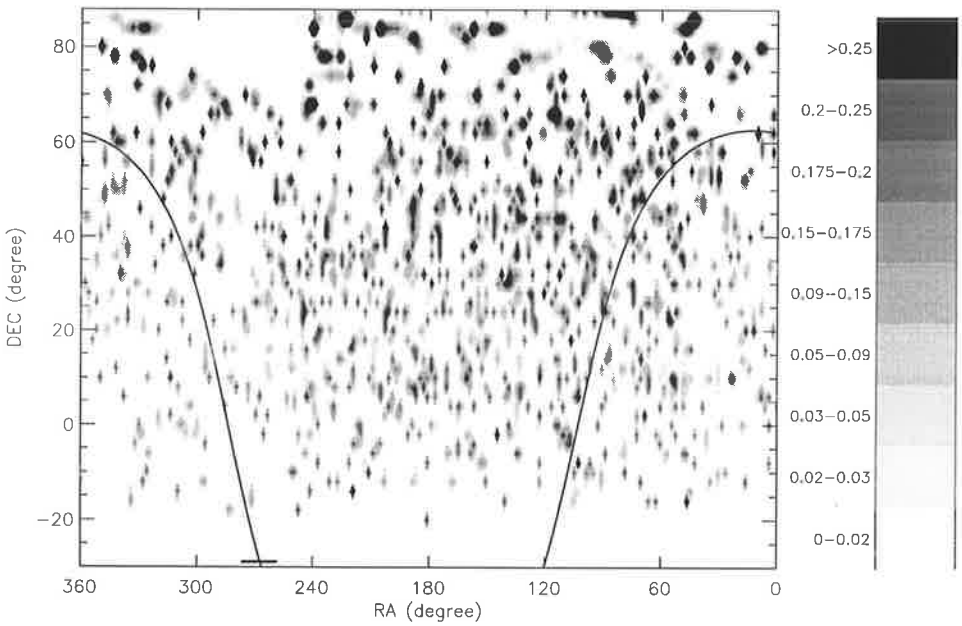

Figure 8.37: Event density map (events per square degree) for the stereo events with energies above 10^{18} eV (998 events). The map is in equatorial coordinates.

Figure 8.40 shows the stereo and mono events with energies above 4×10^{19} eV. Also in this map the AGASA events with energies above 10^{20} eV are shown. Notice

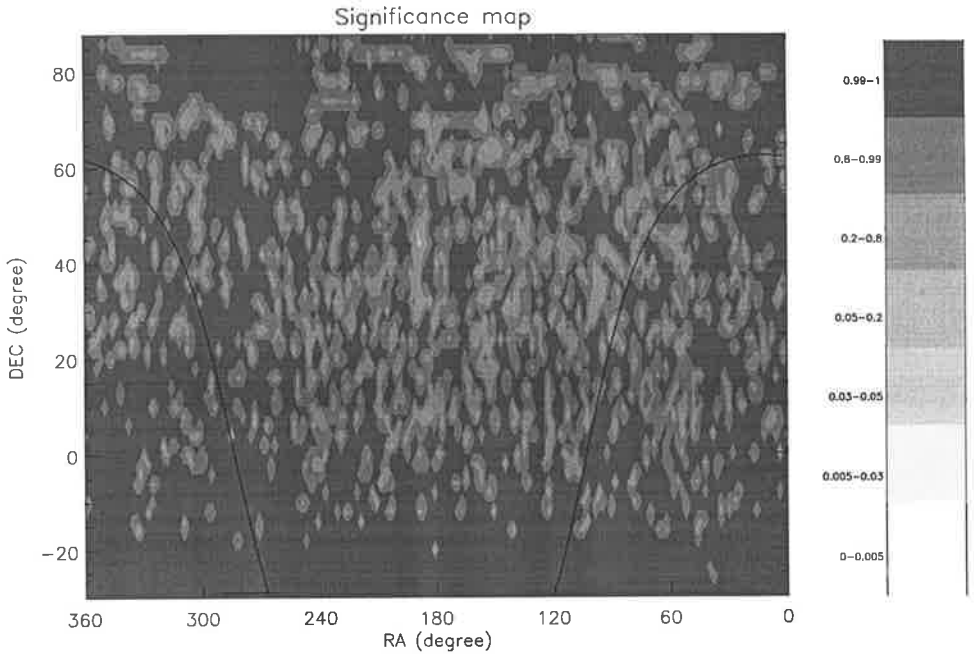

Figure 8.38: Significance map for the HiRes stereo events above 10^{18} eV. The background was estimated using the traditional time shuffling technique.

that there is one stereo event at approximately RA= 130°, DEC= 20°. This point corresponds to the interception of three mono event error functions. The stereo event is different from the three mono events. Also one of the AGASA event is in the nearby region (6° away).

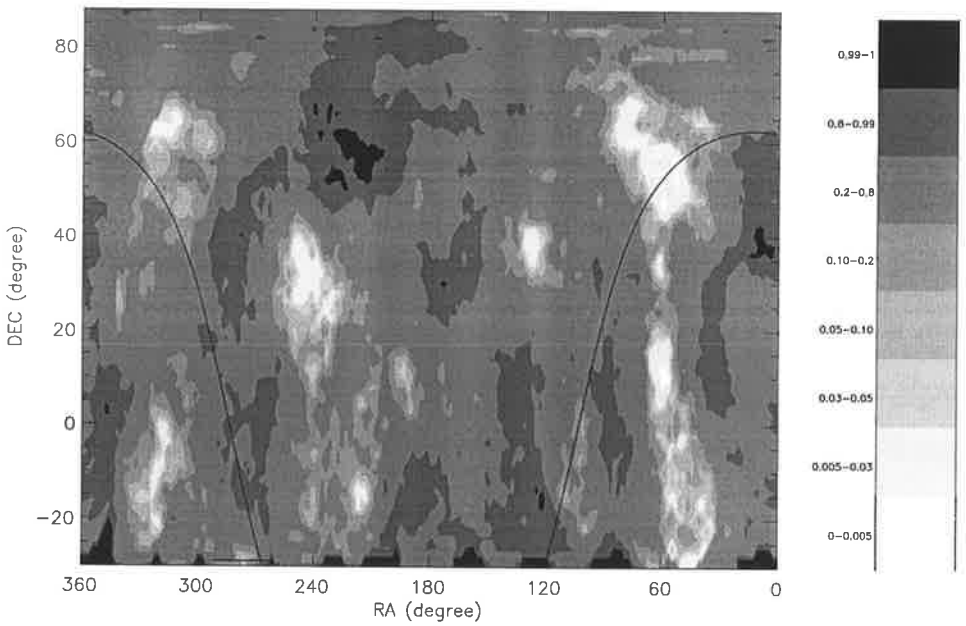

Figure 8.39: Significance map for the HiRes stereo events above 10^{18} eV using a 15° radius smearing size.

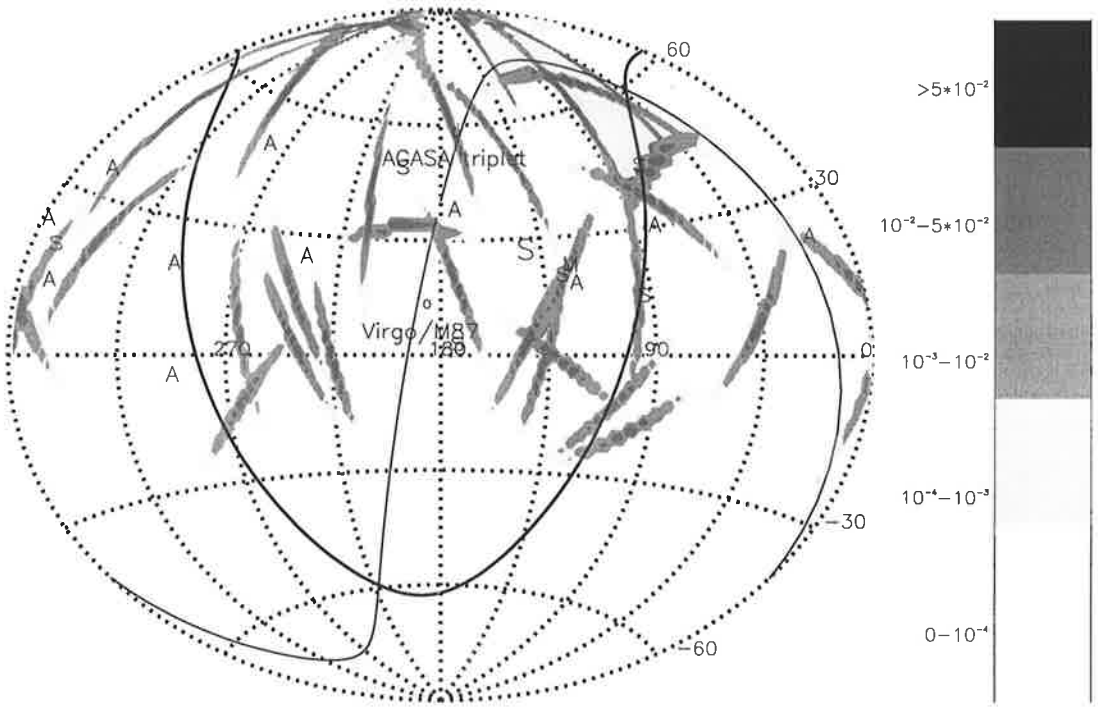

Figure 8.40: Event density map for the mono events with energies above 4×10^{19} eV (30 events). Capital 'M' indicates the reconstructed arrival direction of the single mono event above 10^{20} eV. Also is shown in the map the arriving directions of the 7 stereo events above 4×10^{19} eV (small 's'). The bigger 'S' is for the highest energy stereo event. The arriving directions of the 11 AGASA events above 10^{20} eV are indicated with the letter 'A'. The locations of the AGASA triplet and Virgo/M87 are indicated with small circles. There is one mono event overlapping with the AGASA triplet. The estimated probability of having by chance an ellipse intercepting with the AGASA triplet within 2.5° is 0.04. The map is in equatorial coordinates. The solid lines indicate the galactic (thicker line) and supergalactic (thinner line) planes.

Chapter 9

Summary and Conclusions

The aim of this thesis was to study the arrival directions of the EHECR ($E > 10^{18}$ eV) using the HiRes fluorescence detector. The HiRes data set is classified into monocular and stereo data. The shower reconstruction process is different for each data set. Therefore the reconstruction resolution is also different, with stereo reconstruction being more precise.

In order to perform anisotropy studies with the HiRes data, it was necessary to characterize the monocular and stereo uncertainties in the reconstructed directions. The monocular uncertainty is distributed within the SDP projection on the sky, forming elongated ellipses. By comparing the monocular reconstruction with Monte Carlo inputs and stereo reconstruction, the monocular error sizes were estimated. The suggested sizes of the ellipse errors (in terms of uncertainty in ψ) as a function of the shower energy are summarized in table 6.1. A systematic shift in the monocular reconstructed arrival directions was found. The angle ψ which determines the orientation of the shower axis within the SDP was being underestimated. The suggested systematic ψ angle corrections are also summarized in Table 6.1. No corrections were found necessary for events with energies above $10^{18.5}$ eV.

The estimated uncertainties for the stereo reconstruction were calibrated using vertical flashers and laser shots. The stereo uncertainty depends strongly on the geometry of the shower (and does not depend on the energy of the shower). However, even for

the worst geometries for stereo reconstruction (those showers with small opening angles), the stereo resolution is better than the monocular one. The stereo resolution is better than 0.3° for events with opening angles larger than 20°. For events with opening angles between 5° and 20° the stereo resolution is better than 1°. For events with opening angles smaller than 5° the stereo resolution is better than 3° (see figure 7.4, right hand side plot).

For the HiRes anisotropy analysis using skymaps three energy ranges were selected *a priori*. These energy ranges are 10^{18} eV $< E < 10^{18.5}$ eV, $10^{18.5}$ eV $< E < 10^{19}$ eV and $E > 10^{19}$ eV. The HiRes-1 monocular data contained within these energy ranges were 2309 , 920 and 341 events respectively (after applying quality cuts). Using the shower density contour technique, we searched for point sources and astrophysically smeared sources. We also had some *a priori* source candidates, Cygnus X-3 ($E \geq 10^{18}$ eV), the AGASA triplet ($E > 4 \times 10^{19}$ eV), the galaxy M-87 (Virgo A) ($E > 4 \times 10^{19}$ eV) and the supergalactic plane ($E > 4 \times 10^{19}$ eV)[105].

Despite the poor resolution of the HiRes-1 monocular reconstruction, the monocular data may still be sensitive to point sources. The point source direction can be determined with a resolution better than 1°. However because of the poor monocular resolution, the standard shower density contour plots technique is less sensitive to astrophysically smeared sources. The author showed in chapter 8 that a variation of the technique (using smearing circles) may increase the sensitivity to astrophysically smeared sources.

The results of the HiRes anisotropy studies are:

1. No clear evidence of point sources was observed. This may be due to the limited statistics and to the poor monocular resolution.

2. Some evidence of astrophysically smeared sources was observed.

   (a) **Events with energies between 10^{18} eV and $10^{18.5}$ eV:** At this energy range two significant excesses were observed (fig. 8.27). The direction of the excesses are RA=110°, DEC=39° and RA=242°, DEC=40° respectively.

The smearing sizes are consistent with a 20° and 15° radius respectively. The estimated chance probability of having one excess with similar characteristics anywhere in the HiRes sky is 0.0074. And the estimated chance probability of having two excesses in the HiRes sky is lower than 0.0002.

(b) **Events with energies between $10^{18.5}$ eV and 10^{19} eV:** At this energy range a few significant excesses were observed (fig. 8.28). Most of them may be the result of small statistics. However, the excess at RA=139°, DEC=47° is around the direction of one of the excesses observed in the lower energy range (RA=110°, DEC=39°). The smearing size of this excess is consistent with a 10° radius. Since this direction was already identified as a region of interest, the estimated chance probability of having such excess in that particular direction becomes relevant. This probability is lower than 0.001.

(c) **Events with energies above 10^{19} eV:** As the energy increases the statistics become smaller. In order to work properly, the contour plots technique requires a skymap completely populated with events. Otherwise false excesses may appear. This may be the reason for having several apparent excesses in this energy range (fig. 8.35). Two of the excesses in this energy range are consistent with regions of interest. One excess is at RA=170°, DEC=62°, which is 5° away from the AGASA triplet. The other excess is at RA=140°, DEC=36°, with excesses from that direction also observed in lower energy ranges. Both excesses are consistent with a smearing of 5° radius. The chance probabilities of having such excesses at those particular regions are lower than 0.001 in both cases.

(d) **Stereo events with energies above 10^{18} eV:** The stereo data set has only 998 events above 10^{18} eV (events that successfully passed the reconstruction process). In order to identify regions of possible excesses, despite the small statistics, we used a smearing circle of 15° radius. The analysis

showed six possible excess regions (fig. 8.39). Two of them are consistent with the two excesses observed in the energy range between 10^{18} eV and $10^{18.5}$ eV. The chance probability of observing such excesses at those particular regions in the stereo data are between 0.005 and 0.03 in each case.

Apart from the requirements of a successful stereo reconstruction, no extra quality cuts were applied. The cuts applied to the monocular data were not applied to the stereo data. Therefore, 80% of the stereo events are not part of the monocular dataset. This means that there is not a large overlap between the monocular and stereo data sets used for the analysis.

The analysis showed an apparent astrophysically smeared source at the region around RA=130°, DEC=40°. This source is observed at different energy ranges, and apparently with different smearing sizes. Table 9.1 shows the estimated 95% upper limits[71] on the smeared source flux.

Energy Range log(E) (eV)	size of the anisotropy region (radius)	location of the anisotropy region (RA,DEC)	observed number of events	expected number of events	95% upper limit source flux in terms of the background CR flux
18 < E < 18.5	20 deg	(110°,39°)	200	155	0.44
18.5 < E < 19	10 deg	(139°,47°)	28	16	1.3
E > 19	5 deg	(140°,36°)	3.25	1.22	5.2

Table 9.1: Estimated 95% upper limits of the source flux observed at around RA=130°, DEC=40°.

3. No evidence of any excess of cosmic rays from Cygnus X-3 was observed.

4. **Monocular and stereo events above 4×10^{19} eV:** There are 30 monocular events and 7 stereo events. The ellipse error of one of the monocular events overlaps with the AGASA triplet direction (fig. 8.40). The estimated chance

probability for that overlap is 0.04. There is no event coming from the direction of the galaxy M-87, and no correlation was found with the supergalactic plane.

A clustering region appears at approximately RA= 130°, DEC= 20° (fig. 8.40). This region is the intersection of three mono event error functions and one stereo event. The stereo event is not the same event as any of the three mono events. Also, one of the AGASA events with energy above 10^{20} eV is in the nearby region (6° away).

This analysis has shown possible regions of astrophysically smeared sources and possible clusterings of energetic events. The astrophysically smearing may appear because charged cosmic rays are deflected by turbulent magnetic fields. This diffusing process would be more effective for lower energy cosmic rays. For cosmic rays with energies above $\approx 4 \times 10^{19}$ eV we expect a negligible diffusion of the trajectories, provided that the particles are protons. Note that in our analysis of the possible astrophysically smeared sources the observed diffusion appears to be correlated with the cosmic ray energy in a way that one would expect.

Appendix A

Fermi Acceleration

In 1949 Enrico Fermi first proposed what became known as second order Fermi acceleration[110]. In this scenario clouds of magnetized plasma move in the interstellar medium (ISM). These clouds are believed to populate several percent of the ISM. When a particle is trapped inside these magnetized clouds, the particle begins to diffuse due to the random irregularities of the magnetic field. This is an elastic process, so no energy is lost. The particle may escape the cloud, and gain or lose energy in this process. However, as it is shown below, on average particles gain energy.

Consider Fig. A.1. In the rest frame of the moving cloud the incoming cosmic ray particle has total energy

$$E_1' = \gamma(E_1 - Vcos(\theta_1)p_1), \tag{A.1}$$

where $\gamma = \frac{1}{\sqrt{1-\beta^2}}$ and $\beta = \frac{V}{c}$ are the Lorentz factor of the cloud, V is the cloud velocity, and the primes denote quantities measured in the frame moving with the cloud. The angle θ_1 is shown in Fig. A.1. Assuming that the particle is already sufficiently relativistic so that $E \approx pc$ or $p \approx E/c$, equation A.1 can be written as

$$E_1' = \gamma E_1(1 - \beta cos(\theta_1)). \tag{A.2}$$

The energy of the particle just before escaping the cloud is

$$E_2' = E_1' \tag{A.3}$$

(since it is an elastic process), where E_1' is the particle energy in the cloud frame just after entering to the cloud. The energy of the particle in the laboratory frame just after escaping the cloud is

$$E_2 = \gamma E_2'(1 + \beta cos(\theta_2')), \tag{A.4}$$

the angle θ_2 is also shown in figureA.1.

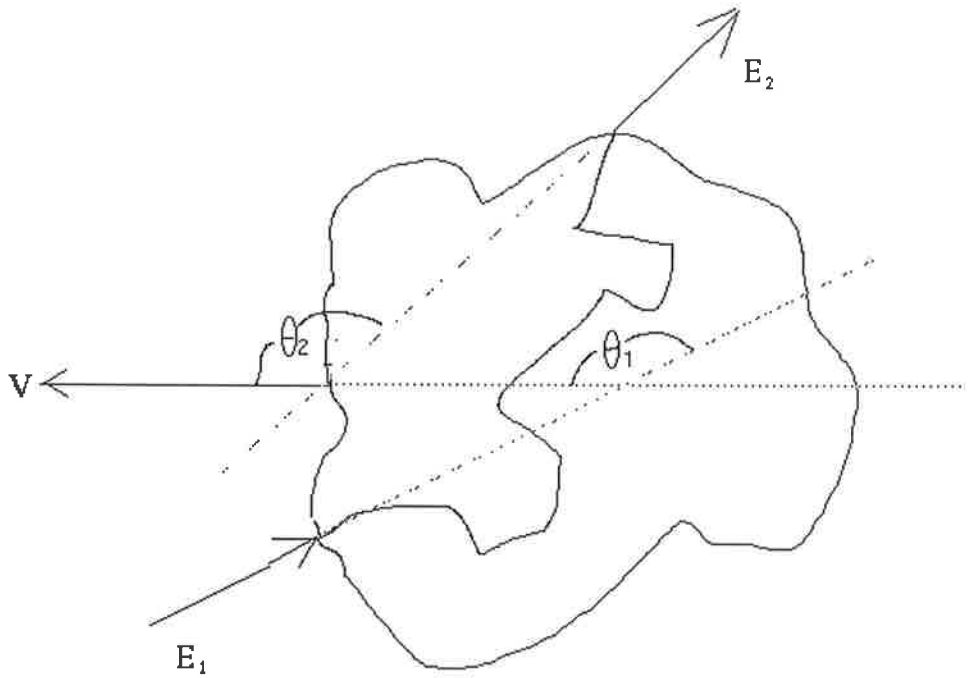

Figure A.1: Accelaration by a moving magnetized cloud. θ_1 and θ_2 are the relative angles which the particles enter and leave the cloud. E_1 and E_2 are the particle energies before and after interacting with the magnetized cloud, and V is the cloud velocity

Substituting equations A.2 and A.3 into equation A.4 we obtain the particle energy change for the encounter characterized by θ_1 and θ_2'

$$\frac{E_2 - E_1}{E_1} = \frac{\Delta E}{E_1} = \frac{1 - \beta cos(\theta_1) + \beta cos(\theta_2') - \beta^2 cos(\theta_1) cos(\theta_2')}{1 - \beta^2} - 1. \tag{A.5}$$

The average energy change per encounter is obtained by replacing the average values

of $cos(\theta_1)$ and $cos(\theta_2')$ into equation A.5. The average cosines are obtained evaluating

$$< cos(\theta_i) >= \frac{\int cos(\theta_i)\frac{dP}{d\Omega_i}d\Omega_i}{\int \frac{dP}{d\Omega_i}d\Omega_i} \tag{A.6}$$

where $\frac{dP}{d\Omega_i}$ is the probability per unit solid angle of having a collision at angle θ_i [111] and $d\Omega_i$ is the differential of solid angle

$$d\Omega_i = \sin\theta_i d\theta_i. \tag{A.7}$$

For clouds, the probability of having a collision at angle θ_1 is proportional to the relative velocity between the cloud and the particle

$$\frac{dP}{d\Omega_1} \propto u - V cos(\theta_1), \tag{A.8}$$

for relativistic particles $u \simeq c$ then

$$\frac{dP}{d\Omega_1} \propto (1 - \beta cos(\theta_1)), \qquad -1 < cos(\theta_1) < 1. \tag{A.9}$$

When the particle is inside the cloud the probability of escaping in any direction is the same, then

$$\frac{dP}{d\Omega_2'} = constant, \qquad -1 < cos(\theta_2') < 1. \tag{A.10}$$

Substituting equations A.9 and A.10 into equation A.6 respectively, we obtain the average cosines $< cos(\theta_1) >_{2nd} = -\frac{\beta}{3}$ and $< cos(\theta_2') >_{2nd} = 0$, where the subscript '2nd' denotes Fermi 2nd order acceleration. Then the average energy change (eq. A.5) per encounter is

$$\xi = \frac{1 + \frac{1}{3}\beta^2}{1 - \beta^2} - 1 \sim \frac{4}{3}\beta^2, \tag{A.11}$$

an encounter is defined as one complete cycle (into and out of the cloud). Notice that the energy change goes as the square of β, hence the name of second order acceleration.

In the 1970's a modified Fermi acceleration process was introduced[112]. This is the shock wave acceleration or Fermi first order acceleration (see section 1.1.1.2 for a description). In shock wave acceleration the magnetized cloud is replaced by a shock wave. Figure A.2 shows the geometry of this scenario. For shock acceleration, equation

A.5 is still valid. However the probability functions of having collisions at angles θ_i are

$$\frac{dP}{d\Omega_1} \propto cos(\theta_1), \qquad -1 < cos(\theta_1) < 0 \tag{A.12}$$

and

$$\frac{dP}{d\Omega_2'} \propto cos(\theta_2'), \qquad 0 < cos(\theta_2') < 1. \tag{A.13}$$

Replacing equations A.12 and A.13 into equation A.6, we obtain the average cosines values $< cos(\theta_1) >_{1st} = -\frac{2}{3}$ and $< cos(\theta_2') >_{1st} = \frac{2}{3}$ (the subscript '1nd' denotes Fermi 1nd order acceleration). Finally, replacing these values in equation A.5, the average energy change per encounter in shock acceleration is

$$\xi = \frac{1 + \frac{4}{3}\beta + \frac{4}{9}\beta^2}{1 - \beta^2} - 1 \sim \frac{4}{3}\beta = \frac{4}{3}\frac{V}{c}, \tag{A.14}$$

where $V = -u_1 + u_2$ in this case is interpreted as the velocity of the shocked gas ("downstream") relative to the unshocked gas ("upstream"). This process has the energy gain proportional to β (Fermi 1nd order acceleration) and is hence much more efficient than Fermi's original second second order process.

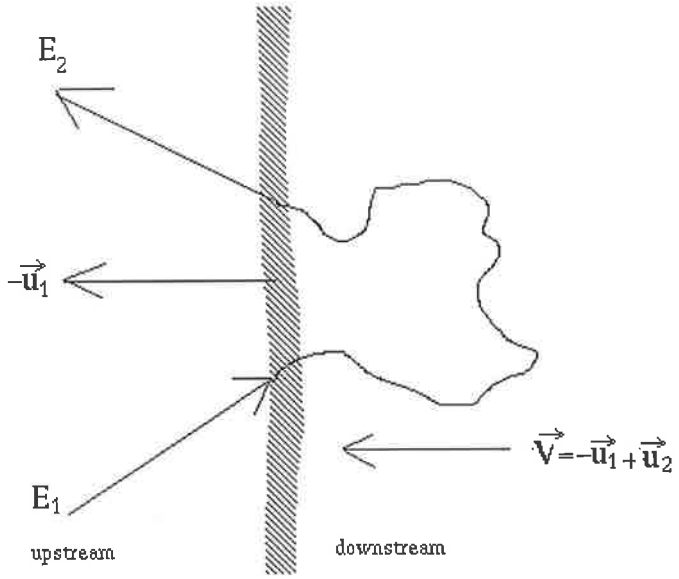

Figure A.2: Acceleration at a shock wave.

Appendix B

The Profile Constrained Geometry Fit (PCGF)

HiRes-1 mono data use information from the shower development as well as timing information to determine the event geometry. This is known as the Profile Constrained Geometry Fit (PCGF) method. Fundamentally we compare the observed tube amplitudes with expected tube amplitudes, and the observed times with expected times, given a trial shower profile with a trial geometry. The tube signal amplitudes are compared using a χ^2 function given by:

$$\chi^2_{pfl} = \sum \frac{1}{\sigma_i^2}(S_i^{(m)} - S_i^{(p)})^2 \tag{B.1}$$

where the sum is over triggered tubes. The terms $S_i^{(m)}$ and $S_i^{(p)}$ are the measured and predicted tube signals respectively. The tube signals are given in photo-electrons. The σ_i^2 terms are obtained by adding in quadrature the Poisson fluctuation in the signal ($\sqrt{S^{(m)}}$) and the sky background fluctuation. The sky background fluctuation measured *in situ* was 200 pe for a 5.6μs integration window, so:

$$\sigma_i^2 = S_i^{(m)} + 200 \tag{B.2}$$

The predicted tube signals depend on the Gaisser-Hillas shower profile parameters

(X_0, X_{max}, and N_{max}) and on the shower geometry parameters (R_p, ψ and the SDP).

In PCGF fitting, the parameter X_0 is fixed to $X_0 = 40$ g cm^{-2}, reducing the number of free parameters. The value used for X_0 represents an average over proton and iron showers. In addition, the parameter X_{max} is constrained to the following values: 685, 720, 755, 790, 825, or 860 g cm^{-2}. The range of values for X_{max} takes into account that a 10^{18} eV proton shower has an average X_{max} of 725 g cm^{-2}, and a 10^{20} eV proton shower has an average X_{max} of 835 g cm^{-2} (based on MC results). The geometry that minimizes the χ^2_{pfl} is estimated for each of the six values of X_{max}.

The χ^2_{pfl} minimization is carried out in two steps.

- Step 1: In step 1 the SDP is kept fixed. The parameters R_p and ψ are related by the timing equation (eq. B.3).

$$t_i = t_0 + \frac{R_p}{c} tan\left(\frac{\pi - \psi - \chi_i}{2}\right) \tag{B.3}$$

  where t_0 is the time at which the shower passes the point of closest approach, R_p is the distance to the point of closest approach, ψ is the inclination angle of the track within the SDP, and χ_i is the tube viewing angle. This relation is used to calculate R_p for a given ψ.

  The profile χ^2 is linear in N_{max}, the shower size at maximum development. So, N_{max} is uniquely determined for any trial shower when all other parameters have been specified. A trial shower of "standard size" is used during the search. Then the predicted tube signals are scaled up or down by a constant factor to minimize χ^2_{pfl}.

  The angle ψ is now the single free parameter remaining. Thus, the χ^2_{pfl} is minimized by performing a search in ψ. The angle ψ is restricted to the range (0,180°). A first rough search over the entire range of ψ is performed using steps of 1°. The ψ angle that minimizes the χ^2_{pfl} is used as a "first guess" for a more refined search.

- Step 2: In step 2, a refined search in ψ is performed. The search is carried out

in the neighbourhood of the "first guess" estimated in step 1. This search is performed using the *amoeba* minimization routine, which implements the downhill simplex method. In this search, the SDP normal is allowed to change (within a limited range), and finer steps in ψ are taken.

At this stage we have the shower geometry that minimizes the χ^2_{pfl} for each given X_{max} (we have six geometries). Each of these geometries are used to estimate the timing χ^2 (eq. 7.11). The choice of the best geometry is now made according to which fit minimizes a combined $\chi^2_{com} = \chi^2_{pfl} + \chi^2_{tim}$ function.

References

[1] R. M. Barnett *et al.* [Particle Data Group Collaboration], "*Review of particle physics. Particle Data Group*," Phys. Rev. D **54**, 1 (1996).

[2] P. Bhattacharjee, "*Ultrahigh energy cosmic rays from topological defects: Cosmic strings, monopoles, necklaces, and all that*," arXiv:astro-ph/9803029.

[3] S. L. Dubovsky and P. G. Tinyakov, "*Violation of Lorentz invariance and neutral component of UHECR*," Astropart. Phys. **18**, 89 (2002) [arXiv:astro-ph/0106472].

[4] H. Sato, "*Extremely high energy and violation of Lorentz invariance*," arXiv:astro-ph/0005218.

[5] L. A. Anchordoqui, J. L. Feng, H. Goldberg and A. D. Shapere, "*Black holes from cosmic rays: Probes of extra dimensions and new limits on TeV-scale gravity*," Phys. Rev. D **65**, 124027 (2002) [arXiv:hep-ph/0112247].

[6] "*Cosmic Bullets: High Energy Particles in Astrophysics*," by Roger Clay & Bruce Dawson (Addison-Wesley), (1997).

[7] X. Bertou, M. Boratav and A. Letessier-Selvon, "*Physics of extremely high energy cosmic rays*," Int. J. Mod. Phys. A **15**, 2181 (2000) [arXiv:astro-ph/0001516].

[8] D. J. Bird *et al.* "*Study of Broad-Scale Anisotropy of Cosmic-Ray Arrival Directions from* 2×10^{17} *to* 10^{20} *Electron Volts from Fly's Eye Data*,", Ap. J. **511**, 739 (1999).

[9] M. Takeda *et al.* "*Small-Scale Anisotropy of Cosmic Rays above* 10^{19} *eV Observed with the Akeno Giant Air Shower Array*," Ap. J., **522**, 225 (1999).

[10] P. Bhattacharjee and G. Sigl, "*Origin and propagation of extremely high energy cosmic rays*," Phys. Rept. **327**, 109 (2000) [arXiv:astro-ph/9811011].

[11] OWL experimet web page, `http://owl.gsfc.nasa.gov/science.html`

[12] EUSO experimet web page, `http://www.ifcai.pa.cnr.it/~EUSO`

[13] A.M.Hillas, "*The origin of ultra-high energy cosmic rays*," Ann. Rev. Astron. Astrophysics., **22**, 425 (1984)

[14] M. Ostrowski, "*Mechanisms and sites of ultra high energy cosmic ray origin*," Astropart. Phys. in press [arXiv:astro-ph/0101053].

[15] P. Blasi, R. I. Epstein and A. V. Olinto, "Ultra-High Energy Cosmic Rays From Young Neutron Star Winds," Astrophys. J. **533**, L123 (2000) [arXiv:astro-ph/9912240].

[16] E. Boldt and P. Ghosh, "Cosmic rays from remnants of quasars?," arXiv:astro-ph/9902342.

[17] "*Cosmic Rays and Particle Physics*," by Thomas K. Gaisser, (Cambrige University press) (1990).

[18] J.P. Rachen and P.L. Biermann, "*Extragalactic ultra-high energy cosmic rays*," Astron. Astrophys. **272**, 161 (1993)

[19] L. C. Drury, "*An introduction to the theory of diffusive shock acceleration of energetic particles in tenuous plasmas*," Rep. Prog. Phys. **46**, 973 (1983)

[20] M. Vietri, "*On the acceleration of ultrahigh-energy cosmic rays in gamma ray bursts*," Astrophys. J. **453**, 883 (1995) [arXiv:astro-ph/9506081].

[21] E. Waxman, "*Cosmological gamma ray bursts and the highest energy cosmic rays*," Phys. Rev. Lett. **75**, 386 (1995) [arXiv:astro-ph/9505082].

[22] V. Berezinsky, "*Ultra high energy cosmic rays*," Nucl. Phys. Proc. Suppl. **70**, 419 (1999) [arXiv:hep-ph/9802351].

[23] S. L. Dubovsky and P. G. Tinyakov, "*Galactic anisotropy of ultra-high energy cosmic rays produced by CDM-related mechanisms*," arXiv:hep-ph/9810401.

[24] V. Berezinsky, M. Kachelriess and A. Vilenkin, "*Ultra-high energy cosmic rays without GZK cutoff*," Phys. Rev. Lett. **79**, 4302 (1997) [arXiv:astro-ph/9708217].

[25] T. W. Kibble, "*Topology Of Cosmic Domains And Strings*," J. Phys. A **9**, 1387 (1976).

[26] P. P. Kronberg, Q. W. Dufton, H. Li and S. A. Colgate, "*Magnetic Energy of the Intergalactic Medium from Galactic Black Holes*," ApJ **560**, 178 (2001) [arXiv:astro-ph/0106281].

[27] P. P. Kronberg, Rep. Prog. Phys. **57**, 325 (1994)

[28] Günter Sigl, Martin Lemoine and Peter Biermann "*Ultra-high energy cosmic ray propagation in the local supercluster*," APh. **10**, 141 (1999)

[29] Y. Uchihori, M. Nagano, M. Takeda, M. Teshima, J. Lloyd-Evans and A. A. Watson, "*Cluster analysis of extremely high energy cosmic rays in the northern sky*," Astropart. Phys. **13**, 151 (2000) [arXiv:astro-ph/9908193].

[30] R. Lampard, R.W. Clay, B.R. Dawson, "*Limits on Source Distances for the Most Energetic Cosmic Rays in Intergalactic Magnetic Fields*," Astropart. Phys. **7**, 213 (1997)

[31] R.W. Clay, S. Cook, B.R. Dawson, A.G.K. Smith, R. Lampard, "*The angular deviation of ultra high energy cosmic rays in intergalactic mahnetic fields*," Astropart. Phys. **9**, 221 (1998)

[32] *The Pierre Auger Project Design Report*, Fermilab, October 1995 (Web site: `www.auger.org/admin/`).

[33] Kenneth Greisen, "*End of the Cosmic-Ray Spectrum?*," Phys. Rev. Lett., **16**, 748 (1966)

[34] Zatsepin, G. T., & Kuzmin, V. A. 1966, Zh. EKsp. Teor. Fiz., **4**, 114 (Soviet Phys.- JETP Lett., **4**, 78)

[35] J. Knapp, D. Heck, S. J. Sciutto, M. T. Dova "*Extensive air shower simulations at the highest energies*," APh. In Press

[36] J. Kempa and M. Samorski, " *The investigation of the structure of extensive air shower cores*," Nucl. Phys. B Proc. Suppl. **75**, 262 (1999)

[37] R. N. Coy, G. Cunningham, C. L. Pryke and A. A. Watson, " *The lateral distribution of extensive air showers produced by cosmic rays above* 10^{19} *eV as measured by water-cerenkov detectors*," APh, **6**, 263 (1997)

[38] J. Linsley, L. Scarsi, and B. Rossi, "*Energy Spectrum and Structure of Large Air Showers*," J.Phys. Soc. Japan, (supp. A-III) **17**, 91 (1962)

[39] J. Linsley, "*Evidence for a Primary Cosmic-Ray Particle with energy* 10^{20} *eV*," Phys.Rev.Lett. **10**, 146 (1963)

[40] M.A Lawrence, R.J.O. Reid, and A.A. Watson, "*The Cosmic Ray Energy Spectrum above* 4×10^{17} *eV as measured by the Haverah Park array*," J. Phys., **G17**, 733 (1991)

[41] M.M. Winn *et al.*, "*The cosmic-ray energy spectrum above* 4×10^{17} *eV* ," J. Phys., **G12**, 653 (1986)

[42] N.N. Efremov *et al.* Extremely High Energy Cosmic Rays: Astrophysics and Future Observations, ed by M. Nagano, (Institute for Cosmic Ray Research, University of Tokyo), 418 (1996)

[43] R.M Baltrusaitis *et al.*, "*The Utah Fly's Eye Detector*", Nucl. Inst. Meth., **A240**, 410 (1985)

[44] N. Chiba, *et al.* 1992, "*Akeno Giant Air Shower Array (AGASA) covering 100* km^2 *area*," Nucl. Instr. and Meth., A **311**, 338 (1992)

[45] H. Ohoka, *et al.* "*Further development of data acquisition system of the Akeno Giant Air Shower Array*," Nucl. Inst. and Meth., A **385**, 268 (1997)

[46] J. Lloyd-Evans and A.A. Watson, Invited Talks, 8th European Cosmic Ray Symposium, Iucci *et al.* eds. Bologna (1983).

[47] N. Hayashida *et al.* "*The anisotropy of cosmic ray arrival directions around* 10^{18} *eV*," Astropart. Phys., **10**, 303 (1999) [arXiv:astro-ph/9807045].

[48] N. Hayashida *et al.* [AGASA Collaboration], "The anisotropy of cosmic ray arrival direction around 10^{18} eV," Proceedings of the 26th ICRC, Salt Lake City, 256 (1999) [arXiv:astro-ph/9906056].

[49] L.W. Jones, "Direct neutrons of over 0.5 EeV from CYGNUS X-3," Proc. 21st Int. Conf. Cosmic Rays (Adelaide), University of Adelaide, **2**, 75 (1990)

[50] Map by Y.M. Georgelin and Y.P.Georgelin(1998), Cambrige Atlas of Astronomy, ed. by J. Audouze and G.Israel, (Cambrige University Press, Cambridge), p308.

[51] G.L. Cassiday, *et al.* "*Eveidence for* 10^{18}-*eV Neutral Particles from the Direction of Cygnus X3*," Phys. Rev. Lett. **62**, 383 (1989)

[52] M. Teshima, *et al.* "*Neutral Particles from Cygnus X-3 above* 5×10^{17} *eV*," Phys. Rev. Lett. **64**, 1628 (1990)

[53] M.A. Lawrence, D.C. Prosser and A.A. Watson, "*Upper limit to the flux of neutral particles from Cygnus X-3 above* 5×10^{17} *eV*," Phys. Rev. Lett. **63**, 1121 (1989)

[54] AGASA experimet web page,
`http://www-akeno.icrr.u-tokyo.ac.jp/AGASA/results.html`

[55] J.Wdowczyk & A.Wolfendale, "*Galactic cosmic rays above* 10^{18} *eV*," J.Phys. G: Nucl.Phys. **10**, 1453 (1984)

[56] A.A.Watson, "*The Highest energy Cosmic Rays*," Nucl. Phys. B (Proc. Suppl) **22B**, 116 (1991)

[57] T. Stanev, *et al.* "*Arrival Directions of the Most Energetic Cosmic Rays*," Phys. Rev. Lett., **75**, 3056 (1995)

[58] L. J. Kewley, R. W. Clay, & B. R. Dawson, "*Arrival directions of the southern highest energy cosmic rays*," Astropart. Phys., 5, 69 (1996)

[59] Lloyd-Evans J. Ph.D thesis, University of Leeds (1982)

[60] V. S. Berezinsky, & S. I. Grigor'eve, "*A bump in the ultra-high energy cosmic ray spectrum*," , Astron. & Astrophys, **199**, 1 (1988)

[61] S. Yoshida, & M. Teshima, "*Energy Spectrum of Ultra-High Energy Cosmic Rays with Extra-Galactic Origin*," , Prog. Theor. Phys. **89**, 833 (1993)

[62] Gustavo A. Medina Tanco, "*On the Significance of the Observed Clustering of UltraHigh-Energy Cosmic Rays*," Astrophysical Journal Letters **495**, L71 (1998)

[63] N. Hayashida, *et al.* "*Possible Clustering of the Most Energetic Cosmic Rays within a Limited Space Angle Observed by the Akeno Giant Air Shower Array*," , Phys. Rev. Lett., **77**, 1000 (1996)

[64] D. J. Thompson, *et al.* ApJS **101**, 259 (1995)

[65] J.P. Huchra, M.J. Gellar and H.G. Corwin, Jr. ApJS **99**, 391 (1995)

[66] M.P. Veron-Cetty, and P. Veron, ESO Sci. Rep. 18 (1998)

[67] J. A. Bellido, R. W. Clay, B. R. Dawson and M. Johnston-Hollitt, "*Southern hemisphere observations of a* 10^{18} *eV cosmic ray source near the direction of the galactic centre*," Astropart. Phys. **15**, 167 (2001) [arXiv:astro-ph/0009039].

[68] M. Nagano *et al.*, "*Energy spectrum of primary cosmic rays above* $10^{17.0}$ *eV determined from extensive air shower experiments at Akeno*," J.Phys.G:Nucl.Phys., **18**, 423 (1992)

[69] G.L. Cassiday *et al.*, Nucl. Phys. B (Proc. Suppl.) **14A**, 291 (1990)

[70] R.G. Brownlee, "*A Directional Analysis of Very High Energy Air Showers*," Ph.D. Thesis, University of Sydney (1970).

[71] R.J. Protheroe, "Statistical analysis in gamma ray astronomy: The upper limit," Astronomy Express **1** 33 (1984)

[72] W. Reich *et al.*, in "*New Perspectives on the Interstellar Medium*", ASP Conference Series 168 (A.R. Taylor et al. eds) Astron. Soc. of the Pacific, 78 (1999)

[73] V. Schönfelder *et al.*, Astron. Astrophys. Suppl. Ser **120**, 13 (1996)

[74] R.W. Clay, "*The Propagation of Cosmic Rays from the Vicinity of the Galactic Centre*", Publ. Astron. Soc. Aust. **17**(3) (2000).

[75] Gregory C. Archbold, "*A Study of the Composition of Ultra High Energy Cosmic Rays Using The High Energy Cosmic Rays Using the High Resolution Fly's Eye*," Ph.D Thesis, University of Utah, (2001)

[76] Kevin Reil, "*The High Resolution Fly's Eye Detectors*," Ph.D Thesis, University of Utah, (2001)

[77] A. Bunner, "*The atmosphere as a Cosmic Ray Scintillator*," Ph.D Thesis, Cornell University, (1967)

[78] G. Davison and R. O'Neil, J. Chem. Phys. **41**, 3964 (1964).

[79] F. Kakimoto, E.C. Loh, M. Nagano, H. Okumo, M. Teshima, S. Ueno, "*A mearument of the air fluorescence yield*" Nucl. Instrum. Meth. A **372**, 527 (1996).

[80] John H. Boyer, Bruce C. Knapp, Eric J. Mannel, Michal Seman, "*FADC-based DAQ for HiRes Fly's Eye*", Nucl. Instrum. Meth. A **482**, 457 (2002).

[81] D. Bird, Presented at the Tokyo Worshop on Techniques for the Study of Extremely High Energy Cosmic Rays, p. 269. September 1993.

[82] S. Moore, "*Calibartion at HiRes-1*," BS Honors Thesis, Univerity of Utah (in preparation)

[83] J. H. Girard *et al.*, "*A Fiber-Optic-Based Calibration System For The High Resolution Fly's Eye Cosmic Ray Observatory*," Nucl. Instrum. Meth. A **460**, 278 (2001).

[84] "*Atmospheric Monitoring at HiRes - Hardware Systems 2*," 27th ICRC (Hamburg) **1**, 635 (2001)

[85] Tareq Ziad AbuZayyad, "*The Energy Spectrum of Ultra High Energy Cosmic Rays*," Ph.D Thesis, University of Utah (2000)

[86] M.D Roberts, "*Atmospheric analysis techniques at HiRes*," 27th ICRC (Hamburg) **1**, 645 (2001)

[87] L.R.Wiencke, "*Atmospheric Monitoring at HiRes Hardware System2*," 27th ICRC (Hamburg) **1**, 631 (2001)

[88] R.W. Clay *et al.*, "*Cloud Detection at the High Resolution Fly's Eye*," 27th ICRC (Hamburg) HE143 (2001)

[89] T.K.Gaisser and A. M. Hillas, "*Reliability of the Method of Constant Intensity Cuts for Reconstructing the Average Development of Vertical Shower*," 15th ICRC (Plovdiv) **8**, 353 (1977)

[90] Pierre Sokolsky, "*Introduction to Ultrahigh Energy Cosmic Ray Physics*," (Addison-Wesley), (1989)

[91] John A. J. Matthews, Roger Clay, "*Atmospheric Monitoring for the Auger Fluorescence Detector*," 27th ICRC (Hamburg) (2001); Auger Collaboration technical note, GAP-2001-029.

[92] T. Abu-Zayyad *et al.* [High Resolution Fly's Eye Collaboration], *"Measurement of the spectrum of UHE cosmic rays by the FADC detector of the HiRes experiment,"* arXiv:astro-ph/0208301.

[93] C. Song, Z. Cao, B. R. Dawson, B. E. Fick, W. Y. Lee, P. Sokolsky and X. Zhang, *"Energy estimation of UHE cosmic rays using the atmospheric fluorescence technique,"* Astropart. Phys. **14**, 7 (2000) [arXiv:astro-ph/9910195].

[94] T. Abu-Zayyad *et al.* [High Resolution Fly's Eye Collaboration], *"Measurement of the flux of ultrahigh energy cosmic rays from monocular observations by the High Resolution Fly's Eye experiment,"* arXiv:astro-ph/0208243.

[95] Particle Data Group, "Review of Particle Physics", The European Physical Journal, **3**, 76 (1998)

[96] J. Linsley, Proc. 18th ICRC, Bangalore, India, **12** (1983) 144

[97] C. R. Wilkinson, "*The Application of High Precision Timing in the High Fly's Eye Cosmic Ray Detector*,", Ph.D Thesis, University of Adelaide, 1998, Section 4.3.3.2.

[98] C. R. Wilkinson, "*The Application of High Precision Timing in the High Fly's Eye Cosmic Ray Detector*," Ph.D Thesis, University of Adelaide, 1998, Page 64.

[99] T. AbuZayyad, 'The Energy Spectrum of Ultra High Energy Cosmic Rays", PhD Thesis, Section 8.3.3, University of Utah (2000)

[100] J. W. Elbert, "*Track Reconstruction and Geometrical Resolution in HiRes*,". Presented at the Tokyo Worshop on Techniques for the Study of Extremely High Energy Cosmic Rays, September 1993.

[101] C. R. Wilkinson, "*The Application of High Precision Timing in the High Fly's Eye Cosmic Ray Detector*," Ph.D Thesis, University of Adelaide, 1998, Section 5.3.3.1.

[102] C. R. Wilkinson, "*The Application of High Precision Timing in the High Fly's Eye Cosmic Ray Detector*,", Ph.D Thesis, University of Adelaide, 1998, Section 5.1.1.2.

[103] J.D. Smith. et al., "*Absolute GSP Time Event Generation and Capture for Remote Locations*," Proceedings of the 27th ICRC Hamburg, (2001)

[104] William H. et al., 1992, Numerical recipes in FORTRAN (New York: Cambrige University press), Chapter 15.6.

[105] J. A. Bellido, J. Belz, B. R. Dawson, M. Schindel, and B. Stokes, "*Anisotropy Studies of Ultra-High Energy Cosmic Rays as Observed by the High Resolution Fly's Eye (HiRes)*" Proceedings of the 27th ICRC Hamburg, (2001)

[106] Ben Stokes, Ph.D Thesis, University of Utah, (to be completed in 2003)

[107] Malina A. Schindel, Ph.D Thesis, University of Montana, (in progress)

[108] Ben Stokes private communication.

[109] Zhen Cao private communication.

[110] Enrico Fermi "*On the Origin of the Cosmic Radiation*," Phys. Rev. **75** , 1169 (1949)

[111] R. J. Protheroe, "Acceleration and interaction of ultra high energy cosmic rays," arXiv:astro-ph/9812055.

[112] W.I. Axford, E. Lear and G. Skadron, 15th ICRC (Plovdiv) **11**, 132 (1977)